Fluidically-coupled dielectric elastomer actuator structures for tunable optics and microfluidics

THÈSE N° 6305 (2014)

PRÉSENTÉE LE 22 OCTOBRE 2014
À LA FACULTÉ DES SCIENCES ET TECHNIQUES DE L'INGÉNIEUR
LABORATOIRE DES MICROSYSTÈMES POUR LES TECHNOLOGIES SPATIALES
PROGRAMME DOCTORAL EN MICROSYSTÈMES ET MICROÉLECTRONIQUE

ÉCOLE POLYTECHNIQUE FÉDÉRALE DE LAUSANNE

POUR L'OBTENTION DU GRADE DE DOCTEUR ÈS SCIENCES

PAR

Luc MAFFLI

acceptée sur proposition du jury:

Prof. M. Gijs, président du jury
Prof. H. Shea, Dr S. Rosset, directeurs de thèse
Prof. F. Carpi, rapporteur
Dr J. Rossiter, rapporteur
Dr T. Scharf, rapporteur

EPFL

ÉCOLE POLYTECHNIQUE
FÉDÉRALE DE LAUSANNE

Suisse
2014

Therefore I have uttered what I did not understand
Things too wonderful for me, which I did not know
Hear, and I will speak
I will question you, and you make it known to me
— Job 42:3-4

Acknowledgements

Acknowledgements

Abstract

This thesis presents fundamental advances in Dielectric Elastomer Actuator (DEA) research by the analytical modeling, experimental validation and parameter exploration of novel actuator structures which extend the features of DEAs to out-of-plane bistable or multi-stable operation modes, miniature fluidically-coupled structures, the use of reliable liquid electrodes and high speed capabilities. Several applications of those new structures are presented and characterized in details: long lifetime tunable lenses with liquid electrodes, large tuning range lenses with high optical quality, sub-mm fluidically-coupled actuators for microfluidics and high-speed tunable lenses with the fastest response reported regardless of technology.

In the scope of manufacturing microfluidic actuators, three generations of DEAs operating in zipping mode have been built and characterized. This new actuation mode consists in electrostatically pulling the single compliant electrode of a flexible membrane towards a rigid one that covers the sloped sidewalls of a chamber. Zipping DEAs offer a set of previously unachievable features such as highly tunable bistable operation mode that may be extended to virtually any deflection versus voltage characteristic including multi-stable states. Bistable operation was predicted by an analytical model and observed on mm-size conical chambers, and vertical deflection up to $385\,\mu$m was measured on 2 mm side chambers. The analytical model is discussed by comparing the bistable zipping threshold voltages and the shape of the deflected membrane, and the role of each design parameter is discussed in details.

Application of miniature DEAs to microfluidic actuators raises a difficult challenge: the operation of DEAs in contact with liquids. Most liquids penetrate a few 10's of μm into membranes, degrading the actuator performance and leading to device failure. In the few papers which report on the use of DEAs to drive fluids, the active membranes are protected by a passive layer, at the cost of lower actuation performance. The alternative taken in this project is to couple the motion of the DEA to a passive membrane using an encapsulated liquid known as being compatible with the sensitive actuator membrane. The compatibility of 12 liquids with silicone membranes was monitored over up to 37 days and both silicone un-crosslinked bases and the ionic liquids TF_2N were found to fulfill the requirements for being used as encapsulated fluidic coupling media. Sub-mm passive membranes coupled to zipping DEAs have been fabricated and characterized. Compared to membrane passivation, this approach is more reliable and offers extended design freedom (displacement-force conversion, redirection of the motion).

Outlooks of such miniature fluidically-coupled devices powered by DEAs may be the breakthrough of silicone-based microfluidic chips by the replacement of the very successful pneu-

Abstract

matic valves of Lab-on-chips by electrically actuated ones, making this technology truly portable. Indeed, this most promising class of Lab-on-chips nowadays still require bulky off-chip pumps and pneumatic valves, preventing their use for point-of-care devices.

Research on tunable lenses is an expanding field that mostly targets the market of embedded optical systems. A wide class of those lenses relies on the deformation of a flexible transparent membrane that encloses a liquid, hence varying the focal length. This type of lenses has broad tuning ranges but the integration of a compact actuation mechanism with large displacement, fast response and low power consumption is very challenging. DEAs match these requirements with the additional advantage of being made in the same elastomer membranes, which enables a high degree of integration.

Three generations of fluidically-coupled tunable lenses have been built, characterized and compared with three analytical models. The most advanced of these models includes the hyperelastic mechanical parameters of the elastomer membrane. A simple tunable lens structure demonstrated in particular the possibility of using the ionic liquid TF_2N as reliable liquid electrode for DEAs. This is the first time that a reliable liquid electrode is used, and it opens a broad set of new design possibilities. On the second generation of devices, eight 3.9 mm diameter actuators drive a single 6.5 mm diameter lens, and tuning range of up to 60% of the focal length was achieved (from 28.5 to 45.5 mm). A last design inspired from a work published in 2011 was optimized for response speed and achieved a 0 to 90% settling time of 172 µs, the fastest response ever reported for tunable lenses regardless of technology. This device has a flat response up to 2 kHz and a resonance frequency of 4.7 kHz. Its focal length tuning range is -28% (from 19.4 to 14 mm). Detailed electrical, mechanical and optical characterizations as well as movies taken with a high-speed camera provide an in-depth understanding of the device transient response. Future application of this high-speed lens may include light sheet microscopy or real-time shape from focus.

Keywords: Dielectric Elastomer Actuator, microfluidics, tunable lenses, adaptive optics, zipping, silicone, PDMS.

Résumé

Cette thèse présente des progrès fondamentaux dans le domaine de la recherche sur les Actionneurs Diélectriques à Elastomère (DEA) par la modélisation analytique, la validation expérimentale et l'exploration des paramètres de nouvelles structures d'actionnement qui étendent les caractéristiques des DEAs à des modes d'opération hors-plan bistables ou multi-stables, des structures miniatures avec couplage fluidique, l'utilisation d'électrodes liquides et des potentialités haute vitesse. Plusieurs applications de ces nouvelles structures sont présentées et caractérisées en détail : des lentilles accordables à longue durée de vie avec électrodes liquides, des lentilles à grande plage d'ajustement à haute qualité optique, des actionneurs submillimétriques couplés fluidiquement pour applications microfluidiques et des lentilles à haute vitesse dont le temps de réponse est le plus rapide publié à ce jour, indépendamment de la technologie.

Dans le but de fabriquer des actionneurs pour la microfluidique, trois générations de DEA fonctionnant en mode *zipping* ont été construites et caractérisées. Ce nouveau mode d'action-nement consiste à attirer électrostatiquement l'électrode étirable unique d'une membrane flexible contre une électrode rigide qui couvre les parois inclinées d'une cavité. Les DEA fonc-tionnant en mode zipping offrent une série de propriétés inédites, comme un mode bistable hautement ajustable qui pourrait virtuellement être étendu à n'importe quelle caractéristique de déflexion en fonction du voltage, y compris des états multi-stables. Le mode d'opération bistable avait été prédit par un modèle analytique avant d'être observé sur des cavités coniques de taille millimétrique, et des déflexions verticales allant jusqu'à 385 µm ont été mesurées sur des chambres de 2 mm de côté. Le modèle analytique est discuté en comparant le voltage de seuil du *zipping* bistable et la forme de la membrane défléchie, puis le rôle de chaque paramètre de conception est discuté en détail.

L'application de DEA miniatures pour des actionneurs microfluidiques soulève un défi de taille : le fonctionnement de DEAs en contact avec des liquides. La plupart des liquides pénètrent de quelques dizaines de µm à l'intérieur des membranes, ce qui dégrade les per-formances d'actionnement et provoque l'arrêt de fonctionnement du dispositif. Dans les quelques publications qui traitent de l'utilisation des DEAs pour manipuler des fluides, la membrane active est protégée par une couche passive, au détriment des performances d'ac-tionnement. L'alternative adoptée dans ce projet et de coupler le mouvement du DEA à une membrane passive en utilisant un liquide encapsulé qui est connu pour être compatible avec la membrane sensible de l'actionneur. La compatibilité de 12 liquides avec des membranes en silicone a été mesurée sur une période allant jusqu'à 37 jours, et deux liquides qui satisfont le

Abstract

cahier des charges pour être encapsulés comme solution de couplage ont été identifiés : des bases de pré-polymères pour silicones et le liquide ionique TF$_2$N. Des membranes passives submillimétriques couplées à des DEA opérant en mode zipping ont été fabriquées et caractérisées. En comparaison avec la passivation des membranes, cette approche est plus fiable et étend la liberté de conception (conversion force-déplacement et redirection du mouvement). Les perspectives futures de tels dispositifs miniatures couplés fluidiquement et actionnés par des DEAs pourraient être une percée sur le marché des puces microfluidiques en silicone, en remplaçant les valves pneumatiques qui ont fait le succès de ces *Lab-on-chips* par des valves actionnées de manière électrique, ce qui rendrait cette technologie portable. En effet, cette gamme de *Lab-on-chips* extrêmement prometteuse requiert encore aujourd'hui des équipements externes lourds tels que des pompes et des valves pneumatiques, empêchant leur utilisation pour des dispositifs portables utilisables au point de service.

La recherche dans le domaine des lentilles accordables est un champ en pleine expansion qui vise principalement le marché des systèmes optiques embarqués. Une large palette de ces lentilles est basée sur la déformation d'une membrane flexible transparente sous laquelle est encapsulé un liquide, ce qui change la longueur focale. Ce type de lentilles possède de grandes plages d'ajustement mais l'intégration d'un mécanisme d'actionnement compact qui possède un grand déplacement, une réponse rapide et une basse consommation est un défi. Les DEA satisfont à ces critères avec l'avantage supplémentaire d'être fabriqués avec des membranes en élastomères du même type, ce qui permet un haut degré d'intégration.

Trois générations de lentilles accordables couplées fluidiquement ont été réalisées, caractérisées et comparées avec trois modèles analytiques. Le plus avancé de ces modèles prend en compte les propriétés mécaniques hyperélastiques de la membrane en élastomère. Une simple structure de lentille a démontré en particulier la possibilité d'utiliser le liquide ionique TF$_2$N comme électrode fiable pour les DEAs. C'est la première fois qu'une électrode liquide fiable est utilisée, ce qui ouvre un large champ de nouvelles possibilités de conception. Sur la deuxième génération de dispositifs, huit actionneurs de 3.9 mm de diamètre contrôlent une lentille unique de 6.5 mm de diamètre, et des plages d'ajustement allant jusquà 60% de la longueur focale ont été réalisées (de 28.5 à 45.5 mm). Un dernier type de lentille dont la conception est inspirée d'une publication de 2011 a été optimisé pour avoir une réponse rapide et a obtenu un temps de stabilisation de 0 à 90% de 172 µs, le temps de réponse le plus rapide rapporté à ce jour pour une lentille accordable, toutes technologies confondues. Le dispositif a une réponse plate jusqu'à 2 kHz et une fréquence de résonnance de l'ordre de 4.7 kHz. La plage d'ajustement de sa longueur focale est de -28% (de 19.4 à 14 mm). Des caractérisations électrique, mécanique et optique détaillées ainsi que des films enregistrés avec une caméra haute vitesse offrent une compréhension en profondeur du régime transitoire de la lentille. Des applications potentielles de cette lentille à haute vitesse incluent la microscopie par couche lumineuse ou des dispositifs temps réel de forme par le focus.

Mots-clés : Actionneur élastomère à diélectrique, microfluidique, lentille accordable, optique adaptative, zipping, silicone, PDMS.

Contents

1 Introduction

1.1 Background and motivation

Electro Active Polymers (EAP) are a wide class of actuators which use polymer-based materials to convert electrical energy into mechanical work. They are mainly classified in two families: ionic EAPs, which change shape by ion and/or solvent transport through their structure, and electronic EAPs which are activated by electrostatic forces [1]. Some of the EAP sub-classes are sometimes called artificial muscles because of their large stains and high energy densities which can be comparable or even higher than their natural counterparts.

Ionic EAPs are driven with low voltages (a few volts) and are electrically conductive. A typical example is a bending actuator sheet coated with a flexible electrodes on each side [2]. As a voltage is applied across the electrodes, ions are transported through the structure. This results in swelling of one side and shrinking of the other side of the membrane, and the sheet bends. These actuators are sometimes called "wet" because of their need of containing electrolytes.

Electronic EAPs are composed of electrically insulating materials, so that an electric field builds up in the material under application of an electrical potential across the electrodes. These smart materials may have specific electro-responsive effects such as piezoelectricity [3] or liquid crystals [4], or being simply deformed by electrostatic attraction (rubbery dielectric [5]).

This thesis focuses on the development of novel miniaturized structures of a specific EAP actuator type: Dielectric Elastomer Actuator (DEA) for application to tunable optics and microfluidics. Other EAP technologies have also been used for integrating actuators on devices that drive fluids. For instance, Xia and co-workers used the P(VDF-TrFE) piezoelectric polymer for making a valveless micropump [6]. The device made with this stiff polymer (1 GPa Young's modulus) is comparable to micropumps realized with piezoelectric ceramics, with higher strains (4.5%) but lower driving frequencies (60 Hz). Ionic Polymer Metal Composites (IPMCs) have also been used to build tunable lenses [7] or microvalves [8].

DEAs are of the simplest, and so far probably the most successful member of the EAP family.

Chapter 1. Introduction

Dielectric Elastomer Actuators (DEA) take advantage of the flexibility and electrically insulating properties of elastomers to electrostatically deform elastomer membranes. This very simple transduction mechanism efficiently converts electrical energy into mechanical work with the feature of large strains, high energy density and fast response. Specificity of DEAs compared to other standard actuation means (magnetic, piezoelectric, ...) can be used to fulfill the needs of many applications. DEAs can for instance feature planar driving mechanisms [9], soft robots [10], variable stiffness structures [11] or active damping mechanisms [12], to name only a few.

Among the different EAP families, DEAs are ideally suited to be integrated into small-scale devices, which would greatly benefit from their large strains and high energy density [13]. The direct and energy-efficient conversion of electrical energy into mechanical energy makes them even more appealing, since the few other technologies that would enable such large strains (shape memory polymers in particular) have much lower efficiency [14]. These unique properties are achievable thanks to their compliant nature, which however sets engineering challenges: while it is for instance easy to glue a rigid piezoelectric ceramic disc on a microsystem to actuate it, what are the options to integrate a membrane which is 4 orders of magnitude softer, doubles its surface upon actuation and has to be driven with kilovolts?

The scientific community has put a lot of effort into realizing new structures that truly exploit the potential of DEAs and enables their integration. This work presents novel miniature DEA structures for application to tunable optics and microfluidic devices. Both these application fields are interesting not only because they need the actuation features of DEAs, but also because they enable a high degree of integration thanks to the presence of elastomer membranes in their constitutive parts which are similar to those used for building DEAs.

But beyond the realization of devices, this work also targets the basic understanding of those novel actuator structures so that their strengths, weaknesses, sensitive parameters and further developments can be identified and that other field of applications will be able to benefit from those developments.

At a first choice, one would in principle not select DEAs as a mechanism to drive a device with a fast response. Indeed, mechanical softness is related to low resonance frequencies. However, as for other systems, the resonance frequency of DEAs scales approximately inversely with the size. Miniaturization of DEAs is therefore advantageous regarding fast response applications. More importantly, the use of some specific castable silicone elastomers with low viscoelastic losses and precision patterned ultrathin electrodes opens the door to high frequency applications. The LMTS has developed a considerable know-how in the fabrication of high quality membranes with a set of several high performance silicone elastomers, and a fabrication process to pattern μm-thick electrodes which have a low impact on the device damping. One last element presented in this thesis is a tunable lens device based on a design published in 2011 that uses high-performance silicones and semi-automated fabrication processes to achieve ultrafast responses.

2

1.2 Thesis outline

The main contribution of this thesis is the development of novel miniature Dielectric Elastomer Actuator (DEA) structures with the specificity of fluidic coupling and of zipping mode operation, for applications in tunable optics and microfluidics. Three generations of zipping microfluidic actuators, two generations of fluidically-coupled tunable lenses and one generation of high speed tunable lenses have been built and characterized. Detailed analytical models have been developed for zipping actuators and fluidically-coupled lenses.

Chapter 2 explains the basics of operation of Dielectric Elastomer Actuators. Advantages linked to their miniaturization are addressed, as well as the engineering challenges of developing structures that truly exploit their unique actuation features. New device structures are proposed as ways of achieving mechanical work on liquids for application to tunable optics and microfluidics.

Chapter 3 stresses on the importance of the physical properties of the rubbery dielectric membrane on the device performance, and discusses trade-offs regarding the choice of the elastomer. The fabrication process of silicone membranes is presented and options for making electrodes of miniature DEAs are discussed. Finally, the dynamic performance of DEAs is addressed and their use for fast response applications is reviewed.

Chapter 4 contains a state of the art on silicone-based DEAs operating in contact with liquids and an experimental investigation of 12 different liquid as mechanical coupling media. It is proved experimentally that liquids previously considered as compatible on bulk silicone parts do actually leak through thin silicone membranes. Two types of fluids perfectly match the listed specifications.

Chapter 5 presents zipping DEAs as a new type of actuators with a set of unique features among which the most remarkable is a highly tunable displacement versus voltage characteristic that includes bi- or multi-stable modes. An analytical model which enables quick evaluation of design parameters has been developed. Three generations of actuators were built and characterized in the scope of making integrated microfluidic actuators. Corresponding peristaltic pump designs are proposed and discussed. The last generation of actuators combines zipping DEAs and fluidic coupling of the actuator motion to a passive membrane. The operation of conical-shape DEAs with a bias pressure is discussed.

Chapter 6 presents analytical modeling and experimental realization of fluidically-coupled tunable lenses. A state of the art reviews tunable lenses and the integration of their actuators. The use of DEAs for such is motivated and discussed. Three analytical models have been developed and two generation of lenses were built and characterized. Main contributions include the validation of a model with hyperelastic material parameters, the demonstration of ionic liquid as liquid electrode and a tunable lens design with 60% focal length tuning range and adjustable operating point.

Chapter 7 describes a full-silicone DEA-powered tunable lens with the fastest change in focal length reported so far regardless of actuation technology. It is based on a design previously reported in the literature but optimized with a semi-automated fabrication process and high-performance silicones. Extended steady state and dynamic characterization explains the device functioning in depth.

2 Fundamentals of Dielectric Elastomer Acutators

Dielectric Elastomer Actuators (DEAs) are based on a very simple physical mechanism, which however requires to be adequately introduced to understand the particularities and challenges linked to the unique properties of these devices.

Section 2.1 (Basics of DEA operation) presents an introduction to the basic physical working principle of DEAs with their governing equations. Their unique features of electrically-controlled large strains and high energy density is highlighted, and the use of prestretching is commented.

Miniaturization of DEAs is addressed in **section 2.2 (Miniaturization of DEAs)**, with an emphasis on the effect of downscaling on the key figures.

Section 2.3 (DEA structures) stresses on the importance of engineering innovative actuator structures to truly exploit their potential, illustrated by representative examples.

Finally, **section 2.4 (Proposed novel actuator geometries)** presents novel actuation geometries concepts which will be explored experimentally and analytically throughout the thesis.

A part of section 2.4 has been published in L. Maffli, B. M. O'Brien, S. Rosset and H. R. Shea. Pump it up. In *Proc. SPIE*, volume 8340, pages 2Q1–2Q16 (2012).

2.1   Basics of Dielectric Elastomer Actuators operation

The deformation of a material by electrostatic forces is known since the 18th century [15]. However, it is only in 1998 that Pelrine and co-workers of the Stanford Research Institute reported on the large deformation of a rubber membrane by electrostatic actuation [16]: the modern era of Dielectric Elastomer Actuators (DEAs) had just begun. This new actuator type raised worldwide attention of the scientific community, mainly because of its remarkable feature of electrically-controlled large stains. 16 years later, an large number of scientific articles have been published in relation with this transduction mechanism which belongs
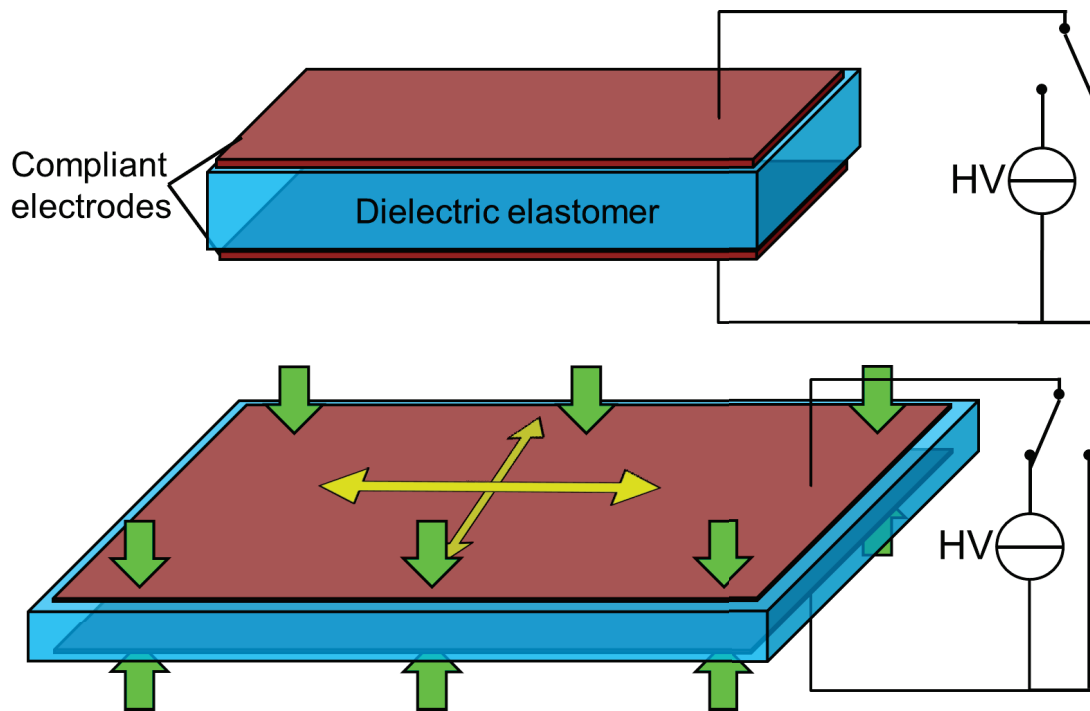
Figure 2.1: Basic working principle of Dielectric Elastomer Actuator with free boundary conditions. By application of a high voltage (HV) across a soft insulating membrane (dielectric elastomer) sandwiched between two compliant electrodes, a high electric field is created and the elastomer compresses in thickness (green arrows) and expands in-plane (yellow arrows).

to a family of actuators sometimes called artificial muscles because of their strain an energy densities comparable to natural muscles [5, 14]. DEAs could revolutionize many areas of application [17]: soft robotics [18], haptic feedback [19, 20], tunable optics [21, 22], loudspeakers [23], cell mechanical stimulation [24], energy harvesting [25, 26] or smart coupled sensing and actuation units [27]. A set of commercial products based on this new technology are already available on the market, such as haptic devices[1] or laser speckle reducers[2]. Numerous patents prove the interest of integrating DEAs into mass-consumer products, such as variable optics of portable device camera [28].

The basic actuator structure can be described as a sandwich of an elastomer membrane between two compliant electrodes (figure 2.1).

By biasing the electrodes at different electrical potentials, an electric field builds up across the insulating elastomer. Membranes which are typically in the range of 20 to 40 μm are biased with kilovolts, thanks to the high breakdown strength of elastomers. This results in large electric fields (typically $100\,\mathrm{V\,\mu m^{-1}}$) [5]. Consequently, the electrostatic attraction forces between the two electrodes are large enough to drastically deform the soft membrane

---

[1]www.artificialmuscle.com
[2]www.optotune.com

(Young's modulus typically in the MPa range) by compressing its thickness (green arrows on the figure2.1).

Elastomers are known to be incompressible materials in the sense that their volume remains constant when subject to deformation, similarly to liquids. Expressed in terms of Hooke's linear material laws, it means that their Poisson ratio ν is very close or equal to the limit value of 0.5. Since elastomer undergo large deformations, they are most of the time expressed in terms of principal stretches λ_1, λ_2 and λ_3 (rather than strains) which are defined by the the deformed over the initial dimension:

$$\lambda_1 = \frac{l_{stop,1}}{l_{start,1}} \tag{2.1}$$

$l_{start,1}$ and $l_{stop,1}$ being the initial and final dimensions in the direction 1. By convention, the indexes 1 and 2 generally represent the in-plane directions of the membrane and the index 3 is the thickness direction [29]. The volume incompressibility expressed in terms of those principal stretches is given by the following relation:

$$\lambda_1 \lambda_2 \lambda_3 = 1 \tag{2.2}$$

Thanks to this property, the thickness compression is mechanically linked to the in-plane deformation of the elastomer. Using equation 2.2, a thickness compression for instance by a factor 2 ($\lambda_3 = 0.5$) results in an area stretch of $\lambda_1 \lambda_2 = \lambda^2 = 2$ and linear in-plane stretches of $\lambda = \sqrt{2}$. The actuated DEA therefore also expands in-plane (illustrated by yellow arrows on the figure 2.1).

The governing equation for the actuation of DEAs can be determined by the differentiation of the electrostatic energy stored in this soft capacitor structure [16]. It leads to an expression of the electrostatic pressure p exerted by the compliant electrodes on the elastomer:

$$p = \epsilon_0 \epsilon_r \cdot \left(\frac{V}{t} \right)^2 = \epsilon_0 \epsilon_r \cdot E^2 \tag{2.3}$$

where ϵ_0 and ϵ_r (typ. comprised between 2 and 5) are the vacuum and relative permittivity of the membrane, V the voltage, t the membrane thickness and E the electric field. By computing the same pressure exerted by the electrostatic actuation of two rigid electrodes, one would obtain half the value of equation 2.3, an expression which is also known as the Maxwell stress. It means that compared to the electrostatic actuation force between rigid conductors, the area expansion of the compliant DEA electrodes contributes to the actuation by a factor 2. Intuitively, it is explained by the fact that not only do opposite charge of the two electrodes attract, but same charges on a single electrode additionally repel each other, helping for the area expansion. Looking at the DEA being a soft capacitor (fig 2.1), both the thickness reduction and area expansion contribute to the increase of capacitance of the deformed state.

Using a simple linear material equation, the compressive thickness strain s_3 can be expressed

with the Hooke's law, Y being the Young's modulus:

$$s_3 = -\frac{p}{Y} \qquad (2.4)$$

It should be noted that p actually depends on s_3 (the electric field increases as the membrane is compressed). Using the same simple approach, the in-plane strains $s_1 = s_2$ can be expressed in function of the electrostatic pressure:

$$s_1 = s_2 = -\nu\frac{p}{Y} \qquad (2.5)$$

ν is the Poisson ratio, which is equal to 0.5 for incompressible materials.

2.1.1 Large actuation strain capabilities

Very large linear strains (typically in the range of 40 to 400% [14], more with specific configurations) are the main specificity of DEAs in comparison with other actuation means (piezoelectric, magnetic, electrostatic, thermal) [30]. The strain of piezoelectric actuators is typically 0.1%, and only one or two orders of magnitude higher for the displacement of electrostatic, magnetic or thermal actuators. Moreover, the energy density of DEAs are comparable to their piezoelectric or magnetic competitors ($0.75\,\mathrm{MJm^{-3}}$ for silicones elastomers, $3.4\,\mathrm{MJm^{-3}}$ for acrylic elastomers) [31].

Looking at equation 2.3 which expresses the mechanical pressure p that will deform the elastomer, two determinant parameters can be identified: the relative permittivity ϵ_r and the maximum electric field E_{bd} that the actuator can sustain before electrical breakdown. The permittivity is directly proportional to the actuation stress, while the electric field is squared. This square dependence means that the dominant part of the actuation happens close to the breakdown. The breakdown strength of the membrane is therefore a critical parameter regarding the maximal achievable strain. The last determinant variable is of course the stress-strain characteristic of the actuator. Indeed, softer material will move from a larger amount for a given electrostatic pressure. It is represented by the Young's modulus in the equations 2.5 and 2.4, but non-linear material laws are required to accurately describe the mechanical properties of the elastomer.

As visible on these quick considerations, the membrane material properties plays a dominant role. Tradeoffs between the key figures of DEAs are therefore principally determined by the choice of the elastomer material. Regarding actuation strain, the widely used VHB acrylic tape from 3M[3] offers the best performance while having a strongly damped mechanical response [32], low reliability and reduced operating temperature range [14]. Silicone elastomers perform better on those points, but have lower achievable strains (lower ϵ_r and E_{bd}). However, since prestretching the membrane increases the breakdown strength, the lower breakdown field commonly observed on silicones is rather related to the lower amount of prestretch that can

---

[3]www.3m.com/vhb

be applied because silicones are stiffer than acrylic elastomers. These material-dependent features will be discussed with more details in the section 3.

The record of actuation stretch belongs to Keplinger *et al.* who published in 2012 1692% area expansion with a structure involving a controlled air volume below an inflated balloon to harness the electrical breakdown [33]. Kolloshe *et al.* report on 360% linear stretch on their simple force-loaded stripe [34]. Both of these work use acrylic elastomers. Area strains of 117% have for been reported in 2000 with silicone elastomers [5], more recently the best performance to date of 156% by Rosset *et al.* [35].

2.1.2 Prestretching

Considering the basic DEA structure of figure 2.1, it is straightforward to see that if the membrane at $0\,V$ was not in free boundary conditions but clamped to a rigid frame, it would buckle when actuated because of the impossibility for the lateral expansion to take place. Buckling-mode actuators have been realized [36], but DEAs are most of the time manufactured with a planar prestretch applied to the membrane before bonding them to their support frame. In such a case (and provided a passive membrane area exists around the actuator to absorb its motion), the actuator operates in-plane.

But the two most important reasons why researchers almost systematically prestretch their DEA membranes are an enhanced breakdown field and, most of all, the suppression of a pull-in instability which triggers electrical breakdown. Prestretching improves the breakdown strength of the elastomer by a considerable amount, such as from 100 to $240\,V\,\mu m^{-1}$ on the Dow Corning Sylgard 186 silicone [37]. For acrylic elastomers, an increase from 18 to $218\,V\,\mu m^{-1}$ has for instance been reported [38]. Huang *et al.* measured a dependence of the same polymer not only on the breakdown field but also to a smaller extent on its thickness [39].

As mentioned, prestretching suppresses the pull-in instability of DEAs. Analyzing the stretch-voltage relationship of DEAs using their hyperelastic material properties indeed leads to a curve which has an instability point at which the actuator would like to jump to a highly deflected state [29]. During this jump, the strong membrane thinning leads to an electrical breakdown. Prestretching modifies the stretch-voltage curve of the elastomer so that this instability can be suppressed. It drastically increases the achievable strains, despite the membrane stiffening induced by its hyperelastic properties [40–42]. As demonstrated by Akbari *et al.* on their single cell stretching device, non-equibiaxial prestretching also provides a way of enhancing the linear strain in one direction compared to the other [24, 37].

2.2 Miniaturization of DEAs

The most common way to fabricate a test DEA is to "paint" carbon grease on the elastomer membrane. Consequently, the size of test devices are typically comprised between a few cm

to some tens of cm, so as for many applications [43–45]. The record probably belongs to Jordi *et al.* whose square meter range actuators propel a blimp [46].

Using the large energy density and strains of DEAs to build new Micro Electro Mechanical Systems (MEMS) is very appealing [13]. However, building soft elastomers below the mm scale is challenging, for instance in terms of electrode patterning or high voltages (which might arc on the surrounding parts).

The success of MEMS relies principally to two things: the drastic decrease of the production price per unit thanks to the massive parallelization of the fabrication processes which can fit hundreds of chips on a single wafer, and the improvement of key figures thanks to the miniaturization of the components. For instance, resonance frequencies of most structures scale with l^{-1} and thermal time constants typically like l so that at small scales, oscillating devices can operate at very high frequencies and thermal actuators respond fast.

Downscaling the membrane thickness has a favorable effect on the driving voltage but actuation stain is reduced because of the relative stiffening induced by the electrodes, which do not contribute to generate the force but have to be mechanically deformed. Keeping their thickness and Young's modulus as low as possible is therefore crucial if one wants to reduce the driving voltage of DEAs. As the dielectric breakdown field is a material property which does not scale with the thickness, the thickness-direction force is independent on the thickness, but the lateral one does so.

Downscaling the actuator in-plane dimensions has several positive effects regarding the probability of defect-triggered failures. Indeed, the apparition of premature dielectric breakdown is common when dealing with a few 10's of µm thick soft elastomer membranes biased with kilovolts. One can actually consider that every single breakdown event appears at the place where there is a weak point, i.e. a local defect in the membrane: thickness inhomogeneity, trapped air bubble or dust particle, etc. As a single defect leads to a complete actuator failure, one can assume that the probability for larger devices to have a premature failure scales with the scale of the in-plane dimensions. For instance, lifetime and probability of failure was a major issue on Jordi *et al.*'s blimp propulsion actuators [46]. Their 1.25 x1 m active area DEAs had to be driven with a large security margin of electric field [18]. If miniature DEAs were mass-produced in parallel processes comparable to the silicon MEMS technologies, one could therefore easily think of a quality control test under maximal electric field conditions that discards those who have a defect.

The lateral strains do not scale with the in-plane dimensions. On its side, as the thickness-direction force multiples the electrostatic pressure with the actuator area, it scales with the square of the lateral dimensions. It can be shown that scaling down the device dimensions increases its resonance frequency because of the reduced mass in motion.

2.3 DEA structures

Having explained the basic DEA structure, let us consider a few fundamental design challenges. The softness of the membrane allows for large displacements, but makes also challenging the use of DEAs to retain a precise shape when submitted to a load. For many applications, one would like out-of-plane displacements to exert mechanical work, or take advantage of the softness of the actuator to achieve complex three-dimensional motions. The use of kilovolts must also be addressed: although not dangerous for humans because involving small currents, one must protect the surrounding equipment such as driving electronics or metallic parts from the high voltage electrodes. If one wants to make a commercial application, the encapsulation of DEAs is therefore critical. However, the main issue of high voltage in commercial products is related to the size and cost of the driving electronics: the reduction of the driving voltage is almost unavoidable, but requires thinner dielectric layers, which must also be stacked in most of the cases to be still able to provide the expected force. These design challenges demonstrate that far beyond the basic DEA in-plane demonstrators, it is mandatory to provide a lot of engineering effort designing new actuator structures to truly exploit all the potential of DEAs [47–49]. Some examples are shown on the figure 2.2.

Figure 2.2a displays the smallest DEA to date, which is able to strain single cells uniaxially. It is composed of crossed $100\,\mu m$ wide stripes [24]. At their intersection, an actuator is formed which expands in a single direction thanks to non-equibiaxial prestretching. The features of miniature DEAs have been discussed in section 2.2. On figure 2.2b, a long film of DEA is rolled around a core which contains a spring under compression. Upon actuation, the multilayer actuator film expands and the spring expands [43]. This type of electrically-powered linear actuator can for instance be used in robotic applications. Adding active actuator area helps achieving large force, but set constraints in the type of elastomer that can be used and affects reliability, as will be addressed in section 3. Figure 2.2c presents another way of achieving multilayer DEA by folding a long actuator stripe [50]. The useful uniaxial displacement results from the thickness compression of the membranes. It works better in compression, because of the risk of de-lamination. Many types of frames have been designed to maintain the shape and direct the motion of the actuators, such as on figure 2.2d [44]. A large stroke mechanically bistable structure with hinges is actuated by a DEA, which triggers the motion between two stable points. This DEA-driven large stroke mechanism is however limited in actuation speed by the viscous component of the dielectric material used (sect. 3), and has carbon grease electrode which rend it fragile. Figure 2.2e display a type of actuators which has a very simple structure but that can take very complex shapes, known as Dielectric Elastomer Minimum Energy Structure (DEMES) [51, 52]. A prestretched membrane is applied on a stiff but flexible frame (in that case a triangle), which results in complex shapes by stress relaxation (left, 0 kV). Upon actuation, part of the in-plane stresses are released and the structure changes its shape.
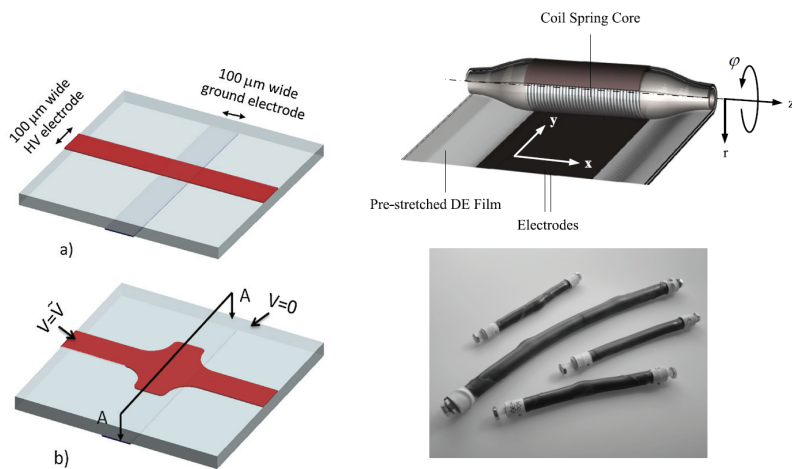
(a) **In-plane uniaxial displacement:** Crossed 100 μm-wide stripes to strain biological cells. (reprinted from [24])

(b) **Uniaxial displacement in area expansion mode:** "spring roll" actuators provide uniaxial displacement along the z-axis. The DEA film is rolled around a spring (reprinted from [43])
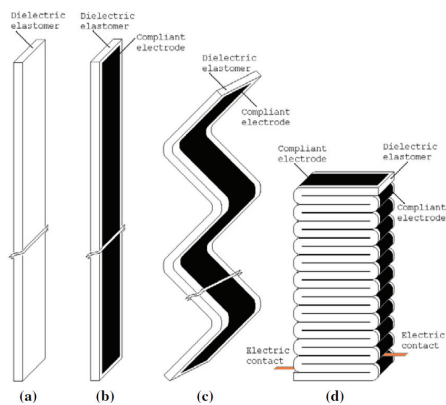
(c) **Uniaxial displacement in thickness compression mode:** the actuator is formed by folding a DEA stripe (reprinted from [50])
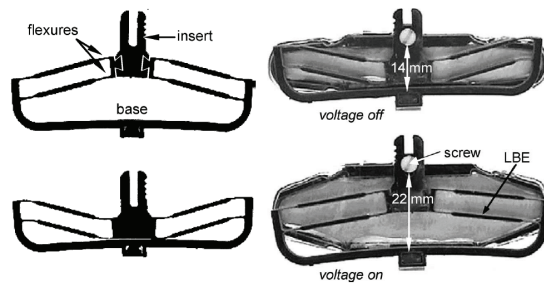
(d) **Bistable actuators:** A DEA membrane triggers a switch between two states of a bistable mechanical frame (reprinted from [44])
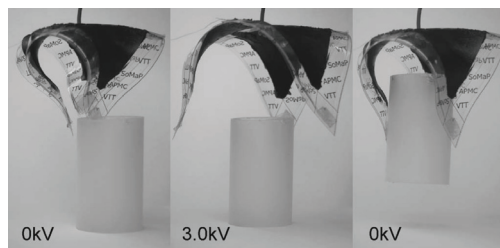
(e) **Variable-shape:** Dielectric Elastomer Minimum Energy Structures (DEMES) provide a complex gripper motion with only one actuator prestretched and mounted on a flexible frame (reprinted from [45])

Figure 2.2: A few examples of DEA structures. A considerable engineering effort must be developed in order to truly exploit the potential of DEAs

2.4 Proposed novel actuator geometries

In the scope of displacing fluids or moving parts, one must produce a mechanical work. Several more or less complex structures have been described as examples in section 2.3. One of the most straightforward ways to exploit the motion of DEAs is to generate out-of-plane motion of the active membrane. S. Rosset *et al.* have for instance built and modeled a bucking-mode DEA (figure 2.3A). A non-prestretched silicone membrane is clamped on a few millimeters diameter aperture [36]. In this type of device, the suspended membrane can be brought from a flat position to out-of-plane motion by going through the buckling instability. The reported out-of plane motion is 25% of the clamped diameter, with a total output pressure in the range of 1 kPa.

Figure 2.3B illustrates a DEA which operates with one patterned top compliant electrode and one liquid electrode. The stiffening impact of the electrode is reduced, and the bottom liquid electrode can be contacted at any point of the fluidic cavity. A tunable lens device built according to this principle will be presented in section 6.3.1.

Compliant electrodes can also be used to actuate a membrane with an electric field that is not applied across the membrane thickness, but that attracts it toward a rigid counter-electrode. This actuation mechanism is known in silicon MEMS devices as zipping, because the motion
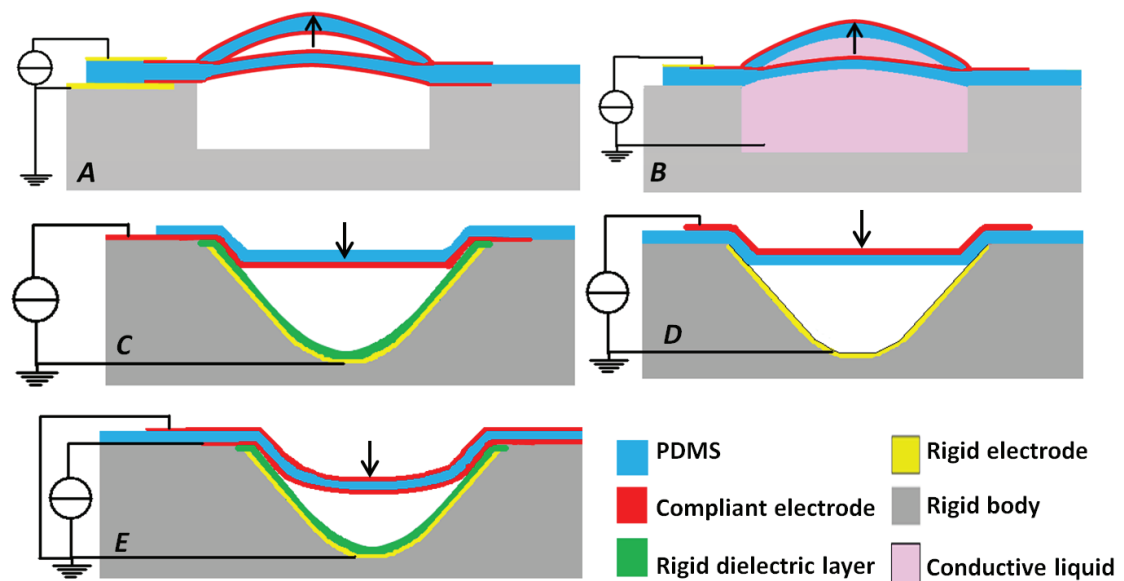
Figure 2.3: Two published and three novel out-of-plane operating DEA structures. **A** Diaphragm out-of-plane, as published by Rosset *et al.* [36] **B** Diaphragm out-of-plane with a conductive liquid as electrode. **C** Zipping across a rigid dielectric, as published by Gebbers *et al.* [53]. **D** Zipping with the membrane as dielectric **E** Combination of diaphragm (squeezing) and zipping. The arrow indicates the direction of deflection under application of a rising voltage step. (A) and (B) can deflect in eigther direction depending on the initial conditions.

proceeds where the electric field is the highest (i.e. the gap between the electrodes is the smallest): at the periphery of the flat suspended part, similar to a zipper.

Figure 2.3C presents a geometry on which the electric field is applied across a thin rigid dielectric. An analytical model of such a structure using was proposed by Saif *et al.* [54]. They do not use elastomeric membrane properties but a few µm thin polyimide with 2.7 GPa Young's modulus. Han *et al.* also used zipping actuation and sensing across a rigid dielectric in their contact capacitive pressure sensors [55], and a folded zipping actuator structure composed of flexible polymers has been extensively studied by Horning [56]. This zipping mechanism applied to DEAs was studied experimentally by Gebbers *et al.* [53]. A model of its behavior will be presented in section 5.2. It is also possible to pattern the compliant electrode on the side of the membrane that does not come in contact with the rigid one, the elastomeric membrane acting as the dielectric (figure 2.3D). A detailed analytical and experimental study of this latter option will be presented in section 5.

Finally, the geometry of figure 2.3E combines zipping and traditional squeezing-mode operation. One of its specificity may be to enhance the zipping behavior by lowering the contact angle between the suspended part of the membrane and the rigid electrode, a sensitive operation parameter.

2.5   Summary

In this chapter, the fundamental geometry and basic equations of DEAs have been developed. Their unmatched feature of large strain and high energy density is due to the combination of the electrically insulating properties and mechanical compliance of the rubbery membrane which constitutes its core. It is possible to play with the highly stretchable and nonlinear characteristic of the membrane by prestretching, which shifts the mechanical operating point and improves the dielectric properties. Scaling laws applied to a basic actuation structure highlight the benefits of miniaturization on reliability, driving voltage and resonance frequency. The large strains of DEAs are achieved thanks to the low stiffness of its constitutive elements, but requires engineering efforts to design actuator structures that fulfill a precise task. Finally, concepts of novel actuation geometries such as using a liquid electrode or zipping mode operation have been presented, in the scope of building miniature actuators for tunable optics and microfluidics.

3 Dielectric elastomer materials and electrodes

Both the steady state and dynamic performance of a DEA are directly determined by the dielectric membrane material and by the compliant electrodes. This chapter aims at comparing the physical properties of the main suitable dielectric elastomer families as well as the electrode technologies applicable for miniaturized DEAs, in the scope of designing sub-mm to cm-scale actuators for tunable optics and microfluidics which combine the large displacement of DEAs with reliability and speed.

Section 3.1 (Families of dielectric elastomer materials and their properties) highlights the key physical parameters of the main types of elastomers used for DEAs. The hyperelastic mechanical properties of those elastomer is introduced together with the use of associated models. Comparisons of performance and sensitivity to environmental conditions will also be presented for the two main families of dielectric materials: acrylic elastomers and silicones.

One of the silicone membrane fabrication processes developed in the LMTS is described in **section 3.2 (Fabrication of silicone membranes)**.

Section 3.3 (Compliant electrodes for DEAs) deals with electrode types suitable for micro-fabricated DEAs and presents the Au ion-implantation and pad printing technologies which have been used in this project.

Finally, the dynamic performance of DEAs will be specifically discussed in **section 3.4 (Dynamic performance of DEAs)** with an extended state of the art of fast response devices as an introduction to the high-speed tunable lens of section 7.

A part of section 3.2 has been published in L. Maffli, S. Rosset, and H. R. Shea. Zipping dielectric elastomer actuators: characterization, design and modeling. *Smart Materials and Structures*, 22(10):104013, 2013.

3.1   Families of dielectric elastomer materials and their properties

Silicones and acrylic elastomers (in the form of the commercially available VHB sheet from 3M) are the most commonly used materials for the dielectric membrane of DEAs. Besides the two already cited, other elastomers exist, such as polyurethanes or natural rubber. Reports on DEAs built with polyurethanes are sparse [57, 58], but companies such as Bayer Material Science [1] are developing those materials. Works reporting on the use of natural rubber are similarly rare, although its use is foreseen as competitive with VHB for dielectric elastomer energy harvesters [59].

As shown on equation 2.3, the principal parameters which determine the electrostatic pressure are the relative permittivity and the dielectric breakdown field. The stiffness of the material determines the amount of deflection resulting from this electrostatic pressure. Table 3.1 presents typical values of these parameters for the elastomers mentioned above. Let us first consider the relative permittivity ϵ_r. The actuation pressure is directly proportional to its value: the higher, the better. Polyurethanes may have very high permittivities, in the range of 7 or more. The value of 5.4 for acrylic elastomers is very good [60], and contributes to its first rank in terms of steady state performance. Silicones and natural rubber have permittivities in the range of 3.

The breakdown strength is extremely important as well since it determines the maximal electric field that can be applied across the membrane, and the output force is proportional to the square of the electric field. For acrylic elastomers it goes up to $500\,\mathrm{V\,\mu m^{-1}}$ under high prestretch conditions [39]. Prestretching is systematically used on VHB-based devices for this reason and to overcome the pull-in instability (section 2.1.2). A similar increase of the dielectric strength is reported for silicones [37], which can however sustain less prestretch, hence operating often at lower electric fields. Values of 160 and $67\,\mathrm{V\,\mu m^{-1}}$ were reported for polyurethanes and natural rubber respectively [61], but a larger set of experimental data is lacking.

The mechanical properties of the elastomers is also difficult to quantify, since their stretch-stress characteristic is highly non-linear. A simple comparison uses the Young's modulus, which reflects the stiffness in the first 10's of % elongation. Softer materials will provide more displacement, but less force, and vice versa. Typical values are in the MPa range. Silicones offer the advantage of being available in a very broad set products, so that their hardness can be chosen depending on the application.

Since those material are used at very high stretch levels, the full hyperelastic stress-stretch curve must be used in most of the cases. It is highly non-linear, with a gradual stiffening up to rupture, which might be in the range of 9 times its initial length for uniaxial extension. As illustration, figure 3.1 presents stretch-stress data of an uniaxial pulltest done on a LSR4305 silicone membrane from Silbione[3].

---

[1]http://www.materialscience.bayer.com/en
[3]www.silbione.com

Table 3.1: Table of principal elastomers properties. The dielectric constant value and the breakdown strengths are taken at at low frequencies (typ. 0.1 Hz) without prestretch, unless indicated with an equibiaxial λ.

Elastomer type	Permittivity ϵ_r (-)	BD strength (Vµm^{-1})	Young's modulus MPa	Time constants (s)
Silicones	2.5 - 3	100 250 ($\lambda = 1.75$) [37]	0.2 to 2 or more	0.016 to 0.05 [35]
Acrylic elast. (3M VHB^2)	5.4	34 500 ($\lambda = 6$) [39]	0.22	0.3 to 370 [32]
Polyurethanes PT6100S [61]	7	160	17	~ 0.1 to 1 s [62]
Natural Rubber [61]	2.7	67	0.85	
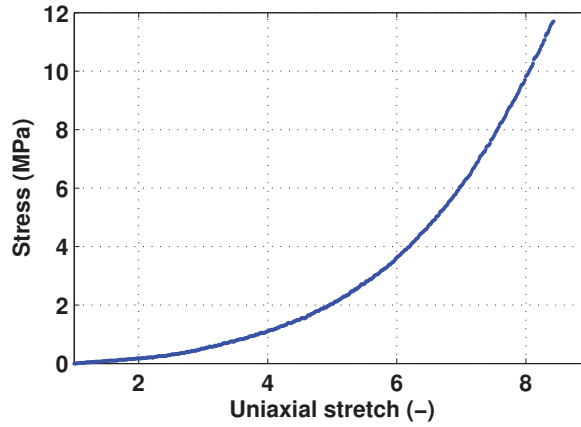
Figure 3.1: Uniaxial pulltest data of a LSR4305 silicone membrane. Young's modulus ~0.2 MPa, dimensions of the sample 60 x 9.8 x 0.131 mm.

The most common function that describes the mechanical properties of elastomers is the energy density W. Expressed in J m^{-3}, it represents the density of mechanical energy stored in the elastomer in a given stretch state. W is a function of the three principal stretches λ_1, λ_2 and λ_3, grouped in the strain invariant I_1:

$$I_1 = \lambda_1^2 + \lambda_2^2 + \lambda_3^2 \qquad (3.1)$$

The stretches are linked by the incompressibility relation (equation 2.2) so that the number of variables is reduced to 2, or 1 for symmetry reasons. Various models have been developed to express this energy density function. For instance, the equation 3.2 is the Gent model, and the

equation 3.3 the three-terms Yeoh model.

$$W_{Gent} = -\frac{\mu J}{2} \log\left(1 - \frac{I_1 - 3}{J}\right) \tag{3.2}$$

$$W_{Yeoh} = C_1 (I_1 - 3) + C_2 (I_1 - 3)^2 + C_3 (I_1 - 3)^3 \tag{3.3}$$

where μ, J, C_1, C_2 and C_3 are material constants. The advantage of using such models is that once those constants are fitted on a particular case (such as an uniaxial pulltest), W can be expressed for an arbitrary combination of stretch state. In reality, no model is perfect and it is more accurate to use material parameters fitted on a test done in the same conditions as the ones that should be modeled [63]. Further descriptions of the steady state behavior of DEAs can for instance be found in Suo's work [29].

The dynamic characteristic of the elastomer material is of major importance in many applications, because it is desirable to reach a steady state as quick as possible. As a general rule, softer elastomers tend to have more intrinsic damping. Representative time responses are given in table 3.1. Notably, silicones perform 1 to 2 orders of magnitude better than acrylic elastomers. A detailed study and state of the art of the dynamic performance of DEAs will be given in section 3.4 as an introduction to section 7, which presents a DEA tunable lens with the best response time reported among all other technologies with integrated actuators.

Finally, for commercial products, other aspects such as performance stability in time, temperature and humidity must be addressed. For VHB, several studies report on the large drift of dielectric constant, mechanical loss factor, breakdown strength and elastic modulus with temperature [60, 64, 65]. Strong decrease of lifetime with humidity was also observed with this material [26]. Silicones clearly outperform acrylic elastomers, as highlighted for instance by Michel *et al.*, who measured a constant elasticity for silicone from −25 to 150°, but almost 2 orders of magnitude drift for VHB on the same temperature range [65]. Kornbluh and co-workers experimentally investigated the strain of several silicones, and report on nearly full actuation on temperature ranges from −100 to 200° with the CV 2287 from NuSil.

For more elaborate comparisons, it is possible to consult several works, mainly from Pelrine and Kornbluh. Among others, energy coupling efficiency [61], electromechanical energy density [5] or other physical values such as the mechanical loss factor [31] are used, as well as qualitative and quantitative comparisons with other actuation techniques [13, 14]. DEAs have among the best performance in terms of strain and energy density, and comparable efficiency as piezo, electrostatic and electromagnetic devices if silicone elastomers are used.

3.1.1 Custom-engineered dielectric materials for DEAs

A quite extensive research has been conducted on ways to improve the elastomer properties of castable elastomer by dispersing particles, using titanium dioxide [66], polyaniline particles

[67] or ferroelectric relaxor ceramics (BaTiO3) [68], to mention only a few. The actuation performance improvement is however not exceptional, the gain in one parameter (such as the dielectric constant) most of the time resulting in a lower performance of other ones (like breakdown strength or Young's modulus [69, 70]). Improvements higher than one order of magnitude could make a breakthrough for instance by lowering the actuation voltages, but this is still under development.

Interpenetrating Polymer Networks (IPN) basically consist in adding and polymerizing a harder polymer onto a pre-strained soft polymer membrane. Once relaxed, the IPN membrane will retain some of its pre-stretch and be able to be operated from this mechanical state [71, 72]. It has been mainly applied on VHB. Studies on the variation of material parameters have been done, as for instance the reduction of viscous losses [73]. No significant advances are linked with this method, although it gives new design options for VHB-based devices.

It is worth mentioning the development of Bistable Electroactive Polymers (BSEP). Yu *et al.*'s material has a Young's modulus which decreases by 3 orders of magnitude between ambient temperature and 70° [74]. This allows the DEA to be heated up for actuation but to maintain its shape without voltage when returning to ambient temperature. The softness of DEAs is an advantage for actuation strain, but a drawback if the deflected position must be kept and sustain a large blocking force, and BSEP combines both. Braille displays have for instance been build using those materials [75].

In this project, several types of silicones have been used as membrane materials. Silicones offer good static and dynamic performance and have a high reliability and lifetime. As they are castable, the thickness of the membrane can be chosen independently on the prestretch, which is not the case for the commercially-available VHB film.

3.2   Fabrication of silicone membranes

Many publications on DEAs use the acrylic elastomer VHB from 3M, which has the advantage of being commercially available in films and can be highly pre-stretched, enabling excellent static displacements. However, high viscoelasticity, temperature sensitivity and reliability are disadvantages for commercial products. One of their other drawbacks is that the thickness cannot be chosen independently of the prestretch. Indeed, it is available in sheets of pre-defined thicknesses and must be prestretched to be thinned down.

Our silicone membrane fabrication process is reported below. Using silicone gives a maximal freedom regarding the choice of the silicone type and thickness. Membranes for DEAs must be defect-free and present excellent thickness homogeneity in order to prevent premature breakdown. Casting a thin silicone membrane on a substrate involves the subsequent separation of the former from the latter. Pulling off the membrane induces a large deformation of the silicone layer, which must be avoided because of the Mullins effect [76]. Our lab has consequently developed different methods based on the application of a silicone layer on a

sacrificial thin-film for a facilitated release. Both spin-coating on silicon wafers and blade casting on glass plates or flexible substrates have been tested, and better thickness homogeneity was obtained with the casting method, which also allows coating larger surfaces in a single run. Regarding sacrificial layers, photoresist as well as water-soluble films such as poly(acrylic acid) (PAA), poly(vinyl alcohol) (PVA) and dextran were tested experimentally. Those sacrificial layers have been successfully used for surface micromachining [77]. Photoresist must be dissolved in acetone, which swells the silicone membrane and can dissolve and wash away some silicone oil, leading to a modification of the mechanical properties [78]. Furthermore, the use of acetone is problematic on larger surfaces such as glass plates of the size of A3 format due to its high evaporation rate. The use of water-soluble sacrificial layers is consequently favored. Among dextran, PAA and PVA, the best results have been obtained with PAA in terms of ease of coating (wettability of the substrate, absence of pinholes), resistance to the temperature used during the cross-linking and low temperature release.

Two main substrates have been used to cast the sacrificial layer and the silicone: glass plates and high quality polyester foils (Melinex ST506[4]). Both of them have a low roughness, which is important for having a homogeneous membrane surface. The surface must also have a good wettability. For glass, it is obtained by a final cleaning step with a Bunsen burner flame, and for the Melinex foil by O2 plasma activation. Regarding fabrication time, it is advantageous to use the disposable Melinex foil, because glass plates need to be carefully cleaned after the process in order to be used again. Among the different techniques, the one with the glass plates as substrates will be described below. The process is described on the schematics of figure 3.2 and the photographs of figure 3.3, and has been published in [79].

The first step is cleaning the glass plates. The surface cleanliness is very critical to obtain layers without defects. These preparation steps both remove all organic residues and lowers the surface tension of the glass. An adjustable gap ZUA2000 Zehnter applicator blade was used, placed on a ZAA2300 automatic film applicator coater. A 30 µm gap is set on the blade, and a 5% Poly(acrylic acid) (PAA) solution in water is casted on a heated glass plate (figure 3.2A and 3.3a). Once dried, this sacrificial layer is less than 1 µm thick. The silicone is prepared by mixing the two components with isooctane or siloxane-based solvents to reduce the viscosity. The dried membrane thickness is lower than the blade gap, and empirical tests must be performed to be able to predict the desired value (figure 3.2B). Once casted, the silicone layer is left at ambient temperature to allow for the solvent to evaporate from the uncured layer, and then placed in an oven to complete the crosslinking (figure 3.2C). A laser-cutted flexible frame is then taped on top of the silicone layer (figure 3.2D and 3.3b). It prevents the fragile membrane from being stretched during the release. When using PAA, the glass plate is dipped into a hot water bath, and the flexible frame with the attached silicon membrane can be easily lifted from the plate (figure 3.2E and 3.3c). The obtained membranes are 20x30 cm^2 silicone sheets (limited by the applicator size) of 15 to more than 100 µm thicknesses (targeted thickness typically reached within ± 3 µm, with a total thickness variation over the

---

[4]http://www.dupontteijinfilms.com/
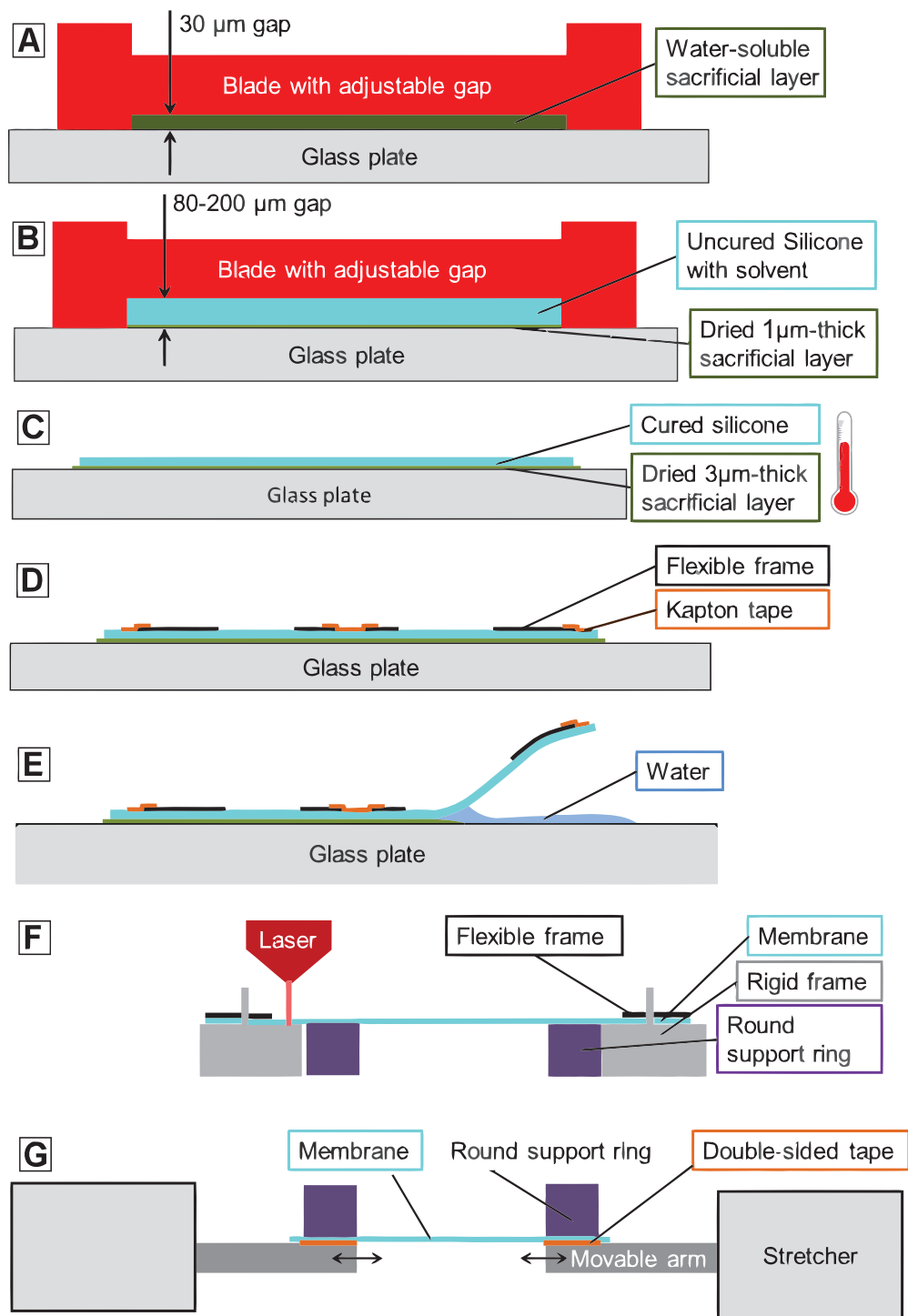
Figure 3.2: Membrane fabrication steps. **A**: Sacrificial layer casting. **B**: Silicone casting over the dried sacrificial layer. **C**: Silicone crosslinknig. **D**: Flexible frame taping. **E**: Release of the silicone membrane by dissolution of the sacrificial layer with water. **F**: Laser cutting. **G**: Prestretching.

(a) Silicone dispensing before bladecasting

(b) Taping the flexible frame onto the cured silicone membrane

(c) Release of the membrane by dissolving the sacrificial layer in water

(d) Laser cutting of the membrane

(e) Prestretching
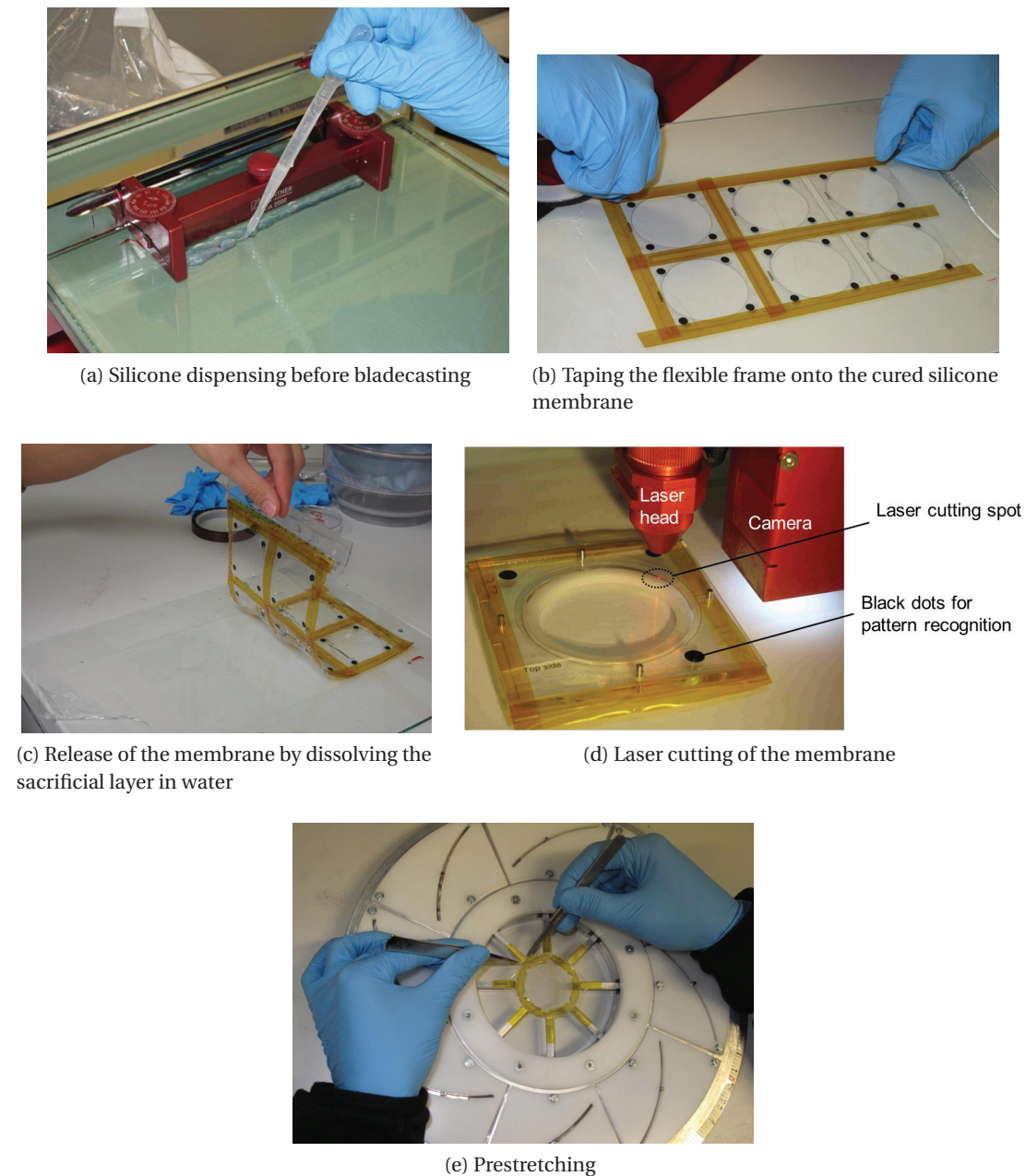
Figure 3.3: Photographs of the membrane fabrication process on a glass plate using a water-soluble sacrificial layer.

whole sheet below 3 μm (<1 μm over a 5x5 cm^2 piece). The coating process was successfully tested with several different silicones including Dow Corning Sylgard 186, Nusil CF19-2186, Nusil CF18-2186, Nusil R32-2186, and others. The most critical point is the amount of solvent needed to reach the good viscosity range, which can lead to the formation of voids in the membrane if the silicone crosslinks before it evaporates. The flexible frames have printed registration marks, so that the silicone membranes can be cut to any shape with very clean

edges at a precision of 100 μm by a Speedy300 laser with optical pattern recognition, from Trotec [5] (figure 3.2F and 3.3d). The clean laser cut avoids all defects that occur when cutting the membrane by mechanical means, which allows applying more prestretch before tearing. The stretch-free cutted membrane remains on a support ring by natural stiction, and is then transferred on the stretcher arms covered with double-sided tape (figure 3.2G and 3.3e).

3.3 Compliant electrodes for DEAs

The ideal requirements of DEA electrodes are 1) a low stiffening impact 2) a high conductivity 3) to be easily, precisely and repeatably patternable and 4) to be resistant to wear and abrasion.

The compliance is critical since as the elastomer is soft, any electrode-induced stiffening will lower the strain performance. The requirements on the conductivity are in principle less demanding, since the important point is that the electrical response time does not affect the mechanical one, a relatively easy task with devices made of elastomers with high mechanical losses (compared to metals or silicon for instance). But the conductivity must remain even under high stretch, to be able to spread the charges in the electrode. Patternability is needed to produce devices that have small features and repeatable performance, and resistance to abrasion is an obvious requirement for any device beyond proof of concept demonstrators.

The most widely used solution to make compliant electrodes is carbon black either directly on the elastomer, or mixed with grease. It offers good performance in terms of compliance, but suffers from several disadvantages: difficulty to be patterned at the mm-scale and below, incompatibility with an industrial fabrication process, long-term reliability and the fact that any contact with the greasy compound will damage the electrode and contaminate the surrounding parts. Thin metallic layers greatly lower the electricaly-induced strain because of their Young's modulus several orders of magnitude higher than that of elastomers, and lose conductivity by cracking before reaching 10% strain. However, their compatibility with industrial fabrication processes has been exploited by the company Danfoss Polypower to make macro-scale linear actuators, depositing a thin metallic film on a wavy elastomer membrane [80]. Other techniques have also been realized, like for instance stacked actuators with carbon powder enclosed in silicone [81], with the difficult issue of contacting the internal layers in a reliable way.

As described in Rosset *et al.*'s 2012 review article about electrodes for DEAs, carbon particles dispersed into a crosslinked elastomer are one of the most promising alternatives [82]. The un-crosslinked compound is used as an ink that can be patterned for instance by inkjet processes or stamping, thus enabling small, precise and repeatable features on the surface of the membrane. Other techniques are also discussed in this publication.

---

[5]www.troteclaser.com

3.3.1 Miniaturized electrodes

Most of the actual DEA devices are macro-scale, but MEMS technologies would greatly benefit from this large strain actuation mode [13]. Miniaturization of DEAs sets new challenges in the manufacture of electrodes: compatibility with cleanroom environment, precision patterning and low stiffening impact. With their automated fabrication process, Lotz *et al.* reach 1 mm resolution [81], which is one of the only reported techniques to produce small and reliable electrodes, yet remaining too big to be used at the scale used in MEMS. Bergbreiter's group worked on the integration of silicone elastomers in silicon MEMS. They report on microfabrication techniques in silicon wafers to mold vertically the electrode and dielectric layers of a bilayer DEA which is less than $200\,\mu$m in total thickness [83].

A way to make miniaturized electrodes for DEAs has been developed in the LMTS by implanting metal ions in silicone membranes [30, 84]. The Filtered Cathodic Vacuum Arc (FCVA) implanter produces gold clusters that can move relative to each other in the top 50 nm of the elastomer when the membrane is stretched [85]. In this way, they keep the electrical contact without producing cracks or inducing too much stiffening in the membrane. The main characteristics of this technology are a clean process (compatible with cleanroom microfabrication), easy-to-use electrode patterning by shadow masking, minimum feature size down to $100\,\mu$m with a steel shadow mask ($43\,\mu$m demonstrated with a photoresist mask) conduction remaining at up to 175% strain, stable resistance in time and less than 10% relative change of resistance after 120 thousand mechanical stretching cycles (20% strain, optimal implantation dose). This makes Au ion implantation one of the possible choices for microfabricated DEAs, with the disadvantage of long fabrication time and the need of a custom-built equipment. Speaking of performances, its main drawbacks are a large impact on the Young's modulus of the membrane (typ. +100%).

Consequently, we have developed another way of making soft electrodes with an indirect stamping technique (Pad Printing[6]). The electrode ink is taken from a metallic "cliché" with arbitrary electrode shape and stamped as an uncured mixture of soft silicone and carbon black. After thermal heating, crosslinking takes place and results in a few μm thick layer of conductive silicone. Their stiffening impact is most of the time negligible (unless printed on thin and soft membranes), and the production throughput is very high. The minimum feature size realized so far is in the order of $200\,\mu$m, with a potential improvement margin. More details on the electrode fabrication and printing process are given in [86].

Both Au-implanted and pad printed electrodes have been used in this project.

3.4 Dynamic performance of DEAs

The dynamic performance of Dielectric Elastomer Actuators can be considered as one of their major weaknesses. It is directly linked to the mechanical properties of the elastomer, as

---

[6]http://www.teca-print.ch/

Molberg showed that the dielectric losses are negligible compared to the mechanical ones [87]. The exceptional strains of DEAs are possible thanks to the softness of the elastomer, hence low stiffness and resonance frequencies. But the viscous component (damping) of the elastomers also plays a dominant role. Rubber-like materials are mechanically described as *viscoelastic*, a combination of viscous and elastic components. Such materials have the following properties: strain rate - dependent hysteresis in the stress-strain curve, stress relaxation (stress decreases after application of a strain step) and viscoelastic creep (strain increases after application of a constant stress step). The Kelvin-Voigt model is composed of a spring and dashpot element. More accurately, viscoelastic materials such as elastomers can be modeled with Prony series, a succession of parallel spring-dashpot elements (fig. 3.4), [32, 88].

Practically, it means that each elastomer possesses a set of time constants, some being very short (ms or below) and other as long as minutes or hours. The time response of elastomers is therefore a combination of exponentials, each one having its amplitude A_i and time constant τ_i (eq. 3.4).

$$x(t) = \sum_i A_i \cdot (1 - e^{-\frac{t}{\tau_i}}) \tag{3.4}$$

A single spring in series is sometimes added to account for the fact that part of the deformation is quasi-instantaneous [12], but fitting such a response with Prony series would simply result in an first spring-damper element with negligible damping (i.e. an infinitely short τ_1).
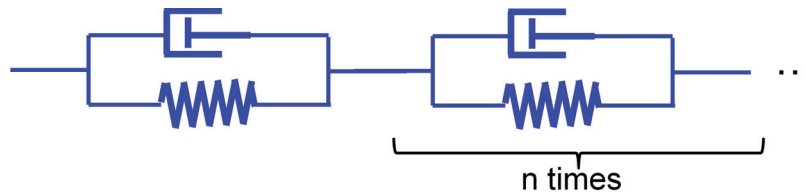
Figure 3.4: Prony series modeling of rubber elastomers

When sinusoidally stressing a viscoelastic material, the measured strain has a phase shift that reflects the mechanical damping of the material. The tangent of this angle, called loss tangent, is a measure of the viscous component of the material. The loss tangent can also be defined as the ratio between the imaginary and real part of the elastic modulus. The viscoelastic parameters obviously depend on the type of material (acrylic elastomers, silicones or less common materials such as natural rubber or polyurethanes). The very commonly used 3M VHB acrylic tape has a large loss tangent (more than 1 at 100 Hz [87]). Wissler fitted a 4-element Prony series with time constants of 0.31, 3.35, 35.7 and 370 seconds with relative amplitudes of 0.57, 0.19, 0.09 and 0.05 respectively. Although excellent in terms of static strains (see table 3.1 for the values of dielectric constant, dielectric strength and Young's modulus), the large viscous components of VHB limits it to applications with a bandwidth of a few Hz and where stable positioning is not mandatory.

Silicones offer the advantage of being commercially available in a wide range of shore hardness.

Depending on the application, the user can therefore choose between a softer material which will yield to more strain for a same electric field, and a stiffer one that will deliver a higher force. From a dynamic performance perspective, the general tendency is that soft silicones have a larger viscous component. Using stiffer silicones therefore both increase the elastic component and decrease the viscous one. Rosset *et al.* measured response times for three different test actuators made with silicone elastomers and a moving mass (table 3.2) [35]. But as they point out, the stiffness is not the only determining parameter: two silicones with same shore hardness might have up to 2 orders of magnitude difference in their time response.

Table 3.2: Response time of test-actuators loaded with a mass with conductive rubber electrodes using 3 different silicones, adapted from [35].

Silicone	Shore A hardness	10% − 90% response (ms)
Sylgard 186	24	16
Nusil CF186-2186	18	36
Silbione 4305	5	49

The influence of electrodes

Rosset *et al.* also compared the influence of the electrodes on the time response and on the static displacement [35], using Au ion implantation [36], a patterned proprietary conductive rubber electrode, and carbon grease. Only a few other publications report on the influence of electrodes on the device's static performance [89], none on the dynamic one. The conclusions are surprising in that for the three silicones studied, the impact on the time response is dominated by the electrode type over the elastomer material. Gold ion implantation yields the fastest response, a factor 3 to 10 better than conductive rubber and carbon grease.

3.4.1   The use of DEAs for fast response applications

In this section, a state of the art of the use of DEAs for applications where a fast response is needed will be presented. The application to tunable lenses will be discussed specifically in section 7.1.1.

For most VHB-based devices, the dynamic performance is not targeted as a feature. Aschwanden characterized his tunable grating up to 12 Hz, where the signal attenuation factor was close to 5.5 [22]. Döring's very strain-sensitive tunable wavelength laser has relaxation times of up to 12 hours [90]. VHB-based Dielectric Elastomer Generators obviously try to match excitation signal with large deformations but at a few Hz only [91,92]. Niu's and co-workers UV-polymerized acrylate-based DEA operates typically below one Hz, with an amplitude decay of a factor 3 at 5 Hz [93]. Kepliger's test device with ionic electrodes had an amplitude strain divided by four between 0.04 and 2 Hz [94]. Closed-loop control with capacitive self-sensing is one of the routes to achieve faster responses with VHB, with demonstrated 0 to 90% rise

times reducing from 3 to 1 s compared to open-loop control [95]. Silicone-based DEAs achieve much larger operating frequencies, such as 1 kHz resonance for an ion-implanted buckling actuator [36].

Loudspeakers are a particular case of high frequency actuation, because the mechanical limitation of actuation can be overcome to some extent by small amplitude vibrations still able to deliver acoustic waves. For instance, even a VHB-based device with a strain amplitude that almost vanishes at 1 kHz can produce some sound up to 20 kHz [94]. However, the vibration amplitude suffers much damping and one would obviously prefer less viscous elastomers to build a loudspeaker. Heydt *et al.*'s DEA loudspeaker has a bandwidth of 20 kHz in small-signal mode, but present distortions related to the square dependence between applied voltage and mechanical actuation [96]. Using polyurethane elastomer films, Sugimoto's *et al.* loudspeaker is bent in a cylindrical shape to transfer the device's area expansion into an out-of-plane sound wave. Its 15 kHz bandwidth is achieved with a thermoplastic polyurethane with a dielectric constant of 7.8 and a Young's modulus of 2.6 MPa [23].

Active damping mechanisms are one of the research field of DEAs. Compared to their passive counterparts, they offer better performance at low-frequency variations and adaptive bandwidth. Unlike loudspeakers, they require both fast response and large amplitudes. Silicone elastomers are therefore preferred for such applications [12]. Sarban *et al.* used the macro scale rolled actuators of Danfoss Polypower [7] that weight 100 g loaded with up to 500 g and measured resonance frequencies as high as 40 Hz [97].

For vibration-mode haptic feedback devices, large amplitudes are also desired at frequencies in the kHz range. Researchers have for instance built visio-haptic devices whose actuation amplitude increases up to the resonance frequency at 1.5 kHz [98]. Their device outputs 4 mN at 500 Hz. Schlaak's group investigated various haptic feedback structures with multilayer DEAs [20, 99, 100]. In particular, Matysek's 30-layers device frequency response shows only little amplitude decay up to 3 kHz in small-signal mode (electric field of $20\,V\,\mu m^{-1}$). All those devices take advantage of the bandwidth 2 to 3 orders of magnitude larger for silicones than VHB. EAP haptic feedback devices for smartphones or integrated into headphones have been commercialized by Artificial Muscle Inc[8].

3.4.2 Electrical response time

Neglecting the contact interconnects and the rise time of the voltage supply, the electrical time constant τ of a DEA can be described by

$$\tau = RC \tag{3.5}$$

---

[7]www.polypower.com/
[8]http://www.artificialmuscle.com/

where R and C are the resistance of the electrode and capacitance of the device. The capacitance of a $1\,cm^2$ DEA with a $30\,\mu m$ thick membrane is in the range of $100\,pF$. Resistances of ion-implanted electrodes are in the range of $200\,\Omega/_\square$, and $100\,k\Omega/_\square$ maximum for pad printed ones. The corresponding electrical time constant is therefore in the range of $10\,\mu s$, which is several orders of magnitude lower than the mechanical time constants of silicones (table 3.1).

This rough approximation shows that the electrical loading time is not limiting the actuation speed of miniature DEAs. As the capacitance scales with the device area, the electrical time constant may become an issue for very large DEAs [18].

3.5 Summary

The mechanical and electrical properties of the dielectric elastomer membrane directly determine the performance of DEAs. The key physical properties of dielectric permittivity, breakdown strength, Young's modulus and mechanical time constant have been discussed for silicones, acrylic elastomer VHB film, polyurethanes and natural rubber. The widely used VHB has the best static strain performance, but silicones outperform in terms of speed (2 orders of magnitude), long time stability, temperature operating range and resistance to humidity. Because it determines so drastically the actuation performance, custom-engineered dielectric materials have been developed by researchers in particular by the dispersion of fillers, which did however not lead to a breakthrough. Interesting materials such as bistable electroactive polymers which change their Young's modulus with temperature nevertheless extend the field of applications of DEAs.

The membrane fabrication process developed in the LMTS produces 20x30 cm silicone sheets of high quality down to $15\,\mu m$ thickness. Thanks to the use of a water-soluble sacrificial layer, the membranes can be released without tearing nor non-uniform stretching, which would soften the membranes anisotropically.

Compliant electrodes are of major importance, obviously in terms of stiffening but also regarding response time. Moreover, miniature DEAs specifically need solid-state clean electrodes which can be patterned with features much smaller than the size of the device. Au-ion implantation performs best in terms of feature size and effect on the mechanical viscous losses, and pad printing of a carbon black-soft silicone ink has the advantages of high throughput and low stiffening impact.

Because the elastomer is soft and has a viscous component, DEAs do in principle not perform well regarding response time. VHB-based devices have not only the problem of a slow response, but also of drifts of position in the order of minutes, which also disqualifies them to hold a static position. Silicones perform better, stiffer materials having in principle also a reduced viscous component. The reported applications so far are loudspeakers operated in small signal mode, active damping and haptic feedback. The electrical response time is in principle not limiting for miniature DEAs.

4 Compatibility of liquids with silicone DEAs

The possibility of having DEAs operating in contact with liquids opens a broad set of new actuator structures and applications, but is extremely challenging in terms of physical and electrical compatibility with the elastomer membrane. Liquids can be directly driven by DEAs, such as for pumps or valves which benefit from the large volume strokes. Second, an encapsulated pocket of fluid can be used as coupling agent between one or several active(s) or passive(s) membranes. Fluidic coupling permits highly flexible designs which include redirection of the the actuator motion and force-displacement conversion. Finally, enabling operation of DEAs in contact with liquids or in important humidity environments is crucial for energy harvesting applications such as from ocean waves.

Silicone membranes are prone to swell and/or let a large panel of solvent pass through the polymer network. They are also permeable to gases, so that if one wants to build devices with encapsulated liquid pockets, their vapor pressure must be kept as low as possible. Finally, hydrostatic coupling liquids should preferably have a low viscosity to reduce viscous losses.

A set of 12 liquids seen as good candidates to match these requirements have been tested by optical observation of the diffusion on a freestanding membrane and measurement of an encapsulated liquid pocket dimensions over up to 37 days. Liquids among two classes of fluids have been found to fulfill the above mentioned specifications: two silicone uncrosslinked bases and one ionic liquid. The conductivity of ionic liquids moreover enables their use as liquid electrodes.

Section 4.1 (Introduction and state-of-the-art) motivates the study of liquid compatibility with silicone membranes with a broad selection of references. Two types of DEA structures that handle liquids can be found in the literature: with a passive membrane that protects the sensitive DEA membrane or with an encapsulated liquid specifically chosen for its compatibility which couples the DEA motion to a passive membrane. The requirements on the liquid properties for this latter application are described.

Section 4.2 (Selection of liquids to be tested as mechanical coupling media) explains the

choices of the 12 investigated liquids (polar solvents, oils, silicone pre-polymers and ionic liquids) and lists their physical properties.

Section 4.3 (Experimental results) first describes the two experimental procedures realized, by optical observation of a drop on a 40 μm thick membrane and by encapsulation under thin prestretched membranes of two silicone types. The results of both tests are then presented and commented.

The fabrication process of the encapsulated liquid test devices is described in **section 4.4 (Fabrication)**.

Section 4.5 (Conclusions and outlook) discusses the results and concludes on the potential uses of the two types of liquid found to perfectly match the compatibility requirements. Other outcomes of the experimental results concern microfluidic chips which handle polar solvents that have been considered before as chemically compatible because inducing negligible swelling, but were proved now to penetrate into the polymer network.

4.1 Introduction and state-of-the-art

Using DEAs in contact with liquids is in development for many type of applications. DEA pumps would benefit from high power density, novel design and good performance when operating at low frequencies but with large stroke volumes [14, 101–103]. Another example which might be the killer application of DEAs is their use as Dielectric Elastomer Generators (DEGs) for wave energy harvesting [26, 104, 105]. The compliant electrodes and dielectric elastomer structure is used as a variable soft capacitor that converts mechanical to electrical energy. Thanks to the soft structure of the the generator, it can for instance match multiple resonance modes of the waves [104]. DEA-powered tunable optics also often uses encapsulated liquid as lenses [21, 106]. Finally, liquids are also used as mechanical coupling media between active and passive membranes [107–110].

4.1.1 Weaknesses of direct contact between DEAs and liquids

Putting a DEA in direct contact with a liquid poses four main problems: damage of the electrode, dimensional change (swelling, release of stress), alteration of the mechanical properties (stress-strain characteristic, viscoelasticity, etc.) and of the electrical parameters (dielectric constant, breakdown field) of the dielectric membrane. Except for the damage of the electrodes, these issues are due to the fact that many types of liquids penetrate into the polymer network.

A large set of DEAs are still manufactured with electrodes that have poor adhesion on the membrane, such as carbon grease. If so, a liquid flow or any hard contact would directly result in local damage in the electrode and in liquid sample contamination. The LMTS developed a technique to pattern stretchable electrodes composed of carbon particles dispersed in a soft

elastomer matrix that adhere strongly on the membrane, so that we do not face this issue [79]. Another example of durable electrode has been developed by Danfoss Polypower[1]: a silver thin film is sputtered on a corrugated membrane pattern [80].

It is well-known that elastomers are prone to absorb a wide range of solvents, as demonstrated for instance on the Dow Corning Sylgard 184 silicone by Lee *et al.* [111]. The swelling ability depends on the crosslinking density, and is even used as a way to measure it [112]. Lee's work was motivated by the widespread use of silicones in microfluidic chips. DEAs based on acrylic elastomers use the commercially available Very High Bonding (VHB) tape from 3M[2]. Because of its use for EAPs by research labs, no systematic study on its compatibility with solvents was found in the scientific literature. However, the datasheet provides information on its adhesion strength after immersion in solvents. Unaffected performance are claimed in liquids such as water, glycerol or motor oil, reduced adhesion by a factor two in isopropanol and down to 5% adhesion with methyl ethyl ketone. On the contrary, the swellability of polyurethanes has been quite extensively studied in reason of their use as biocompatible material [112, 113]. Generally speaking, all these three families of elastomers present average solvent compatibility behavior. Qualitative compatibility charts between elastomers and solvents are available on several rubber products suppliers websites [3].

The penetration of solvents inside the elastomer matrix first degrades its mechanical properties. A membrane which is swollen will release its prestretch, become softer and most likely have an increased viscous component. It is also probable that the dielectric constant as well as the breakdown strength will be affected. By speculation, one could imagine that the electrical properties might improve depending on which solvent is used, but in general any unpredictable and unstable change of the actuation behavior has to be avoided, as well as liquid leakage between the two membrane interfaces. Researchers have observed an increased breakdown strength from $450\,\mathrm{V\,\mu m^{-1}}$ to $800\,\mathrm{V\,\mu m^{-1}}$ by immersing an acrylic VHB actuator in silicone oil, but attributed it to the prevention of thermal runaway that occurs during electrical breakdown events [114].

The use of ionogels as electrodes on VHB-based DEAs has been reported in several works [94, 115, 116]. Ionogels are obtained by polymerization of elastomers in ionic liquids. Thanks to the non-measurable vapor pressure and high conductivity of ionic liquids, the synthesized gels are stable and conductive materials, with the additional feature of optical transparency. This indicates that some ionic liquids are in principle compatible with DEA membranes.

---

[1]http://www.polypower.com

[2]www.3M.com/VHB

[3]**Mykin:** http://mykin.com/rubber-chemical-resistance-chart

BASF: http://www.polyurethanes.basf.de/

Apple Rubber: http://www.applerubber.com/

(a) The DEA is protected by a membrane

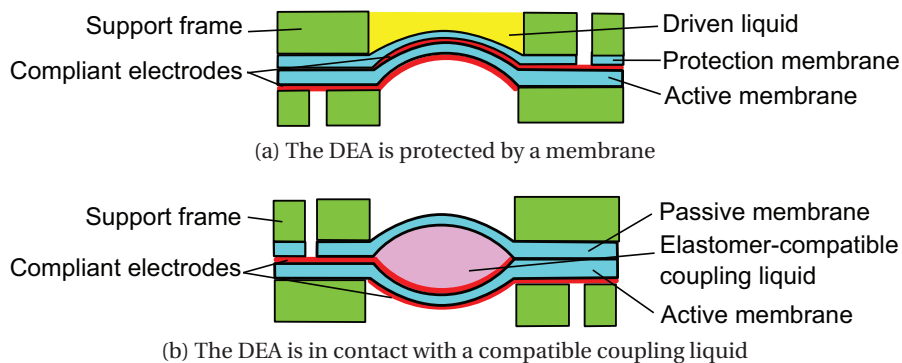(b) The DEA is in contact with a compatible coupling liquid

Figure 4.1: Two main structures of DEAs for driving liquids

4.1.2 Two main structures used for driving liquids with DEAs

As the DEA membrane is mechanically and electrically sensitive to many types of fluids, two main type of routes have been taken to bypass this issue. If the liquid to be processed is driven with the actuator membrane, it is most of the time protected by a separation layer that physically and electrically insulates the DEA membrane from the liquid (fig. 4.1 a), such as for Lotz *et al.*'s micropump [81, 102]. This approach is also used by Murray *et al.*, whose DEA stripes are separated from the microfluidic channels by a 60 µm thick Sylgard 184 silicone layer [117]. In the same manner, Akbari *et al.* passivate a miniature cell stretching device with a silicone membrane, which also avoids the saline solution to act as a electrode [24].

Devices in which the liquid is used as a mechanical coupling agent pose the same problems of physio-chemical compatibility with the elastomer, but with a major advantage compared to devices that control random fluids: since it is encapsulated, the liquid can be chosen specifically (fig. 4.1 b). If a compatible liquid is found, no passivation layer is needed but the closed liquid pocket transfers the mechanical work of the DEA membrane to a passive one [107–110], which might in turn be used to drive a random fluid without risking of altering the sensitive actuator membrane. The alteration of the mechanical properties of the passive membrane by a processed fluid is also a concern for the performance stability of the device, but no requirements are set regarding the electric ones: it is not active. A specifically compatible material for the passive membrane can also be chosen, without requirements on its breakdown strength or permittivity. Hydrostatic coupling additionally improves design flexibility, for instance by playing with different shapes and mechanical properties of the membranes to favor output force or displacement.

4.1.3 Requirements for using liquids with silicone elastomer membranes for encapsulated DEA-driven coupling chambers

In terms of chemical compatibility, water is known as the ideal candidate for silicones [111,118]. However, silicones are gas-permeable so that the encapsulation of a liquid pocket sets an additional constraint: the vapor pressure of the liquid has to be negligibly low to keep the

encapsulated volume constant. Another desirable property is a low viscosity to minimize the energy dissipated by losses during actuation that slow down the response time.

The swelling ratio is an important indication of the penetration of solvent into elastomers [111, 113, 119]. It is commonly measured by comparing the length of pieces before and after a long time immersion (typically 24 h) into the solvent. Non-polar solvents such as hydrocarbons or toluene strongly swell silicones. The direct but not systematic relation between the solubility parameter δ of a solvent and the ability to swell silicones was assessed experimentally: if its value is close to the one of the silicone ($\delta =7.3\,\mathrm{cal}^{1/2}\mathrm{cm}^{-3/2}$), it swells more [111].

4.1.4 State-of-the-art on the use of coupling media with thin silicone membranes

According to Lee *et al.*'s ranking, the 3 most compatible solvents with the Dow Corning Sylgard 184 silicone after water are glycerol, ethylene glycol and dimethylsulfoxide (DMSO). The Zappe group used a proprietary liquid of Cargille[4] in several of their tunable lenses devices without commenting specifically on its chemical compatibility with silicone membranes or on its evaporation rate [120, 121]. A silicone pre-polymer (uncured base) was used in a VHB-based tunable lens [21]. DEAs hydrostatically coupled with passive membranes were presented in several works of Carpi *et al.*. More specifically, water [107], as well as corn oil [108] were used on their silicone-based devices. The use of silicone grease was also assessed on a set of VHB-based hydrostatically coupled DEAs, as well as talcum powder [122]. Despite the comparable performance obtained with these two last coupling media, the use of powders would obviously have a detrimental effect on the mechanical losses due to the high friction between the particles.

4.2 Selection of liquids to be tested as mechanical coupling media

In order to find the best liquid to encapsulate as hydrostatic coupling agent between an active and a passive silicone membrane, the compatibility of 12 liquids with silicone membranes was experimentally tested. Membrane-based tunable lenses do use an encapsulated liquid as compliant optical medium. Any change in volume (evaporation, leak) will shift the operating point of the device, and any formation of droplets due to penetration of the liquid in the membrane renders the lens optically unusable. These requirements are also valid for hydrostatically coupled membranes. For optical applications, transparency is also required: good transmission and absence of light scattering.

Table 4.1 displays information about the tested liquids. A set of polar solvents was first selected: Glycerol, Ethylene Glycol, Dimethylsulfoxide, N,N-dimethylformamide and Propylene Carbonate. Two silicone pre-polymers were then chosen, the one of the Dow Corning Sylgard 184 which has a high optical transparency and the component B of the LSR-20 silicone from Factor

---

[4]www.cargille.com, Series A liquid

2 [5] which is less transparent but has a slightly lower viscosity, an advantage for hydrostatically coupled actuators. Four different oils were also tested: a microscope immersion oil (Leica type F), Safflower oil, a general purpose lubricant oil (Komet, Fessmann & Hecker) and a vacuum pump oil (Edwards Ultra Grade 19). Finally, bis(trifluoromethylsulfonyl)imide (TF_2N), an ionic liquid bought at iolitec[6] was investigated .

The five solvents have been chosen based on Lee's work and are all expected to induce a minimal swelling on silicones [111]. As explained before, another crucial parameter is a low vapor pressure, since silicone membrane are gas-permeable. Among the three polar solvents, Ethylene Glycol and Propylene Carbonate are the best candidates because of their low vapor pressure. The two silicone pre-polymers have negligible vapor pressure, but a very high viscosity. They have already been encapsulated between acrylic VHB membranes [21], but their compatibility with silicone membranes has to be experimentally validated. Whereas apparently suitable for acrylic elastomers [123], silicone oils obviously penetrate into silicone membranes and lower their dielectric strength [108]. Four different oils were also tested, although they are non-polar, since oils are known to have a low vapor pressure and are electrically insulating. High dielectric constant and insulating properties of the coupling fluid are indeed desired: if it penetrates by some extent inside the membranes, conductive liquids would drastically degrade the breakdown strength, leading to an actuator failure. For the 5 polar solvents, conductivity strongly depends on the presence of ion impurities. Finally, the investigated ionic liquid is obviously highly conductive but has a vapor pressure so low that it cannot be measured, with a viscosity comparable to oils. It would only be usable if not penetrating at all in the membrane.

4.3 Experimental results

A first test consisted in placing drops on elastomer membranes and observe optically if any change can be seen. The second test was done by encapsulating a liquid pocket under a silicone membrane, and to measure the height of the balloon in function of time.

4.3.1 Test with a drop on a membrane

As a first quick test, drops of the 5 polar solvents were deposited on un-prestretched 40 μm thick Sylgard 186 silicone membranes. Surprisingly, droplets formed on the bottom of the membrane within less than 30 s with DMSO and N,N-dimethyl-formamide (fig. 4.2). No clear swelling (wrinkles) was observed, but these two solvents clearly penetrate inside the thin silicone membrane. They were discarded but Glycerol, Ethylene Glycol and Propylene Carbonate did not clearly show such a behavior so that they were kept for the second test.

---

[5]www.factor2.com
[6]www.iolitec.de

Table 4.1: Investigated liquids

| Liquid	Swelling ranking after [111]	Vapor pressure T_{amb} (mmHg)	Viscosity (Pa s)	Electrical properties
DI water	38	26.7	8.9×10^{-4}	$\epsilon = 80$
Glycerol	37	1	9.3×10^{-1}	$\epsilon = 47$
Ethylene Glycol	36	0.08	1.6×10^{-2}	$\epsilon = 38$
Dimethylsulfoxide (DMSO)	35	0.42	2.0×10^{-3}	$\epsilon = 49$
N,N-dimethyl-formamide (DMF)	27	2.7	7.9×10^{-4}	$\epsilon = 37$
Propylene Carbonate	30	0.13	2.7×10^{-3}	$\epsilon = 65$
LRS20 silicone component B	-	negligible	3 to 4	insulating
Sylgard 184 prepolymer	-	negligible	3.9	insulating
Leica type F microscope oil	-	low	medium	insulating
Safflower oil	-	low	2.7×10^{-2}	insulating
Tool lubricant oil	-	$<7.5 \times 10^{-2}$	6.07×10^{-2}	insulating
Vacuum pump oil	-	7.5×10^{-9}	1.23×10^{-1}	insulating
Ionic liquid (TF2N)	-	negligible	3.48×10^{-2}	conductive 0.88 Sm^{-1}
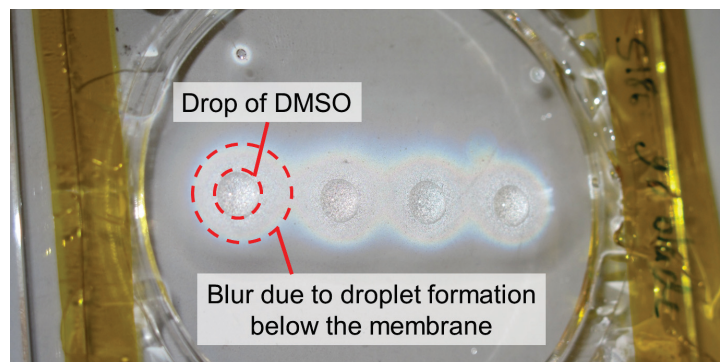
Figure 4.2: Four drops of Dimethylsulfoxide on a 40 μm silicone membrane displays a strong penetration of the solvent by the formation of droplets on the backside within 30 s

4.3.2 Test by encapsulating a liquid pocket

In order to quantify the durability of the liquids as fluidic coupling media, 3 mm diam. liquid pockets were encapsulated between a prestretched membrane and a rigid silicone piece (fig. 4.3). The compatibility of each liquid was assessed by optical inspection of the membrane surface and by measuring the height of the bulge versus time with a white light profilometer (Wyko NT 1100). Two silicones were used, the CF19-2186 from Nusil (27 shore A hardness) and the Silbione LSR4305 from Bluestar (5 shore A hardness), with prestretches between 1.2 and

1.5 and prestretched thicknesses of 19±3 µm for all cases. The membrane thickness at half sphere shape ($z =1.5$ mm) is below 10 µm. No difference in behavior was observed by varying the silicone type nor the prestretch.
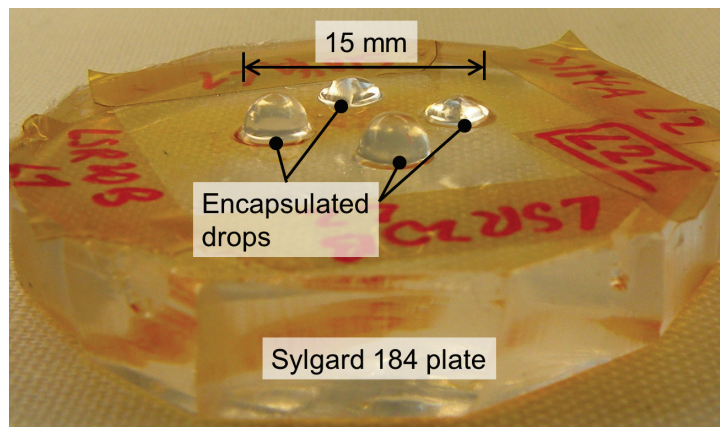

Figure 4.3: Picture of the test device with 4 encapsulated liquid pockets. Pocket diameter: 3 mm

The results are displayed on figure 4.4. Pictures of the bulge apex were taken with an optical microscope, and appear on figure 4.5.

Looking at the figure 4.4 a, the polar solvents are relatively bad candidates, except glycerol which keeps a constant height. However, the microscope picture displayed on figure 4.5 a reveals a pattern of droplets around 2.5 µm in diameter: it clearly passes through the membrane. Ethylene Glycol, Propylene Carbonate and DI water did quickly leak out the chamber, either directly in gas phase or by evaporating once reaching the side of the membrane exposed to air.

Although the oils of figure 4.4 b are retained for a longer time inside the encapsulated pocket than polar solvents, they are unsatisfying candidates. The Safflower oil seems to be very compatible with silicones, as the bulge height only decays from a few percents. However, like Glycerol, looking at the top of the membrane reveals that a film of oil has passed through (figures 4.5 c and d).

The last graph displays the two silicone pre-polymers and the ionic liquid (figure 4.4 c). Both silicone bases keep a nearly constant bulge height over more than one month. The ionic liquid is even more stable, so that the measurement was stopped after 20 days. All these three liquids do not display any sign of penetration inside the thin silicone membrane by optical inspection (figure 4.5 e), and have a negligible vapor pressure.
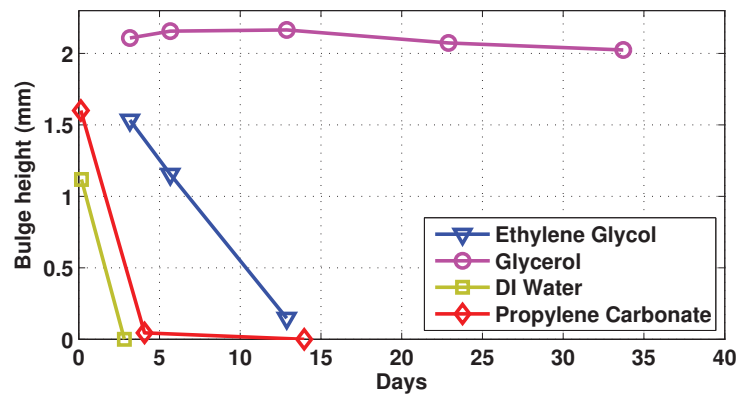
(a) Polar solvents
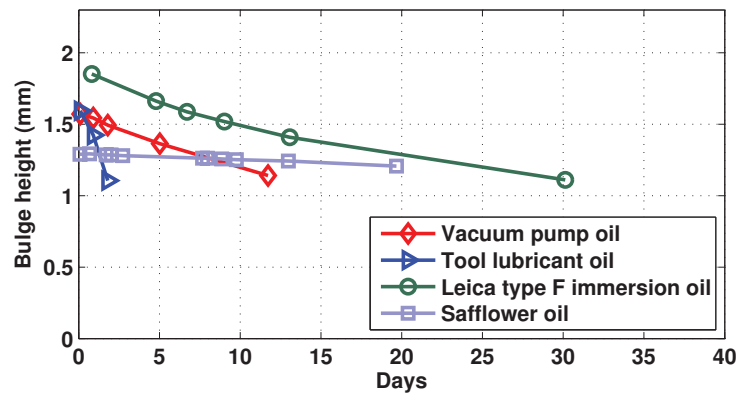
(b) Oils
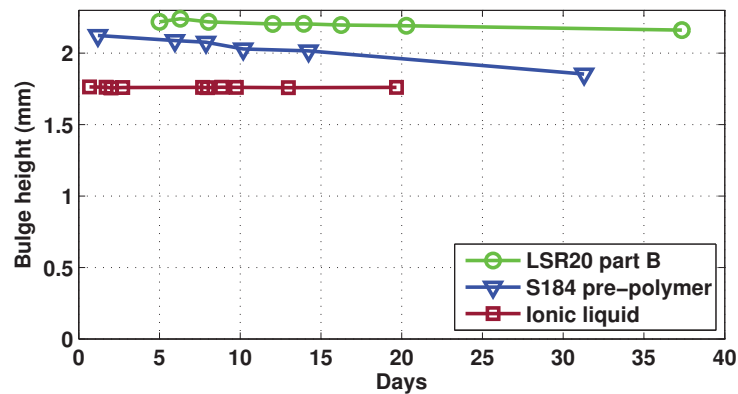
(c) Silicone pre-polymers and ionic liquid

Figure 4.4: Evolution of the bulge height for liquids encapsulated under silicone membranes. No difference was observed between the two silicones tested (CF19 and LSR4305). Liquids which appear good candidates for the bulge height test such as Glycerol and the tool lubricant oil actually form droplets on the other side of the membrane. The best results are obtained with the viscous but electrically insulating unpolymerized bases of the LSR20 and S184 silicones and the conductive ionic liquid, which all perfectly fulfill the requirements of physico-chemical compatibility and evaporation rate.
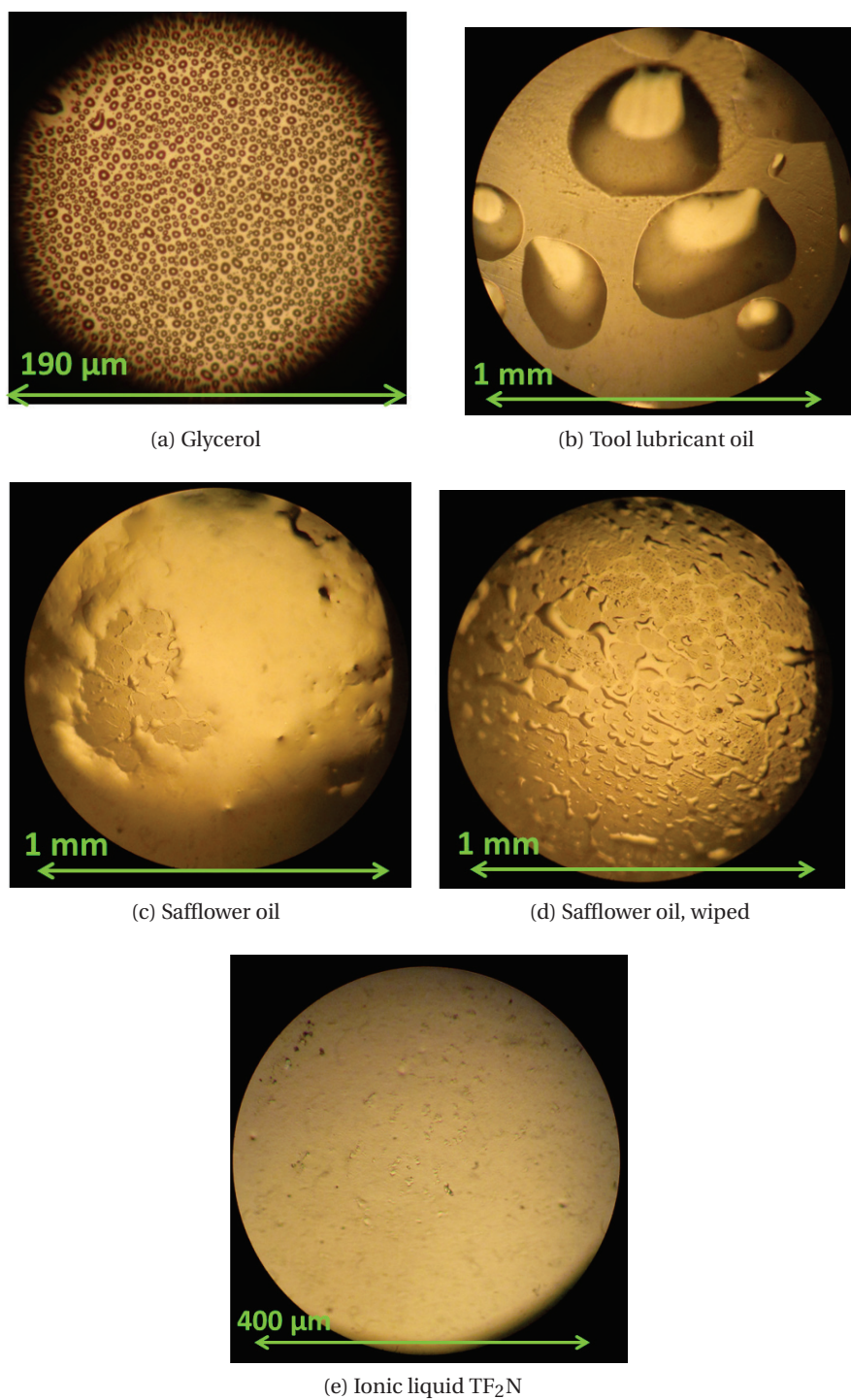
(a) Glycerol

(b) Tool lubricant oil

(c) Safflower oil

(d) Safflower oil, wiped

(e) Ionic liquid TF_2N

Figure 4.5: Optical pictures on the bulge apex of membranes with different encapsulated liquids

4.4 Fabrication

The fabrication of the test device for measuring the suitability of different liquids as encapsulated hydrostatic coupling fluids is illustrated on figure 4.6.

The first step is to activate a $19\,\mu$m thick soft prestretched silicone membrane (Nusil CF19-2186 or Bluestar Silbione LRS4305) and a rigid silicone plate (Dow Corning Sylgard 184) (fig. 4.6 a). The soft membrane is then laid on a CNC-machined vacuum chuck made of a porous material (Metapor[7]) with 4 holes which defines the encapsulated liquid pockets (fig. 4.6 b). As vacuum is applied, the membrane is pulled in the holes and I fill them with four different liquids to be tested (fig. 4.6 c). The rigid silicone plate is then placed on top, and after one hour the bonding is achieved and the test device can be released (fig. 4.6 d). Finally, the membrane frame is separated from the device and the trapped air bubble evaporate within a couple of hours and the first measurement of the bulge height can be performed (fig. 4.6e).

4.5 Conclusions and outlook

12 liquids to be used as mechanical coupling agents for silicone DEAs were experimentally tested. This problem poses severe constrains of phisico-chemical compatibility since the active membrane can be both mechanically and electrically affected by the penetration of liquids in the polymer network, leading to actuation performance degradation or electrical breakdown. Another requirement is a low vapor pressure of the coupling liquids: since silicones are gas-permeable, the volume of the closed liquid pocket volume would decrease by evaporation. Finally, a low viscosity is preferable to avoid mechanical losses. A first test was done by putting drops of solvents on un-prestretched membranes. In a second step, liquids encapsulated under membranes as thin as $10\,\mu$m once inflated of two silicone types were monitored over up to 37 days. Combined with optical observations of the membrane surface, it is found that silicone pre-polymers and ionic liquids match the requirements of encapsulated coupling fluids for DEAs.

Based on previous advanced systematic studies of silicone swelling in liquids [111], polar solvents such as Glycerol, Ethylene Glycol, Dimethylsulfoxide or N,N-dimethyl-formamide are expected to be good candidates. The compatibility requirements for electroactive membranes are more demanding, since they should not be permeable at all to the liquid. When applied on membranes that are a few 10 of μm thick, droplets form on the other side of the membrane within 30 s for DMSO and N,N-dimethy-formamide. The same effect is visible for Glycerol, but in a less visible manner. It seems that it does not induce noticeable swelling (which is coherent with Lee's study [111]), but solvents that do not swell silicones actually penetrate into the elastomer, an effect which is not optically visible on a bulk piece of material but clearly on a membrane. This behavior may also be critical for the design of other silicone-based devices such as microfluidic chips where thin membranes are used or where different solvents are

---

[7]www.portec.ch

sequentially flushed in channels. Four different oils were tested and stayed for a longer time in the encapsulated pocket than the polar solvents, but all of them did also leak through the membrane.

Finally, the volume of pockets filled with silicone pre-polymers was found to remain almost ideally stable over more than one month and their membrane surface did not show any sign of leakage. The TF_2N ionic liquid did also not show any sign of penetration into the silicone membrane either, so that it can also be used as coupling fluid despite its high conductivity. It can also be used as a liquid electrode.

As a conclusion, it is possible to build reliable and long-term stable DEAs with encapsulated liquids as mechanical coupling agents between active(s) and passive(s) membrane(s) thanks to the very good compatibility of silicone membranes with silicone pre-polymers and ionic liquids. No noticeable difference observed between the two silicone membrane materials tested suggests that the type of silicone has little or no influence on the liquid compatibility.

These results are of primary importance for the ongoing development of fluidically-coupled DEAs as out-of-plane operating transducers. More specifically, microfluidic actuators or tunable lenses directly benefit from these conclusions. For this latter application, the fluid is not only used as mechanical coupling agent but also as optical medium, which is possible for both Sylgard 184 pre-polymer and TF_2N ionic liquid thanks to the high transparency.

Based on these results, fluidically-coupled microfluidic actuators with Sylgard 184 pre-polymer as coupling agent will be presented in section 5.5. Chapter 6 will describe two generations of fluidically coupled tunable lenses using either TF_2N (also used as liquid electrode) and Sylgard 184 pre-polymer. Chapter 7 also uses encapsulation of the silicone pre-polymer between two membranes to build a high-speed biconvex tunable lens.
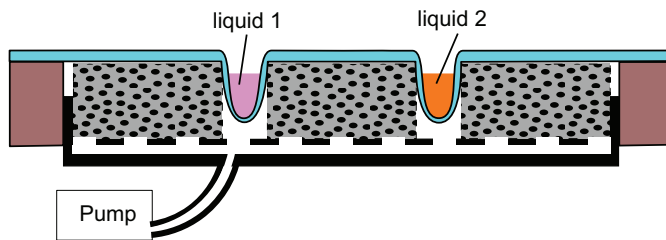
The content of this chapter will be submitted for publication in SPIE EAPAD conference proceedings.
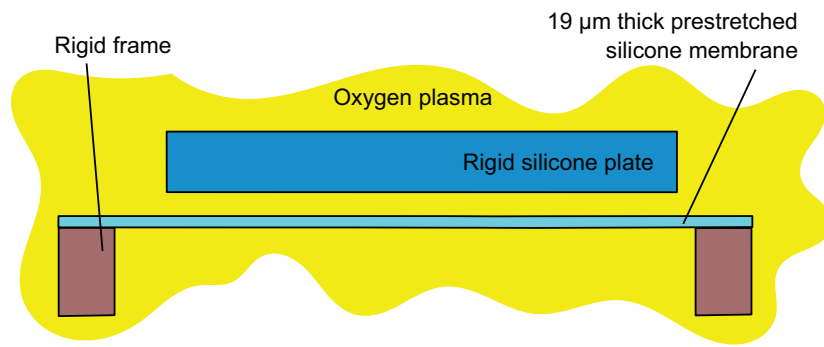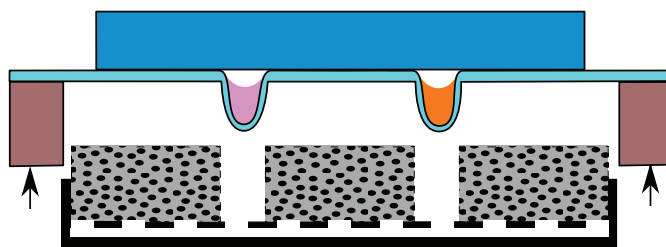
(a) Plasma activation of soft silicone membrane and of a rigid silicone plate
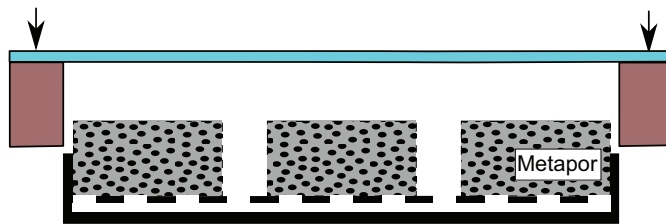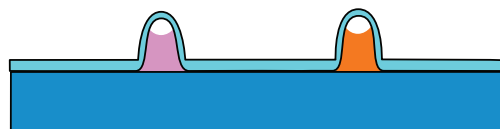

(b) Placement of the membrane on a porous material vacuum chuck with 4 holes

(c) Filling of 4 holes with the liquids to be tested

(d) Bonding the rigid silicone plate and release the test device

(e) The trapped air bubbles evaporate within a few hours

Figure 4.6: Fabrication of a test device for measuring the suitability of different liquids as encapsulated coupling fluids.

5 Zipping DEAs for microfluidic actuators

Electrostatic zipping is a well-known mechanism in silicon MEMS. It basically consists in attracting gradually a bending structure (such as a microfabricated cantilever) in contact with a thin rigid dielectric across which a high electric is applied. It enables to obtain large deformations and forces at lower voltages than for parallel plate electrostatic actuation. This concept is extended to DEAs: instead of squeezing the elastomer between two compliant electrodes, a single compliant membrane is pulled in contact with a rigid one. The compliant membrane deflects inside a sloped cavity by being pulled against its sidewalls like a zipper. This new actuator type is the ideal candidate to build miniature microfluidic actuators to replace the commonly-used pneumatic valves or for tactile displays. It is indeed expected to have characteristics of sealing ability, lower operating voltages and highly tunable voltage versus deflection characteristic including bi- or multi-stable states.

Section 5.1 (Introduction and state-of-the-art) gives an introduction and state of the art of integrated pneumatic silicone-based microfluidic actuators, which are the basic building block of one of the widest class of microfluidic devices. Portability of those chips is an issue, and options for making electrically-controlled integrated actuators are discussed, among which DEAs might be the best choice. The few paper which report on the use of DEAs for microfluidics are reviewed, and a variant of zipping DEAs with the electric field applied across the membrane is presented as a potential improvement of existing solutions.

An analytical model of zipping DEAs is proposed in **section 5.2 (Analytical modeling of zipping DEAs)**. It uses mechanical and electrostatic energy contributions and is computed given the very particular deflection state of the membrane, which is in non-slipping conditions with the sidewalls. The results of the model are discussed in details, and highlight in particular the presence of a bistable state in the deflection versus voltage characteristic with pyramidal- or conical-shape chamber geometries.

Section 5.3 (Zipping in pyramidal anisotropically-etched silicon chambers) presents a peristaltic pump design based on a microfabricated silicon body. The zipping cavity sidewalls are obtained by anisotropic etching of silicon, which yields mm-size pyramidal-shape cavities

with 54.7° sidewalls angle. The deflection of the membrane as well as its shape were measured, and optimized by changing silicone and electrode types. Performance limitations are linked with the achievable shape of the sloped chamber with silicon microfabrication technologies.

Mm-size conical-shape actuators with lower sidewalls angles were therefore studied in **section 5.4 (Zipping in conical low-sloped chambers)**. Full zipping was achieved with a clear bistable behavior, as predicted theoretically. The analytical model was validated with the angle and the membrane prestretch as parameters. A new peristaltic pump design based on this second generation of actuators was proposed, which keeps the processed liquid free from the high electric field, unlike the first pump design. However, the active membrane is still in direct contact with the liquid, which has been identified in liquid compatibility tests as a critical reliability issue (chapter 4).

A third option for microfluidic actuators was therefore considered in **section 5.5 (Sub-mm size microfluidic actuators fluidically coupled to zipping DEAs for application to a peristaltic pump)**, using an encapsulated liquid pocket to hydrostatically couple an active and a passive membrane. This final design makes sure that the sensitive DEA membrane is kept away from the processed liquid. In this configuration, the active membrane is submitted to a bias pressure. Operating conditions are experimentally investigated to find suitable design parameters. Sub-mm passive membranes fluidically-coupled to zipping DEAs were then built and characterized statically and dynamically. The measured displaced volumes did however not reach the expected values, which will be discussed.

Section 5.6 (Fabrication) contains fabrication process details for all devices.

Section 5.7 (Summary and conclusion) concludes with the main achievements linked to the experimental realization and analytical modeling of zipping DEAs, which operate in a novel actuation mode enabling unique characteristics. Three generations of miniature zipping DEAs were built and allowed to stress on the important design parameters, limitations and strengths.

Part of the content of section 5.3 has been presented as a poster: L. Maffli, S. Rosset and H. R. Shea. Zipping Dielectric Elastomer Actuators for microfluidics, *EuroEAP conference 2012*, Potsdam, Germany, 2012.

Parts of this chapter have been published in:

L. Maffli, B. M. O'Brien, S. Rosset and H. R. Shea. Pump it up. In *Proc. SPIE 8340*, volume 8340, pages 2Q1–2Q16, 2012.

L. Maffli, S. Rosset, and H. R. Shea. Zipping dielectric elastomer actuators: characterization, design and modeling. *Smart Materials and Structures*, 22(10):104013, 2013.

L. Maffli, S. Rosset, and Herbert R. Shea. Mm-size bistable zipping dielectric elastomer actuators for integrated microfluidics. In *Proc. SPIE 8687*, volume 8687, pages 2M–2M–10, 2013.

5.1 Introduction and state-of-the-art

5.1.1 Integrated pneumatic silicone-based microfluidic actuators and their portable alternatives

The microfluidic world is developing rapidly. Aside from the favorable scaling effects on fluid handling and sample analysis, one of the ultimate goals of miniaturized fluidic systems is to bring a whole laboratory processing chain on a few square centimeters: Lab-On-Chips (LOC) [124]. However, most of the current LOCs require many heavy and power-consuming off-chip controls like pneumatics and liquid pumps and valves. If the user takes benefit from the large number of operations that can be done on a single chip, the increase in complexity requires more and more off-chip controls. The advantages of miniaturization are therefore questionable, because the small chip remains bound to the lab. But having truly portable devices is required for point-of-care and home use applications, which will probably be the commercial breakthrough of lab-on-chips. Replacing the pneumatic actuators by electrical actuation would greatly reduce the size of the off-chip components.

DEAs for microfluidics are a promising option to face this issue. Their advantage compared to their piezoelectric and electrostatic competitors is the combination of large stroke volumes and high output forces. Indeed, piezoelectric diaphragms achieve excellent pumping performance, but are very limited in term of maximal deformations, which is required to valve the channels. Regarding electrostatic actuators, their variable gap in the channel has to be kept small to have a sufficiently large electric field, which limits their strain. Having an electric field in the channel is also problematic for some applications. Multipurpose software-reconfigurable microfluidic chips composed of arrays of actuated chambers, also called Microfluidic Large-Scale Integrated (MLSI) chips [125–127] (figure 5.1), are devices for which the use of DEAs could be particularly relevant. MLSI chips consist of arrays of independently-controlled pneumatic actuators, with fluidic channels on one level and pneumatic on another level. In the places where they cross, the soft membrane (usually silicone) that is in between deflects and closes or opens the fluidic channel if the air pressure is set on (figure 5.2). These simple and robust actuator units may produce both a pumping and valving action [128].

Electrostatic actuation is seen as a possible means of adressing the portability of MLSI chips [129]. The electric field is applied across a variable gap, which closes a chamber. Chang *et al.* developed small electrostatically active chambers (figure 5.3) [130]. A "roof" made of silicone with a sputtered and microstructured metal track collapses down a gap of approximately $3.8\,\mu m$ height under application of a $5\,MHz$ $40\,V$ signal. The voltage is modulated at radio-frequency to reduce electrolysis, prevent electrode polarization and electrical double layer screening. The estimated pressure is in the range of $0.9\,kPa$, with a flow rate of approximately $1\,nL\,min^{-1}$. In a closed state, a chamber has a dead volume of 18%. Because of the variable gap, electrostatic actuation can only generate small displacements, and one has to keep the channel or chamber height of a few µm only, which is problematic to process large sample volumes.
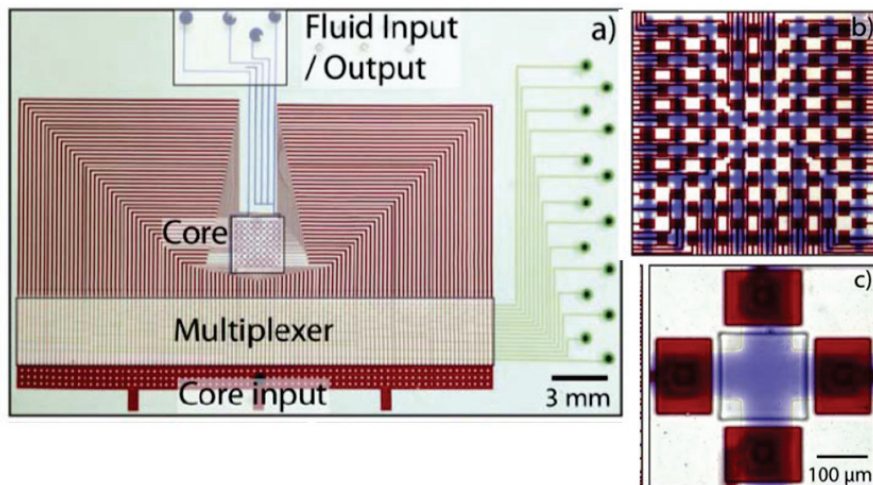
(a) Thanks to a clever multiplexing system, 21 off-chip pneumatic valves open or close channels between 64 chambers. The device additionally needs fluidic pumps to flush the liquid in the channel. (reprinted from [126])
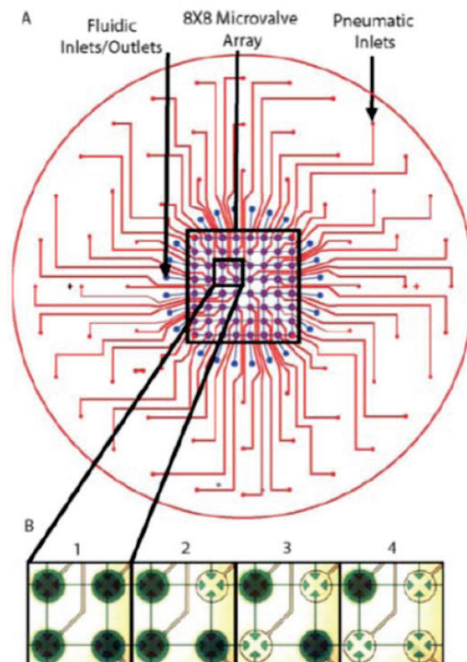
(b) Reconfigurable MLSI device with 64 normally-closed valves. As the actuator is located on the chamber, they produce both pumping and valving action so that no external liquid pump is required (reprinted from [127])

Figure 5.1: Example of MLSI devices based on pneumatic actuation of silicone membranes.

Additionnaly, the processed liquid is subject to electric field, which might for instance cause a problem for handling biological samples.
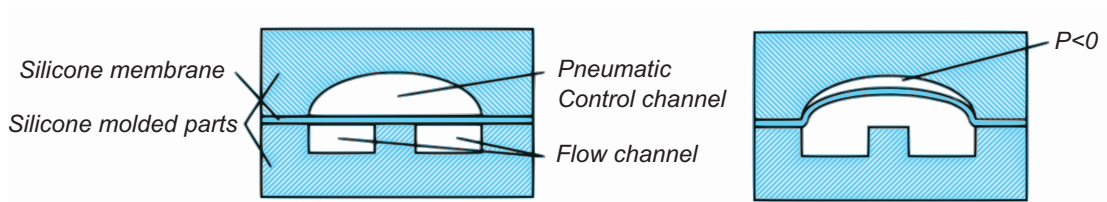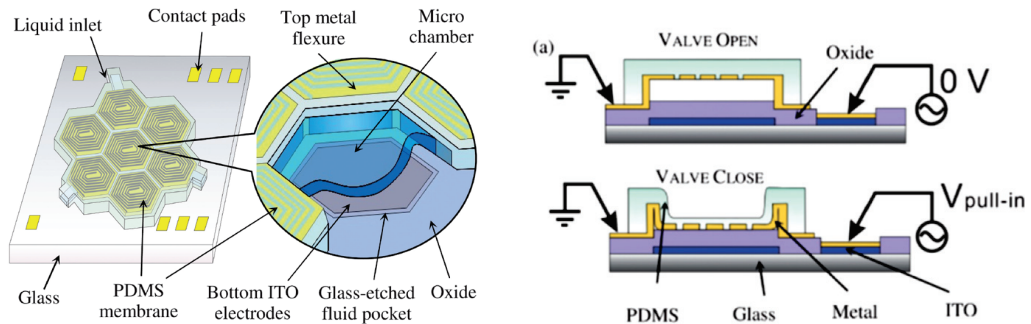
Figure 5.2: Commonly-used pneumatic "normally-off" microfluidic valve [127, 128]

(a) 7 interconneced fluidic chambers can perform various tasks such as mixing, pumping and switching

(b) A serpentine track is electrostatically attracted toward a transparent electrode to close a 3.8 μm gap.

Figure 5.3: Chang's electrostatically actuated reconfigurable device (reprinted from [130])

DEAs could be the alternative to replace the large stroke pneumatic-powered valves by electrically-actuated ones, since both operate by deflecting soft elastomer membranes. The basic operating mode of DEAs is an in-plane motion, where a pre-stretch is released by electrostatic compression of a dielectric membrane. Since its introduction by Pelrine et al. in 1998 [16], most of the efforts of the scientific community have been focused on this successful DEA configuration. To achieve out-of plane motion, frames with joints and hinges [44, 131], minimum energy structures [45], buckling-mode devices [36] or the use of offset pressures [132] have been reported. Another broadly studied way to achieve out-of-plane actuation is to use the thickness compression of stacked or folded layers [133, 134].

Making an actuator for microfluidics is a challenge: well-controlled out-of-plane deflected shape, liquid-tight sealing of chamber sidewalls, low voltage operation, and bistable operation are required. The processed liquid should also be maintained at a floating or grounded potential, and electric fields should be avoided in it not to interact with biological or chemical components. There is a gap to bridge between the state-of-the art DEA and these requirements for exerting a force on conductive liquids.

5.1.2 DEAs for microfluidic actuators

A few papers report on the use of DEAs for microfluidic actuators. Lotz *et al.* built a peristaltic micropump with a row of 8 mulilayer DEAs operating in thickness compression mode [81,
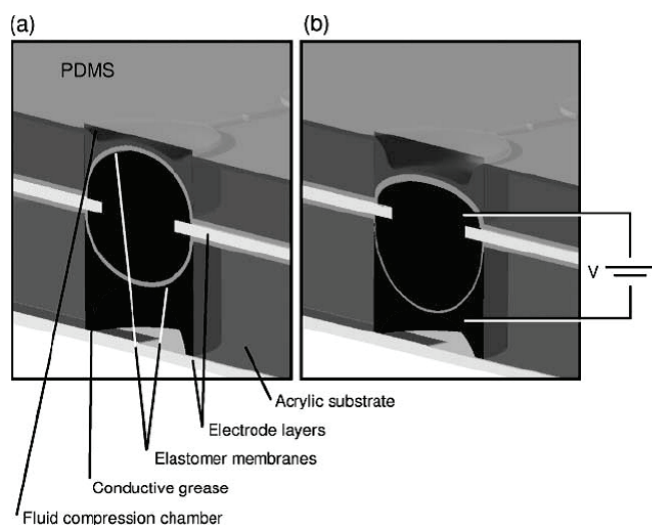
Figure 5.4: Cross-section of Loverich's 1.5 mm diam. actuator, with a closed balloon chamber filled with carbon grease as compliant electrode and fluidic coupling between one active and one passive membrane. (reprinted from [135])

102]. They achieved 0.37 kPa backpressure and up to $10\,\mu\mathrm{L\,min}^{-1}$ flow rate. More impressive, Loverich's clever DEA micropump works with two passive check valves and a pre-stretched VHB 4905 elastomer membrane, and achieves best performance of $77.4\,\mu\mathrm{L\,min}^{-1}$ or 8.45 kPa with a 1.5 mm diameter diaphragm and 30 Hz actuation frequency [135]. This is a very good performance compared to the size of the device. The motion of an active membrane is transferred to a passive one using carbon grease, which also serves as electrode (figure 5.4).

5.1.3 Zipping DEAs as candidates to replace pneumatic silicone-based microfluidic actuators

In the scope of replacing the pneumatic microfluidic actuators, a novel DEA structure called zipping DEA was studied theoretically and experimentally. It moves away from the traditional DEA "sandwich" structure, using a compliant and a rigid electrode, as shortly described in section 2.4. It offers a new set of characteristics including well-controlled out-of-plane deflected shape, sealing ability, and tunable deflection versus voltage profile to virtually any behavior including multi-stable modes.

The zipping mechanism is well-known in silicon MEMS since the 90's [136] and has been used in a variety of devices, from tilting mirrors [137] to microrelays [138]. The zipping actuators allows reaching both high forces and large stable displacements at low voltages thanks to the use of a few µm thick high-quality rigid dielectric onto which a conducting flexure (usually silicon) is unrolled or "zipped". As demonstrated experimentally by Gebbers *et al.* [53], it is possible to fabricate DEA zipping actuators based on this same principle: the soft electrode is pulled in hard contact with the rigid dielectric, and the electric field is therefore applied across

a few μm thick rigid insulator (figure 5.5a). Unlike the conventional DEA actuation mechanism, the elastomer membrane of a zipping DEA is not squeezed by the electrostatic force between two compliant electrodes, but a single soft electrode is attracted toward a fixed one in a sloped cavity. Since solid dielectric coatings such as silicon nitride, silicon oxide or aluminum oxide have high dielectric constants and breakdown strengths, the actuation voltage can be greatly reduced. Gebbers successfully coated a 20 mm diameter rigid aluminium electrode with a relatively thick (10-30 μm) aluminium oxide and achieved 1.4 mm deflection at 200 V (figure 5.5b). Although promising, this approach is quite challenging in terms of fabrication: these very thin layers tend to have defects, so that the realization of a pinhole-free dielectric over a few square mm sloped chamber is critical. The best high-quality dielectrics are available in the well-established microfabrication technologies, however their use raises a new issue: most of their etching processes have been designed to produce vertical trenches, and are therefore badly suited to machine the sloped walls chambers.

(a) Zipping DEA with the electric field applied across a rigid dielectric

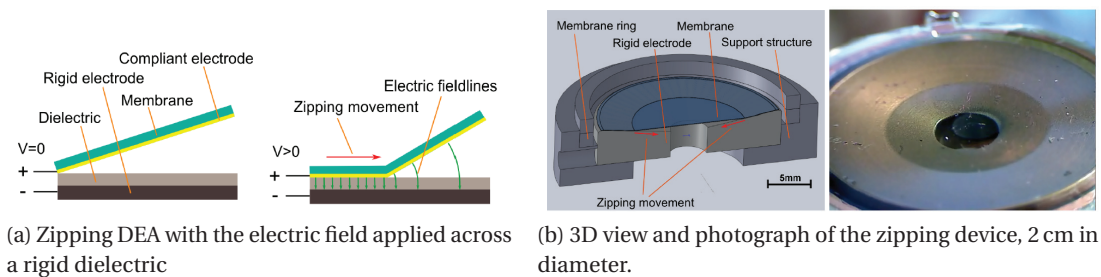(b) 3D view and photograph of the zipping device, 2 cm in diameter.

Figure 5.5: Gebber *et al.*'s DEA zipping device (reprinted from [53])

A variant of zipping DEAs was therefore selected in which the electric field is applied across the elastomer membrane (figure 5.6), avoiding the use of a thin rigid dielectric. In 2014, Gao *et al.* proposed a zipping actuator with this same approach based with a silicon micromachined sloped chamber [139]. Their compliant electrode is made with structured metallized serpentine tracks. Upon an actuation voltage of 200 V across a 10 μm silicone diaphragm, they observe a membrane motion, not quite reaching the 150 μm depth of the zipping cavity.

The cross-section of the figure 5.6 displays the fundamental working principle adopted with its keys geometrical paramters. It consists of an elastomer membrane bonded over a cavity with sloped sidewalls. The suspended membrane is flat in non-actuated state. As the voltage between the compliant electrode and the rigid electrode increases, so does the electric field across the elastomer membrane. Since the electric field is inversely proportional to the gap between the electrodes and due to the sloped sidewalls, the largest force is present at the periphery of the membrane, where the motion starts. The electrostatic force pulls down the membrane like a zipper, generating large out-of-plane deformation. Above a threshold voltage, the energetically most stable position is with a membrane completely deflected: the membrane jumps down to the bottom of the chamber.

Table 5.1 displays a tentative comparison between pneumatic microfluidic actuators based on
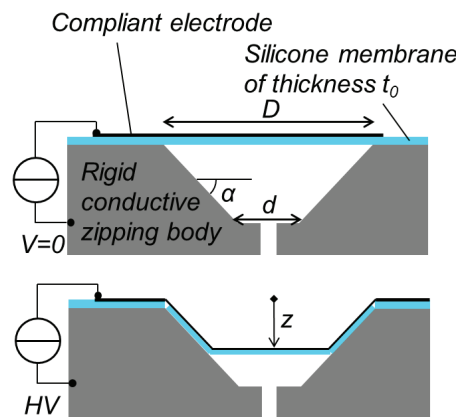
Figure 5.6: Cross-section and key geometrical parameters of a zipping device with an axisymmetric chamber of top diamter D, bottom diameter d and sidewalls angle α. The flat membrane thickness is t_0.

the deflection of an elastomer membrane (figure 5.2) and zipping DEAs (figure 5.6). DEAs have much lower generated pressures, but compete for the other requirements, with the advantage of portability. The first line of the table indicates the ratio between out-of-plane displacement and lateral size of the microfluidic valve. Typical ratios of 0.1 are reported for pneumatic valves, and 0.195 for the larger size studied zipping actuator. The feature of channel sealing reflects the ability for the deflected membrane to comply on the channel walls and hermetically close it. Pneumatic microfluidic actuators commonly achieve this by manufacturing rounded channels and using a large excess pressure. On the contrary, the membrane of zipping DEAs is deflected by being electrostatically pulled in contact with the sidewalls, which eases the channel sealing. Blocking pressures of a valve element are however expected to be much larger for pneumatic actuators compared to zipping DEAs. Regarding portability, the high voltages needed for the operation of DEAs can be generated by commercial converters smaller than $1\,\mathrm{cm}^3$ in size [1]. The size, cost and power consumption of the driving electronics is rather determined by the switching elements.

Table 5.1: Comparison between pneumatic microfluidic actuators and zipping DEAs

Feature	Pneumatic microfluidic actuator [128, 140]	Zipping DEA
Out-of-plane displ / lateral size	typ. $10\,\mu\mathrm{m}/100\,\mu\mathrm{m}=0.1$	$385\,\mu\mathrm{m}/2\,\mathrm{mm}=0.195$ demonstrated
Pressure	$>10\,\mathrm{kPa}$	1 kPa est.
Channel sealing	Channel rounding and excess pressure	Bistable operation
Portability	Bound to the lab	Electrical operation

---

[1] http://www.emcohighvoltage.com/

5.2 Analytical modeling of zipping DEAs

The most common approach to model the static displacement of electrostatic actuators as a function of the voltage and the initial conditions involves computing the energy contributions to find the energy minima. Like when modeling conventional DEAs, one has to introduce the hyperelastic stiffening of the material. Unlike for most DEA modeling, the membrane thickness and stretch state cannot be considered as constant over the actuator, since it is in hard contact with the sidewalls. A model which outputs the vertical deflection z in function of the voltage was developed, taking as parameters the chamber geometry, the elastomer properties (electrical and hyperelastic energy density) and the surface roughness of the rigid electrode, with the goal of designing actuators whose membrane can be zipped down to the bottom of the cavity without reaching the dielectric breakdown of the elastomer.

Saif *et al.* made a detailed analytical study of the behavior of a zipping cavity to be used as a pump [54]. However, his model is not directly applicable to zipping EAPs because of the assumptions linked to the type of materials assumed in his model (5 µm thick polyimide membrane). DEA membranes are between 3 to 4 orders of magnitude softer and work in a hyperelastic stress-strain domain, but also the contact between the rubbery elastomer membrane and the rigid electrode tends toward the hypothesis of non-slipping conditions, which are not used with Saif's low-friction membrane materials.

Two fundamentally different zipping structures were modeled. In the first structure (figure 5.7A), the electric field is applied across the elastomer membrane. It can be seen as a stack compliant electrode - elastomer membrane - rigid electrode. The second one is similar to the silicon MEMS zipping devices: the compliant electrode is patterned on the membrane backside and is pulled in direct contact with a thin high-quality rigid dielectric coating that covers the rigid electrode (figure 5.7B). It can be described as a stack of elastomer membrane - compliant electrode - rigid dielectric - rigid electrode. The electric field is in the thin rigid dielectric, hence needing less voltage to reach the same amount of electrostatic energy. It also means that the mechanical and electrostatic optimization of the device are decoupled between the membrane and the rigid dielectric. As a direct consequence, the actuation is no more limited by the breakdown field of the membrane but by the rigid dielectric. This family of zipping devices were studied experimentally by Gebbers *et al.* [53].

5.2.1 Model assumptions

A set of assumptions are posed to implement the two models. The two dominant energy contributions are the electrostatic energy and the mechanical strain energy in the membrane. The bending energy and the surface energy (stiction) are neglected. The adhesive forces between the membrane and the rigid electrode would become apparent only in dynamic mode, when ramping down the voltage from a zipped state to a lower value of z. The fringing fields are neglected, which would bend down the central suspended part of the membrane. The membrane already in contact with the sidewalls is assumed to be in non-slipping condition,
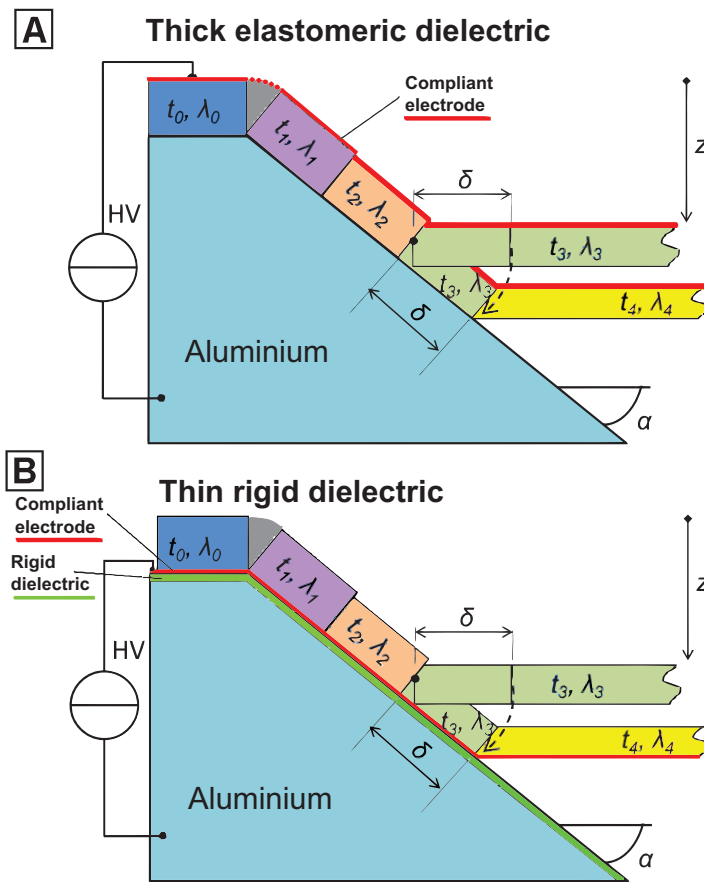
Figure 5.7: Cross-sections to illustrate the model behavior for the two zipping DEA structures. z is the vertical deflection, δ the infinitesimal length of membrane element, t_i the thicknesses, λ_i the equibiaxial stretches, and α the sidewalls angle.
A Membrane dielectric model: the electric field builds up across the elastomer membrane.
B Rigid dielectric model: the compliant electrode is patterned on the bottom of the membrane, and the electric field builds up across a thin high-quality rigid dielectric.

which implies that its thickness t and stretch state λ varies over the zipping depth z (figure 5.7). As illustrated on the topviews of figure 5.8 for a conical and a pyramidal chamber shape, the partially zipped membrane is therefore composed of a series of zipped elements of infinitesimal length, each one having its own dimensions and stretch state (in blue) and a central suspended part (yellow). It is therefore necessary to implement an iterative process to compute the state of membrane elements. The flat suspended central part is considered to be under equibiaxial stretch. The polymer satisfies the volume incompressibility condition. Based on these hypotheses, it is assumed that the next zipped element of length δ comes from a "rotation" of the previous flat part (figure 5.7) and inherits its thickness and stretch state.
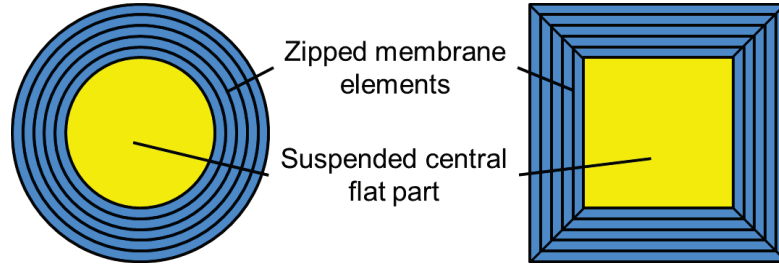
Figure 5.8: Top view of the different parts of the partially zipped membrane assumed in the model, with conical (left) and pyramidal (right) chamber geometries. The blue annuli or trapezoids represent the zipped membrane elements with infinitesimal width, having each one different volumes and stretch states, and the yellow round or square represents the flat suspended part of the membrane.

5.2.2   Procedure of the implemented algorithm

The algorithm which outputs the vertical displacement in function of the applied voltage is structured as follows: *1)* The voltage is set to $U = 0$. *2)* The total energy function in function of the zipping depth $E(z)$ is computed with a resolution of 1 µm or below. *3)* One looks for the first minimum of $E(z)$, which will determine the stable vertical displacement z that corresponds to the current voltage. *4)* The voltage is incremented and one starts again at step *2*. The algorithm ends once the vertical displacement has reached the bottom of the chamber.

5.2.3   Computation of the total energy function

The mechanical strain energy is computed by multiplying the volume of each deflected membrane part by the elastic energy density W of the Gent hyperelastic model in the equibiaxial case (equation 5.1). μ and J are the Gent model parameters, and $\lambda_1 = \lambda_2 = \lambda$ is the equibiaxial linear stretch.

$$W(\lambda) = \frac{\mu J}{2} \ln\left(1 - \frac{2\lambda^2 + \lambda^{-4} - 3}{J}\right) \tag{5.1}$$

The expression of the mechanical strain and electrostatic energies for any deflection z and voltage U are expressed in the table 5.2, V being the volumes, C the capacitance, A the areas and t the thicknesses. The indexes $flat$, mem, lat and $diel$ stand for the central (flat) part, the membrane, the lateral (area), and the rigid dielectric.

The total energy is then:

$$E(z) = E_{MS}(z) + E_{ES}(z) \tag{5.2}$$

Table 5.2: Expression of the mechanical strain and electrostatic energies of the two models (not taking into account the sidewalls roughness).

Model	Mechanical strain energy	Electrostatic energy $E_{ES} = -\frac{1}{2}CU^2$
Thick elastomeric dielectric	$E_{MS} = W_{flat}V_{flat} + \sum_i W_i(\lambda_i)V_i$	$E_{ES} = -\frac{1}{2}\epsilon_0\epsilon_{mem}\sum_i\left(\frac{A_i}{t_i}\right)U^2$
Thin rigid dielectric		$E_{ES} = -\frac{1}{2}\epsilon_0\epsilon_{diel}\frac{A_{lat}(z)}{t_{diel}}U^2$

The first minimum of the function will determine the stable zipping depth. An example of plotted energy curves is visible on figure 5.9 for the case of a pyramidal-shape chamber [103]. The electric breakdown field value of $220\,\text{V}\,\mu\text{m}^{-1}$ is assumed given the amount of stretch in the deflected state, which was found to be too optimistic experimentally. It could also be possible to see the hysteresis (pull-out voltage) commonly observed in silicon zipping devices by finding the minimum starting from a zipped state (i.e. the highest value of z). However, the surface adhesion energy of the elastomer on the sidewall would add a non-negligible contribution that is difficult to estimate.
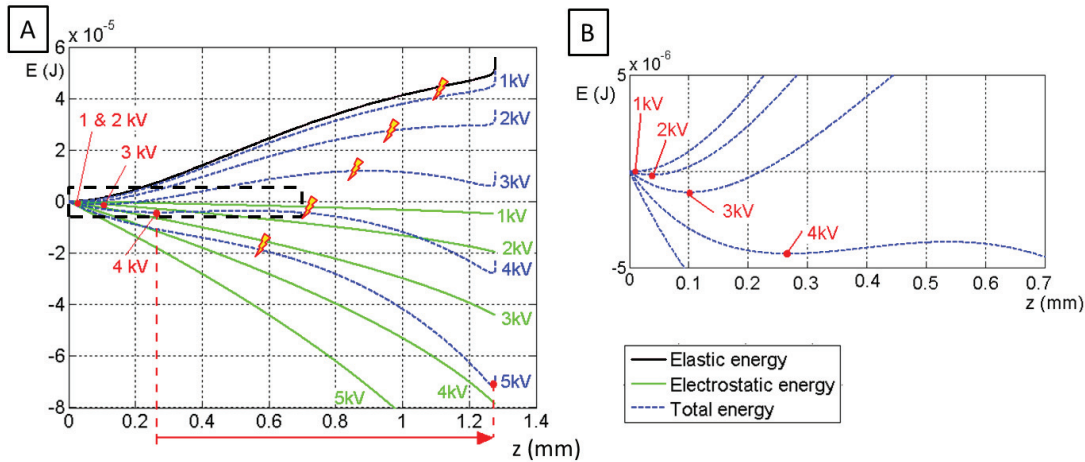
Figure 5.9: **A** Zipping energies for a $50\,\mu\text{m}$ thick Nusil CF19 membrane with a single ion implanted stretchable electrode in a $2\,\text{mm}$-side pyramidal chamber with a sidewalls angle $\alpha = 54.7°$. The lighting bolts indicate the deflections at which the breakdown would occur ($220\,\text{V}\,\mu\text{m}^{-1}$ assumed). The arrow indicates a jump between two stable positions which happens between 4 and 5 kV.
B Zoom on the dashed square (only total energies visible)

5.2.4 Surface roughness of the sidewalls

Since the analysis of the sidewalls profiles of one type of devices studied exhibited a significant roughness (average roughness R_a and RMS roughness R_q have been measured by white light interferometry in the range of 5 and $9\,\mu\text{m}$ respectively, see figure 5.10), the contribution of surface roughness to the electrostatic energy computation was implemented. This rough surface
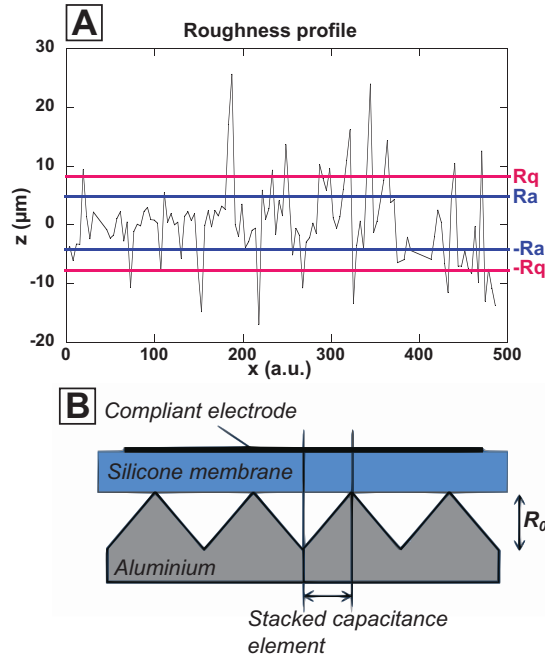
Figure 5.10: **A** Example of arbitrary typical roughness profile with statistical roughness parameters R_a and R_q.
B Roughness modeling. The model has a peak-to-peak roughness parameter R_0.

may leave some air trapped between the membrane and the sidewalls. These air pockets act as a series capacitor of lower dielectric constant and therefore reduce the electrostatic energy.

As a mean to evaluate the contribution of such an effect in the model, a saw tooth-shaped wall capacitance of peak-to-peak gap R_0 can be assumed, with a constant thickness elastomer membrane on top (figure 5.10).

The capacitance C used in the electrostatic energy expression (table 5.2) corresponds to the smooth surface case and can be replaced by the rough surface case (equation 5.3).

$$C_{rough} = \epsilon_0 \frac{A}{R_0} \ln\left(\frac{\epsilon_{r,mem} R_0}{t_{mem}} + 1\right) \tag{5.3}$$

$R_0 = 2 \cdot R_a$ and $R_0 = 2 \cdot R_q$ shall be used as approximations.

5.2.5 Electrical breakdown

A main limitation of every DEA is the electrical breakdown, which defines the maximal achievable deflection. Dielectric breakdown of conventional DEAs (i.e. sandwiched between two compliant electrodes) occurs when the electric field in the dielectric exceeds the maximal

value tolerated by the material. This failure mode may be triggered by the pull-in instability or wrinkling, or happen before these effects are present [40, 141]. But the design of zipping DEAs requires paying attention to electrical failures triggered by actuation characteristics that are not present in squeezing-mode DEAs. The first of these characteristics is linked with the assumption of membrane non-slipping condition on the sidewalls. The highest electric field, and hence the point where dielectric breakdown will occur, is where the membrane is thinnest, i.e. on the outer periphery of the suspended part (fig. 5.7). The increasing stretch with z actually enhances the breakdown field [24], but a constant value is assumed in the model.

Secondly, the deflection versus voltage characteristic of the zipping DEAs exhibits a very abrupt slope above a threshold voltage (onset of complete zipping, see figure 5.11). If the breakdown occurs during this zipping jump, the device fails, similarly to the well-known snap-in instability. Keplinger et *al.*'s closed chamber volumes has been proposed to harness the snap-in instability, which resulted in giant voltage-triggered deformations [33]. Zipping DEAs offer even more design freedom to tune the bistable behavior of the actuators, since one can play with all the geometrical parameters of the cavity and with the membrane material. For instance, it is possible to avoid the breakdown during this zipping jump by mechanically limiting the maximal displacement of the membrane by truncating the chamber.

A last issue related to the electrical failure of zipping DEAs is the electrocreasing effect, which occurs when high electric fields are applied across elastomers bonded on a rigid substrate [142]; which is similar to the case of the membrane zipped on the sidewalls. The extrapolation of Wang's data for the polymer which was mostly used (Nusil CF19) would indicate a critical electric field in the range of $100\,\mathrm{V\,\mu m^{-1}}$. Since it is close to the breakdown field of the elastomer, the possibility of an electrocreasing-triggered breakdown cannot be excluded.

5.2.6 Model results and actuator design applied to conical-shaped chambers

In figure 5.11, results of the thick elastomeric dielectric model in conical chambers have been plotted using the following parameters (defined on figure 5.6 and section 5.2.3): $D = 2\,\mathrm{mm}$, $d = 0.6\,\mathrm{mm}$, $\alpha = 20°$, $t_0 = 25\,\mathrm{\mu m}$, $\lambda_0 = 1.1$, $\epsilon_{mem} = 3$, $R_0 = 0$ (no roughness), unless otherwise specified. The targeted application for the zipping actuators is a micropump. The main pump performance are the pressure and the flow rate, which depends on the displaced volume and period of an actuation cycle. Stiffer silicones provide less deflection and thus limit the stroke volume, but increase both the response time and the pressure exerted on the fluid. A relatively stiff elastomer was therefore chosen, the CF19 from Nusil (0.8 to 1.2 MPa Young's modulus). However, for the first type of zipping chambers studied (anisotropically etched silicon, section 5.3), two other softer silicones were also investigated to improve the vertical deflection. The Gent model parameters (μ and J) were fitted of uniaxial pulltests data on CF19 elastomer stripes with and without electrodes and a Young's modulus of the electrodes of 1.93 MPa was extracted using a bilayer approach (equation 5.4), with Y and T the Young's modulus and

relative thickness of the bilayer stack, membrane and electrode [143].

$$Y_{bil} = Y_{mem} T_{mem} + Y_{elec} T_{elec} \tag{5.4}$$

Out of this formula, the shear modulus $\mu = Y/3$ (needed for the Gent model) can be recomputed for any membrane thickness, keeping $J = 80.4$ constant. The breakdown field of the elastomer was measured at $96\,V\,\mu m^{-1}$ in a non-stretched membrane, and is taken as constant in the model.

On figure 5.11A, both models with the electric field applied across a) a rigid dielectric or b) across an elastomer membrane are compared. One can clearly see that thanks to the high electrostatic energy stored in the thin rigid dielectric, a) has a much lower zipping threshold (0.5 kV) than b). On figure 5.11B, the effect of roughness is clear: it lowers the electrostatic energy at a given voltage, which shifts the zipping jump at higher voltages. Looking at figure 5.11C, prestretching the membrane has a strong influence on the zipping voltage. In traditional DEAs, the prestretch improves drastically the maximal displacement by overcoming the pull-in instability, indirectly keeping the voltage low thanks to the thickness reduction. One cannot think in the same way for zipping DEAs, since the actuator structure is different (in hard contact with the sidewalls and without electric field en the central part, figure 5.19A). Low-prestretched zipping actuators work at lower voltages and have a more controllable zipping depth (smoother $z(V)$ slope), but the risk of the membrane remaining stuck to the chamber wall during the voltage ramp-down is increased. Indeed, less mechanical energy is stored in a zipped membrane which is not prestretched. Highly-prestretched zipping actuators work at higher voltages, exhibit a more pronounced bistable characteristic and have more mechanical energy for a given deflection, which counters membrane sticking and provide more force to move parts or fluids. The prestretch adds an energy barrier to the total energy curve and keeps the deflection at $z = 0$ until being overcome by the electrostatic energy. Increasing the sidewalls angle (figure 5.11D) has a strong effect on both the zipping voltage and the maximal deflection (provided the chamber is not truncated). A smaller angle chamber zips at lower electric field, but provides less force and needs somewhat more prestretch to ensure a quick membrane release from the sidewalls. For a 40° sidewalls chamber and the CF19 elastomer, the breakdown is expected to occur during the zipping jump. The figure 5.11E shows that the zipping jump scales almost linearly with the thickness, but one obtains more margin after the zipping jump before the breakdown occurs.
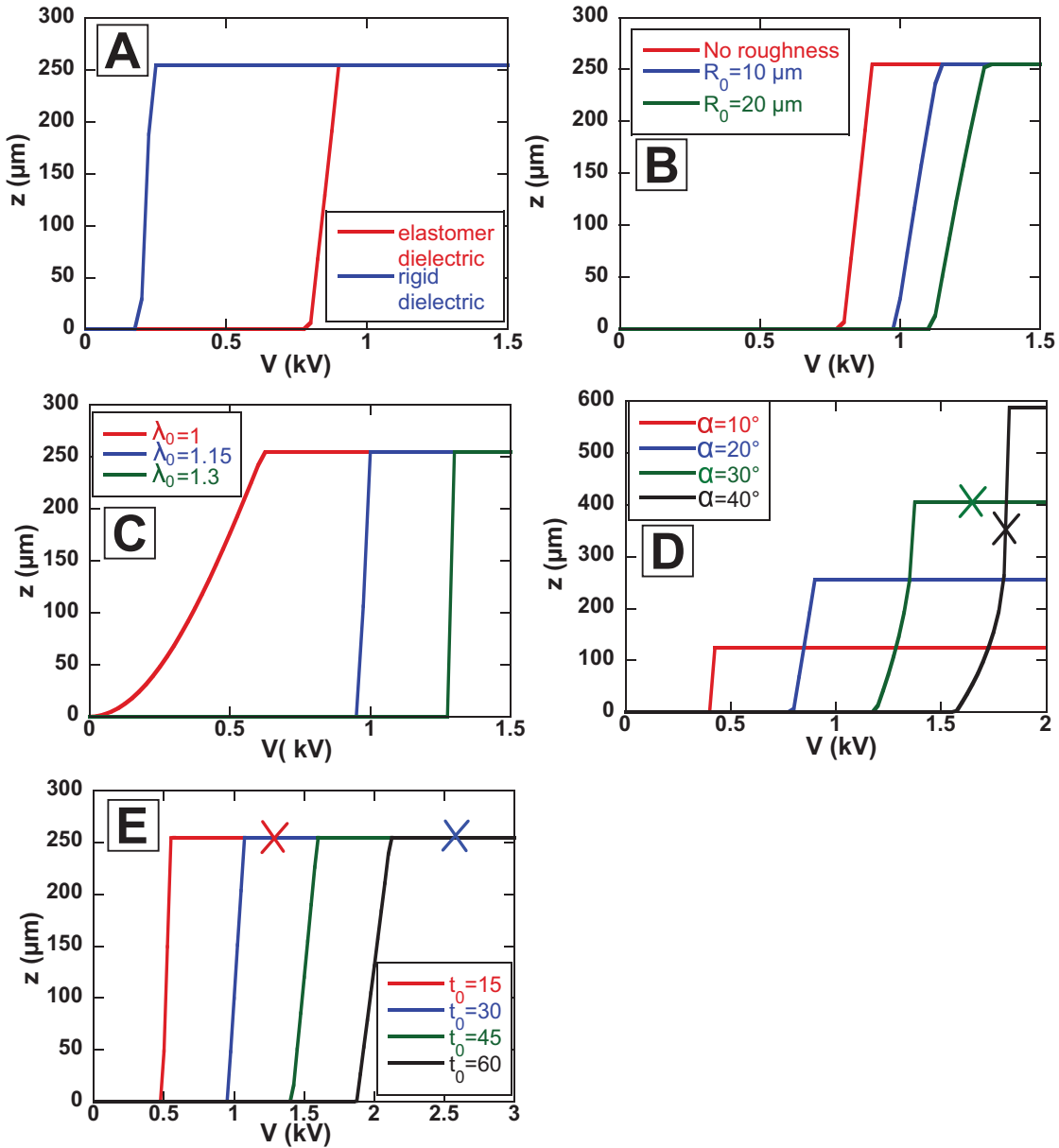
Figure 5.11: Results of the thick elastomeric dielectric model for a conical chamber (except comparison of the 2 models on **A**). Main parameters (unless otherwise specified): $D = 2\,mm$, $d = 0.6\,mm$, $\alpha = 20°$, $t_0 = 25\,\mu m$, $\lambda_0 = 1.1$, $\epsilon_{mem} = 3$, $R_0 = 0$ (no roughness). The breakdowns are indicated by crosses.

A Comparison of the two models. The rigid dielectric has a thickness of $2\,\mu m$ and a relative permittivity of $\epsilon_{diel} = 3.12$. **B** Variation of roughness. **C** Variation of prestretch. **D** Variation of angle. **E** Variation of membrane thickness. The breakdown voltages for the 45 and 60 μm membranes are at 3.8 and 5.1 kV.

5.3 Zipping in pyramidal anisotropically-etched silicon chambers

The very first pump concept that has been studied is based on a microfabricated silicon body. On the contrary to replica molding techniques, etching a silicon wafer from both sides allows realizing both sloped zipping chambers in a conductive substrate (needed for the rigid electrode) and a fluidic channel in a single chip, with very precise control on the dimensions, as will be described in the next section. Moreover, a thin oxide can be grown to keep the fluidic channel at a floating potential and to perform oxygen plasma bonding of the actuator membrane.

5.3.1 Silicon microfabricated zipping chambers and zipping peristaltic micropump

Most silicon etching techniques (such as Deep Reactive Ion Etching) are designed to produce vertical trenches, but one would like to have sloped sidewalls zipping cavities. Means of isotropically etching silicon exist, but the obtained profile cross-section do not have the desired shape since the angle at the top is large. Anisotropic etching was therefor chosen: with certain types of wet etchants such as potassium hydroxide (KOH), the etch rate of the different crystalline planes greatly differ depending on the wafer orientation and on the etch mask apertures. The most common designs rely on the fact that 111 crystalline planes etch several hundreds of times slower than other ones. Therefore, a long etch time will make these planes apparent unless other ones are masked during the process. A square opening will give out typical pyramidal holes with 54.7° sloped walls respective to the horizontal. In 2014, Gao *et al.* published a fabrication process of a zipping micropump with a silicon body etched by grayscale lithography [139]. It consists in structuring a photoresist masking layer with varying thicknesses, so that the gradual mask etching during the DRIE progressively exposes the surface to be etched, resulting in a sloped sidewall.

A view of the proposed micropump with three zipping chambers is visible on figure 5.12. In the top view, one can see the pyramidal chambers with their four sloped walls. The bottom view shows the embedded channel that links the three chambers. Whereas one sees the channel on the AA cross-section, it is not visible on the BB cross-section. The full device cross-section is a schematic diagram of the silicon body, with a silicone membrane bonded on top and a hard silicone block on the bottom to close the channel. Three compliant electrodes are patterned on top of the membrane by Au ion implantation. Au ion implantation is a technique which has been developed in the LMTS by S. Rosset *et al.* [36, 84]. High-density, low energy pulses of Au ions are accelerated towards a biased substrate. Clusters are formed in the few 10's of nm below the elastomer surface. Under sufficient dose, a percolation path forms between the clusters and the surface of the elastomer becomes conductive, yet remaining stretchable. This electrode type has been used during the first part of the project, before an indirect printing technique of an ink composed of carbon black dispersed in a soft elastomer matrix was developed. The fluid to be pumped is displaced in a peristaltic manner along the

channel by sequential actuation of the electrodes. Zipping actuation is performed through the membrane, keeping the liquid electrically insulated from the actuation potentials. Thanks to a thin oxide layer on the silicon surface, the liquid is at a floating potential. A hard stop (not visible on the picture, but realized by a transparent Teflon chip over the device) prevents the upward inflation of the membranes when they are not actuated. A detailed description of the fabrication process is given in section 5.6.1. Scanning Electron Microscope (SEM) pictures of the microfabricated silicon body are also visible in this section (figure 5.42), on which the 3D structure of the silicon body appears clearly.
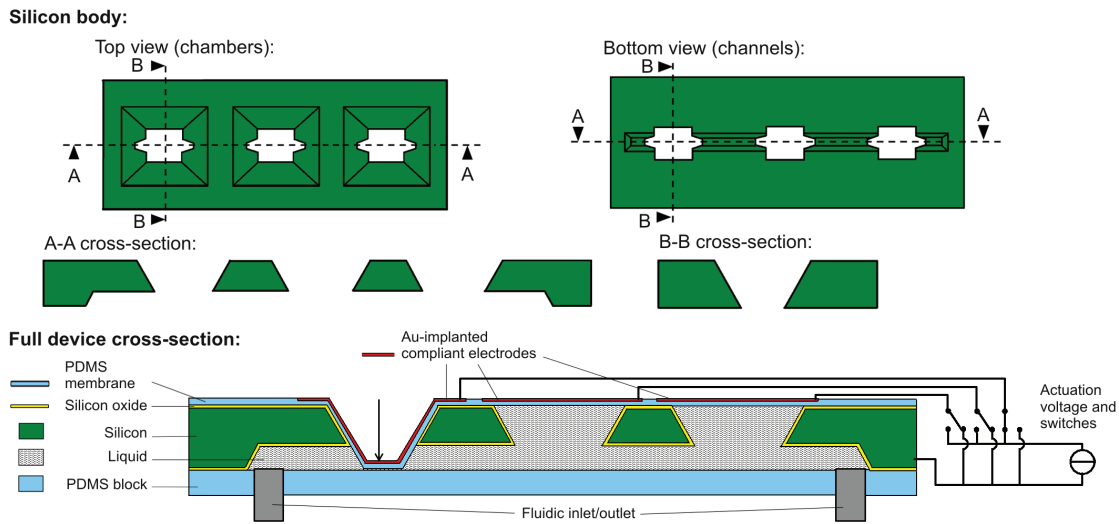
Figure 5.12: Schematic of the peristaltic micropump with silicon microfabricated body featuring zipping cavities and embedded channels

5.3.2 Design of the zipping DEA micropump with anisotropically-etched silicon body

The question of the size of the channels brings a tradeoff between the hydraulic resistance (that should be minimized to reduce the losses in the pump) and the zipping area on the sidewalls (since the channel penetrates in the chamber and therefore consumes area). In previous experiments with DEA on tunable lenses chips , response times in the order of 0.5 s were measured with fluidic resistances around $10 \times 10^{10}\,\mathrm{kg\,m^{-4}\,s^{-1}}$ (see section 6.3.1). Values in the same range are obtained with trapezoidal cross-section channels having openings of 400 and 250 μm, heights of 248 and 142 μm respectively, and a few mm long. The biggest channel design favors the fluidic resistance, whereas the smallest channel design favors the zipping area. These channel heights lead to the choice of 525 μm thick silicon wafers. The chamber lateral dimensions will define the maximal deflection achievable before breakdown. The model predicts that 1250 μm chamber side are needed to zip down the wafer thickness. Two other chamber sizes (1000 and 2000 μm) have also been included in the design. As illustrated on the figure 5.13, a predicted vertical deflection of the membranes into pyramidal-shaped chambers presents first a relatively low deflection, followed by a zipping jump. This might be

problematic if the dielectric breakdown occurs during this zipping jump. The solution is to play with the lateral dimensions as well as the wafer thickness so that the deflecting membrane hits the bottom of the chamber before the breakdown.
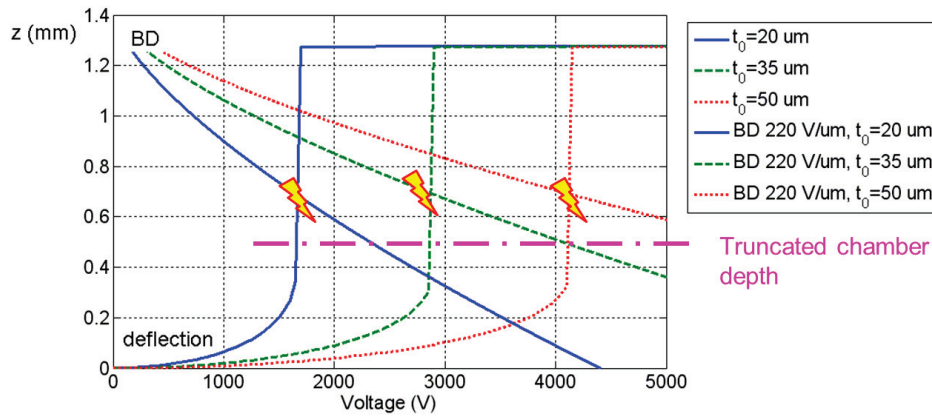

Figure 5.13: Calculated deflection as a function of the voltage for a 2 mm-side pyramidal KOH-etched chamber, with three different membrane thicknesses. Truncating the chamber depth (pink line) allows blocking the membrane motion during the zipping jump before breakdown occurs.

The whole silicon surface is coated with an electrical insulator layer in order to keep the liquid insulated from the electrode potential. Thermal oxidation of silicon is a good solution, because it covers the whole silicon surface, and is therefore able to insulate even the sharp edges of the structure. Additionally, it provides an ideal surface to make the oxygen plasma bonding with the silicone membrane and silicone block that seals the channel backside (fig 5.12). With our actuation principle, the addition of a dielectric layer one order of magnitude thinner than the membrane theoretically slightly reduces the electrostatic energy at constant voltage and enhances the resistance to breakdown; but these contributions are negligible (around 5% each).

5.3.3 Experimental results with ion-implanted electrodes on CF19-2186 silicone membranes (27 shore A)

To measure the static deflection of zipping membranes, a test chip with KOH through-etched cavities of different sizes was used. Unlike the chambers of the peristaltic pump, they do not have a channel that would consume zipping area. A 53 µm thick CF19-2186 membrane is bonded on top of the chip by oxygen plasma, and an Au ion compliant electrode is patterned on top of the membrane with a steel shadow mask. The implanted electrodes are contacted with a conductive acrylic varnish, with wires soldered to a rigid device holder.

The two devices used in this section appear on the two first lines of table 5.3. This table also contains the three other variants that will be presented in the next sections as well as their maximal deflection achieved.

Table 5.3: Dimensions and parameters of the zipping DEAs in pyramidal-shape chambers, with their maximal deflection achieved (sections 5.3.3 to 5.3.5). No prestretch was applied on the membranes.

Chamber side (mm)	Silicone	Electrode	Mem. thickness (μm)	Max. deflection (μm)
2.6	CF19-2186	Ion-impl.	53	300
1.8	CF19-2186	Ion-impl.	53	245
2	LSR4305	Ion-impl.	33	140
2	R32-2186	CB-silicone	59	335
2	CF19-2186	CB-silicone	63	385

The shape of the membrane under deflection was measured with a white light interferometer Wyko NT1100 DMEMS. For this measurement, the main limitation of the interferometer is the angle of the surfaces that can be measured. Therefore, it will only be possible to measure a part of the center of the zipped membrane. The position of this central part of the membrane is then compared with the height of the membrane surrounding the chamber.

Zipped membrane shape

The figure 5.14 presents the deformation of the membrane for a 2.6 mm chamber at different actuation voltages. As visible on figures 5.14e and 5.14f, the shape of the central part of the membrane is not perfectly flat, but takes a star-shape pattern along the edges of the pyramidal cavity. As visible by the low amount of deflection on the 2 kV profile of figure 5.14d, the membrane is not yet in hard contact with the sidewalls at this voltage.

Static deflection vs. applied voltage

Using the same white light interferometer setup, the deflection of the lowest point of the zipped membrane relative to its flat position was measured. Two chambers were measured, with sides of 1.8 and 2.6 mm, and compared with the model. A small residual stress of 20 kPa due to the fabrication process was assumed in the non-prestrained membranes.

The data in figure 5.15 show a good agreement with the model. The observation that the data lies slightly below the predicted curve could for instance be attributed to the fact that the membrane shape is not as ideal as assumed in the model (figure 5.14), to an underestimation of the stiffening induced by ion implantation or a not perfect modeling of the implanted elastomer by the Gent hyperelastic model.

For the two devices, breakdown occurred at 5.5 kV, probably during the zipping jump. Up to 300 μm deflection was measured on the 2.6 mm side chamber. If breakdown occurs at a deflection z between 300 and 525 μm, the theoretical corresponding thicknesses are 40.8 and 32.5 μm. The theory predicts that the thickness at the bottom of a 525 μm deep chamber is

(a) 2 kV. The high slope zones (black) could not be measured

(b) 3 kV

(c) 4 kV

(d) 2 kV, y-profile at the center of the chamber (dashed pink line on A). The membrane is not yet in contact with the sidewalls.

(e) 2 kV, 3D view of the center of the membrane

(f) 2 kV, 3D view of the center of the membrane
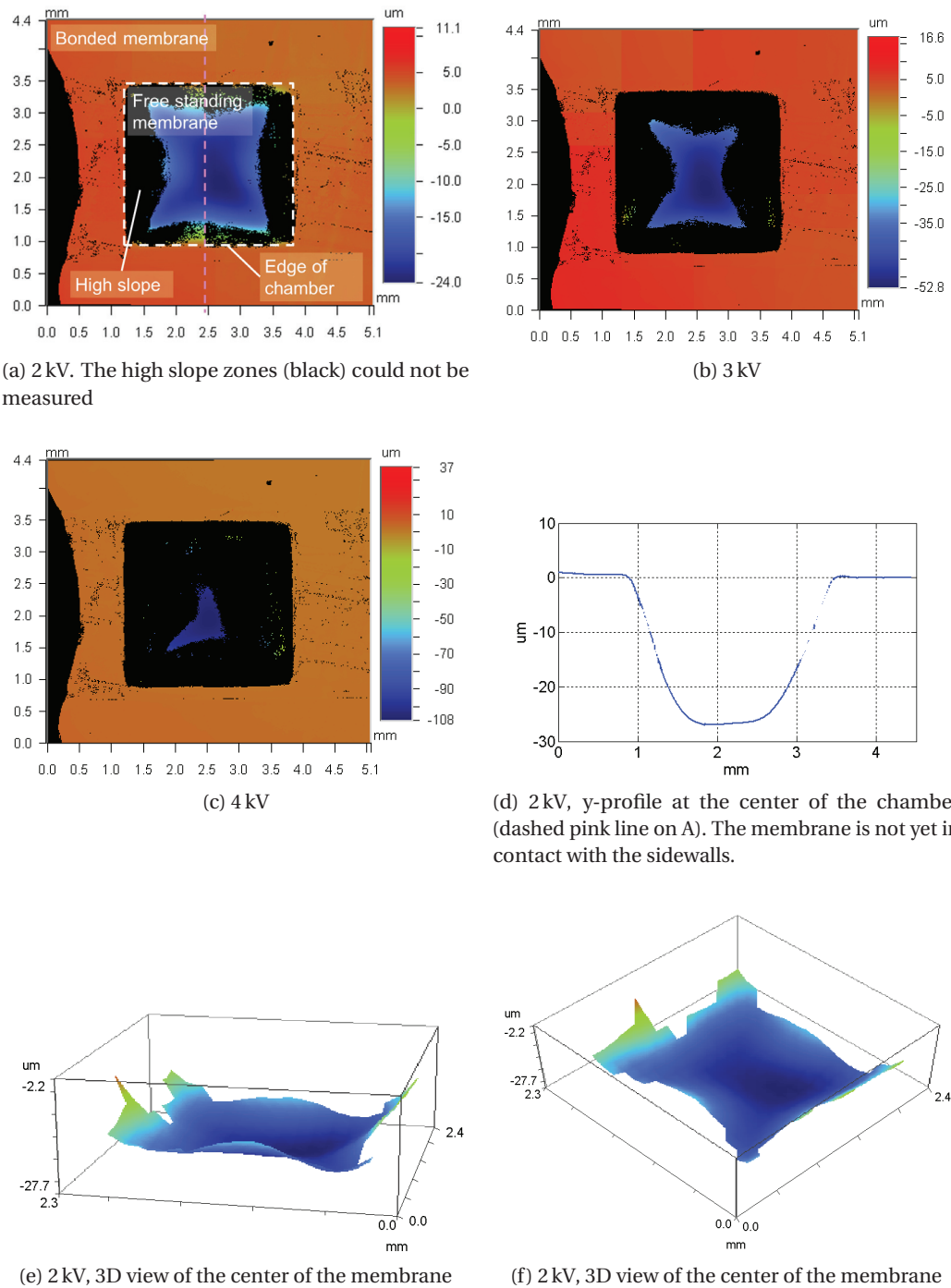
Figure 5.14: Shape of a 53 µm thick deflected membrane in a 2.6 mm side KOH-etched chamber at 2, 3 and 4 kV

half the one of the flat membrane. It seems that the breakdowns occurred preferentially along the pyramid inner edges. Although there is no experimental evidence, it could be due to the presence of air pockets which have a lower breakdown strength than the membrane.
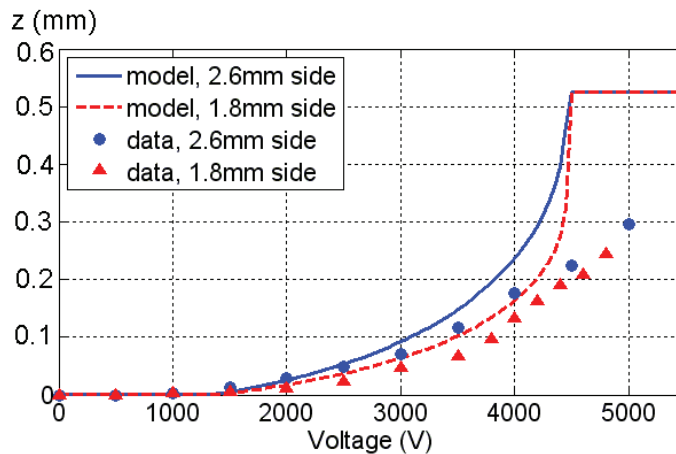
Figure 5.15: Static deflection, model and experiment. The deflection limit of 525 μm of the model is imposed by the wafer thickness.

5.3.4 Experimental results with ion-implanted electrodes on LSR4305 silicone membranes (5 shore A)

In the first set of devices with CF19-2186 elastomer and ion implanted electrodes (section 5.3.3), up to 300 μm deflection in pyramidal-shape KOH-etched silicon chambers was achieved. As silicon microfabrication allows to produce sets of electrically conductive chips with very precisely machined chambers having an embedded channel (which is not obvious with other techniques such as milling or replica molding), it was decided to move forward in this direction to obtain membranes deflecting completely down the 525 μm of the wafer.

The first option taken is to use softer silicone elastomers. Indeed, soft silicones will be more easily deflected inside the zipping cavity.

Static deflection vs. applied voltage

The Bluestar LSR4305 silicone has a very low shore A hardness of 5, which corresponds to 0.2 MPa Young's modulus, versus 27 shore A (0.8 MPa) for the CF19-2186. Softer silicones have in principle lower breakdown fields. This silicone was implanted and bonded on the chamber, in the scope of achieving more deflection than the CF19-2186. The static deflection was measured in two ways, by acquiring the position of the membrane center with a white light interferometer (z_{center}) and by by measuring the depth of the zipped membrane in contact with the sidewalls on pictures taken with a USB microscope (z_{zip}). The portion of the membrane which is in contact with the sidewall is indeed very clearly visible though the semi-transparent Au-implanted electrode (figure 5.16). Due to the slightly bulged membrane shape, the values measured with the USB camera are approximately 20 μm lower than the center of the membrane. This difference reflects the downwards-bulging of the central suspended part of the membrane due to the fringing fields, an effect which was assumed negligible

in the model. As it represents the portion of the membrane which is in hard contact with the sidewalls, the value z_{zip} is closer to the deflection computed in the model than z_{center}. For reasons of electrode transparency (all the next set of devices will be manufactured with opaque electrodes), this is the only set of measurements which measures the modeled value z_{zip} instead of z_{center}.
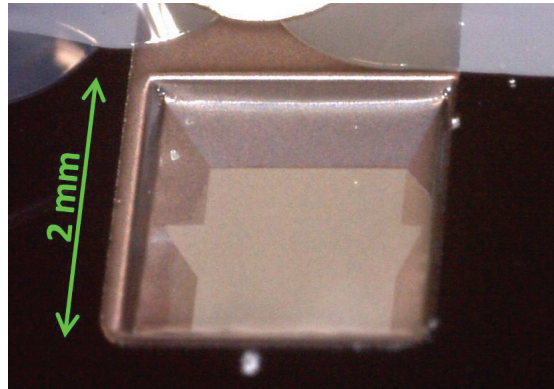
Figure 5.16: Optical photograph of a partially zipped LSR4305 membrane inside a 2 mm side silicon chamber. Thanks to the Au implanted electrode transparency, measurement of the zipped depth can be performed on optical pictures.
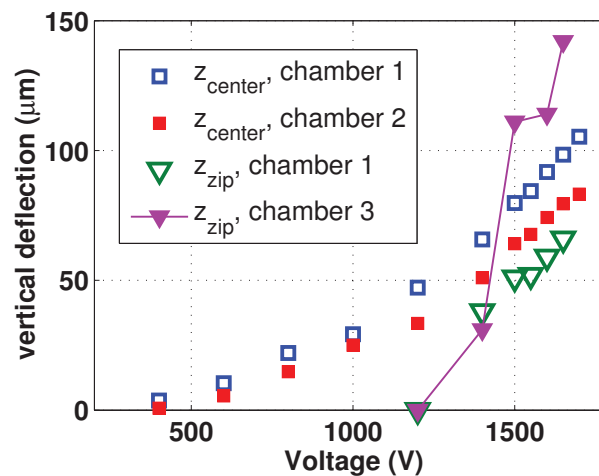
Figure 5.17: Deflection of an Au-implanted 33 μm thick LSR4305 membrane inside a 2 mm silicon zipping chamber. z_{zip} data have been measured with a USB camera and z_{center} data with a white light interferometer.

Three devices with identical properties have been measured (third line of table 5.3). The best deflection obtained with this silicone is 140 μm, far below the previous results. This can be attributed to two things: the electric breakdown strength and the implantation-induced stiffening. Softer elastomer tend to have lower breakdown strengths, which is indeed the case for the LSR4305 compared to the CF19-2186. By estimating the membrane thickness in function of the deflection using the model, the breakdown field of the CF19-2186 silicone

of the previous dataset was $132\,\mathrm{V}\,\mu\mathrm{m}^{-1}$ (fig. 5.15, $300\,\mu\mathrm{m}$ deflection), versus $58\,\mathrm{V}\,\mu\mathrm{m}^{-1}$ for the LSR4305 (fig. 5.17, $140\,\mu\mathrm{m}$ deflection). The Au ion implantation process produces a Au-silicone composite which is only $30\,\mathrm{nm}$ thick, but with a Young's modulus in the order of several GPa [85]. Although the LSR4305 silicone is 4 times softer than CF19, the relative increase of its Young's modulus is higher. In other words, the Young's modulus of an implanted membrane increases much faster on a softer silicone.

However, it is clear from the data that the driving voltage is strongly reduced compared to the stiffer CF19. This reduction of approximately $2.3\,\mathrm{kV}$ can be attributed to the elastomer Young's modulus rather than thinner membrane, comparing the nominal electric fields. This would also tend to consider the breakdown strength as dominant parameter over elastomer stiffness to achieve large deflection in such zipping structures.

The three chambers with LSR4305 silicone membranes of figure 5.17 have identical dimensions (table 5.3, line 3), but a considerable difference in their deflection characteristic. It is due to the different implantation parameters of the electrodes, which are difficult to obtain at their optimal value (i.e. lowest stiffening impact but sufficient conductivity) and in a repeatable manner [84].

5.3.5 Experimental results with carbon black-soft silicone electrodes on R32-2186 (15 shore A) and CF19-2186 (27 shore A) silicone membranes

Based on the conclusion that the use of LSR4305 softer elastomer membranes does not improve the maximal deflection achievable but rather reduces it by a factor 2, two other ways to reach a fully deflected shape in a $525\,\mu\mathrm{m}$ thick silicon chip were investigated.

The first one is to use a silicone which is also softer than CF19-2186, the R32-2186 from NuSil, but which has a higher breakdown strength according to the datasheet. In general, the breakdown field values given in the datasheet are broadly exceeded when working with membranes (close to a factor 4 for the CF19). This is attributed to the statistically reduced amount of defects present in a thin layer compared to a bulk piece of elastomer, and to the security margin taken by the manufacturer. However, it is a good starting point for comparing dielectric properties of silicones, especially if they come from the same manufacturer. On its datasheet,the R32-2186 from NuSil has a shore hardness A of 15 (about 2 times softer than CF19) with a better dielectric strength ($35.6\,\mathrm{V}\,\mu\mathrm{m}^{-1}$ versus $28.7\,\mathrm{V}\,\mu\mathrm{m}^{-1}$). It should therefore definitively enhance the maximal deflection achievable. This elastomer is sold as an adhesive, but thanks to our membrane fabrication process with sacrificial layers (section 3.2), this does not pose fabrication problems for the release. However, the silicone:solvent ratio that must be used to lower the viscosity prior bladecasting is 1:1.25 (solid fraction of 0.44), higher than for the other silicones commonly used in this project.

Secondly, our laboratory developed meanwhile an indirect stamping technique (pad printing) to precisely pattern µm-thick electrodes composed of carbon black dispersed in a soft elas-

tomer matrix. They induce much less stiffening on the membrane than ion implantation, so that it should also contribute to an enhanced deflection. Moreover, their stiffening impact is much easier to control than ion implantation, which is a critical point if one wants to compare experimental data with a model since the material parameters may vary for each device.

Static deflection vs. applied voltage

The deflection of the center of the membranes as a function of the applied voltage is displayed on figure 5.18, together with model curves. A maximal deflection of 335 µm was observed with R32, 385 µm with the CF19, in both cases better than the 300 µm of ion-implanted CF19 membranes. The model curves were plotted using Gent model parameters fitted on uniaxial pulltest data on samples without electrodes. These two devices appear on the fourth and fifth line of table 5.3.
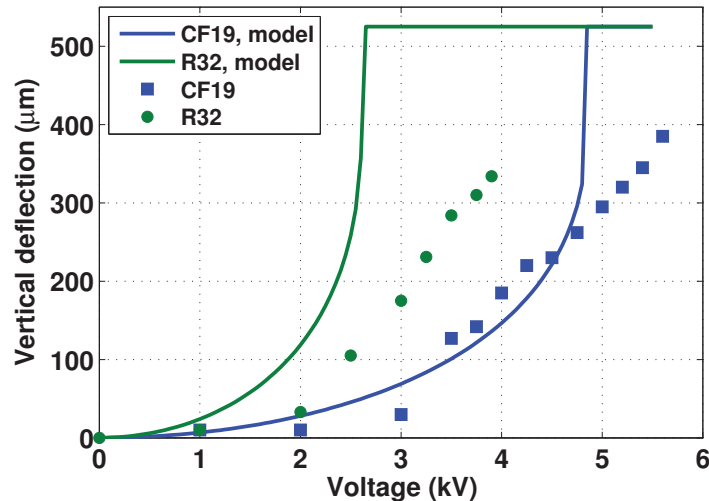
Figure 5.18: Deflection of a 59 µm thick R32 and a 63 µm thick CF19-2186 membranes with CB-silicone electrodes. The chamber side is 2 mm. The models curves are plotted using fitted Gent model parameters on uniaxial pulltests of membranes without electrodes.

The reason why the R32 silicone did not perform better than CF19 is not completely clear, but most likely its breakdown strength is not as good as one could expect from the datasheet. This could possibly be due to the fabrication process which requires more solvent, hence increases the possibility of trapped air pockets in the membrane. The agreement with the model is satisfying for the CF19, but in the range of 1 kV more optimistic than the data for the R32. The neglected stiffening impact of the carbon black-silicone electrodes for plotting the model curves would shift them slightly towards more voltage for a same deflection, and the R32 one more significantly than for the CF19 because of its lower initial stiffness, but this cannot completely explain the difference.

5.4 Zipping in conical low-sloped chambers

Having determined that zipping actuation with the electric field applied across the membrane is possible but difficult if the sidewalls angle is too large, simpler zipping DEA structure were chosen for the next study, in order to determine the relevant parameters (size, sidewalls angle, membrane thickness, prestretch) for making integrated microfluidic actuators. Conical chambers were conventionally machined in aluminium. Compared to the anisotropically-etched silicon chambers, the sidewalls angle can have smaller values and be easily varied. Moreover, a conical shape most likely offers better performance for symmetry reasons and avoids the suspected effect of breakdowns triggered in air pockets on the inner pyramid edges.

5.4.1 Low-sloped conical zipping DEAs and peristaltic micropump with "flipped design"

Conical-shape devices were fabricated, with a top diameter of approximately 2.3 mm and a cavity milled in an aluminum plate, which acts as rigid electrode. A hole is drilled at the bottom of the chamber to let the air out during actuation. A 25 μm thick pre-stretched silicone membrane with a silicone-carbon black compliant electrode patterned on top is bonded over the chambers. (figure 5.6 and 5.19).
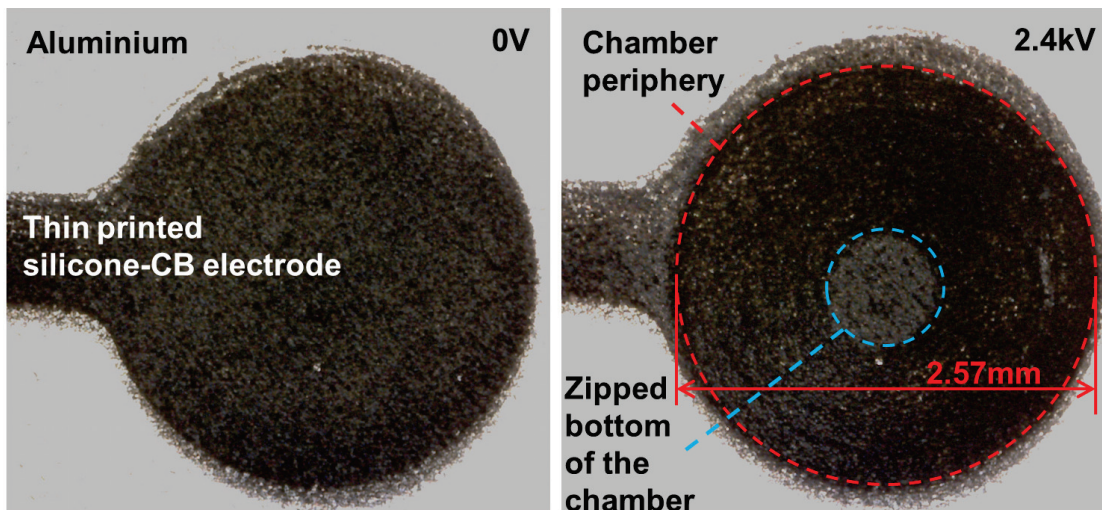
Figure 5.19: Photograph (top view) of an unactuated (left) and actuated (right) zipping actuator. Sidewalls angle $\alpha = 15°$, membrane thickness 23.5 μm, prestretch 1.32, geometrically-constrained zipping depth $z = 280$ μm.

The figure 5.20 represents a peristaltic zipping micropump based on three such normally-off actuators. As the voltage is turned on, the membrane zips inside the cavity, pumping the liquid inside the chamber and opening the valve. Compared to other pump structures such as presented in the section 5.3 [103], this flipped actuator design keeps the liquid free from the electric field. This allows handling fluids regardless of their conductivity, and prevents

affecting biological samples such as cells. However, the penetration of the processed liquid in the actuator membrane might degrade its performance.
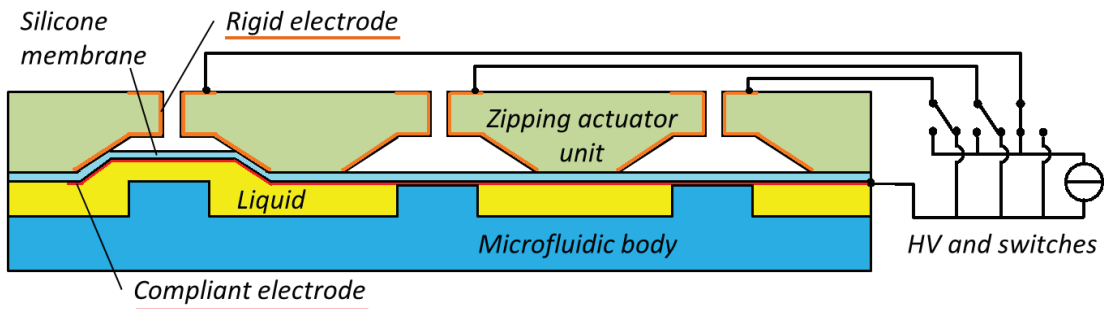
Figure 5.20: Cross-section along the channel of a peristaltic zipping micropump composed of three actuators. In this configuration, no electric field is applied in the liquid.

5.4.2 Experimental results on conical low-sloped chambers

The profile of the zipped membranes were measured by automated frame stitching on a white light interferometer Wyko NT1100 DMEMS from Veeco. The top diameters D and membrane thicknesses t_0 of the 6 measured actuators can be found in table 5.4. The bottom diameters d are comprised between 0.6 and 1 mm. Two different equibiaxial prestretch levels λ_0 have been investigated.

Table 5.4: Measured prestretches and dimensions of the actuators. λ_0 is the biaxial pre-stretch, and α the cone sidewalls angle.

λ_0		$15°$	$22.5°$	$31°$	$45°$
			α		
1.13	D (mm)	2.38	2.14	2.14	2.10
	t_0 (µm)	23.7	24.4	24.4	24.4
1.27	D (mm)	2.42	2.55		
	t_0 (µm)	24.6	24.6		

Zipping behavior

Unless the sidewalls angle is large (54° for KOH-etched silicon chambers, section 5.3) zipping DEAs need to be prestretched to provide the restoring force to counter the adhesion forces between the aluminium and the silicone at a cost of a higher driving voltage, as explained in section 5.2.6. This effect is difficult to predict theoretically, and I therefore prestretched equibiaxially two set of CF19 membranes with $\lambda_0 = 1.13 \pm 0.01$ and $\lambda_0 = 1.27 \pm 0.01$. All membranes were able to come back in their initial position within a few seconds of turning off the voltage, which means that a prestretch of 1.13 or lower is enough for our devices.

The figure 5.21 represents the zipping curves of the measured samples. The 15° and 22.5°
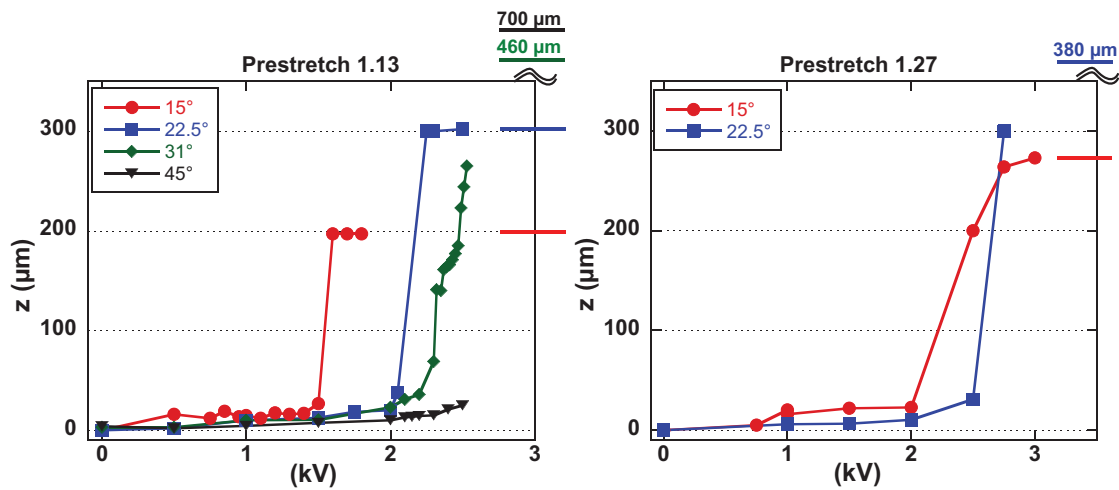
Figure 5.21: Vertical deflection of the zipped membranes. The maximal deflections (limited by the bottom of the chambers) are indicated by the bold lines at the right of the plot. The lines are guides to the eye.

chambers with low-prestretched membranes could zip down to the bottom of the chamber, but only the 15° one on the set of devices with high prestretch.

Shape of deflected membrane

The membrane profiles during the actuation have been plotted on the figure 5.22, together with the aluminium sidewalls.

5.4.3 Comparison of the results with the model

Shape of the deflected membrane

As seen on figure 5.22, the measured shape of the membrane is very close to the one assumed in the model: completely in contact with the sidewalls, and a flat part in the center. However, one can notice that at 2.3 kV, the membrane is clearly not yet in contact with the sidewalls, but is bending down because of the electric field. This effect is visible on the $z(V)$ plots (figure 5.21, for which the deflection is a few tens of µm before starting to zip. Secondly, the membrane is visibly thinner in the top of the cavity ($0 < z < 100$ µm), and somewhat thicker below ($100 < z < 200$ µm). This might possibly be a discrepancy coming from the automated stitching measurements, since there are less datapoints and more noise on the sidewalls.

Zipping voltages

Measured and predicted zipping voltages V_{zip} were compared, with V_{zip} defined as the voltage in the middle of the steep zipping slope (figure 5.21), taking the average between the voltages
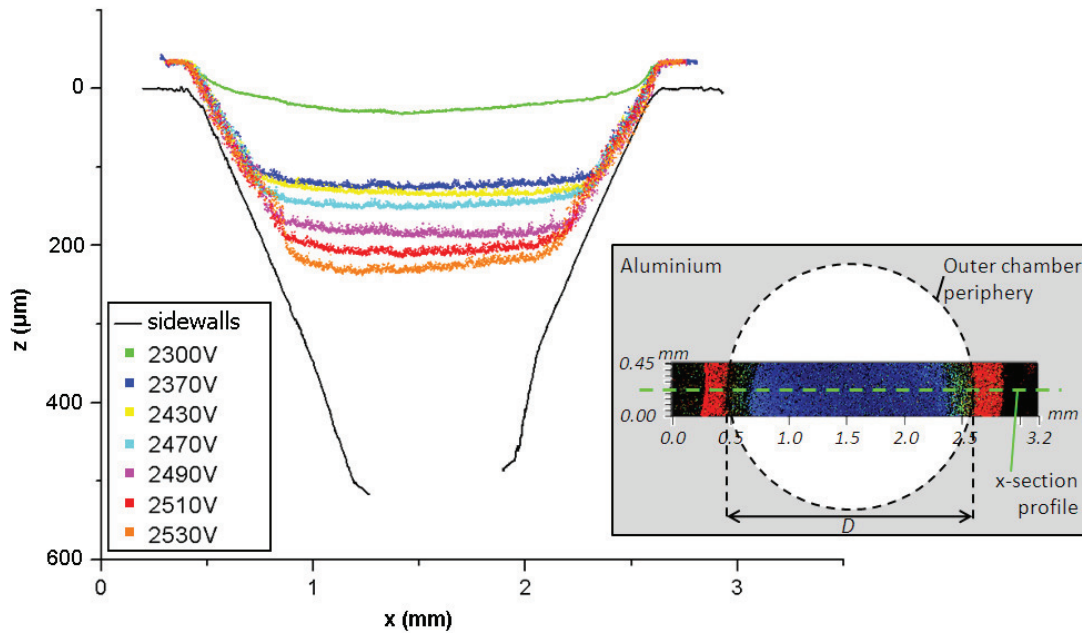
Figure 5.22: Membrane profile of the device with $\lambda_0 = 1.12$ and $\alpha = 31°$. (x and y axes not at the same scale). The insert shows a 3D dataset from the white light interferometer, from which the cross-section profiles have been extracted.

of the start of zipping and when the membrane is fully zipped. For a few devices which had a dielectric breakdown just before reaching the bottom of the chamber, the zipping voltage is computed using a linear approximation, since the maximal zipping depth is known.

The figure 5.23 presents the measured zipping voltages at both low and high prestretch (in red) together with the zipping voltages from the model. Since every device has small variations of diameters and membrane thickness, each point from the model is computed using the exact measured values of the device. Two roughness values R_0 of 10 and 20 μm of the chamber sidewalls (section 5.2.4) are shown together with the case without roughness. According to our surface measurements, a value of $R_0 = 10$ μm seems reasonable and a value of 20 μm the upper limit.

While the predicted voltages are about 1 kV lower than the measured ones, the model accurately predicts the effect of changing the sidewalls angle on the zipping voltage, the difference between the measured and predicted zipping voltage being constant for a same prestretch. With the assumption of a 10 μm roughness, the difference is in the range of 0.7 kV at low prestretch and 1.3 kV at high prestretch. This difference indicates that our model is more accurate at lower prestretches. I indeed measured a good agreement between the model and the data in pyramidal-shape chambers covered by membranes which were not prestretched to provide a mechanical restoring force thanks to the large angle (54.7°), see section 5.3.3 [103].

The effect of surface roughness cannot explain the full discrepancy. Even with the hypothesis
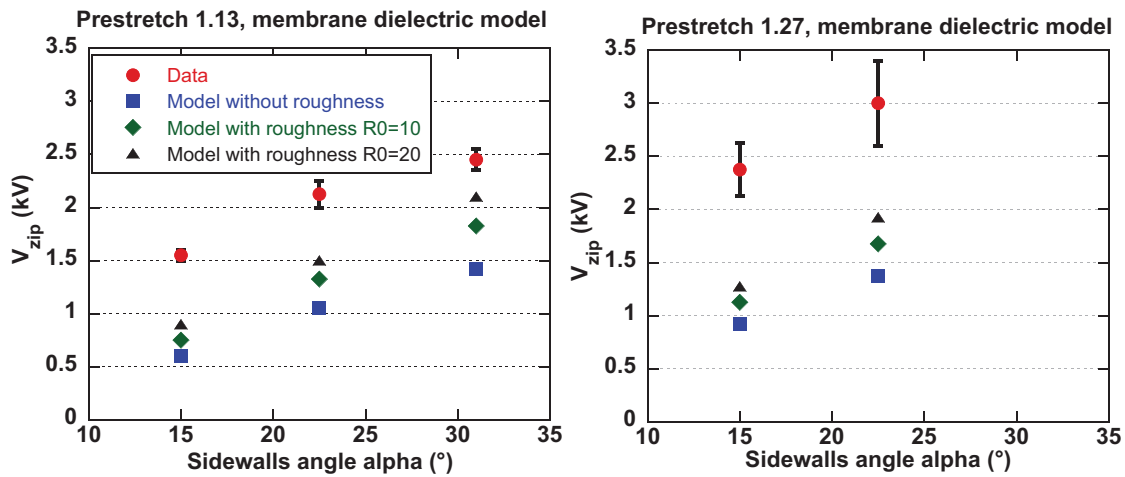
Figure 5.23: Zipping voltages of the measurements and the model without sidewalls roughness and with a peak-to-peak model roughness of 10 and 20 μm.

of $R_0 = 20$ μm, the difference between the predicted and measured zipping voltages remains too large. The larger difference of the highly prestretched devices compared to the lower prestretched ones (figure 5.23) could possibly reflect that if the membrane is more prestretched, it conforms less inside the valleys of the rough surface and leaves larger air gaps.

It is very reasonable to assume that the membrane is in non-slipping conditions with the sidewalls given the high shear forces that can be observed between silicone membrane and metals. The resulting computed thickness reduction for a geometry similar to the figure 5.22 is in the order of -25% at 250 μm, which is not verifiable given the large measurement noise on the sloped sidewalls using a white light interferometer, and the fact that the exact location of the sidewalls cross-section cannot be guaranteed (the device must be removed from the setup to peel off the membrane).

The most likely explanation for the larger measured than simulated V_{zip} is because our model neglects the membrane bending energy. The maximum of the mechanical stretching energy ranges from a few μJ to 20 μJ depending on the parameters of the actuator. The bending energy needed to bend from a flat position into the zipped shape (figure 5.22) is in the range of 0.3 to 1 μJ. Also, the bending energy increases in the first tens of μm of zipping and is then nearly independent of zipping depth. Including the bending energy would thus lead to an increase in predicted V_{zip}, as it effectively adds an energy barrier that must be overcome to initiate zipping. The bending energy could also be the explanation of the smaller difference between theoretical and experimental V_{zip} of the low compared to the highly prestretched actuators (figure 5.23), since it is proportional to the effective Young's modulus which increases with the prestretch, given that the membrane thicknesses of all studied devices are equal after prestretch.

5.5 Sub-mm size microfluidic actuators fluidically coupled to zipping DEAs for application to a peristaltic pump

Fully functional zipping actuators have been realized and characterized in the previous section. The pump concept of figure 5.20 displayed a possible implementations of those actuators to make a pump. This pump solved the issue of the first design (fig. 5.12) by having the processed liquid on the other side of the membrane, hence avoiding any high electric field in it. This design has still a major weakness: the DEA membrane is in direct contact with the liquid to be processed, which might affect its mechanical and electrical properties, leading to performance degradation or failure. Indeed, as demonstrated in section 4, even liquids considered among the most compatibles with silicones do penetrate in the thin membranes.

5.5.1 Fluidically-coupled zipping DEA pump

A third pump design is therefore presented, which strongly improves this reliability issue: the motion of the zipping actuator is transferred to a passive membrane by hydrostatic coupling, which keeps the sensitive membrane far from the processed liquid (figure 5.24). The base of the chip is a structured PCB-like board which has three in-line metal-covered conical zipping cavities and electrical interconnects. On this zipping body is glued the core of the device, a stack of three silicone parts: the active membrane, a 0.2 mm thick rigid silicone foil with holes which is plasma-bonded on top, and a top passive membrane which is also bonded over the rigid silicone foil. As visible on the cross-section, the diameter of the active membrane is larger than the coupling hole. The diameter of both freestanding membranes can actually be chosen independently, which adds design freedom for the mechanical coupling. Moreover, the silicone type, thickness and prestretch of each membrane can be adjusted to set the operating point of the device (initial pressure and deflections).
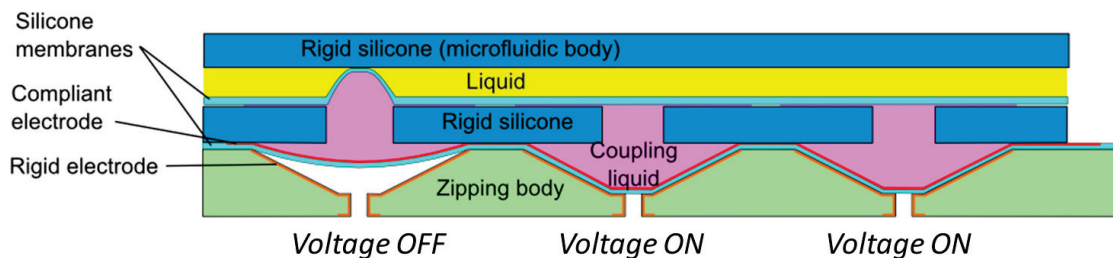
Figure 5.24: Cross-section of the peristaltic pump with fluidically-coupled zipping DEAs.

5.5.2 Estimation of the behavior of a pressure-loaded zipping actuator

The actuators of the pump on the figure 5.24 do not operate in the same condition as studied in the section 5.4: the position of the membrane is biased with a pressure, which considerably changes their operating characteristics. Indeed, the part which defines the actuation behavior

is the zone where zipping proceeds, i.e. close to the contact point between the suspended part of the membrane and the sidewall. On the contrary to non-biased membranes, the angle at which the membrane comes in contact with the sidewalls and the evolution of the stretch state are much more difficult to define, so that analytical modeling would become very complex.

Experimental measurements are therefore used in order to find a suitable actuator design for the pump. Zipping devices on which a bias air pressure can be applied were built, so that the actuation of different device geometries can be measured while sweeping the pressure as a parameter, as illustrated on figure 5.25.
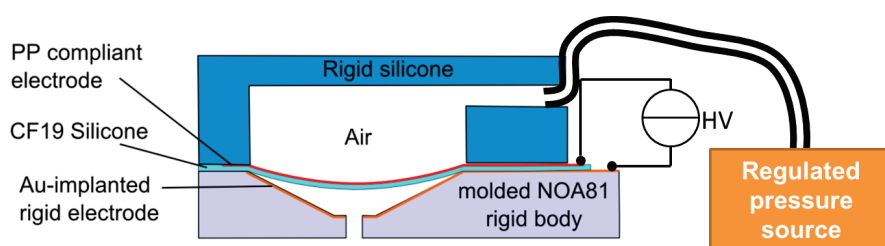
Figure 5.25: Cross-section of the zipping DEA with bias air pressure device.

The zipping body is composed of an optical adhesive suitable for replica molding (NOA81 from Norland Adhesive[2]) molded on electo discharge machined conical bumps of different shapes. The rigid electrode is patterned with Au ion implantation, which demonstrated a very good adhesion on this thyol-based curable polymer. Based on my previous results, the CF19 silicone is kept as active membrane material, on which a compliant electrode is patterned by pad printing. On top comes a rigid silicone molded part which provides a closed chamber to apply the pressure bias and clear optical access over the actuators. A 3D view and a picture of the fabricated test device are illustrated on figure 5.26. A more detailed description of the fabrication process can be found in section 5.6.3.

---

[2]www.norlandprod.com

(a) 3D view

(b) Device with 4 zipping DEAs
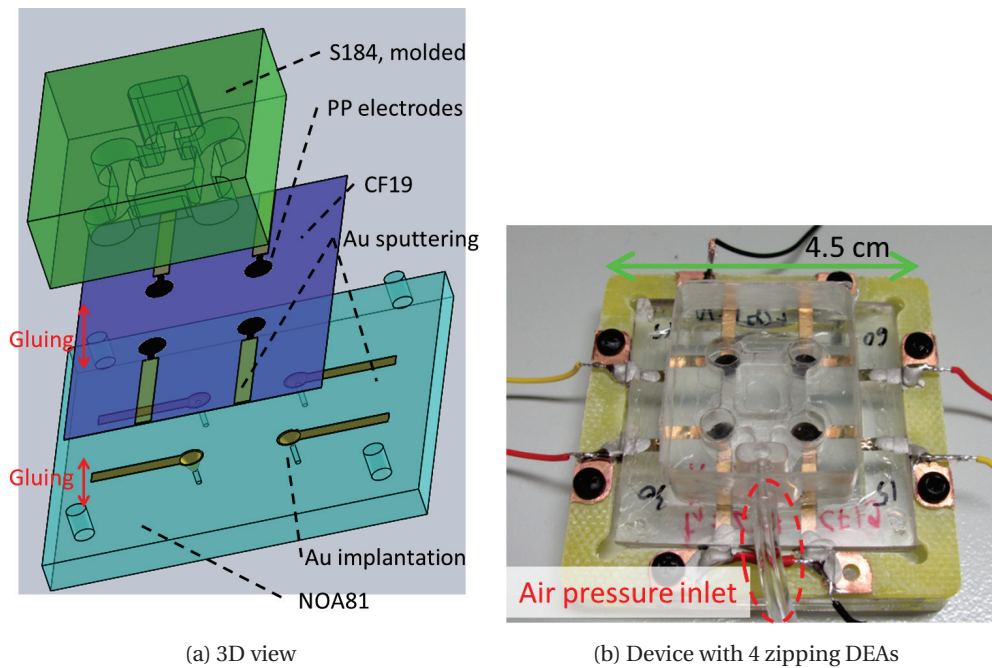
Figure 5.26: Zipping DEA with bias air pressure device. It is composed of three parts: a bottom replica molded plate in optical adhesive (NOA81) with conical holes and patterned Au rigid electrodes, a zipping membrane with pad printed (PP) electrodes on its topside, and a top chamber molded in rigid silicone (Sylgard 184) which provides a way to apply a bias air pressure while keeping optical access over the chambers.

Experimental procedure

The bias pressure is applied with a regulated pressure source (MFCS system from Fluigent[3]) with an accuracy of 0.025 mbar. A square wave signal from 0 to the high voltage value actuates periodically the membrane. In this manner, the voltage-induced motion can be measured by comparing the two alternating positions, at $0\,\mathrm{V}$ (due to the pressure only) and at high voltage (due to the pressure and the applied voltage). The same voltage steps are kept but the pressure is gradually increased, which shifts the operating point of the zipping DEA by pushing the membrane lower in the chamber. The key parameter which must actually be measured is the voltage-induced displaced volume, since it indicates the ability of the actuator to open or close a valving unit of a given size.

The measurement of the voltage-induced displacement is critical. Indeed, optical measurement methods such as white light interferometry profilometer commonly used for this purpose cannot be used, because of the optical path difference induced by the pressure chamber roof. The approach which was finally adopted is to measure the motion of the membrane with an optical microscope. As illustrated on figure 5.27, two distances d_1 and d_2 are measured through the transparent molded pressure chamber. The voltage-induced displaced volume is

---

[3]www.fluigent.com

computed by subtracting the volume at high voltage and the volume at 0 V. On the right of the figure, the assumption taken to compute the voltage-induced displaced volume is displayed: instead of the two real shapes with bulged suspended part (left), I assume two truncated cone shapes. If the central suspended part of the membrane has a bulged shape determined by the pressure but not by the electric field, the error linked to this assumption of truncated cone volumes underestimates the displaced volume compared to the reality. Indeed, the volume of the inflated cap under high voltage is smaller than the one at 0V, when it is assumed that they cancel out by taking truncated cones.
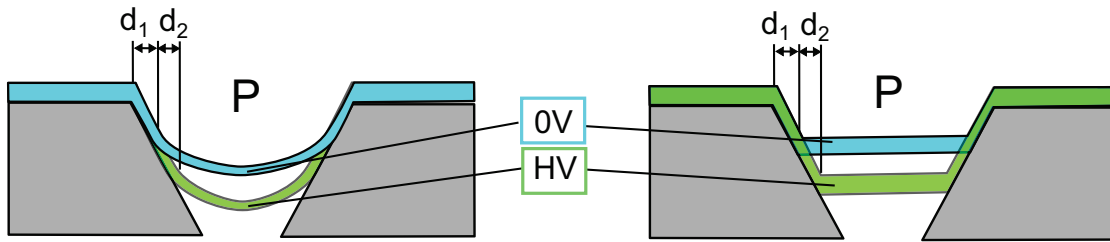
Figure 5.27: Real (left) and assumed (right) shapes to compute the voltage-induced displaced volume in a conical zipping cavity with bias pressure. If the influence of the electric field on the suspended membrane shape at high voltage is negligible, the error induced by the assumption of two truncated cone shapes (right) rather than two bulged ones (left) underestimates the real displaced volume. d_1 is the pressure-induced contact length with the sidewall, d_2 is the voltage-induced contact length with the sidewall.

Experimental results of zipped volume with air pressure bias and discussion

The voltage-induced displaced volume of a set of actuators was measured, varying the parameters of sidewalls angle α (30, 45 and 60°), chamber diameter D (1.5 and 2.25 mm) and prestretch λ_0 (1.06 and 1.14). The pressure is progressively increased for each step of nominal electric field. Examples of complete datasets for a 1.5 mm diameter, 60° sidewalls angle and a 2.25 mm diameter, 30° sidewalls angle are visible on figures 5.28 and 5.29 respectively.

The dashed lines of the corresponding colors indicate the maximal volume that can be zipped, i.e. the total volume enclosed below the membrane without voltage. A full line that meets the corresponding dashed one therefore indicates a membrane reaching the bottom of the chamber by electrostatic zipping. Those maximal volumes were determined experimentally based on the measure of d_1 (fig. 5.27), hence their step-wise shape. A peak was repeatedly observed between 0 and 50 mbar, jumping to the record value of 0.3 mm^3 for the 60° device: when the pressure is relatively low, the membrane is not stretched to a too large extent and a partial zipping motion proceeds, at angles much larger than those on which a full zipping without pressure were observed (section 5.4.2). A full zipping was observed on a device with an angle $\alpha = 30°$ on a pressure range between 40 and 70 mbar (visible on the figure 5.30).

As visible on figure 5.29, the first peak is followed by a nearly constant plateau after 50 mbar up to 200 mbar. For all devices, a decay of the displaced volume obviously appears when the
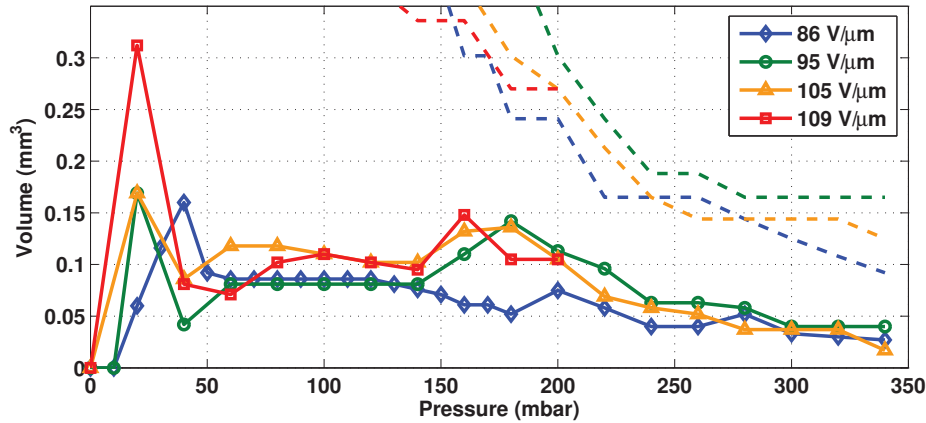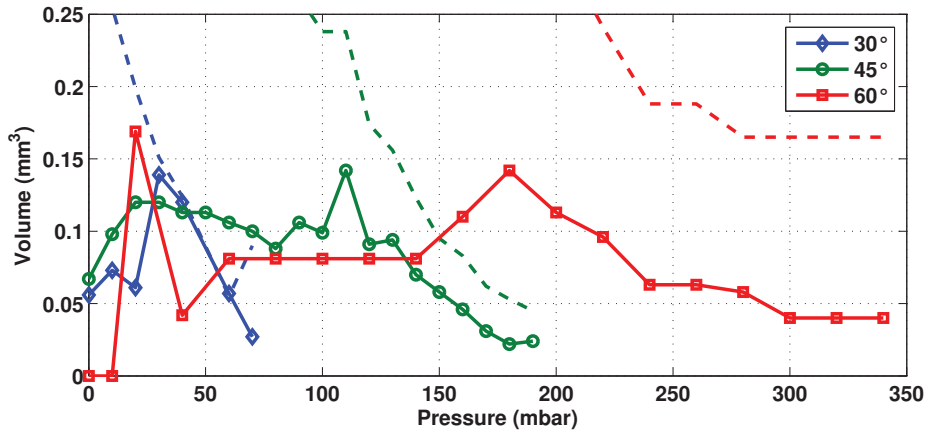
Figure 5.28: Voltage-induced displaced volume in function of the offset pressure, full data. Conical zipping chamber with diameter D =1.5 mm, sidewalls angle α=60°, prestretch λ_0=1.13, prestretched membrane thickness t_1=21 µm. The dashed lines indicate the remaining volume to be zipped down to the bottom of the chamber.
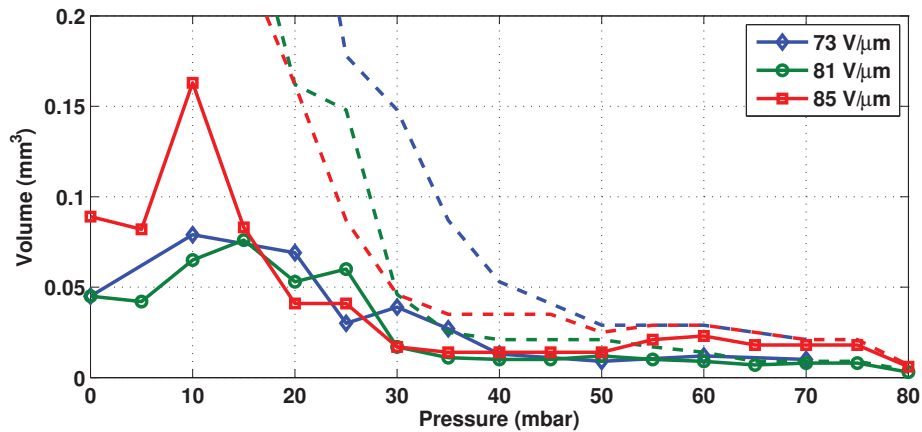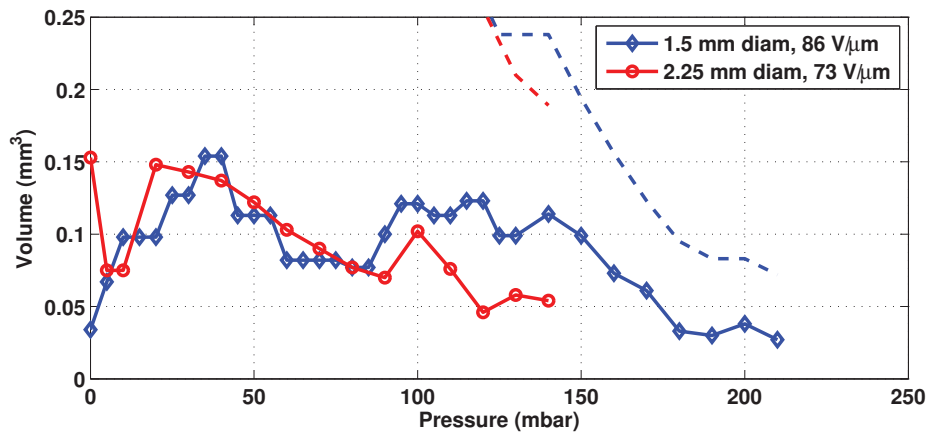

Figure 5.29: Voltage-induced displaced volume in function of the offset pressure, full data. Conical zipping chamber with diameter D =2.25 mm, sidewalls angle α=30°, prestretch λ_0=1.14, prestretched membrane thickness t_1=25 µm. The dashed lines indicate the remaining volume to be zipped down to the bottom of the chamber.

offset pressure pushes the membrane down to the narrower bottom of the chamber. This plateau can be exploited to keep a sufficient amount of displaced volume while working at high pressures, which is desirable for a pump.

The figure 5.30 compares the effect of sidewalls angle at same nominal electric field of $95\,\mathrm{V\,\mu m^{-1}}$. As expected, larger angles enable larger pressure ranges: the membrane can be pushed further before reaching the bottom of the chamber. What is more surprising is that the achieved displaced volume remains nearly constant even at those higher pressures. For instance, the displaced volume by a full zipping of the 30° chamber is in the same range than

with a partial zipping on a 60° device. For the fluidically-coupled microfluidic actuator design, a higher pressure of the encapsulated liquid pocket means an improvement in performance: more blocking pressure of a valve and higher pressure generated by the pump. As a conclusion, a design with 60° sidewalls angle rather than lower angles was chosen, because it should allow to move the passive membrane from a comparable amount while keeping the pressure high.

Figure 5.30: Voltage-induced displaced volume in function of the offset pressure, effect of sidewalls angle. Conical zipping chamber with diameter D =1.5 mm, prestretch λ_0=1.13, nominal electric field 95 V μm^{-1}. The dashed lines indicate the remaining volume to be zipped down to the bottom of the chamber.

The data of two devices of different diameters operating in comparable conditions have been plotted on figure 5.31. It was expected that a larger cross-sectional area would directly result in larger displaced volumes. However, the displaced volume is surprisingly similar: despite a large ratio of 2:3 between the two investigated diameters, the difference in displaced volume is barely visible. This difference may at least partially be attributed to the higher electric field applied on the smaller actuators. However, since comparable performance can be obtained and that smaller diameter actuator enable more compact integration, 1.5 mm diameter chambers are selected. Keeping the actuators closer one to each other reduces the fluidic resistance losses.

Finally, two prestretch value were also tested. As demonstrated in the section 5.4, the main purpose of prestretching the membrane of zipping DEAs is to provide an additional restoring force to counter the membrane stiction on the sidewalls and restore it to its initial position. However, less prestretch keeps the membrane softer and eases its motion. The optimal prestretch level is therefore the lowest value at which the membrane has enough restoring force to come back to its initial position. On the actuators operating without bias pressure of section 5.4, this optimal value was found to be λ_0 =1.13.

The data of two actuators of same geometry but different prestretches (λ_0=1.06 and 1.14) was compared on a α =45° chamber with a 2.25 mm diameter. It was expected that the lower prestretched actuator would move much easier and provide full zipping with the help of the

Figure 5.31: Voltage-induced displaced volume in function of the offset pressure, effect of chamber diameter. Conical zipping chamber with sidewalls angle α =45°, prestretch λ_0=1.13. The dashed lines indicate the remaining volume to be zipped down to the bottom of the chamber.

offset pressure. It was however not the case and both actuators had a similar behavior. The gain in volume was only approximately 0.05 mm^3 by having a prestretch of 1.06 rather than 1.14, at the cost of a slower motion to come back in its flat position due to the stiction forces. Moreover, a slightly higher electric field was applied on the low-prestretched one, which also contributes to this difference. It can therefore be concluded that the use of a prestretch in the range of 1.15 is a good choice, because it provides more restoring force while affecting negligibly the displaced volume.

5.5.3 Peristaltic pump powered by fluidically-coupled zipping DEAs.

Device structure

Based on the conclusions of the previous section, a set of three in-line fluidically-coupled zipping DEAs to be used as a peristaltic pump were built. From the point of view of fabrication, the first critical part of the process is to make three conical chambers (1.5 mm in diameter and 60° sidewalls angle), in a material which allows to have a conductive coating only inside the chamber but not on its side (reduced risk of breakdown on the contacting tracks). This was achieved by machining 2 mm thick sheets of a proprietary plastic of the Cicorel company[4]. The surface of this plastic can be activated by a laser and metallic layers can be grown on these areas by electroplating. This process of selective electroplating on plastic substrates has been developed for the fabrication of 3D PCBs (3D-MID technology[5]). As illustrated on figure 5.32, the obtained zipping body has three metal-coated zipping chambers (left) whose holes at the bottom act as electrical vias connected to electrical interconnects (right).

---

[4]www.cicor.com
[5]http://www.cicor.com/3d-mid
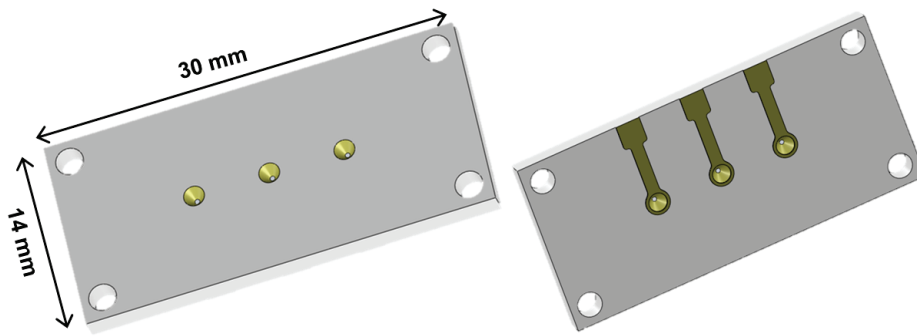
Figure 5.32: 3D view of the 3D PCBs from Cicor (left: top view with conical zipping chambers, right: bottom view with electrical vias and tracks.).

The core of the pump is composed of two silicone membranes bonded on both sides of a rigid silicone sheet and enclosing an excess volume of coupling liquid (figure 5.33 top). The fabrication process consists in pulling down the active membrane area by vacuum in a chuck, plasma-bonding the rigid silicone bonding foil, filling the cavity and plasma-bonding the passive membrane on top. The holes in the rigid silicone sheet are punched with a 0.75 mm diameter Harris Uni-core puncher, which actually results in 800 µm diameter holes. The fabrication process is described with more details in section 5.6.3.

Optical pictures of the passive and active membranes are displayed on figure 5.33. Thanks to different silicones (LSR4305 and CF19) as well as membrane thicknesses and prestretches, their shape can be adjusted. In this case, the internal pressure inflates the passive membrane over a half sphere (fig. 5.33 left).

A 3D view of the fabricated device mounted on a PCB is visible on figure 5.34, and a picture on figure 5.35. The device outer dimensions are 15 by 30 mm. As a last step for making the pump, a channel molded in rigid silicone has to be bonded on top of the three in-line actuators.
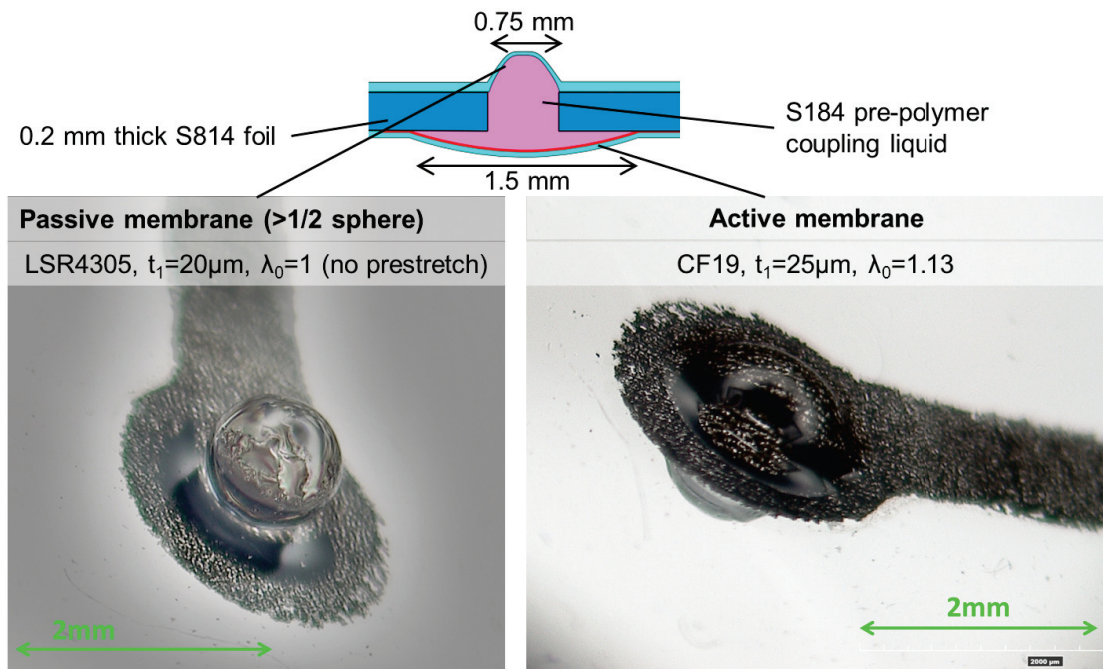
Figure 5.33: Pictures of a passive and an active membrane coupled by a liquid (silicone pre-polymer). Due to overfilling, the passive membrane is inflated slightly over a half sphere.
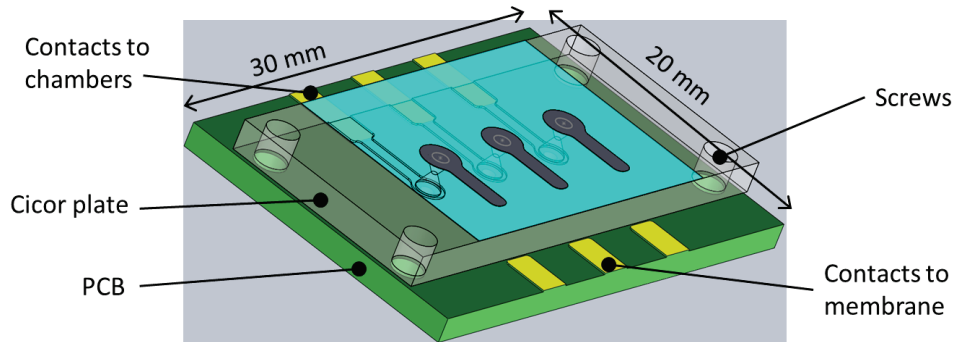
Figure 5.34: 3D view of the peristaltic zipping pump
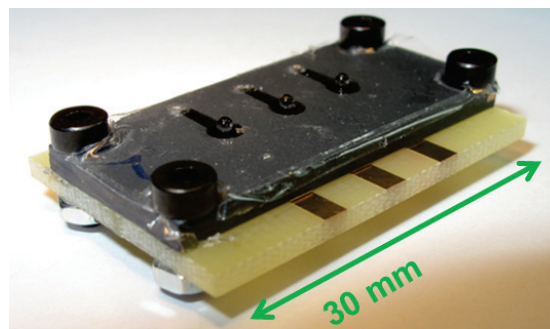
Figure 5.35: Photograph of the 3 in-line fluidically-coupled inline zipping actuators for a peristaltic pump.

Characterization of the steady state displacement of single microfluidic actuators

The steady state displacement of four fluidically-coupled zipping DEAs of different initial pressures has been characterized with a white light interferometer. The zipping actuator parameters are kept constant and chosen based on the results of the section 5.5.2 (thickness $t = 30\,\mu m$, prestretch $\lambda = 1.15$, sidewalls angle $\alpha = 60°$ and diameter 1.5 mm). Both the initial pressure (which defines the active membrane initial deflection) and the passive membrane deflection at rest are adjusted by choosing the properties of the passive membrane (silicone, thickness, prestretch) and the filling level of the encapsulated cavity. The dimensions and parameters of the four actuators which have been measured are displayed on table 5.5.

Table 5.5: Dimensions and parameters of the measured fluidically-coupled zipping devices. Active membrane: CF19, 1.5 mm diameter. Passive membrane: LSR4305, 0.80 mm diameter. The deflection at 0 V is used to compute the start pressure.

Active membrane		Passive membrane			
Thickness (μm)	**Prestretch** (-)	**Thickness** (μm)	**Prestretch** (-)	**Defl. at 0 V** (μm)	**Pressure** (mbar)
29	1.13	20	1	888	25
31	1.15	11	1.8	450	60
33	1.11	49	1.46	230	125
33	1.11	46	1.46	269	135

The initial pressure of the coupled actuators has been derived from the passive membrane deflection at 0 V using a model of inflated clamped elastomer membranes with hyperelastic material parameters (see section 6.2.3). The absolute and relative deflections of these four coupled actuators are plotted on figure 5.36. Their maximal motion is comprised between 50 and 75 μm, much less than needed to come back to their flat position. Their comparable displacements actually represent different amounts of displaced volume because of the inflation levels: 50 μm motion of a balloon inflated up to a half sphere represents a larger displaced volume than 75 μm of a sphere inflated at 35% of its diameter. In order to compare the achievable displaced volumes of the active membranes in function of the pressure, one therefore has to plot the displaced volumes, as illustrated on figure 5.37. It shows clearly that the greatest amount of displacement among these four actuators (0.07 mm^3) is achieved with the lowest pressure of 25 mbar. It is slightly more than the half of the targeted volume of 1.3 mm^3, that would be required to deflate a half sphere of 800 μm diameter to a flat level.

The expected amount of displacement based on the measurements of the zipping devices biased with an air pressure (section 5.5.2) together with the ones measured by the passive membrane motion are summarized on figure 5.38 for two nominal electric field levels. Whereas a displaced volume of 1 mm^3 is close to be met based on the first measurement method, the displaced volume measured on the passive membrane height is in the range of half the expected one up to 60 mbar and only one fourth of the expectations ah higher pressures. Part of the lower performance of the zipping DEAs fluidically-coupled to passive membranes could

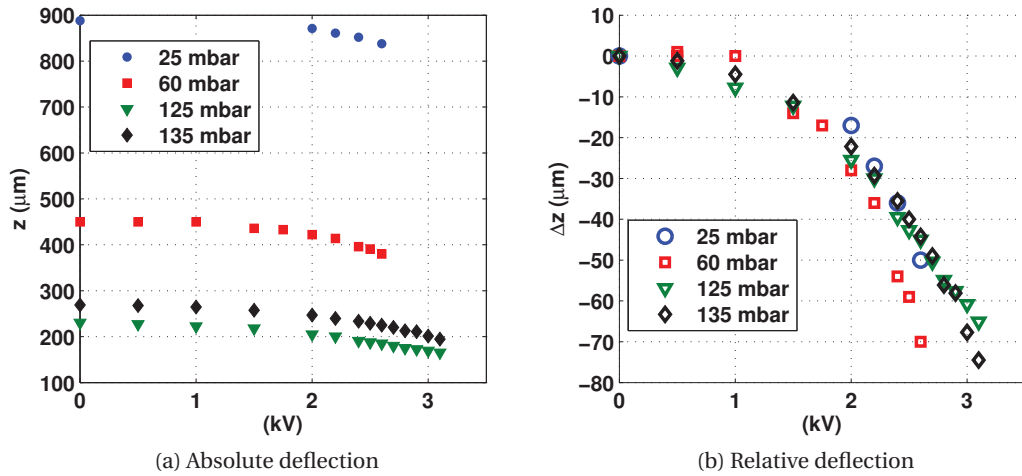(a) Absolute deflection

(b) Relative deflection

Figure 5.36: Deflection of the passive membranes coupled to the zipping DEAs (properties visible on table 5.5). All of them moved up to approximately 70 μm, which corresponds to different volumes. The legend indicates the initial pressures, which are set by the membrane parameters and the encapsulated volume.

be possibly be attributed to a non-ideal shape of the membrane around the zipping cavity (few 10's of μm thick adhesive layer, bending of the glued rigid silicone foil due to the membrane prestretches). However, much care has been taken to minimize these practical issues and the fact that the active membrane is pressurized guarantees that the sensitive first portion of the deflection must not be achieved electrically.

As the measurement method of the passive membrane height with a white light interferometer is more reliable than measuring the in-plane zipped lengths with a microscope, one can conclude that the latter method overestimates the achieved volume. Imprecision in the measurement of the in-plane dimensions d_1 and d_2 (figure 5.27) results in a larger error of computed volumes if the sidewall angle is large. The chosen value of 60° might therefore potentially induce a larger error. However, this is probably not sufficient to explain the total difference between the two measurement methods.

A last source of overestimation of the displaced volume on the first set of measurement is related to the shape of the deflected membrane. As illustrated on figure 5.39, the cross-section of the suspended membrane deformed by a high electric field might be more flat than assumed, still having the same values for the pressure- and voltage-induced zipped lengths d_1 and d_2. Zipping might indeed possibly pull the suspended membrane sidewards more than downwards, resulting in a smaller amount of displaced volume.
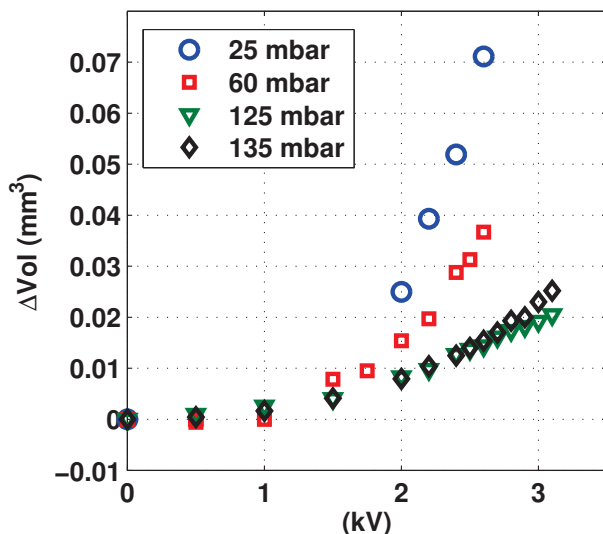
Figure 5.37: Displaced volumes of the passive membranes coupled to zipping DEAs (properties visible on table 5.5). The maximal volume of 0.07 mm^3 is achieved with a starting pressure of 25 mbar on the actuator. The legend indicates the initial pressures, which are set by the membrane parameters and the encapsulated volume.
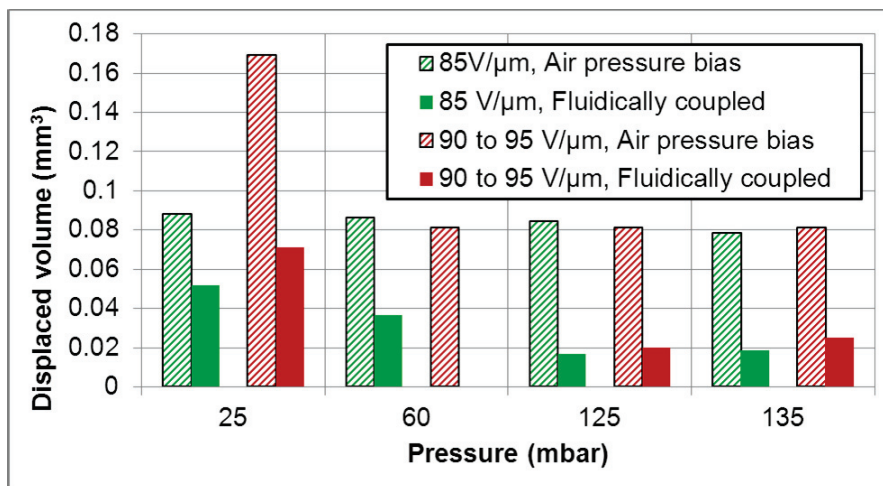
Figure 5.38: Comparison of the displaced volumes estimated with the measurement of zipping with an air pressure bias (fig. 5.28) and by measuring the motion of passive membranes fluidically-coupled to zipping DEAs (fig 5.37, 60° sidewalls angle, 1.5 mm diameter). The measurement method with an air pressure bias overall overestimates the achievable deflection, in particular at high pressures. A volume of 0.1 mm^3 corresponds to a deflection from a half sphere to a flat position of a 750 µm diameter passive membrane.
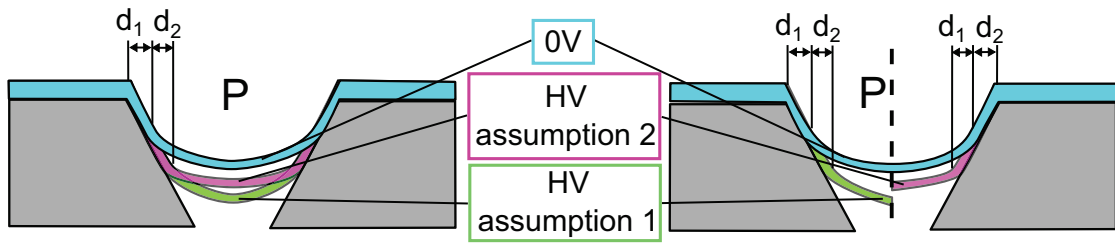
Figure 5.39: Illustration of an initial membrane cross-section at $0\,\text{V}$ with pressure-induced zipped length d_1 and two potential membrane cross-sections at high voltage with same voltage-induced zipped length d_2 but different volumes. The membrane shape is indeed difficult to predict when electric field is applied. For the sake of clarity, the scheme on the right displays the same case but with only half of each actuated membrane.

Characterization of the time response of single microfluidic actuator

The flow rate of a pump depends on the actuation frequency of its moving parts. I therefore measured the time response of a fluidically-coupled zipping actuator (60 mbar initial pressure device, see table 5.5) using a Laser Doppler Vibrometer from Polytec[6] and a displacement decoder. As visible on figure 5.40, the 0 to 90% response is about 45 ms, with a negligible drift in position. This would correspond to driving frequencies in the range of 25 Hz, and is a good performance given the high viscosity of the silicone pre-polymer coupling liquid which has to be pushed through the 800 µm diameter hole of the rigid silicone sheet. Compared to this damping contribution, the viscous component of the elastomer membrane is negligible.
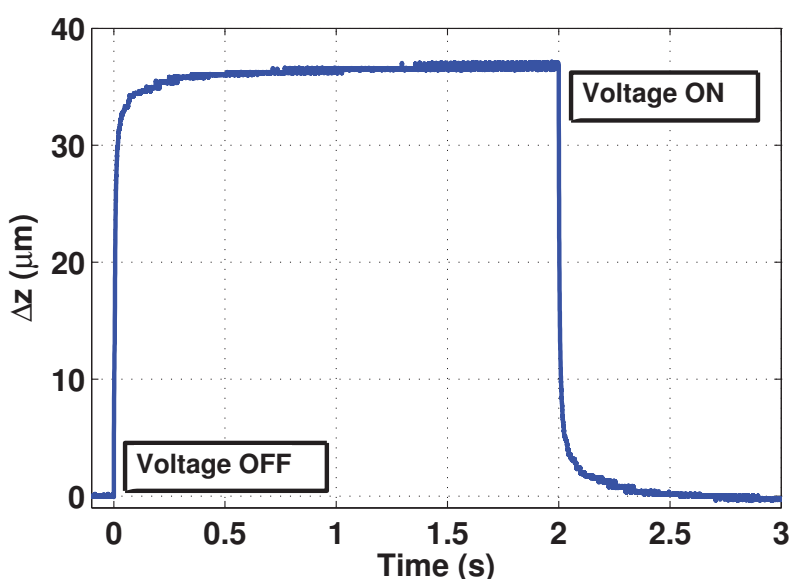
Figure 5.40: 0-90% time response of 45 ms measured on the top of a passive membrane of a fluidically-coupled DEA. 1.5 mm diameter, 60° sidewalls angle, 60 mbar initial pressure.

5.6   Fabrication

5.6.1   Zipping DEAs in anisotropically-etched silicon chambers

The zipping chambers were etched in silicon using conventional microfabrication techniques (figure 5.41). To achieve sloped walls of the chambers with an embedded channel, anisotropic crystalline wet etching was performed in a KOH bath on both sides of a silicon wafer. The substrates are 100-oriented, 525 µm thick, doped wafers. As a first step, an etching mask is deposited on both sides of the wafer by low pressure chemical vapor deposition (LPCVD). 600 nm of silicon oxide followed by 250 nm of silicon nitride was used (A). The photoresist was patterned by photolithography on the topside of the wafer to define square openings

---

[6]www.polytec.de

for the chambers (B). Then, the mask is etched by reactive ion etching (RIE) (C) and the photoresist is stripped (D). A second photolithography step (E) and RIE (F) is done on the wafer backside to define the apertures for the channels, aligned on the topside structured mask. After resist stripping (G), a quick dip in buffered hydrofluoric acid (BHF) removes the oxide residues on the apertures. In the KOH bath, both sides (chambers and channels) are etched simultaneously, but the etching process is stopped at $245\,\mu m$, before they meet, leaving a channel with trapezoidal cross-section since the 100 plane is still visible (H). A $1.7\,\mu m$ thick thermal oxide is grown on the wafer, to be used as a mask for the second KOH etching step (I). Since thermal oxide grows on both sides of the wafer, it needs to be removed on the topside. This is done by a spraycoated photoresist layer on the whole backside (J) followed by a BHF etch, that removes the oxide on the topside (K), and then stripping (L). Spraycoating allows covering even the deep channel structures. By doing so, I prevent opening other crystalline planes than the 111 when both etching cavities will meet. I finish the through-wafer etching of the chambers in KOH (M). Wet baths of hot phosphoric acid and BHF remove the nitride and oxide masking layers respectively (N). Finally, a $1.5\,\mu m$ thick thermal oxide is grown on both sides of the wafer as electrical insulation of the channel and as PDMS bonding layer. SEM pictures of the microfabricated pump body are visible on figure 5.42.

An un-prestretched silicone membrane is bonded by oxygen plasma activation on top of the chambers. Both Au ion implanted electrodes and pad printed carbon black-silicones electrodes have been used. The Au ion implanted compliant electrodes are patterned on the membrane with a shadow mask after bonding of the membrane on the chip. The carbon black-silicone electrodes are stamped with a pad printing machine before being the membrane is bonded onto the silicon chip.
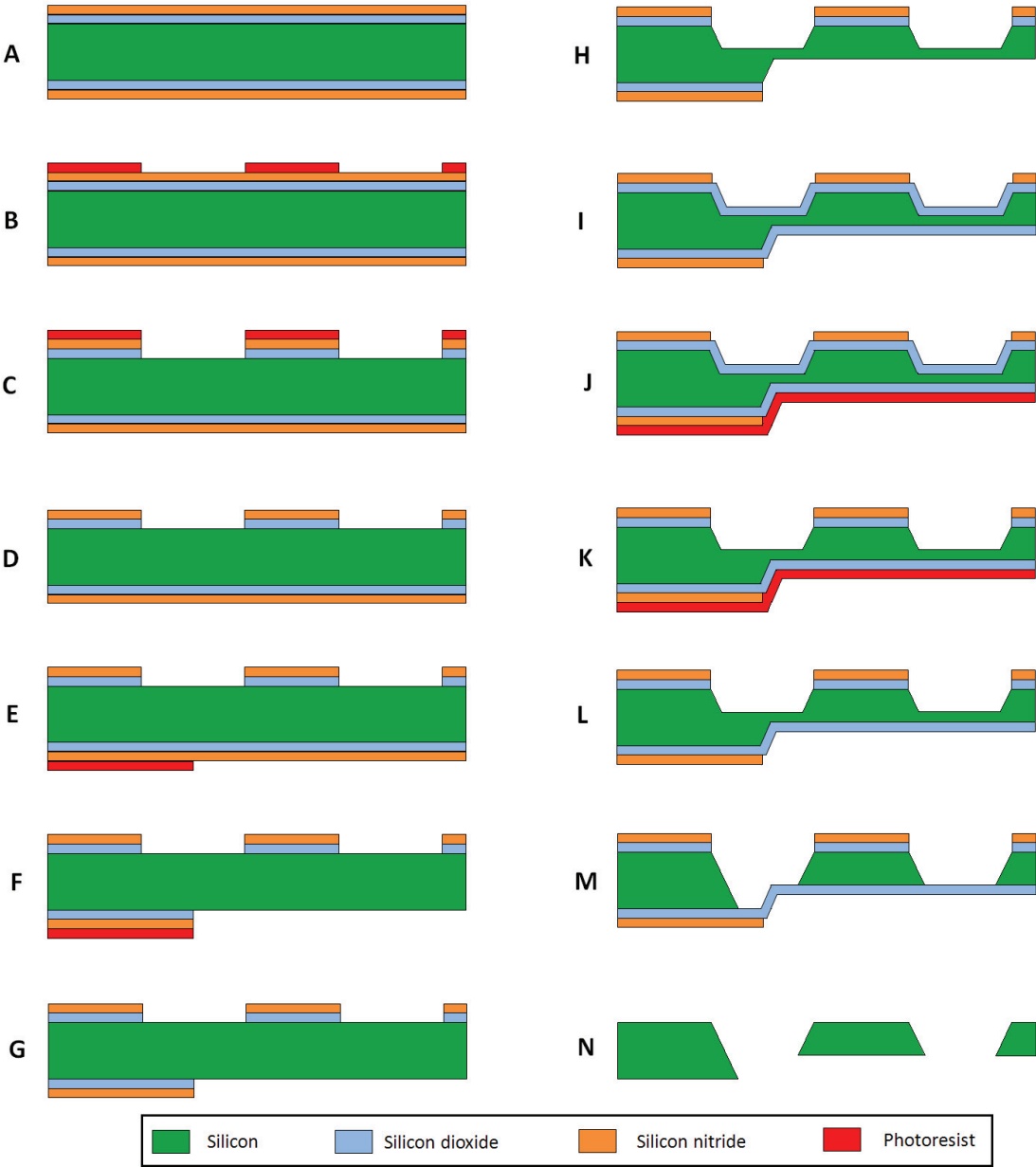
Figure 5.41: Microfabrication process of the silicon pump body. View along the channel (like the A-A cross-section of figure 5.12), with 2 chambers
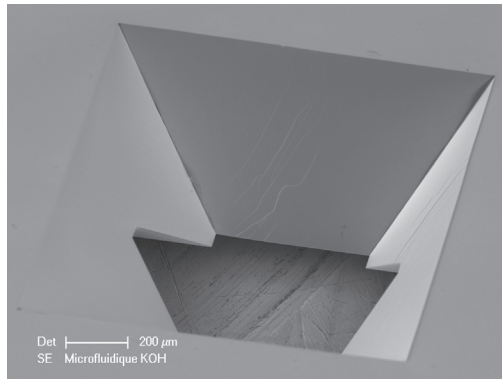
(a) Top view of a zipping chamber with a crossing embedded channel. Scale bar 200 μm
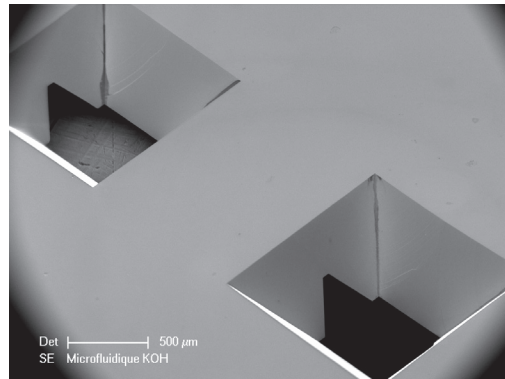
(b) Top view of 2 zipping chambers linked by a channel. Scale bar 500 μm
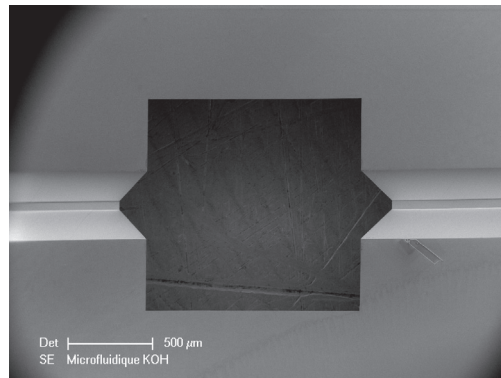
(c) Bottom view of an embedded channel. Scale bar 500 μm

Figure 5.42: Scanning electron microscope pictures of the microfabricated silicon pump body

5.6.2 Zipping DEAs in low-slope aluminium chambers

A 3D view of the fabricated zipping devices is exposed on figure 5.43. It consists in a silicone membrane with compliant electrodes patterned on top, bonded on an aluminium body that embeds machined conical chambers.

The fabrication process is described on figure 5.44.

The conical chambers were milled in an aluminium plate with a CNC from Step-Four basic series [7]. The conical tip of the drillbits was used to achieve the conical shape of the chambers, hence the set of angles α obtained of 15, 22.5, 31 and 45° (fig. 5.44a). The silicone membrane was pre-stretched to the desired value using a home-made stretcher with eight movable fingers, and the equibiaxial prestretch is computed using the ratio of the measured thicknesses before and after prestretch. A compliant electrode composed of 1:10 wt of carbon black and a soft silicone was printed on top of the membrane by an indirect stamping technique (pad printing) (fig 5.44b). These polymer-carbon composite electrodes have the advantages of being well bonded to the membrane, but are stiffer than if dispersed in grease. It is therefore needed to keep them thin relative to the membrane thickness to reduce the stiffening impact [82]. Electrode thicknesses between 1 and 3.5 µm were measured, which increases the Young's modulus of a 20 µm membrane by less than 10%. The printed membranes were irreversibly bonded onto the aluminum chambers by activating the silicone and the native oxide with an oxygen plasma (fig. 5.44c). Over the conical holes, the membrane is suspended and the surface activation of the silicone decays within a few hours so that it has no influence when actuating the device at a later stage. The devices were clamped to a PCB to which electrical contact was made using a conducting varnish (fig. 5.44d).

---

[7]http://www.step-four.at
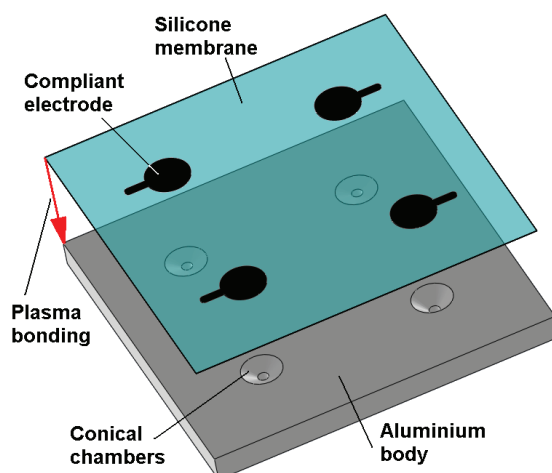
Figure 5.43: 3D view of the fabricated zipping devices. The compliant electrodes are patterned on top of the silicone membrane, and contacted with a PCB.
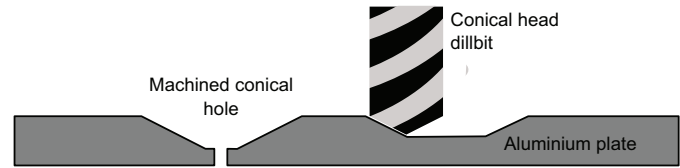
(a) CNC milling of conical chambers in an aluminium plate with conical head drillbits
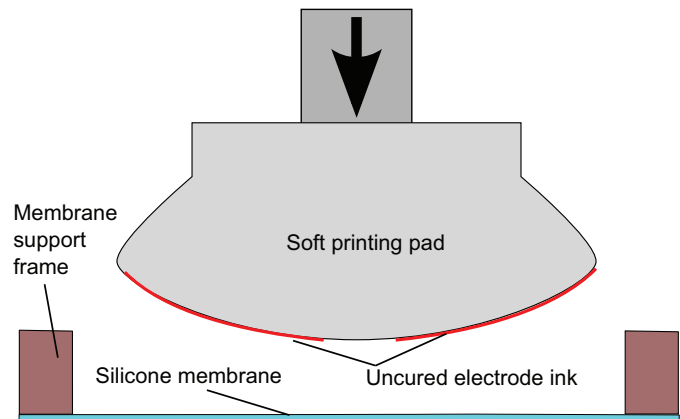
(b) Indirect stamping of compliant electrodes composed of carbon black - silicone ink on a prestretched membrane
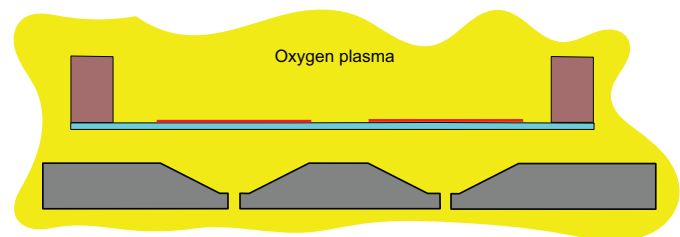
(c) Activation of the Aluminium oxide layer and the silicone membrane with oxygen plasma for bonding
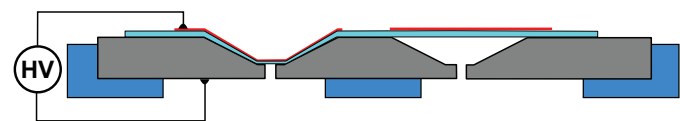
(d) Bonding the active membrane on top of the conical holes and electrical contact

Figure 5.44: Fabrication process of the low-sloped zipping chambers with aluminium body

5.6.3 Fluidically-coupled zipping DEAs

Air pressure-loaded zipping DEA

The figure 5.45 describes the fabrication process of the zipping DEA device with a surronding pressure chamber which was used to measure the displacement of the actuator with a pressure

bias (sect. 5.5.2).

A compliant electrode is first patterned by indirect stamping on a prestretched silicone membrane (fig. 5.45a). The conical chambers of the zipping body are done by replica molding of a rigid UV-curable glue, NOA81 from Norland Adhesives[8] (fig 5.45b). This polymer is known for its ability to replicate structures such as microfluidic channels [144]. The mold master is made of a steel plate with holes in which Electro Discharge Machined pins are inserted. As illustrated, these pins have a conical shape of various diameters and angles. The NOA81 glue is exposed to UV light to achieve curing. Once it is done, it is released from the mold and an extra curing step is done on the backside, which received less dose due to UV absorption in the top of the layer. Holes are punched with Harris Uni-core punchers at the bottom of the chambers to allow the air to be pushed out during actuation (fig 5.45c). The rigid electrode is patterned by Au ion implantation using a Filtered Cathodic Vacuum Arc setup [36] (fig. 5.45d). The requirements on the rigid electrode are excellent adhesion on the sidewalls (not to be peeled off by the silicone membrane) and low stiction to the silicone membrane (eases the upward motion of the membrane when the voltage is switched off). Au ion implantation was found to perfectly fulfill these requirements, better than sputtering regarding electrode adhesion. The adhesion of the gold clusters in the first few 10 of nm of the cured NOA81 is even excellent, probably because it is based on thyols. Extension tracks of the rigid and compliant electrodes are then patterned with Au sputtering through shadow masks (figure 5.45e). This is mandatory to have electrical access to the electrodes from outside the air pressure chamber. As a last step, both the actuator membrane and the rigid silicone pressure chamber are glued using a thin layer of room-temperature vulcanizing silicone (Dow Corning RTV 734), to form the final device (fig 5.45f).
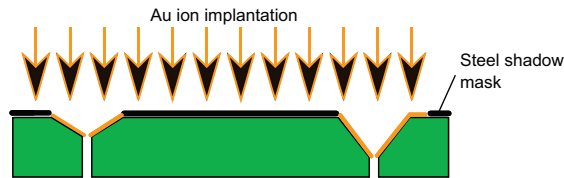
---

[8]https://www.norlandprod.com
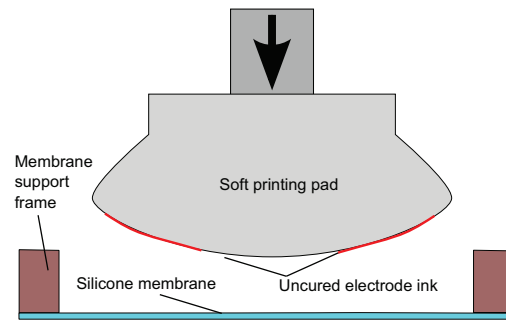
(a) Indirect stamping of compliant electrodes composed of carbon black - silicone ink on a prestretched membrane
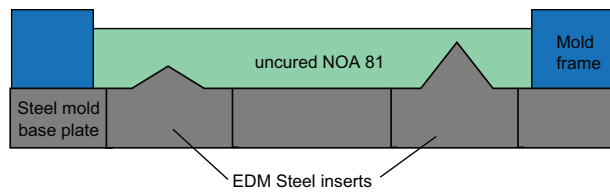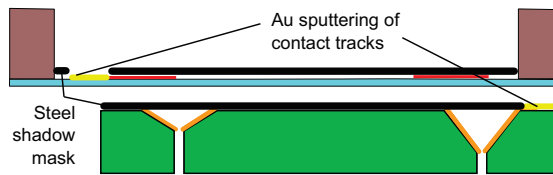

(b) Casting uncured NOA81 adhesive on a steel mask with conical Electro Discharge Machined inserts.
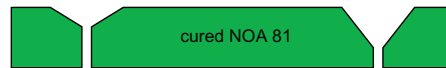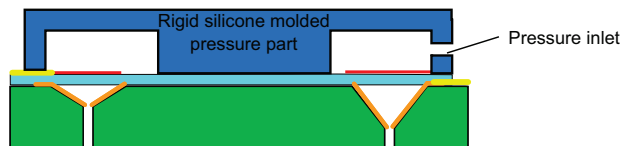

(c) Release of the UV-cured NOA81 body from the mold. Holes are punched at the bottom of the chambers

(d) The rigid electrode is patterned inside the conical chambers by Au ion implantation.

(e) Au sputtering through a shadow masks defines the conductive tracks that run to the sides of the membrane and of the zipping body.

(f) The active membrane is glued on top of the NOA81 zipping body, as well as a rigid silicone pressure chamber.

Figure 5.45: Fabrication process of the air pressure-loaded test zipping DEA.

Fluidically-coupled zipping DEA pump

The fabrication process of the fluidically-coupled zipping DEA peristaltic pump is illustrated on figure 5.46.

As a first step (not visible on the figure), an active and a passive membrane as well as a rigid silicone sheet with holes are activated with oxygen plasma. The active membrane (which is prestretched and has pad printed compliant electrodes) is then placed on a vacuum chuck that has three 1.5 mm holes in a rigid silicone (Dow Corning Sylgard 184) pad (fig. 5.46a). Based on the results of section 5.3, the Nusil CF19-2186 silicone is used as active membrane material. Vacuum is then applied, so that the membrane is pulled down inside the holes on the parts which are printed with electrodes (fig. 5.46b). The deflected cavities are then filled with a coupling liquid (Sylgard 184 pre-polymer, based on the results of section 4) using an automated dispenser (fig. 5.46c). Thanks to the use of the dispenser, a precise and repeatable volume of liquid is deposited in each hole. In the next step, the previously plasma activated rigid silicone coupling body and passive membrane are sequentially bonded on top of the active membrane (fig. 5.46d). The rigid coupling body is a bladecasted 0.2 mm thick Sylgard 184 sheet. Three fluidic coupling holes are punched with a 0.75 mm Harris Uni-Core puncher, which actually results in 800 μm diameter sizes. Three other holes are also punched in this sheet prior bonding to provide access to the compliant electrode contacts (only one of them is illustrated on the cross-section). Once the bonding is achieved, the vacuum is released and the trapped air leaks through the silicone membranes of the fluidically-coupled structure that has been fabricated. The next step consists in gluing it to a zipping body with conical cavities covered with a rigid electrode (fig. 5.46e). A thin silicone adhesive sheet is laser-cut and applied on a 3D-MID PCB from Cicor[9]. The PCB is made in plastic with three 1.5 mm diameter holes which are copper-plated on the inside, with a copper track running from the bottom of the hole to the side of the chip (section 5.5.3). Once glued on the PCB, the frame is cut apart from the device (fig. 5.46f). Separating the fluidically-coupled structure (silicone membranes and sheet which enclose the liquid) from the frame before gluing it would make it wrap on itself because of the prestretch applied in the membranes. Finally, the contact to the compliant electrode is done using silver varnish, and a fluidic channel can be bonded on top of the three coupled actuators to make a pump (fig. 5.46g).
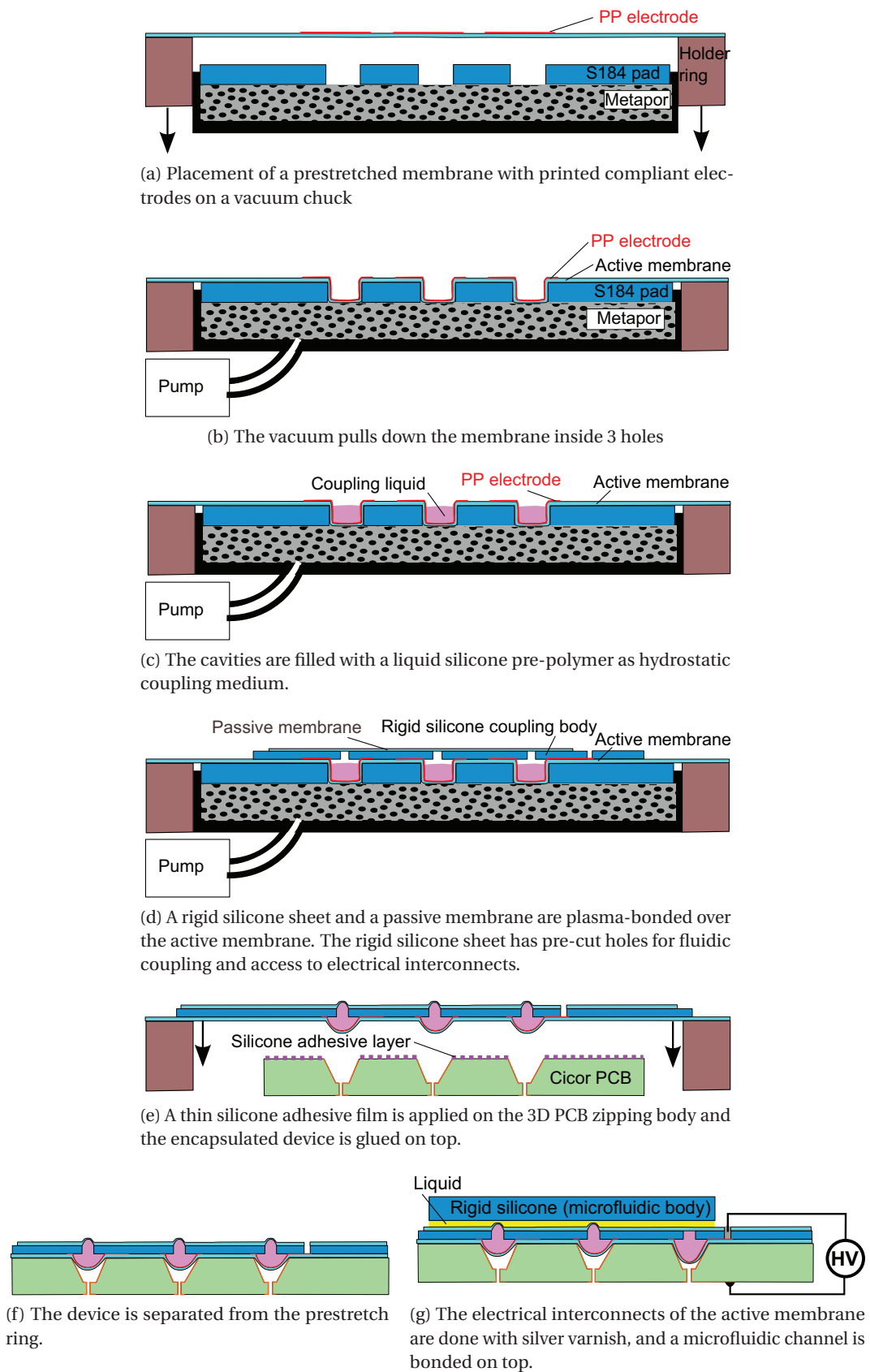
---

[9]http://www.cicor.com/3d-mid

(a) Placement of a prestretched membrane with printed compliant electrodes on a vacuum chuck

(b) The vacuum pulls down the membrane inside 3 holes

(c) The cavities are filled with a liquid silicone pre-polymer as hydrostatic coupling medium.

(d) A rigid silicone sheet and a passive membrane are plasma-bonded over the active membrane. The rigid silicone sheet has pre-cut holes for fluidic coupling and access to electrical interconnects.

(e) A thin silicone adhesive film is applied on the 3D PCB zipping body and the encapsulated device is glued on top.

(f) The device is separated from the prestretch ring.

(g) The electrical interconnects of the active membrane are done with silver varnish, and a microfluidic channel is bonded on top.

Figure 5.46: Fabrication process of the fluidically coupled zipping DEA peristaltic pump

5.7   Summary and conclusion

Zipping DEAs are a class of actuators which was never reported before, and they were studied both theoretically and experimentally. Two analytical models have been developed, and correspond to two zipping DEA structures, the electric field being either applied across the elastomer membrane or across a rigid dielectric. The models take as input a wide range of parameters (actuator geometry, sidewalls roughness, dielectric properties and membrane hyperelastic behavior), so that any configuration can be quickly evaluated. It uses the mechanical and electrostatic energy contributions to compute the stable point of the membrane, a method which is common in electrostatic actuation modeling. However, non-slipping conditions between the membrane and the cavity sidewalls must be assumed, which results in non-uniform thickness and stretch state along the zipped part of the membrane. The large deflection of the membrane also requires the implementation of the hyperelastic energy density function to correctly account for the mechanical behavior of elastomers. The most interesting feature predicted by the model is a bistable operation mode which is highly controllable, unlike the one that can be observed in some standard DEAs [33].

A peristaltic micropump composed of three in-line zipping DEAs and of a microfabricated silicon body was realized. The sloped sidewalls chambers were obtained by anisotropic etching of silicon, and the electric field is applied across the elastomer membrane. This is the first time that such a zipping DEA device was reported. The first set of actuators had a breakdown before reaching the bottom of the 525 μm deep chamber, so that the use of both softer silicones and more compliant electrodes was investigated. It can be concluded that softer silicones do not perform better because of their lower breakdown strength, but softer electrodes helped to reach 385 μm maximal deflection. More specifically, CF19-2186 was found to be the silicone which has the best performance. The limit in deflection is due to the large sidewalls angle of 54.7°, a sensitive parameter in the design of zipping DEAs. Pyramidal-shaped cavities also seem to be more sensitive to breakdown than axisymmetric ones would be, because breakdowns appear preferentially in the corners. Both of these limitations are linked to the difficulty to control the shape of low-sloped chambers in silicon, which is critical since most microfabrication techniques (such as Deep Reactive Ion Etching) have been design to etch vertical trenches.

The zipping chambers of the next generation of devices were milled in aluminium, and have 2.3 mm diameter with axisymmetric (conical) shape and lower sidewalls angles. With 15° and 22.5° sidewalls angle, the devices zip in a bistable manner down to the bottom of the chambers. The highly tunable bistable behavior is controllable by both chamber geometry and membrane parameters. The membrane dielectric model was experimentally validated, showing that the effect of sidewalls angle on the zipping voltage behaves as predicted by our model, although a systematic shift of the zipping voltage was observed on all samples. This shift is in the range of 1 kV for the devices prestretched to 1.23 and of 1.5 kV with a prestretch of 1.27, and is attributed to the bending energy which was not included in the model. These actuators could be used in a second pump design, which keeps the processed liquid free from

electric field.

However, the sensitive actuator membrane remains in contact with the liquid to be processed, which poses problems of actuator failure. A third variant was therefore explored, which couples the motion of a zipping DEA to a passive membrane using a carefully chosen compatible liquid (silicone pre-polymer). The coupling fluid of this design provides a bias pressure to the actuator, which could be expected to lower the zipping voltage by having a smaller angle between the membrane and the sidewalls. Prediction of the behavior of such a device is however very difficult analytically, so that test devices with an offset air pressure chamber were built to experimentally find the best design parameters of sidewalls angle, chamber diameter, operating pressure and prestretch. 1.5 mm diameter zipping DEAs coupled to 800 µm diameter passive membranes were built and measured statically and dynamically. The measured displaced volumes did however not reach the expectations based on the experimental design tests. The most likely explanation is that the electric field deforms the central suspended part of the membrane rather by pulling it sidewards than downwards, which results in a smaller displaced volume than assumed by measuring the zipped length on the experimental design tests.

Other outcomes of the work include the demonstration that Au ion-implanted electrodes can be successfully patterned on thyol-based microfluidic substrates. High conductivity and strong adhesion of the conductive layer are obtained while retaining retaining a high transparency level of the substrate.

5.8 Outlook: zipping DEAs as a new class of actuators offering unique characteristics

Zipping DEAs are a new type of DEA actuators which open new design spaces and could fit the needs of many applications. The deflected shape is very well controlled as it is given by the geometry of the chamber, which can be conventionally machined, molded or micromachined [103]. The voltage vs. displacement characteristic can be tuned to virtually any shape by changing the sidewalls profile. The bistable behavior observed on some conventional DEAs relies on the softening and then hyperelastic stiffening of the stress-strain characteristic of the elastomer materials [33]. If one wants to operate in bistable mode, a careful choice of the elastomer and operating conditions (such as pre-stretch or offset pressure) is necessary, and imposes strong design restrictions. In the case of zipping DEAs, the presence and/or threshold voltage of one or several bistable jump(s) can be chosen by playing not only with the elastomer and the prestretch state, but also with the chamber geometry. This opens the door to a fine tuning of bistable or multi-stable modes, for applications like braille displays or step-by-step positioning systems. By including specific features like embedded channels or holes in the chamber [103], one also benefits from the electrostatic pressure of the membrane on the sidewalls to hermetically seal these apertures, building for instance effective pumping and valving devices for integrated microfluidics or gas control. Variants of the measured

zipping DEA structure are also possible. Instead of being applied across the membrane, the electric field can also build up across a solid layer deposited on the rigid electrode or a stack of both [53–55]. Hybrid actuators including squeezing and zipping modes might also be of particular interest (fig. 2.3E). Important voltage reductions can be expected if the electric field is applied across a rigid dielectric. These devices would need a few μm-thick high quality rigid dielectric to be coated or grown on the rigid electrode, and the compliant electrode is patterned on the lower side of the membrane so that it comes in contact with the dielectric. If the enhancement of relative permittivity and foremost breakdown voltage would theoretically drastically lower the actuation voltage, it is practically difficult to fabricate a homogeneous and pinhole-free rigid dielectric. The well-established microfabrication technologies would be well suited to build such zipping DEA structures, but the critical point would then be the realization of the sloped chamber sidewalls, since most of the microfabrication processes are designed to yield vertical etching.

5.9   Outlook: zipping DEAs for microfluidic actuators

The replacement of the pneumatic valves of lab-on-chips by electrically-powered DEAs could not be demonstrated, but several routes could lead to such a development.

It has been shown that the operation of zipping DEA devices biased with a large offset pressure does not yield the needed displacements, and narrows the bistable operating range. Since the displacement versus voltage characteristic can be arbitrarily designed, a first series of improvements could be done by adjusting the shape of the zipping chamber, moving away from a conical shape to a design that precisely matches the pressure bias conditions. Practically, such devices can be realized by replica molding of electro discharge machined or 3D-printed bodies, in a similar way as test chips with air pressure bias were fabricated (section 5.6.3).

A second route which might be even more likely successful is to actuate the active membrane of the coupled design in the traditional "squeezing mode" of DEAs, with two compliant electrodes . As demonstrated by Loverich *et al.* on a 1.5 mm diameter actuator, this design can produce impressive pumping performance. High driving voltages would however still remain an issue.

An advantage of zipping DEAs was indeed the expected reduction of actuation voltages, which was not as impressive as expected for the case where the electric field is applied across the membrane. In terms of portability, high voltages sources are less than $1\,\mathrm{cm}^3$ in size, but a matrix of independently controlled actuator also needs a set of switches. SMD high voltage transistors can switch signals in the range of 600 V, up to 4.5 kV for larger ones but with higher power consumption [10]. Low driving voltages are desirable for portable designs of driving electronics, operation safety and compact integration (arcing between parts). As highlighted in the previous section, further developments of zipping DEAs with the electric field applied

---

[10]http://ixapps.ixys.com, part no. IXTA02N450HV

across rigid dielectrics such as parylene could reach this goal.

Regarding integration in a matrix of fluidically-coupled DEAs, the ideal target would be to have the active membrane of the same size as the passive one. The size of the active membrane indeed defines the minimum pitch between the actuators. Pneumatically actuated large-scale-integrated microfluidic chips do not face this integration issue, since the actuation power is not generated below each actuator but outside of the chip. On the realized fluidically-coupled device, the actuator size is roughly twice the one of the passive membrane. This integration constraint of DEA-powered large-scale-integrated microfluidic chips which makes its downscaling more challenging is however not an issue for numerous applications. For instance, point-of care detection of low concentration molecules need to process large (µL or above) sample volumes, such as for HIV viral load [145].

6 DEA-driven fuildically-coupled tunable lenses

Tunable lenses have raised extended interest of researchers and industry for their potential to reduce the cost and improve compactness of optical systems. The integration of the actuator required for embedded systems is however an issue because of the requirements on large displacements, fast response, electrical control and low power consumption. DEAs are one of the best options, not only because they perform well on all these points but also because they are built in an elastomer membrane similar to the one used for the lens of pressure-driven devices.

Section 6.1 (Introduction and state-of-the-art) introduces tunable lenses and presents a state-of-the art of the available technologies, commercial products and options for integrated actuators. The use of DEAs to drive membrane-based tunable lenses is motivated, and the specifications targeted in this work are listed.

The theoretical approach to predict the behavior of fluidically-coupled tunable lenses is presented in **section 6.2 (Models for the prediction of the steady state performance of fluidically-coupled EAP-driven tunable lenses)**. The critical point is to predict the pressure-volume characteristic of an inflated membrane, a complex problem due to the non-uniform deflection state of the membrane and the hyperelastic properties of elastomers. Three models have been developed throughout the project. The first one linearizes the pressure-volume characteristic of a linear material model developed in other works by a single constant value of hydraulic compliance. The second model extends the same linear material model to a large strain case and uses its full pressure-volume characteristic. The third and last model combines a well-known equation of thin pressure vessels and empirical fitting of experimental data of an inflated bubble to integrate the hyperelastic material parameters in the computation of the pressure-volume curve. The models are compared and discussed.

Section 6.3 (Experimental results and their discussion with the the models) presents two generations of fluidically-coupled tunable lenses and compares the static experimental results with models. The first generation was realized at the very beginning of the project and is composed of a single active and a passive (lens) membrane. The coupling fluid is an ionic

liquid, which is also used as liquid electrode. The second generation of devices was realized three years later, and is composed of eight actuators fluidically-coupled to a single 6.5 mm diameter lens. The lens body is made of rigid laser-cut PMMA plates and includes a feature of operating point adjustment. The agreement between analytical and experimental results are discussed for both generations of devices. The fabrication process of the second generation of devices has been optimized for optical performances, which are characterized experimentally by a Shack-Hartmann wavefront sensor setup.

The details of the fabrication process are given in **section 6.4 (Fabrication)**.

Finally, the results are summarized in **section 6.5 (Conclusions and outlooks)**.

Part of the content of sections 6.2 and 6.3 have been presented as a poster: L. Maffli, S. Rosset and H. R. Shea, Response time of tunable lenses driven by ion-implanted DEAP actuators,*EuroEAP conference 2011*, Pisa, Italy, 2011.

The hyperelastic material tunable lens model and the second generation of lenses will be submitted for publication.

6.1   Introduction and state-of-the-art

The vast majority of tunable optical systems translate solid, fixed focal length lenses along the optical axis in order to vary focus or zoom. Optical objectives hence enclose a large set of lenses and linear stages. Changing the focal length of a lens without moving it would result in multiple advantages: reduced number of components, hence gain in size and complexity, cost and integration possibilities, smaller displaced masses thus faster speeds, shock robustness, lower power consumption and even advanced features such as correction of optical aberrations.

Graham fabricated the first lens with variable focus in 1940 [146], deforming two thin glass slides enclosing a liquid, paving the way for optical systems where properties can be adapted without moving the lenses. Many working principles for tunable lenses have been developed, including electrowetting of an oil droplet immersed in another fluid (fig. 6.1 a) [147], pressure-driven deformation of soft membranes [148, 149], tuning of refractive indexes with liquid crystals [150] (fig. 6.1 b) [1], or optofluidic chips that shape laminar flows of fluids with different refractive indexes (fig. 6.1 c) [151], among others. The markets ready to be conquered by this technology are huge, mostly in the field of miniaturized systems and embedded electronics where low-cost, compact and robust optics are needed (e.g. optical media players, mobile phone cameras, surgical endoscopes, barcode readers, security cameras, etc.) [152]. Novel features such as Zernike modes correction [153] or image stabilization[2] are also targeted by these adaptive lenses.

A major class of tunable focal length devices are based on encapsulating an optical liquid

---

[1]www.lensvector.com

[2]www.varioptic.com
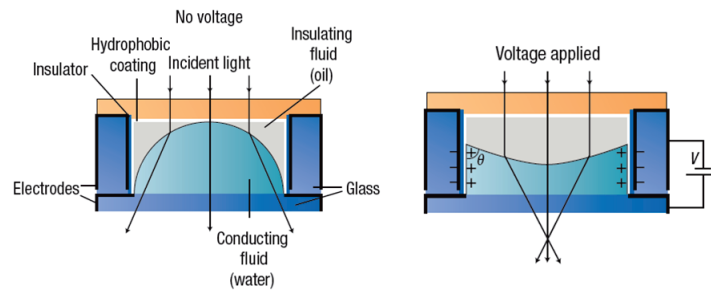
(a) Change of focal length by electrowetting of an oil droplet (reprinted from [152])
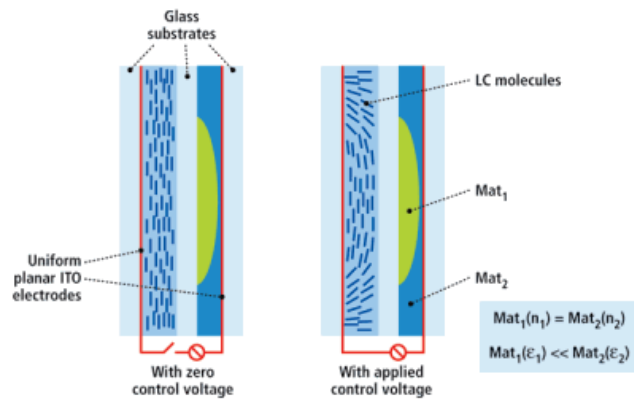
(b) Changing orientation of liquid crystals with electric field. The shape of the electric field is created by a different permittivity in a transparent rigid layer (www.lensvector.com)
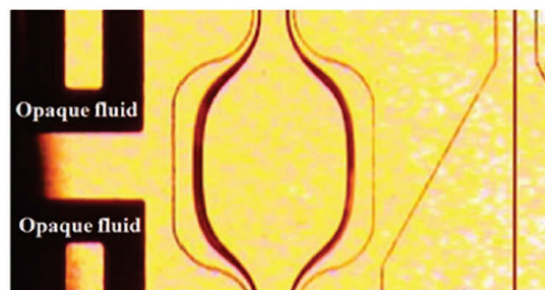
(c) Optofluidics: the lens is formed by a laminar flow between liquids of different refractive indexes (reprinted from [151])

Figure 6.1: Examples of technologies for making tunable lenses

between flexible transparent membranes, most of the time silicones [121, 148]. Indeed, silicone elastomers have good optical properties, can be easily casted in fluidic bodies or thin membranes, can be efficiently bonded by oxygen plasma activation, have large temperature operating ranges and are tear-resistant. Some groups have also built solid-body silicone deforming lenses [154]. The absence of liquid implies larger forces to deform the lens, but they have some advantages in terms of reliability or immunity to gravitational sag.

Thanks to the flexibility of the membranes, very large focal length tuning ranges can be obtained, such as from $400\,\mu m$ to infinity [121], or even changing shape from convex to concave [120]. However, the large tunable range of such lenses relies most of the time on external actuation means (pumps, etc.): compact integration is very challenging. Electromagnetic actuation often requires external driving coils [155] or magnets if a coil is integrated [156]. Although power-consuming, integrated thermal actuation is able to provide the needed mechanical work to achieve large tuning ranges. Its main drawbacks is a high power consumption and a slow response, time constants in the order of fractions of a second being among the best achievable performance [123]. The response time of thermal systems scales down with the size of the devices, making them more suitable for microlenses.

The ideal integrated actuation mechanism of membrane-based tunable lenses is electrically-controlled and has a large work output that produces rather large displacement than pressure, so that no motion amplifier mechanism is needed. For instance, a high pressure piezoelectric actuator cannot be used directly to provide the volume stroke needed to tune an inflatable membrane [157]. High power is also desirable so that the device responds fast. Electromagnetic actuation such as for Optotune's lenses provides the required specifications, but need large electrical power to supply constantly a current in the actuator (1 Watt), which is problematic for embedded applications [3]. In addition to the high power consumption, downscaling degrades the performance of electromagnetic actuators and poses complex fabrication problems (coils, ...). Looking at these ideals requirements for integrated actuation mechanisms of membrane-based tunable lenses, it becomes straightforward that Dielectric Elastomer Actuators (DEAs) are among the best suited if not the best solution. Moreover, their active component is precisely a dielectric elastomer membrane, so that it can be combined with the lens membrane [21, 158, 159] (fig. 6.2).

6.1.1 Specifications targeted by the developed fluidically-coupled DEA-powered tunable lenses

Regarding size, tunable lenses of several cm diameter such as in large camera objectives are still difficult to realize by the current technologies. But a few mm in diameter or smaller tunable lenses have been manufactured by plethora of research groups and technologies and are getting mature for the market. Regarding optical quality, fixed focal length lenses still overcome tunable ones, but there exist many application which do not require top imaging quality (lighting systems and embedded low-cost cameras to name only a few). The use of tunable lenses for mobile applications is seen as one area which could drastically benefit from more compact optical systems, if the lens quality meets a sufficient level and the power consumption is kept low. This is demonstrated by the area of activity of the companies mentioned in the previous section.

The two fluidically-coupled tunable lenses generations that are studied theoretically and

---

[3]www.optotune.com

(a) DEA-controlled fluidically-coupled tunable
lens (reprinted from [158]).

(b) DEA-controlled tunable lens driven by a change in encapsulated liquid pocket shape (reprinted from [21]).
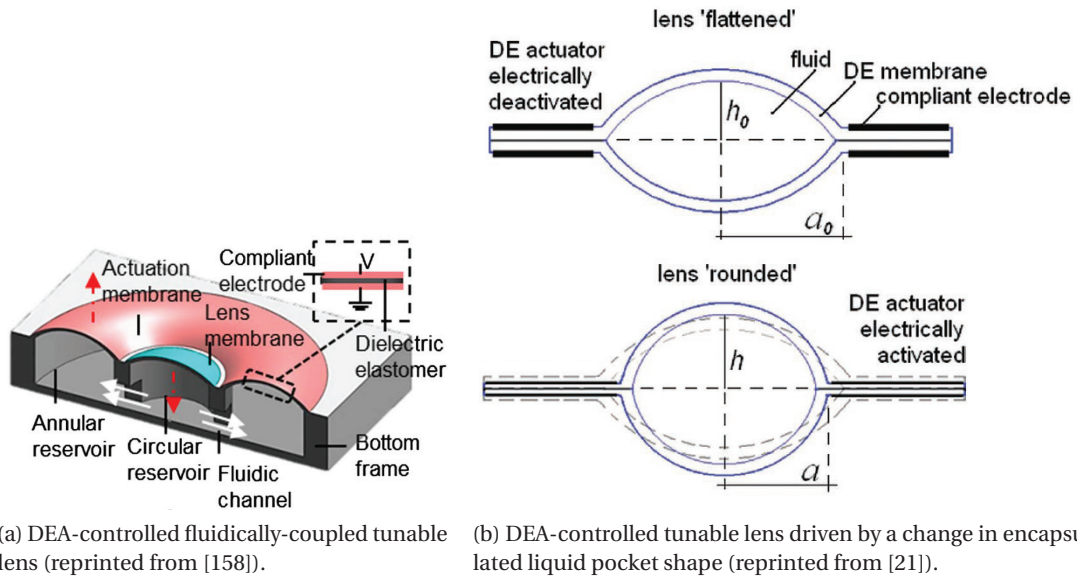
Figure 6.2: DEA-controlled tunable lenses with the actuator integrated in the same membrane as the lens.

experimentally in this chapter follow this trend, by having diameters of a few mm and focal lengths of a few 10's of mm. Another type of tunable lenses which achieved the best dynamic performance to date will be presented in section 7. In the first generation of devices of this chapter, a novel way of integrating the DEA using a liquid electrode is demonstrated and response times in the order of 1.4 s are measured. The second generation of devices drastically improves many features of the first generation, in particular the tunable range and the optical properties.

6.2 Models for the prediction of the steady state performance of fluidically-coupled EAP-driven tunable lenses

Two generations of tunable lenses were built, based on the hydrostatic coupling between a single or several active (DEA) and one passive membrane that acts as a lens. Their basic working principle and structure is described on figure 6.3. When a voltage is applied across the DEA membrane, it contracts in thickness and expands in area, and therefore moves up. As the volume of the coupling liquid is constant, this motion is transferred to the single passive lens membrane, which moves down. The pressure of the liquid P is equal everywhere in the device and sum of the actuator(s) and lens volume is constant. By putting N active membranes in parallel instead of a single one, the total actuated volume increases by the same factor and more focal length tuning range can be achieved on the lens.

The critical point of an analytical model which describes the steady state performance of
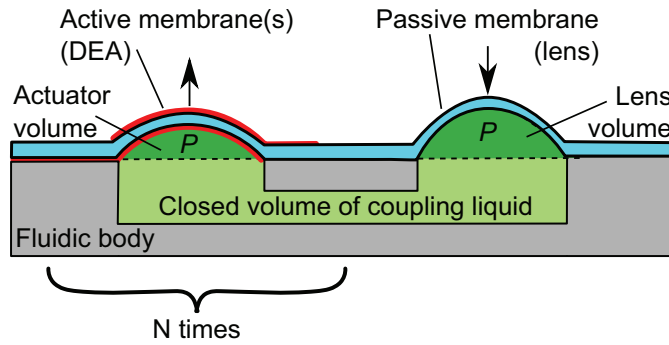
Figure 6.3: Basic structure and working principle of the studied fluidically-coupled tunable lenses. As the DEA(s) is actuated, it moves up and the passive (lens) membrane moves down, increasing its radius of curvature and focal length. The pressure P is equal everywhere and the sum of the actuator(s) and lens volume is conserved.

such a device comes down to the determination of the pressure-volume characteristic of clamped circular elastomer membranes, without and with applied voltage. This is a very difficult problem, and several complex modeling approaches have been proposed [160, 161]. Indeed, the thickness varies over the inflated membrane, so does the stretch state. The stretch state in the top of the bubble is equibiaxial and decreases in an non-equibiaxial manner along the arc length.

Three models were developed. The first model is based on a linear material model developed by S. Rosset *et al.* [36] and on the assumption of a linear pressure versus volume characteristic on the considered range which allows using constant hydraulic compliances. The second one is based on the same set of linear materials equations improved for large strains, but uses the full pressure-volume characteristic. These two linear material models assume an homogeneous thickness over the whole membrane surface, as well as a spherical shape.

As linear material formulas fail at describing elastomers under large strain conditions such as when using prestretch or under large inflation, a third model that includes hyperelastic material parameters and an predicted equibiaxial stretch state at the top of the membrane was developed. The predicted stretch at the apex is derived from experimental data of an inflated bubble. Whereas the equations of this third model are based on observations at the bulge apex only, a spherical shape is assumed for the computation of the volume.

6.2.1 Model 1: Simplification of the linear material model of S. Rosset *et al.* by a constant value of hydraulic compliance

The modeling of microfluidic circuits commonly uses the concept of hydraulic compliance, which corresponds to a change of volume Vol versus pressure P [162].

$$C_h = \frac{dVol}{dP} \tag{6.1}$$
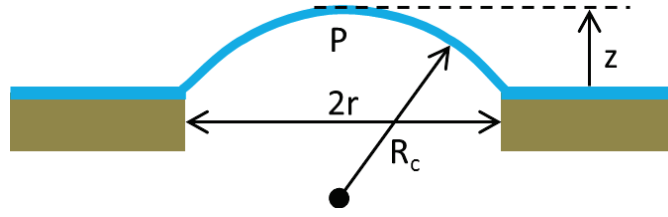
Figure 6.4: Inflated elastomer membrane

It reflects to the presence of compressible elements in the system, such as bubbles. For the case of a device which is rigid except for one active and one passive membrane, it represents their ability to change volume when submitted to a pressure difference between the liquid and the ambient air. An expression of the pressure-volume relationship of inflated membranes can be estimated with a linear material relation derived by Rosset *et al.* [36]:

$$P = \frac{8(1 - 0.24\nu)\,Y\,t_0}{3(1 - \nu)(r^2 + z^2)^2}z^3 + \frac{4\sigma_{0,fab}z\,t_0\,r^2}{(z^2 + r^2)^2}z - \frac{4\epsilon_0\epsilon_r\,V^2}{t_0\,r^2}z \tag{6.2}$$

where ν is the Poisson ratio, Y the Young's modulus, t_0 the initial membrane thickness, z the vertical deflection and r the cylindrical hole radius (figure 6.4). $\sigma_{0,fab}$ is an initial stress due to the membrane fabrication process. ϵ_0 and ϵ_r are the vacuum and relative permittivity of the elastomer. On this figure, R_c is the radius of curvature.

The volume of the spherical cap of an inflated bubble (dark green on fig. 6.3) is given by the following relation:

$$Vol = \frac{\pi}{6}z\left(3r^2 + z^2\right) \tag{6.3}$$

Alternatively, it can be expressed in function of the radius or curvature R_c:

$$Vol = \frac{\pi}{3}z^2\left(3R_c - z\right) \tag{6.4}$$

Using equations 6.2 and 6.3, one can plot the pressure-volume relationship of a pressurized spherical cap. If it is close to be linear in the considered range, it can be reduced to a single constant parameter: the compliance (eq. 6.1). The electrical circuit analogy of the compliance is the capacitance, so that the total compliance of a device that has one active and one passive membrane is computed like a combination of two series capacitances:

$$C_{h,tot} = \frac{C_{h,lens}C_{h,act}}{C_{h,lens} + C_{h,act}} \tag{6.5}$$

with $C_{h,lens}$ the passive membrane compliance, $C_{h,act}$ the active membrane compliance and $C_{h,tot}$ the total compliance. Under high inflation levels (close to a half sphere, as realized experimentally), it is assumed that the value of the compliance of the active membrane does not change with the voltage.

The difference in pressure induced by the actuation can be found in the last term of equation 6.2. From equation 6.1, it is found that the voltage-induced change in volume can be described by this change in pressure multiplied by the total compliance of equation 6.5:

$$\Delta Vol = \frac{4\epsilon_0\epsilon_r V^2}{t_0 r^2} z_0 \cdot C_{h,tot} \tag{6.6}$$

This is the volume pumped by the upward motion of the actuator, which is transferred to the lens membrane.

6.2.2 Model 2: Pressure-volume characteristic of the linear material model of S. Rosset *et al.* modified for large strains.

A more precise way to predict the steady state performance of tunable lenses directly uses the pressure-volume curves of inflated membranes, without linearizing it with a constant compliance value. A more accurate version of the linear material equation 6.2 is given in [30]:

$$P = \frac{4(1-0.24v)Y}{1-v} \cdot \frac{\left(\frac{z^2+r^2}{2zr}\arcsin\left(\frac{2rz}{z^2+r^2}\right)-1\right)zt_1 r^2}{(z^2+r^2)^2} + \frac{4\sigma_0 z t_1 r^2}{(z^2+r^2)^2} \tag{6.7}$$

In this equation, the engineering strain s_{eng} is represented by the following term

$$s_{eng} = \frac{\Delta L}{L_0} = \frac{z^2+r^2}{2zr}\arcsin\left(\frac{2rz}{z^2+r^2}\right)-1. \tag{6.8}$$

Where ΔL and L_0 are the deflection-induced change in arc length and initial arc length of the inflated bubble. The engineering strain significantly diverges from the true strain expression with strains larger than 10%, a value which is easily exceeded in our case. It is therefore replaced by the true strain expression

$$s_{true} = \ln(s_{eng}+1) \tag{6.9}$$

which finally gives an expression of the pressure of an inflated membrane at zero volt:

$$P_{0V,lin} = \frac{4(1-0.24v)Y}{1-v} \cdot \frac{\ln\left(\frac{z^2+r^2}{2zr}\arcsin\left(\frac{2rz}{z^2+r^2}\right)\right)zt_1 r^2}{(z^2+r^2)^2} + \frac{4\sigma_{0,lin} z t_1 r^2}{(z^2+r^2)^2} \tag{6.10}$$

$\sigma_{0,lin}$ is the in-plane stress in the non-deflected membrane due to the fabrication process and the prestretch. If some prestretch λ_p is applied, the fabrication process-induced stress (in the range of a few 10 of kPa) becomes negligible. The thickness before and after prestretch are t_0 and t_1 respectively. $\sigma_{0,lin}$ is expressed by the following equation, with the term $\frac{Y}{1-v}$ that represents the biaxial Young's modulus.

$$\sigma_{0,lin} = \frac{Y}{1-v}\left(\lambda_p - 1\right) + \sigma_{0,fab} \tag{6.11}$$

Upon application of a voltage (and keeping the deformation z constant), the pressure decreases. The pressure under application of a voltage is therefore expressed by the following relation:

$$P_{HV,lin} = P_{0V,lin} - \frac{4\epsilon_0\epsilon_r V^2}{t_1 r^2} z \tag{6.12}$$

Equations 6.10 and 6.12 combined with 6.3 yield the pressure-volume characteristics of the linear material model.

6.2.3 Model 3: Pressure-volume characteristic with hyperelastic material parameters and predicted equibiaxial stretch state at the bubble apex.

Linear material models such as the two previous ones diverge when the elastomer is subject to large stretches, which is the case when the inflated membranes gets closer to a half sphere or when a prestretch is applied in the membrane. Indeed, the stress-strain characteristic of elastomers is highly non-linear.

Prediction of the stretch state at the top of an inflated membrane and main model assumptions

An approach which uses hyperelastic model parameters and a prediction of the equibiaxial stretch state at the top of the inflated membrane is proposed. The real behavior of an inflated elastomer membrane is a very complex problem: the thickness is theoretically equal to its un-deflected value around the clamping aperture, and is minimal on the top. Both radial and tangential stretches are maximal on the apex and minimal on the clamp, where the tangential one actually remains constant (equal to the prestretch value). The only place which is in equibiaxial conditions is at the apex [160, 161, 163]. This model circumvents the problem by using a relation of thin-walled pressure vessels derived by Adkins and Rivlin in 1952 [160], in which one considers only what happens at the top of the inflated membrane. An empirical parameter is determined based on datapoints of curvature and stretch at the apex which allows predicting the stretch at that point thanks to the theoretical membrane area stretch. This is then used to compute the pressure of the membrane thanks to the thin-walled pressure vessel relation. The main assumptions of the model are an equibiaxial stretch and stress state on top in unactuated and actuated state, as well as the superposition of mechanical and electrical stresses at that point. A spherical shape assumption is used for the computation of the cap volume using the radius of curvature at the apex.

We built a setup to characterize the mechanical parameters of elastomer membranes in equibiaxial stretch state [63] based on Reuge *et al.*'s work [164]. The motivation behind it was that most material characterization are done with uniaxial loading, and the fitting of model coefficients on uniaxial data leads to substantial error when applied to a biaxial case. The

setup consists in measuring the stretch and curvature radius on the top of an inflated bubble, increasing gradually the pressure.

The critical point is now to predict the equibiaxial stretch λ^* that is at the top of the membrane. In a planar equibiaxially stretched DEA, the in-plane stretches λ_{planar} are linked to the area stretch $\lambda_{area,planar}$ by the exact relation

$$\lambda_{planar} = \sqrt{\lambda_{area,planar}} \tag{6.13}$$

The same approach is taken for the inflated bubble case, using an empirical parameter β to link the geometric area stretch of a bubble λ_{area} to the predicted equibiaxial stretch state at the apex λ^*. A_{defl} and A_{flat} are the deflected and flat areas of an inflated membrane.

$$\lambda_{area} = \frac{A_{defl}}{A_{flat}} = \frac{\left(r^2 + z^2\right)}{r^2} \tag{6.14}$$

$$\lambda^* = \sqrt{\lambda_{area} \cdot \beta} \tag{6.15}$$

The parameter β is fitted on data of curvature radius R_c versus stretch measured at the apex with our bubble inflation setup. The figure 6.5 displays the computed curves, in red without correction (i.e. $\beta = 1$), and in green with β fitted on the datapoints. The good correspondence of the data and the computed curve on the entire span by adjusting only the β parameter proves the suitability of this approach.
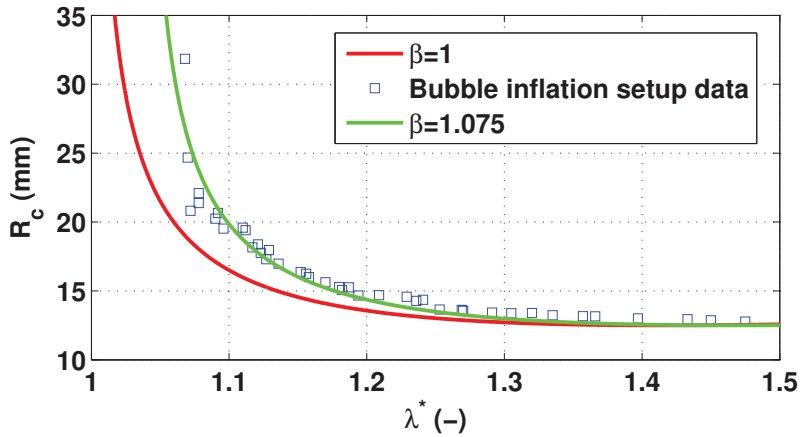
Figure 6.5: Determination of β factor to link the area stretch of the membrane to a predicted equibiaxial stretch at the apex λ^*. CF19 silicone, membrane diameter 25 mm, thickness 59.3 μm

Relation between pressure and stretch-stress state at the bubble apex

Now that a mean to predict the stretch state at the bubble apex for any deflection of the membrane has been found, the corresponding pressure must be computed. In the case considered, the flat membrane has a thickness t_1 and equibiaxial prestretch λ_p. The membrane thickness before prestretch is t_0.

The thin pressure vessel equation derived by Adkins and Rivlin links the pressure P with the sate of the membrane at its apex, given its full equibiaxial conditions (stress σ, curvature radius R_c and linear stretch λ^*) The initial (flat) membrane thickness without prestretch is t_0 [160, 164]:

$$\sigma = \frac{PR_c(\lambda^*)^2}{2t_0} \tag{6.16}$$

The hyperelastic mechanical stress σ_{mech} at the apex is computed using a polynomial fit on equibiaxial stress-stretch data directly taken from [63], which best fits the material behavior.

$$\sigma_{mech} = p_0 + p_1(\lambda_p\lambda^*) + p_2(\lambda_p\lambda^*)^2 + p_3(\lambda_p\lambda^*)^3 \tag{6.17}$$

More elaborate implementations of the effect of equibiaxial prestretch on the mechanical stress and stretch at the inflated membrane apex have been developed [165]. The approach adopted means that prestretch acts like shifting the mechanical operating point of the elastomer. The coefficients for the CF19 silicone are $p_0 = -4.87$, $p_1 = 9.76$, $p_2 = -6.57$, $p_3 = 1.67$, in MPa [63]. I take eq. 6.16 and obtain the mechanical pressure for the predicted stretch state at the apex at $0\,\mathrm{V}$:

$$P_{0V,hyp} = \frac{2t_0\sigma_{mech}}{R_c(\lambda_p\lambda^*)^2} \tag{6.18}$$

The index hyp stands for the third (hyperelastic) model. The electrical stress induced by a voltage V on a DEA of thickness t is well-known:

$$\sigma_{elec} = -\epsilon_0\epsilon_r\left(\frac{V}{t}\right)^2 = -\epsilon_0\epsilon_r\left(\frac{V(\lambda_p\lambda^*)^2}{t_0}\right)^2 \tag{6.19}$$

The superposition of mechanical and electrical stresses is a common way of treating such problems [163]. Assuming that an identical relation is valid for our two type of stresses, it yields the corresponding pressure with applied high voltage:

$$P_{HV,hyp} = \frac{2t_0(\sigma_{mech} + \sigma_{elec})}{R_c(\lambda_p\lambda^*)^2} \tag{6.20}$$

(a) Without prestretch

(b) Prestretch $\lambda_p = 1.3$. The clear divergence point of the linear model from the hyperelastic one is at a ratio of vertical deflection over radius $z/r \approx 0.7$
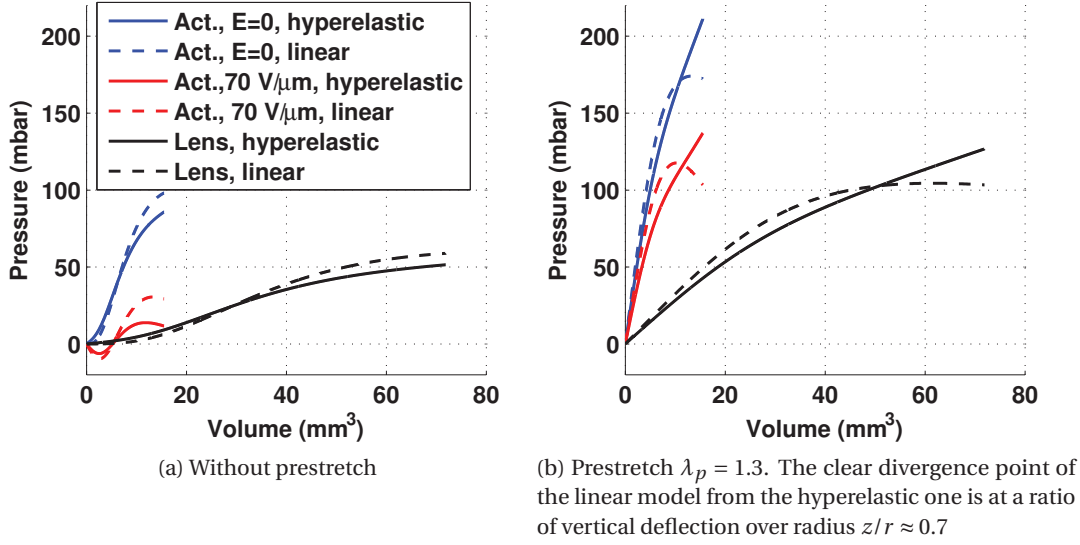
Figure 6.6: Pressure-volume curves of one actuator and of the lens inflated up to a half sphere shape with the hyperelastic and linear models. CF19 silicone, $t_1 = 31\,\mu m$, $r_{act} = 1.95\,mm$, $r_{lens} = 3.25\,mm$. Nominal electric field $70\,V\,\mu m^{-1}$. Legend applies for both graphs.

6.2.4 Comparison and discussion of the pressure-volume models of an inflated bubble

The obtained pressure-volume characteristics of one actuator with and without voltage as well as the lens are visible on figures 6.6a (without prestretch) and 6.6b (with prestretch) for the models 2 and 3 (sections 6.2.2 and 6.2.3). For the linear material case (model 2), a Young's modulus of $Y = 0.78$ MPa has been measured in [63] on the same dataset as for the polynomial expression of the stress used in the hyperelastic case (model 3, eq. 6.17). $\nu = 0.5$ is the Poisson ratio for incompressible materials. The first model (that uses constant hydraulic compliances, section 6.2.1) would correspond to a linearization of the $P(Vol)$ curves by a straight line.

As visible on figure 6.6a, the pressure of the actuated membrane has a negative dip, which reflects a bucking behavior not present when prestretching. On the same figure, one can see that both models have a comparable behavior, except with applied electric field where the linear model predicts less voltage-induced change of pressure. With the prestretching conditions of figure 6.6b, the linear model clearly underestimates the pressure after a ratio of vertical deflection over radius $z/r \approx 0.7$, an effect which becomes more important with increasing prestretch.

6.2.5 Computation of the focal length with and without applied voltage using pressure-volume characteristics of the actuators and of the lens

In a much more elaborate way than with constant compliances, the full pressure-volume characteristics of the lens and the actuator developed in the previous sections can be used to find the steady state change in focal length. Two basic assumptions must be set: the volume is conserved (i.e. the volume increase by the upward motion of the actuators will decrease the lens volume by the same amount) and the pressure is equal between each actuator and the lens. One also needs to measure the absolute deflection of the lens or of the actuator at 0 V to know the starting point of the device. On the second generation of tunable lenses, the starting inflation level can be varied experimentally as a parameter.

It is now considered that the coupled lens device has a set of N actuators which drive a single lens (figure 6.3). Using the previous results (similar to fig. 6.6b), the volume of a single actuator is simply multiplied by N for both actuator curves, which are now equal to $N \cdot Vol_{a,0V}$ and $N \cdot Vol_{a,HV}$ (fig. 6.7) where the indexes a, $0V$ and HV stand for actuators, at zero volt and at high voltage, respectively.

The initial pressure P_{start} inside the device is found by knowing the initial height of the lens (pink dashed line on fig. 6.7). The total volume Vol_{tot} is computed by summing the lens volume and the actuator volume:

$$Vol_{tot} = N \cdot Vol_{a,0V}(P_{start}) + Vol_l(P_{start}) \tag{6.21}$$

where the index l stands for the lens. On the figure 6.3, Vol_{tot} corresponds to the dark green volumes enclosed under the spherical caps.

Under application of an electric field across the $N = 8$ actuator membranes, their curve move towards more volume for the same pressure. The characteristic that must be taken into account now on the figure 6.7 for the actuators is the red one (with electric field). The pressure variable P is then gradually decreased on the graph from P_{start} (pink dashed line) to P_{stop} (green dashed line), until the sum of the volume of the lens and of the active actuators reaches the same value Vol_{tot} as at zero volt:

$$P_{start} \geq P \geq P_{stop} \tag{6.22}$$

$$Vol_{HV}(P_{start}) = N \cdot Vol_{a,0V}(P_{start}) + Vol_l(P_{start}) = Vol_{tot} \tag{6.23}$$

$$Vol_{HV}(P) = N \cdot Vol_{a,HV}(P) + Vol_l(P) \geq Vol_{tot} \tag{6.24}$$

$$Vol_{HV}(P_{stop}) = N \cdot Vol_{a,HV}(P_{stop}) + Vol_l(P_{stop}) = Vol_{tot} \tag{6.25}$$

This defines the final stable state of the lens, with its corresponding volume $Vol_{l,HV} = Vol_l(P_{stop})$.
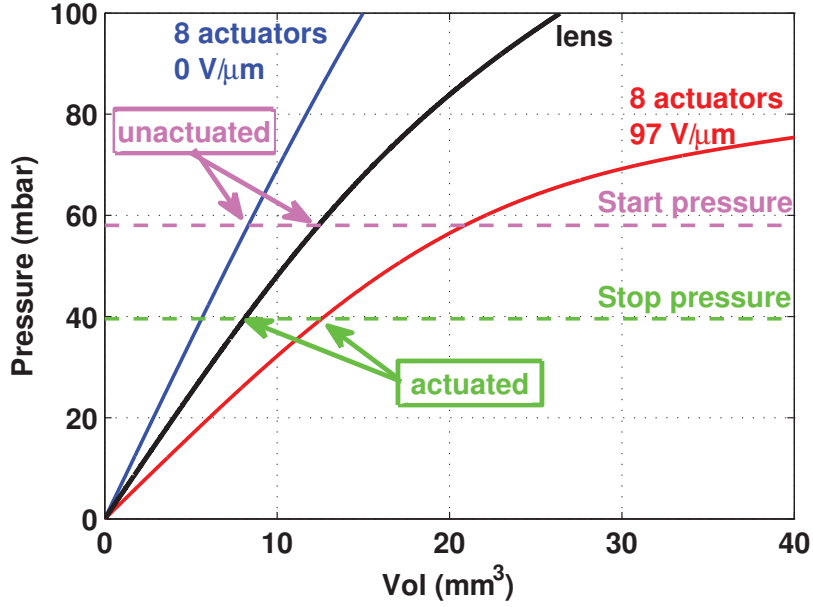
Figure 6.7: Pressure-volume curves of the lens and of 8 actuators at rest and activated using the hyperelastic model. The second generation of devices (section 6.3.2) features a tunable operating point, i.e. the start pressure can be chosen freely and adjusted after the device has been sealed. Such graphs are used to compute the stable unactivated and activated points. CF19 silicone, $t_1 = 31\,\mu m$, $\lambda_p = 1.26$, $r_{act} = 1.5\,mm$, $r_{lens} = 2.75\,mm$.

The vertical deflection of the lens z is found by solving the equation 6.3, with r the lens radius:

$$0 = z^3 \left(\frac{\pi}{6}\right) + z\left(\frac{\pi r^2}{2}\right) - Vol_{l,HV} \tag{6.26}$$

$$z = \frac{\left(\left(\pi^2 r^6 + 9Vol_{l,HV}^2\right)^{1/2} + 3Vol_{l,HV}\right)^{1/3}}{\pi^{1/3}} - \frac{\pi^{1/3} r^2}{\left(\left(\pi^2 r^6 + 9Vol_{l,HV}^2\right)^{1/2} + 3Vol_{l,HV}\right)^{1/3}} \tag{6.27}$$

The radius of curvature is found using the following relation valid for a spherical cap:

$$R_c = \frac{r^2 + z^2}{2z} \tag{6.28}$$

The focal length f in function of the voltage is finally computed using the plano-convex lens

formula:

$$\frac{1}{f} = (n-1)\frac{1}{R_c} \tag{6.29}$$

where n is the refractive index of the coupling liquid and R_c is a function of the applied voltage.

6.3 Experimental results and their discussion with the models

6.3.1 Generation 1: Single-actuator tunable lens with liquid electrode

During the early phase of the project, a set of tunable lenses with a single active (DEA) and a passive (lens) membrane coupled by a liquid were built. The fluid is conductive so that it can be used as the bottom electrode, and the top electrode is ion-implanted on top.

For this proof-of-concept device, no particular attention was paid to optimizing the optical properties of the devices (focal length or optical aberrations) but more on the possibility to use this new actuator structure with liquid electrode and to have an estimation of the response time of actuators coupled to fluids. It was studied with the model 1 (using fluidic compliances) to predict the static displacement of the membranes.

Single actuator tunable lens device with liquid electrode

The device is a full-silicone fluidic body (Dow Corning Sylgard 184) that encloses a buried channel with, at both ends, 3 mm diameter cylindrical openings reaching the surface (figs. 6.8 and 6.9). An un-prestretched membrane seals both holes, forming the actuator and the tunable lens. The outer electrode of the actuator is patterned by Au ion implantation [36], and the inner electrode is a conductive liquid. The use of liquid electrodes is not common for DEAs. Some researchers have used encapsulated liquid metal [166], ionic liquids in gels [94] or encapsulated pockets of carbon grease [135]. The ionic liquid bis(trifluoromethylsulfonyl)imide (TF_2N) from iolitec[4] was chosen for its optical transparency, compatibility with silicones and because it does not evaporate (sect. 4). Its high conductivity ensures that the time response is mechanically-dominated. The ionic liquid is contacted with a copper wire embedded in the channel sidewalls during crosslinking. The dimensions of the measured devices are given in table 6.1. The fabrication process is described with more details in section 6.4.1.

Table 6.1: Dimensions of the devices

Device	Lens and act. in-plane diam. (mm)	Thickness (μm)	Initial act. deflection z_0 (μm)	Channel dim. w/l/t (mm)
1	3	61	704	2.61/14.1/0.62
2	3	58	410	2.73/14.3/0.64

---

[4]www.iolitec.de
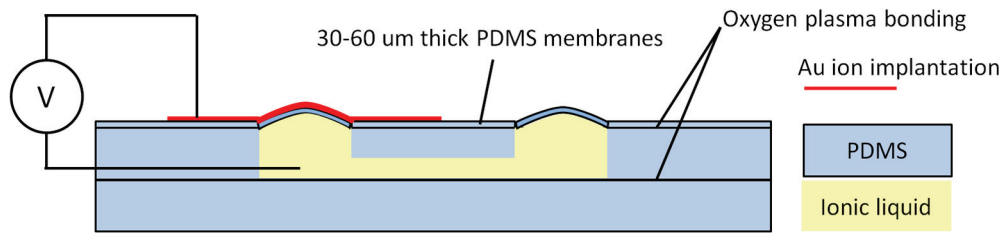
Figure 6.8: Cross-section of the tunable lens with liquid counter electrode.
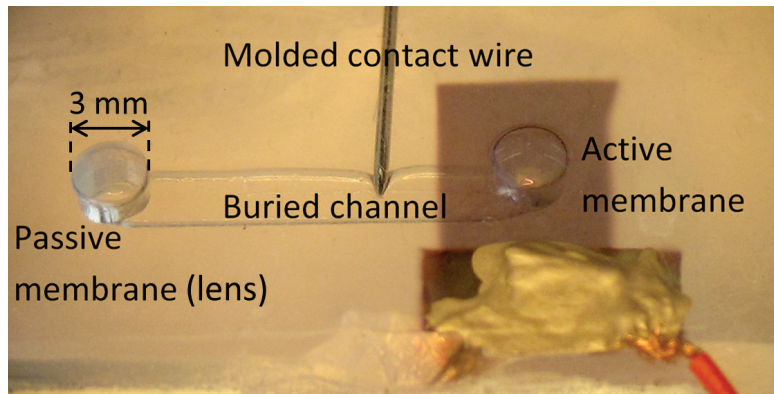
Figure 6.9: Fabricated tunable lens with liquid counter electrode. The liquid has been removed so that the channel becomes visible.

The same membrane was bonded on top of both holes, and is made of Sylgard 186 from Dow Corning (24 Shore A hardness). The membranes were bladecasted directly on a thin polyimide (PI) substrate without sacrificial layer. As a result, both membranes suspended over the cylindrical holes experienced a large anisotropic stretch as the PI film was peeled off, which results in large optical aberrations. This was solved in the second generation of fluidically coupled tunable lenses by improving the membrane fabrication process.

The DEA operates in its basic actuation mode. The area expansion of a membrane suspended over a hole results in upward motion, which sucks the ionic liquid up. The liquid acts not only as electrode, but also as mechanical coupling medium, so that the actuation is transferred to the passive (lens) membrane. As it moves down, its radius of curvature as well as focal length increases.

The advantage of using a liquid electrode are multiple. First, it obviously creates less stiffening than having one electrode on each side, hence more deflection for the same voltage. The second one is related to the fabrication process. Indeed, the actuator membrane needs to hermetically close the circular openings of the device. The best way to achieve a mechanically-resistant and hermetic bonding when working with silicones is by using oxygen plasma activation. However, the bottom of the membrane has to be covered with an electrode contacted by a conductive track that runs on the membrane surface. As hermetic plasma bonding is only possible on pristine silicone, this would create a leak. By using a conductive liquid electrode,

there is no need of patterning the backside electrode, and the problem of the electrical contact is shifted to any accessible point of the liquid. Inserting a wire in the silicone channel sidewalls during its polymerization easily provides a reliable and hermetic electrical connection.

Computation of the compliances

On this early study of fluidically-coupled based lenses, the model 1 (with the constant compliances, section 6.2.1) was used. The parameters which have been used for the computation of the compliances are listed in table 6.2

Table 6.2: Young's modulus Y, pre-stress σ_0 and compliances C_h of the devices 1 and 2.

	Y (MPa)	σ_0 (kPa)	C_h (m^{4}s^{2}kg^{-1})	$C_{h,tot}$ (m^{4}s^{2}kg^{-1})
lens	1.83	38.4	2.38×10^{-14}	1.02×10^{-14}
act.	2.42	50.1	1.79×10^{-14}	

The value of the lens and actuator compliances has been computed using Y and σ_0 measured with a bulge test setup described in [30] (table 6.2). Both devices are made using the same membrane.

Steady state vertical motion

A UBM profilometer was used to record the steady state profile (initial deflection) and the time-dependent displacement of the top of the active membrane. It consists in a laser beam which passes through a scanning lens similar to a CD player, finds the best focus on a surface and delivers the vertical displacement information with 0.01 µm accuracy.

Experimental results are shown together with the model 1 (equation 6.6 from which the voltage-induced deflection Δz is derived) on the figure 6.10. The initial deflections z_0 of the actuators of devices 1 and 2 are of 704 µm and 410 µm respectively (table 6.1). The corresponding changes in focal length are small, in the order of -2.5 % maximum for the device 2 at 3.25 kV. The tuning range in the next generation of devices was improved by adding more actuators for a single lens, using different actuator and lens diameters, softer active membranes and by adjusting the starting focal length.

The overall agreement between the model and the data is good. The model slightly underestimates the voltage-induced deflection.

Step response

The vertical displacement of the actuator as a function of time was measured under application of a voltage step. A function generator was connected to a Trek 609-E high voltage amplifier. The figure 6.11 displays the rising and falling edges of the displacement. The average 0 to 90%
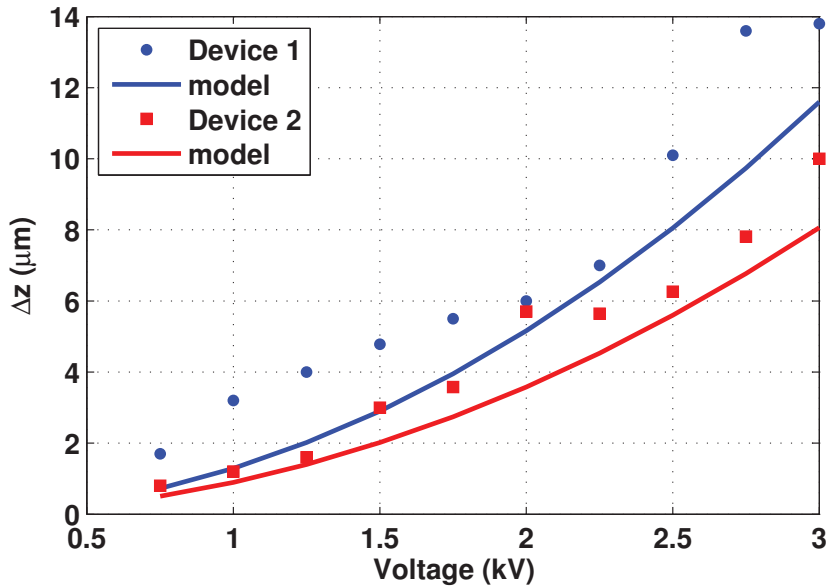
Figure 6.10: Actuation-induced change in vertical deflection of the active membrane, experimental data and model 1 (based on hydraulic compliances)

response time is 1.38 s, except for 1 kV where it lays around 2.94 s.

Discussion of the experimental results and their agreement with the model 1

Although the agreement between the measured and modeled static displacement is very good, the expression of the compliance is subject to discussion. Indeed, the model does not take in account the material hyperelasticity nor the Mullins effect [76]. When stretching elastomers, the polymer becomes permanently softer and its stress-strain curve more non-linear [63]. As a consequence, the value of the compliance as well as the assumption that it is constant are questionable, moreover because the membranes have been subject to much higher stresses than the value at which they work. With this design, the chamber is filled at once and then hermetically sealed, so that the excess volume to push the air bubbles needs to be sufficiently large to make sure that all the air can leak out, hence drastically overstretching the membranes. The next design will include the possibility to control the offset volume gradually once the device is already sealed.

However, the material parameters Y and σ_0 have been obtained on a bulge test setup which measures the bulge height after it has been inflated once so that they reflect a membrane softening, but not as large as the one applied to push the air out on the device. A more accurate model using fluidic compliances would also need to be validated in the dynamic responses with fluidic resistances and impedances.

The time response of the device is relatively slow, in the range of what can be achieved with
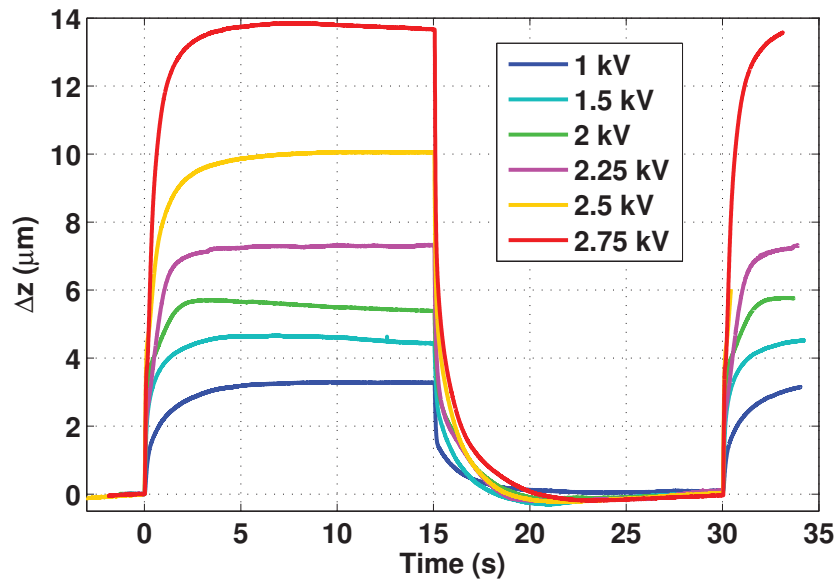
Figure 6.11: Step response of the actuator vertical displacement, device 1. The average 0 to 90% response is 1.38 s for voltages between 1.5 and 2.75 kV.

thermal actuation. No particular attention was paid on optimizing the fluidic circuit (channel dimensions), so that a similar process with optimized design could certainly improve it by one order of magnitude. The use of prestretch, which stiffens the elastomer membrane and increases its resonance frequency, would also be a way to enhance the time response.

6.3.2 Generation 2: Multi-actuator tunable lens with printed electrodes and variable operating point

Three years after the first generation of tunable lenses described in the previous section, a completely new design of fluidically-coupled tunable lenses was proposed. It solves the major weaknesses of the first generation of lenses. First, regarding optical quality, which is directly linked to the amount of overstretching and anisotropic stretch experienced by the lens membrane. Both of these issues were solved by using a membrane fabrication process with a water-soluble sacrificial layer and a way to gradually increase the pressure inside the device after it has been sealed. Secondly, the small tuning range of the device is addressed by using multiple active membrane of different diameters than the lens. Finally, a completely redesigned fabrication process ensures compact size, immunity to bending, tunable operating point and integrated electrical interconnects to a PCB.

Multi-actuator tunable lens device with enhanced optical properties and tunable operating point

The tunable lens device with patterned electrodes has an all-PMMA fluidic body (fig. 6.12). Compared to the first device with liquid electrode (sect. 6.3.1), it possesses the feature of controllable offset pressure. This has two major advantages. The first one is that the focal length at 0 V can be adjusted, changing simultaneously the initial deflection of the actuator. This latter parameter is important since the focal length span strongly depends on the initial pressure. Secondly, having a way to tune the pressure of the device after the fluidic chamber has been closed provides a precise control on the overpressure one needs to apply to push the trapped air bubbles out through the silicone membranes. This is intended to avoid any excessive stretch on the lens membrane, which may degrade its optical performance because of local softening with the Mullins effect [76], as will be discussed later (sect. 6.3.3). The pressure control is achieved by pressing teflon beads on suspended membranes with a removable plate (figs. 6.12 and 6.13). Changing the number and size of the beads provides a precise control on the operating point of the device.

The lens is formed in the same membrane like the actuators, and deflates under their pumping action by the coupling vessels principle, which increases its focal length. Compared to the first tunable lens with coupling chambers (sect. 6.3.1), both electrodes are made of carbon dispersed in a soft elastomer matrix, which have a negligible stiffening impact. Less electrode stiffening is produced by having two soft polymer-based electrodes rather than a single ion-implanted one and a liquid one. The sealing of the bottom electrode track by plasma bonding was one of the issues solved on the first generation of the lenses by using a liquid electrode. For the new design, the fluidic body is composed of laser-cut PMMA pieces on which oxygen plasma bonding is not possible, hence the use of a silicone adhesive sheet which simultaneously solves the problem of hermetic sealing of the electrode track. It therefore turns out to be better to use an electrically-insulating liquid (Sylgard 184 pre-polymer, see results of section 4) which offers more safety regarding the risk of electrical shocks in case of device damage or breakdown. Based on the previous results of actuation performance comparing different silicones (section 5.3), the CF19-2186 is chosen as membrane material.

The figure 6.13 shows a photograph of the device. The electrodes of the 8 actuators are visible in black, and are all connected to the same potential. Thanks to the rigidity of the PMMA fluidic body, the device is immune to the change of performance that would be induced by bending or squeezing a silicone body. Two PMMA laser-cut pressure parts are fixed with screws and press teflon beads on passive membranes to tune the operating point of the device. Contact between the compliant electrodes and the PCB are achieved by filling holes pre-cut in the PMMA plates with silver varnish.
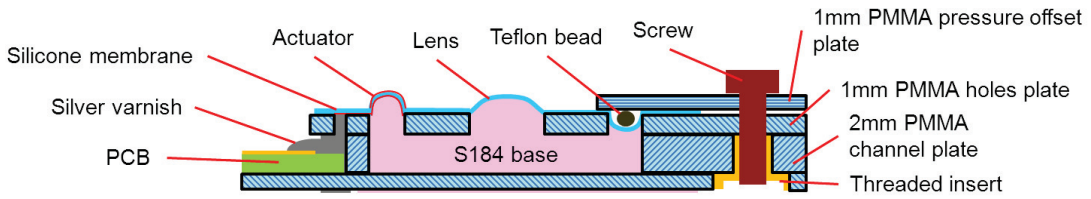
Figure 6.12: Schematic cross-section of the tunable lens with offset pressure adjustment
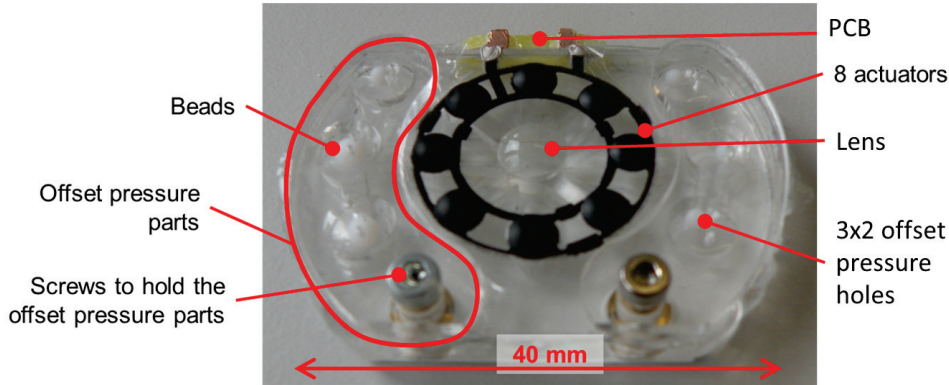
Figure 6.13: Fabricated tunable lens with 8 actuators and 6 offset pressure holes

Experimental results of the steady state focal length change and discussion of the agreement with the model 3

The focal length versus applied voltage was measured for two different devices, varying the initial focal length by changing the size and numbers of the beads that provide the offset pressure. The data are plotted together with the model on figures 6.14 and 6.15. The starting point of the model curves (i.e. the initial lens deflection) was adjusted to the focal length at 0 V. The thicknesses, prestretch and inflated membrane diameters have been measured. Table 6.3 shows the parameters of the two devices which have been characterized, and the relative permittivity is $\epsilon_r = 2.5$ [87].

Table 6.3: Measured dimensions of the devices

Device	Lens in-plane diam. (mm)	Actuator in-plane diam. (mm)	Prestretch	Thickness (µm)
1	6.5	3.9	1.26	31
2	6.5	3.9	1.30	30

Table 6.4 details the focal length at 0 V, at 3 kV and its relative change for the two devices at their two inflation levels. A maximal change of 60 % of the initial focal length was reached, from 28.5 to 45.5 mm. The maximal nominal electric field applied was $97\,\mathrm{V\,µm^{-1}}$, close to the breakdown. One can therefore consider that the maximal focal length has been reached in all cases.
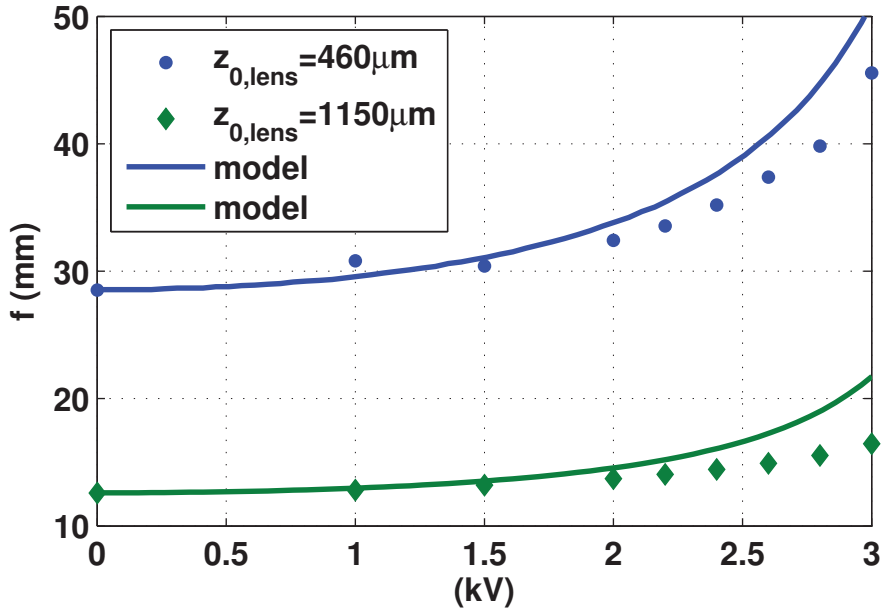
Figure 6.14: Predicted and measured focal length versus voltage for device 1 using the model 3 (hyperelastic).

Table 6.4: Focal length tuning range

Device	f_{0V} (mm)	f_{3kV} (mm)	relative change (%)
1	12.6	16.5	31
	28.5	45.5	60
2	15.0	18.8	25
	30.3	41.7	37

On all curves, the model slightly underestimates the driving voltage to achieve a given deflection. The difference is more pronounced at higher voltages. This might basically be due to an overestimation of the electrical stress, an underestimation of the pressure of the actuators or an overestimation of the pressure of the lens. The compliance of the pressure offset membranes may also absorb part of the volume stroke produced by the actuators, although an additional membrane has been bonded on top of them and that they are kept under tension with the beads.

It was assumed that up to a half sphere shape, the volume of the lens cap can be approximated by a sphere that has a radius of curvature equal to the one at its apex. Reuge *et al.* conducted thickness measurements on natural rubber membranes to validate the spherical shape assumption, and observed significant deviations of relative thicknesses between theory and assumptions, close to a factor 2 at a half sphere shape [164]. This speaks in favor of a non-ideal spherical shape. However, their ratio between membrane diameter and thickness of their setup is low (60 mm diameter and 2 mm thickness, 4.3 times lower than for the stud-
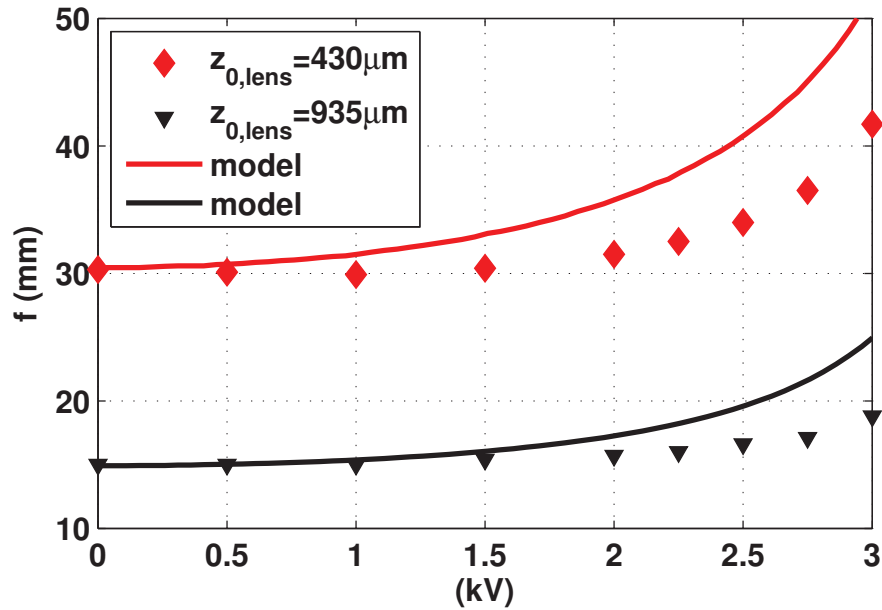
Figure 6.15: Predicted and measured focal length versus voltage for device 2 using the model 3 (hyperelastic).

ied actuators) which increases non-linearities. Vaughan specifically computed the effect of prestretch on the inflated membrane shape: it slightly flattens the profile [165], prestretching might therefore also weaken the spherical shape assumption.

Further work should include a direct experimental validation of the pressure-volume data of inflated membranes using bubble profiles extracted from the experimental setup [63]. Because the β factor of the model has been fitted on a large diameter to thickness ratio membrane (fig. 6.5, 25 mm diameter and 59 µm thickness, 3.2 times higher than the actuators), it is possible that non-linear effects which result in non-spherical shape would be more present on the tunable lens device than assumed by the model.

6.3.3 Optical characterization of the 2nd generation tunable lens device

Care was taken in the design of the second generation of tunable lens devices to have good optical properties. An ideal lens is a portion of a sphere, and working with shape-changing materials may rend this point critical. Geometrical aberrations are commonly described using Zernike polynomials, by fitting a measured wavefront and comparing it with an ideal one. This set of equations are widely used in optics. Thanks to their orthogonality on the unity circle, each polynomial describes a specific aberration type.

A first source of aberrations may specifically be present on lenses whose focal length is tuned by changing the in-plane diameter rather than the pressure of a clamped membrane, such as the design of Carpi *et al.* (fig. 6.2b) [21] which was adopted for high-speed lenses in the

last part of this work (section 7). Indeed, small actuation inhomogeneities of the active part of the membrane are directly coupled to the lens and results in non-circular in-plane shape. Important deviations from a sphere are therefore expected with such a design. With the fluidically-coupled tunable lenses, the lens membrane is clamped on a rigid hole, hence decoupled from the inhomogeneities of the actuator because controlled only by the liquid pressure.

Another very important source of aberrations is linked to the Mullins effect [76]. Care must be taken to avoid both anisotropic and excessive stretches in the membrane which will serve as lens, first during the membrane fabrication but also during the assembly. On the contrary to the first generation of lenses, a membrane production process with a water-soluble sacrificial layer was used (section 3.2), so as to avoid any anisotropic stretch during the release. The use of offset pressure holes on the device allows the lens membrane to remain stress-free during the filling step: the excess pressure needed to push the air bubble out is then gently controlled by a gradual offset pressure increase once the device is sealed.

The characterization of the optical aberrations was conducted at the Hans Zappe lab of the IMTEK, Freiburg, Germany. A powerful automated Schack-Hartmann setup was used to acquire the wavefront of the light focused by the device 1 (table 6.3) and to fit it with Zernike polynomials. As a general rule, a Shack-Hartmann wavefront sensor setup is less sensitive to possible local defects (such as trapped dust particles) compared to methods with a higher spatial resolution, such as setups using a high resolution CCD (surface profiler, interferometry). In this case, the pitch between the microlens of the array is of $300\,\mu m$, and the polynomials have been fitted on around 615 datapoints, with a 2 mm aperture.

Generally speaking, for such membrane-based lenses, Zernike coefficients below $0.1\,\mu m$ can be considered as good. Fuh *et al.* fitted zernike coefficients on their pressure-inflated tunable lens [167]. It is 1 mm in diameter, and the membrane of the lens is made from a commercial PVC stretch film to ensure best optical quality. Except a very large de-focus, their values are below $0.1\,\mu m$. Werber *et al.* measured a maximal aberration of $0.12\,\mu m$ on their membrane-based silicone lens [168].

The results of 6 Zernike coefficients are presented on figure 6.16. The first Zernike coefficient (piston) contains no information about the aberrations. The second and third coefficients (X and Y tilt) were not considered either, since they represent the flatness at which the lens is placed on the setup stage. Whereas the magnitude of the defocus of the tunable lens is very good (far below $0.05\,\mu m$ except one single value) it has noticeable astigmatism, in the range of -0.1 and $-0.15\,\mu m$ for the two first inflation levels and up to $-0.3\,\mu m$ for the unbalanced case of the highest inflation level (fig. 6.16c). The distribution of the values between the 0° and the 45° astigmatism is indeed orientation-dependent, turning the device on the setup would therefore results in more balanced coefficients between them. Moreover, the position of the lens had to be changed between the three sets of measurements to adjust the offset pressure, so that they cannot be compared individually between the three figures. The magnitude of X

and Y coma coefficients is in the range of 0.05 µm, with an exception for the X coma of figure 6.16b where it exceeds 0.1 µm. The spherical aberration is overall good, in the range of 0.5 µm or below, and seems to be very dependent on the initial inflation level but less on the voltage. Another straightforward but rough way to quantify the overall lens aberrations is to extract the peak to valley (i.e. the maximal span between any coefficients), which can be interpreted as the maximal wavefront error [168, 169]. In this case, this would lead to a relatively average lens quality since non-negligible aberrations are present both in positive and negative values.

The interpretation of the evolution of the Zernike aberration coefficients is obvious: more membrane deflection leads to more aberrations. This is visible both for actuation (higher voltage means less inflation) and for the initial lens deflection (offset pressure). This tendency has also been observed in other works [168, 169]. A refractive index mismatch between the liquid and the silicone membrane might play a small role: the refractive indexes have been measured at 1.452±0.013 by optical transmission interference for the membrane and 1.41 by a refractometer for the Sylgard 184 silicone pre-polymer. The presence of non-negligible aberrations such as astigmatism is most likely linked to the membrane homogeneity, both in local thickness and in local stretch history. Local defects (trapped dust) could also lead to fitting of large aberrations, although this has not been investigated experimentally on our device. This could be improved by working in a cleanroom environment. One could think of two ways improving the local stretch history. First, not using any prestretch on the lens membrane could reduce the aberrations which would be enhanced by the prestretch. Second, over-prestretching the membrane and relaxing it afterwards before printing the electrodes could level up all prestretch history of the membrane. However, looking at the experimental evidence that more inflation induces more aberrations, the first solution seems more reasonable. Membrane-based tunable lenses with high optical quality could also benefit from the ongoing development of silicone membrane fabrication by industrial processes. One of the limitations that will however remain with such devices is the membrane thickness (and stretch state) inhomogeneity due to the clamped conditions at the membrane periphery, which can be potentially solved by molding inhomogeneous membranes [170].
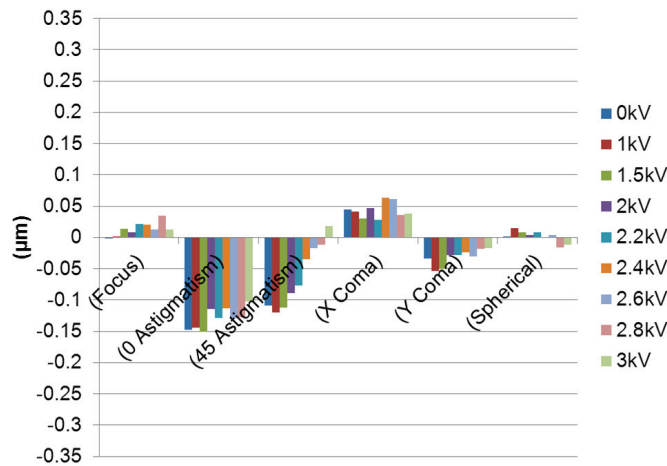
(a) Initial lens vertical deflection 0.47 mm
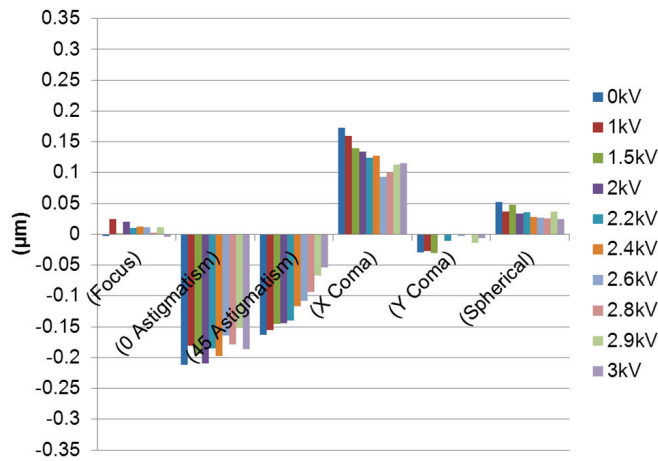
(b) Initial lens vertical deflection 0.93 mm
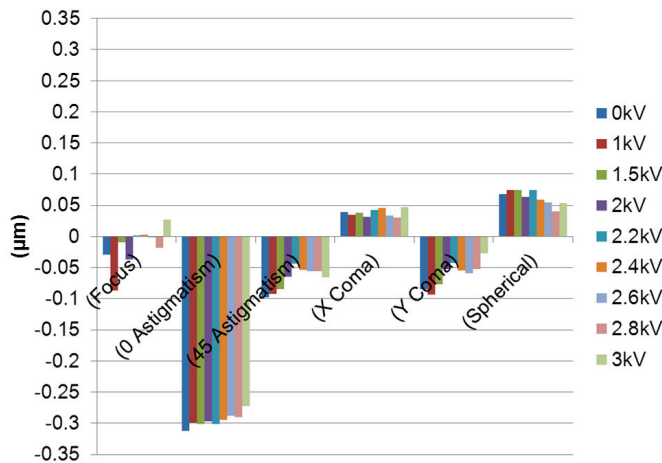
(c) Initial lens vertical deflection 1.19 mm

Figure 6.16: First Zernike coefficients in function of the voltage at three filling levels. Except noticeable astigmatism whose balance between the 0 and 45° values depend on the orientation of the chip, the overall values in the range or below 0.1 µm indicate a good lens quality. More inflation of the lens (larger initial deflection and lower voltages) increases the aberrations.

126

6.4 Fabrication

6.4.1 Single-actuator tunable lens with liquid electrode

The tunable lens with liquid electrode was made using a molded silicone body with the Sylgard 184 from Dow Corning (50 Shore A hardness). The first fabrication step consists in cutting stripes in stacked adhesive tape layers and glue them on a glass slide, which will form the channel mold (fig. 6.17a). Since mm-size cross-sectional channel dimensions are targeted to keep a low fluidic resistance, this method provides a fast, flexible and efficient way of manufacturing. A copper wire is plugged into the channel stacked layers, and suspended up to the side of the glass slide. A rigid silicone (Dow Corning Sylgard 184) is then molded on top (fig. 6.17b). Once it is cured, the fluidic body is released from the glass slide and cut on its sides. The copper wire which has been embedded inside the sidewall while it was molded provides a reliable and hermetic electrical connection. Two holes are punched on the fluidic body, using Harris Uni-Core punchers (fig. 6.17d). This fluidic body as well as the top membrane are activated in an oxygen plasma and bonded together (fig. 6.17e). The membrane is composed of a bladecasted Sylgard 186 silicone mixed with 47% weight isooctane to lower its viscosity. It is casted directly on a polyimide (PI) sheet, without using a sacrificial layer. No prestretch is applied on the membrane. Once the bonding is achieved, the PI film is peeled off from the membrane (fig. 6.17f). This step is critical regarding optical quality because of the anisotropic stretch history of the membrane. The device is then placed in a custom-made Filtered Cathodic Vacuum Arc (FCVA) vacuum chamber [30] to implant a compliant electrode on top of the active membrane (fig. 6.17g). The device is then plasma-activated together with a Sylgard 184 silicone closing plate (fig. 6.17h). Both are bonded together and once the bonding is achieved, the device is filled with ionic liquid (fig. 6.17i). One syringe is used to push the liquid inside while the other one allows sucking the air out of the closed chamber. An excess pressure is kept to allow the trapped air bubbles to leak through the gas-permeable silicone membranes. As a last step, a small amount of room temperature-curing silicone is applied on the sidewalls of the device to close the small holes made by the syringes (fig. 6.17j).

(a) Preparation of the channel mold with stacked stripes of adhesive tape. A suspended copper wire is inserted in the channel.

(b) Molding of Sylgard 184 silicone on top of the channel.

(c) Unmolding and cutting around the channel. The copper wire provides a hermetic electrical connexion inside the channel.

(d) Punching of the 3 mm diam. holes for the actuator and the lens.

(e) Bonding of a Sylgard 186 membrane on top of the fluidic body.

(f) Release of the PI film which supports the membrane.

(g) Patterning of an Au-implanted compliant electrode on the membrane of the actuator.

(h) Bonding the fluidic body with a Sylgard 184 closing plate.

(i) The device is filled with ionic liquid. One syringe pushes the liquid in the channel, the other pulls the air out. An excess pressure is kept to let the air leak through the gas-permeable silicone membranes.

(j) Some room temperature-curing silicone is disposed on the holes made by the syringes. The device is ready to be actuated.

Figure 6.17: Fabrication process of the single actuator fluidically-coupled tunable lens with liquid electrode.

6.4.2 Multi-actuator tunable lens with printed electrodes and variable operating point

The body of the tunable lens with patterned electrodes is composed of laser-cut PMMA plates (fig. 6.18). The fabrication process is illustrated on figure 6.19. As a first step, compliant electrodes are patterned on both sides of a prestretched membrane by indirect stamping (pad printing, fig. 6.19a) A silicone adhesive layer (ARclear 8932EE [5]) is applied on PMMA plates and on a transparent PET sheet. They are laser-cut with a Speedy 300 system, and form the elements of the tunable lens body (fig. 6.18 and 6.19b). In the next setp, the top plate with holes, the channel plate and the PET sheet are fixed together thanks to the silicone adhesive. Metallic threaded inserts are pressed inside the assembled body from the back (fig. 6.19c). Compared to threading the PMMA assembly, they offer more durability when screwing and unscrewing the offset pressure parts. The next fabrication step involves gluing the silicone membrane in the same manner (fig. 6.19d). To avoid any dust to stick on the membrane, the lens part is protected by foils on both sides up to that step, where it should be removed on one side to allow gluing. The protective foil on the other part of the lens is kept until the last step, when the device is pressurized. Additional membranes are bonded using plasma O2 activation on the offset pressure holes (but not on the lens), to stiffen them and to enhance their mechanical robustness (not drawn on the process flow). Tear-resistance is desired because the beads will press mechanically on them, and stiffness so that they do not absorb the actuation volume being too compliant. The device is flipped and the fluidic channels are filled with a silicone prepolymer (Dow Corning Sylgard 184) using a pressurized dispenser (fig. 6.19e). The liquid is transparent and has a refractive index very close to the one of the membrane. Moreover, it does not penetrate into silicone membranes nor evaporate (sect. 4). Closing the device will inevitably leaves some trapped air pockets. This dead volume should be minimized, because a corresponding offset volume should be applied later on to push the air out. As the open surface is large, a PET sheet with smaller apertures on top was glued before on the back, which allows a more efficient filling. Spilling of prepolymer liquid on the PET film can be wiped with solvents. Finally, the bottom closing plate is fixed on the back to seal the liquid cavity. This PMMA part was also coated with the ARclear adhesive film, except under the lens hole to ensure an optimal transparency (fig. 6.19f). Hence, the closing plate and its adhesive film were cut separately. Beads are progressively inserted between the removable offset pressure pushing parts and the suspended membranes (fig. 6.19g) to provide a pressure offset able to push the trapped air pockets out of the device across the gas-permeable silicone membranes. If no bead is applied in a hole, a 0.2 mm thick S184 sheet covers its membrane to prevent them being pinched between the pressure pushing part and the fluidic body. Finally, a PCB is glued on the side and silver varnish is used to connect it to the conductive tracks which extend from the compliant electrode (fig. 6.19h). 1 mm holes were pre-cut in the PMMA plates so that one only has to fill these channel with silver varnish to provide a clean and reliable electrical connection. The operating point of the device can be adjusted by changing the number and size of the beads.

---

[5]http://www.adhesivesresearch.com
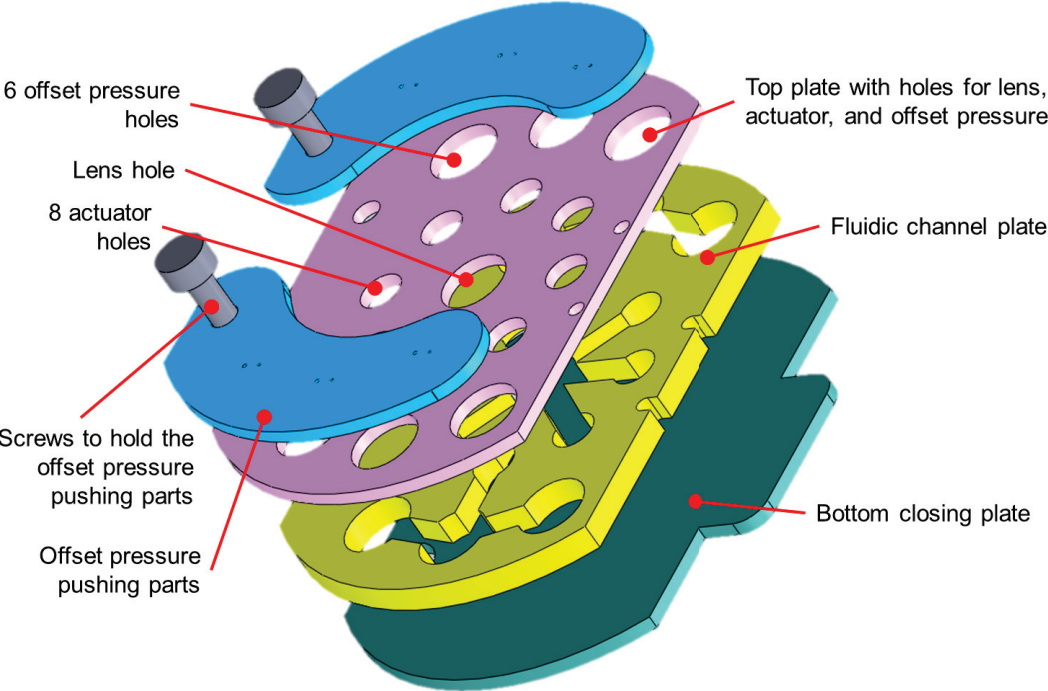
Figure 6.18: The body of the tunable lens is composed of 3 laser-cut PMMA plates assembled together with a silicone glue film, and of 2 PMMA removable offset pushing parts held by screws. The PDMS membrane is glued on top of the top plate.

(a) Printing of compliant electrodes on both sides of a prestretched silicone membrane.

(b) Laser cutting of 4 parts covered with a silicone adhesive film.

(c) Assembling the top plate, channel plante and a the PET sheet. Press-fit metallic threaded inserts.

(d) Gluing the 2-sided printed silicone membrane on top of the device

(e) The device if flipped and filled from the back with the S184 prepolymer.

(f) Sealing of the filled device with the closing plate.

(g) Screwing offset pressure pushing parts that press on beads and on passive membranes. The trapped air leaks out.

(h) Gluing a PCB and contact it to the membrane tracks with silver varnish. The device is ready to be operated.

Figure 6.19: Fabrication process of the fluidically-coupled tunable lens with patterned electrodes.

6.5 Conclusions and outlooks

Two types of membrane-based tunable lenses were built. Both devices operate by changing the pressure of an encapsulated liquid using a DEA made in the same silicone membrane as the lens. The motion of the active(s) membrane(s) are fluidically-coupled to a passive one which acts as a lens.

Static performance of fluidically-coupled tunable lenses has been integrated in three model iterations. The most advanced model includes material hyperelasticity and membrane pre-stretch to predict the pressure-volume relationship of inflated clamped membranes with and without actuation.

6.5.1 First generation of tunable lenses

The first type of tunable lens uses an ionic liquid as counter-electrode, mechanical coupling agent and optical medium. The static displacement of the device was accurately predicted by a simple approach based on the fluidic compliance and a buckling actuator model with linear material properties [36]. This is the first time that a DEA using an ionic liquid as electrode was built. This opens new design concepts that move away from the traditional actuator structures. Using liquid electrodes indeed minimizes their stiffening impact and offers new freedoms in the fabrication processes regarding electrical interconnects (contact at any point where the liquid flows) and patterning (electrode shape precisely defined by the fluidic structure). 0 to 90% response times in the order of 1.4 s have been measured. Although not investigated specifically, the devices that have been studied survived for 10 to 20 thousand cycles before breakdown under various high electric field excitation schemes, and with no evidence that the breakdown should be specifically attributed to the use of a liquid electrode. It proves the suitability of using ionic liquids as reliable compliant electrodes for silicone DEAs. Other outcomes of this work include the development of a ultrafast prototyping method for making microfluidic channels by stacked layers of structured adhesive tape.

6.5.2 Second generation of tunable lenses

A set of weaknesses of the first generation of the devices has been addressed in the second one. The number of actuators has been increased to obtain more tuning range. Eight DEAs pump the liquid of a single lens, which enabled tuning range of up to 60% of the initial focal length. The modeled and measured focal length match closely. The lens is made in a compact all-PMMA laser cut fluidic body. Thanks to the rigidity of PMMA, the device does not bend, which changes the lens shape of rigid silicone-based devices. Nonetheless, optical quality has been enhanced by avoiding any anisotropic stretch in the membrane, which results in direction-dependent stiffness and optical aberrations. This has been done both by using a new membrane fabrication process with a water-soluble sacrificial layer and by a way to control the pressure in the device after it has been sealed to gradually push the trapped air bubbles

through the membrane. This latter feature of tunable operating point also enables to change the starting focal length of the lens. A characterization of the optical aberrations of the lens under three initial filling levels and nine actuation voltages indeed confirms a good optical quality and a trend of smaller aberrations with less membrane deflection.

This device has a very broad optimization field ahead, for instance by changing the number, size or shape of the actuators, membrane thickness and prestretch, or building arrays of lenses.

7 High-speed tunable lens

If tunable lens devices have large focal length tuning ranges, their time response is surprisingly slow, regardless of technologies. DEAs can be generally considered as actuators with slow responses, mainly because of the softness and viscous damping of elastomer materials. However, thanks to a very efficient structure published by other researchers in 2011 and an optimized combination of materials and fabrication process, a DEA-powered tunable lens with the fastest response ever reported was built and characterized.

The introduction and state of the art of **section 7.1 (Introduction and state-of-the-art)** follows two other ones, the first about the dynamic performance of DEAs (section 3.4) and the second one about tunable lenses (section 6.1). It focuses on the responses time of tunable lenses with integrated actuators, with a sub-section dedicated to DEA-driven tunable lenses.

Section 7.2 (High-speed full-silicone tunable lens device) describes the fabricated device and presents a theoretical estimation of the in-plane resonance frequency of the lens.

Section 7.3 (Steady state focal length) first links the focal length measured optically with the one deduced from 3D profiling and the thin lens formula. The steady state change in focal length is then measured and discussed for four devices with different inflation levels.

Section 7.4 (Time responses to a step input) describes the measurement procedure of the electrical, mechanical and optical responses to a voltage step input. The electrical response integrates a measured current, the mechanical responses uses a high-speed camera to track the displacement of the electrode edge and the optical response records the light intensity with a high-speed photodiode. The results provide a detailed insight in the operation of the device. The displacement of the top of the lens under a step excitation is also recorded and discussed.

To complete the dynamic characterization, the amplitude and phase of the optical response under large signal excitation was measured, as presented in **section 7.5 (Frequency response)**.

The fabrication process of the lens is described in **section 7.6 (Fabrication process)**.

Conclusions on the main results obtained with the high-speed lens are summarized and discussed in **section 7.7 (Conclusions)**, which also includes a discussion about the use of DEAs for fast response applications.

This chapter is about to be submitted for publication as a RSC Soft Matter full paper.

7.1 Introduction and state-of-the-art

A review and state of the art concerning the dynamic performance of DEAs has been presented in section 3.4. The predominant importance of the viscous component of the elastomer material has been highlighted, as well as the tradeoff between hardness and response time for silicones, which are probably the first choice elastomer type for fast response applications. The essential influence of the electrodes was discussed based on Rosset *et al.*'s 2012 publication [35]. Finally, a state of the art on the use of DEAs for fast response applications was presented. Section 6.1 contained a state of the art about tunable lenses. Following these two introductions, the dynamic performance of tunable lenses with integrated actuators is reviewed hereafter, and compared with DEA-powered ones.

7.1.1 Response time of tunable lenses with integrated actuator

Tunable lenses with fast (µs to ms) responses are desired for many applications, such as fast autofocus, quasi-simultaneous imaging at different focal planes [171], laser focusing [172] or light sheet microscopy [173]. Unfortunately, the values for lens tuning speed reported in the literature are often inconsistently documented. The choice of the time constant used does not directly reflect the actual device behavior, for instance, the use of the 63% asymptotic value should only be used if the response characteristic is clearly exponential. Moreover, in most of the literature consulted, the definition of the measured time constant is not given. The broadly applicable values of time to 90% or the even more robust settling time should be preferred since they give a clear insight on the useful performance of the device: the time to reach a stable focus.

The fastest tunable lens reported so far is the commercially available tunable acoustic gradient (TAG) lens [174] [1], with sub-µs focus change. It modulates the density of a liquid and hence its refractive index with a mechanical wave, creating a time-modulated gradient index (GRIN) lens. When imaging with a constant light source, the focus is permanently changing. In order to have a stable focal length, one needs to synchronize a pulsed illumination or acquisition frame rate with the driving signal, reducing the exposure time compared to a fixed focal length device.

Ren et al. measured 200 µs response time on an array of 450 µm diameter nanosized polymer-dispersed liquid crystal droplets lenses [175], while the vast majority of other liquid crystal

---

[1]www.tag-optics.com

lenses respond in 1 s range [150]. The fastest electrowetting lenses change in the range of 10 ms [176]. Among commercially available systems other than TAG, Varioptic's electrowetting lenses have time to focus of 20 ms [2], and the specs of the EL-10-30 electromechanically actuated lens from Optotune has 2.5 ms 10 to 90 % response time [3]. Nevertheless, accurate comparisons should always take into account size, as it naturally plays an important role in limiting response speed, with larger lenses taking longer to reach a stable configuration than very small ones.

DEA-controlled tunable lenses

Tunable lenses using liquid coupling such as those presented in section 6 are not optimal structures for achieving fast responses. Indeed, the liquid has to be pushed in channels, whose hydraulic impedance cannot be neglected.

In 2011, Carpi et al. reported a bioinspired lens consisting of a liquid encapsulated between two elastomeric membranes, where the focal length of the lens is tuned not by changing the inflation level but modifying the lens shape with an in-plane force generated by a DEA integrated in the same membranes as the ones which enclose the soft lens liquid (figure 7.1) [21]. Compared to the coupled chamber devices, this design is extremely efficient to transfer the actuation work into a change of focal length. The lens is surrounded by an annulus-shaped DEA, consisting of an annular elastomeric membrane sandwiched between two compliant electrodes. The actuator works in the basic in-plane mode: as the electrodes are electrically charged by an applied voltage, the electrostatic attraction between the electrodes compresses the membrane, which reduces in thickness and expands in area thanks to its volume incompressibility. The resulting in-plane force compresses the soft lens, which thus changes its curvature and focal length. In their work, Carpi *et al.* used an acrylic elastomer film (VHB 4905 from 3M, USA) and carbon grease electrodes, reporting a focal length variation of -26.4%, close to that of the human crystalline lens (-29.1%). Detailed computations of the steady state performance of this design have been recently published [177].

Shian et al. recently took advantage of transparent electrode materials to place the actuation membrane on the optical axis and built compact tunable lenses [106, 109]. DEAs made of the 3M VHB acrylic elastomer are renowned for their high electromechanical transduction performance and are convenient for rapid prototyping (membranes are commercially available as thin films, sticky film eases encapsulating the liquid), but that material is also known to have a high viscous component, such that creep limits the response speed, owing to a slow response and a drift in position. For instance, Carpi et al. reported a response to a step stimulus with a time constant of 60 ms [21], while Shian et al. reported a response time (90% of final value) of 25 ms [106, 109]. Wei's lens with an annulus-shape VHB actuator has response times ranging from 0.65 s to some 20 ms which strongly depend on the actuation voltage,

---

[2]www.varioptic.com
[3]www.optotune.com
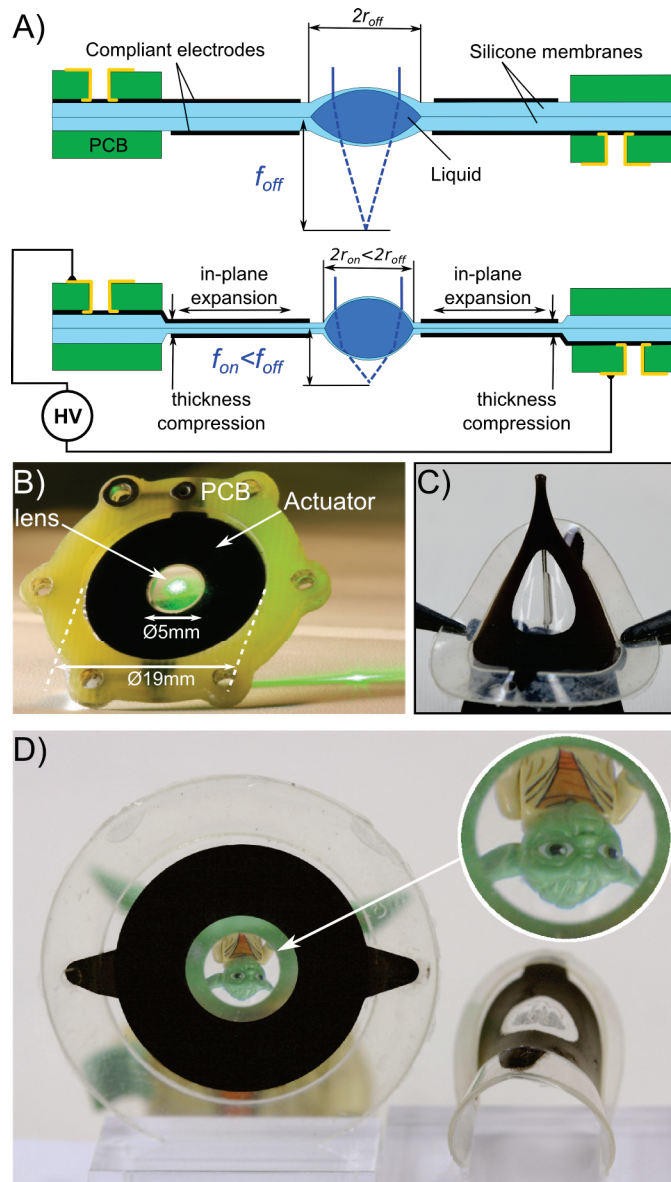
Figure 7.1: A) Schematic cross-section of the tunable lens. As a voltage is applied across the membrane, it contracts the lens with an in-plane force, changing its focal length. B) Picture showing the lateral dimensions of the tunable lens clamped between two PCB frames. C) The resilience of the actuator is shown by an extreme deformation of the lens over a needle head. D) Flexible version of the lens revealing a green Lego creature hidden behind.

without specification on the measurement method nor giving a time constant definition [158]. All these three papers do not comment on the large additional creep commonly observed on VHB-based devices, which tends to keep on changing the focal length on timescales as long as one minute, and makes the practical use of such lenses more challenging. Acrylic-based DEAs are limited to actuation frequencies lower than some 10's of Hz and do not provide a stable focus over seconds or minutes, unless complex closed-loop control is used [95].

In the frame of a Short Term Scientific Mission (STSM), the LMTS hosted Michele Ghilardi, an exchange MSc student from the Research Center E.Piaggio in Pisa (Italy). The goal of the project was to adapt of a lens design of Carpi *et al.* [21] to a device based on silicone elastomers. Thanks to a novel semi-automated fabrication process, we aimed at producing precise, compact and reliable devices with comparable steady stated and enhanced dynamic performance compared to VHB. This STSM was reconducted twice, in 2013 and 2014, in order to fabricate enough device and gather characterization data. M. Ghilardi was mostly involved in the fabrication of the device and of the steady state focal length measurement setup, and produced a large set of devices thanks to his good experimental skills.

The silicone lens described here does not need any feedback control to hold a fixed position and has the shortest response time ever reported in the literature for a non-modulated focus among all different technologies. The issue of using carbon grease electrodes is also addressed, which set numerous problems in terms of reliability and manufacturability as well as affect the speed of the device [35].

7.2 High-speed full-silicone tunable lens device

As visible on fig. 7.1A, the device is composed of a PCB frame, an annulus-shape DEA, and a tunable lens in the center. The tunable lens is made of a transparent liquid encapsulated between two silicone membranes. The liquid is the silicone Sylgard 184 unpolymerized base, which does not penetrate into the membranes, does not evaporate, and has the same refractive index as the membranes (section 4). The two silicone membranes also act as active material around the lens: they are sandwiched by two compliant electrodes composed of carbon black dispersed in a soft silicone matrix. As a high electric field is applied across the electrodes, the silicone membranes compress in thickness, which results in in-plane expansion that reduce the lens diameter and decreases its focal length. The in-plane expansion of the electrodes would result in buckling (loss of tension) if the membranes were not pre-stretched before fixing them on the frame. This pre-stretch also avoids the pull-in instability [26], but it should be chosen low enough to limit the membrane stiffening. Each membrane was equibiaxially prestretched by a factor 1.2, leading to a final actuator thickness of 2x18 μm at electrical rest. The PCB frames serve as mechanical holders to keep the pre-stretch and provide the electrical interconnects.

Many silicone elastomers are commercially available, with Young moduli varying over several orders of magnitude. For this device, both a large displacement and a low viscous component are needed. As explained earlier, stiffer silicones tend to have a lower viscous component, and their resistance to deformation is somehow compensated by larger breakdown strengths, at the cost of higher driving voltages. I therefore chose the Nusil CF19-2186 (shore A 25).
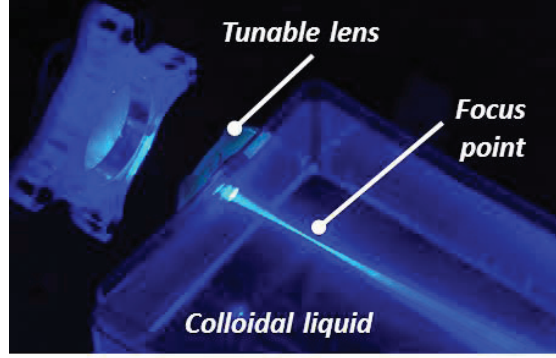
Figure 7.2: The tunable lens focuses a collimated laser beam into a colloidal liquid

7.2.1 Theoretical estimation of the lens resonance frequency

In order to estimate the in-plane resonance frequency of our tunable lens, I use the standard relation for a mass-spring system (eq. 7.1), with m^* the effective mass and k the spring constant. The viscous component of the elastomer is neglected.

$$2\pi f = \sqrt{\frac{k}{m^*}}$$
(7.1)

Since the mass of the lens is 1 order of magnitude smaller than the one of the membrane, it is neglected. The reason for using an effective mass is because not all parts of the device move in the same way: on its periphery ($r_{max} = 10$ mm) and on its center the membrane is motionless, and its maximal displacement is assumed to be at the electrode border $r_{elec} = 2.5$ mm. A weighting function $\alpha(r)$ is therefore used (eq. 7.2) and integrated along the radius of the device (eq. 7.3).

$$\alpha(r) = \begin{cases} \frac{r}{r_{elec}} & \text{for} \quad 0 < r < r_{elec} \\ \frac{r_{max}-r}{r_{max}-r_{elec}} & \text{for} \quad r_{elec} < r < r_{max} \end{cases}$$
(7.2)

$$m^* = \rho \int_0^{r_{max}} 2\pi t r \alpha(r) \cdot dr$$
(7.3)

The effective mass is found to be $m^* = 4.58 \times 10^{-6}$ kg, with $\rho = 1 \times 10^3$ kg m^{-3} the density and $t = 35\,\mu$m the thickness.

The in-plane spring constant is derived from the Yeoh hyperelastic model of the CF19, fitted on

an uniaxial pulltest. Its coefficients are C_1 =0.128 MPa, C_2 =4.76 kPa, C_3 = 0. The equibiaxial in-plane stress σ_{11} is given by the equation 7.5:

$$I_1 = 2\lambda^2 + \frac{1}{\lambda^4} \tag{7.4}$$

$$\sigma_{11} = 2\left(\lambda^2 - \frac{1}{\lambda^4}\right)((I_1 - 3) \cdot (3C_3 (I_1 - 3) + 2C_2) + C_1) \tag{7.5}$$

The force is obtained by multiplying the stress with the lateral area of the membrane (eq. 7.6):

$$F = 2\pi r^2 t \tag{7.6}$$

The spring constant is computed by derivation of the force by the in-plane diameter $D = 2r$ and a value of k =3.31 × 10^3 N m^{-1} is obtained at D =20 mm, which corresponds to the applied prestretch of 1.2 by choosing corresponding initial membrane dimensions (eq. 7.7).

$$k = \left. \frac{dF(D)}{dD} \right|_{D=20mm} \tag{7.7}$$

Inserting these results in eq. 7.1 yields f =4.3 kHz.

7.3 Steady state focal length

7.3.1 Lens focal length when DEA is not actuated

The focal length was measured by shining collimated light through the tunable lens, and moving a screen on which the number of pixels of the spot size was counted by image processing to determine the focal point. The setup consisted of a 633 nm laser beam attenuated with cross-polarizers, which passed through a beam expander and a diaphragm before being focused by the tunable lens. The imaging screen and a 5 Megapixel µEye camera with a 3.3x macro objective were mounted together on a micrometer stand.

One can compare the optically-measured focal length of our lenses with the one computed with the thin lens formula (eq. 7.8), where n is the refractive index and R_{top} and R_{bot} are the top and bottom radii of curvature, respectively. The sign of R_{bot} is negative by convention. The thin lens formula applies since a very small amount of liquid is sufficient to obtain a focal

length in the range of 10's of mm, thanks to the biconvex shape.

$$\frac{1}{f} = (n-1)\left(\frac{1}{R_{top}} - \frac{1}{R_{bot}}\right)$$
(7.8)

In order to compare the theoretical focal length estimated from this equation with our exper-imental values, the 3D topology of both sides of a lens was measured with a Wyko NT1100 white light interferometer, fitting the cross-section profiles with circles and extracting the top and bottom radii of curvature of $R_{top} = 26.09$ and $R_{bot} = -20.90$ mm. Furthermore, the refractive index of the encapsulated fluid was measured with an AR7 refractometer and was found to be 1.41. The computed focal length is 28.30 mm, and the optically measured one 29.34 mm.

Besides the good agreement between theoretical and experimental values, one can notice that the 'bottom' membrane of the lens (i.e. the one which has been over-stretched by an underlying low pressure to create a cavity and fill it with the fluid, sect. 7.6) presented a smaller radius of curvature. This reflects a membrane softening, due to the Mullins effect [76]. Care must also be taken on prior steps during membrane handling to avoid anisotropic stretch, as this would lead to anisotropic membrane stiffness and therefore in optical aberrations. This was addressed by using a sacrificial layer during the membrane fabrication process and by molding a spherical cavity in the chuck (fig. 7.11d).

7.3.2 Focal length tuning range

A purely geometrical study of the lens showed that an equal reduction of the diameter of the lens from d_{OFF} to d_{ON} results in a larger change of focal length if the initial radius of curvature is larger. In other words, filling the lens with a smaller amount of liquid offers a broader absolute tuning range. This is clearly visible in figure 7.3, which presents the focal length dependence on the applied voltage for different filling levels. The device with an initial focal length of 19.4 mm exhibited a span of about 5.4 mm, while the device with an initial focal length of 10.2 mm exhibited 2.2 mm span. The relative changes of the focal length range between -28 % and -14 %.

A tunable lens was mounted directly in front of a CCD camera without objective in order to demonstrate the use of the lens as an autofocus. The tunable lens is the only lens used to focus the image on the CCD. The focal plane is switched between three objects located at 80 mm, 20 cm and 3 m, equivalent to infinity (figures 7.4 and 7.5). The figure 7.6 shows the approximate focus distance of the setup. A large diaphragm (4 mm for a 5 mm diameter lens) was used to favor a narrow depth of focus versus image sharpness.
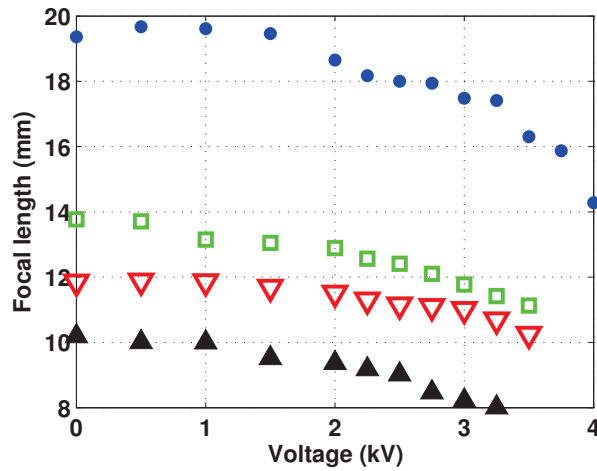
Figure 7.3: Change of focal length with applied voltage for 4 devices. Their initial focal lengths are comprised between 10.2 and 19.4 mm. For geometrical reasons, a larger initial focal length (i.e. less filling) provides more tuning range.
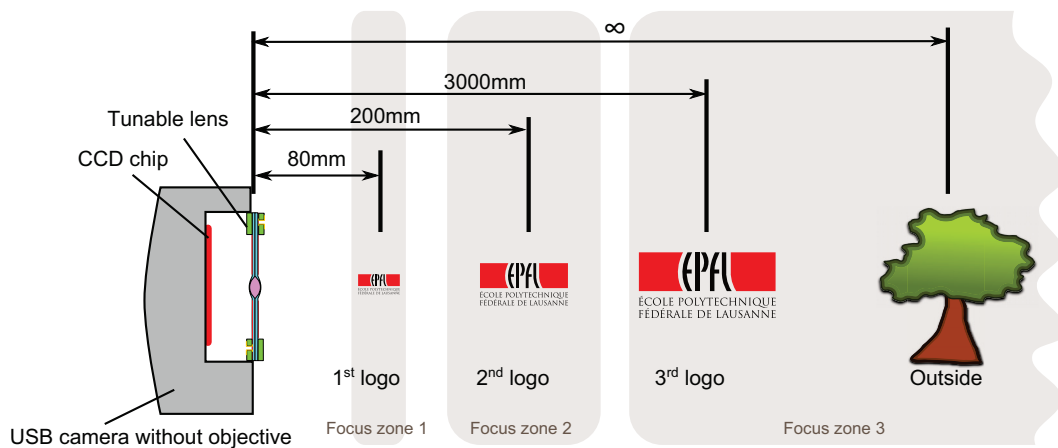
Figure 7.4: Setup for switching the autofocus of a CCD camera between 3 objects

7.4 Time responses to a step input

To provide an in-depth understanding of the response of the lens, three different response times were characterized: electrical (electrode loading time), mechanical (in-plane motion of the electrode) and optical (time for the focal length to stabilize).

7.4.1 Electrical response

The electrical response is affected by two elements: the ability of the high voltage supply to deliver the high voltage on the load (it has a finite slew rate) and the R-C charging time of the device, which is a R-C-R series circuit. A large bandwidth high-voltage amplifier (Trek 609E-6)

143

(a) Voltage OFF, focus to infinity.

(b) 2.5 kV, focus at 20 cm

(c) 3.5 kV, focus at 80 mm
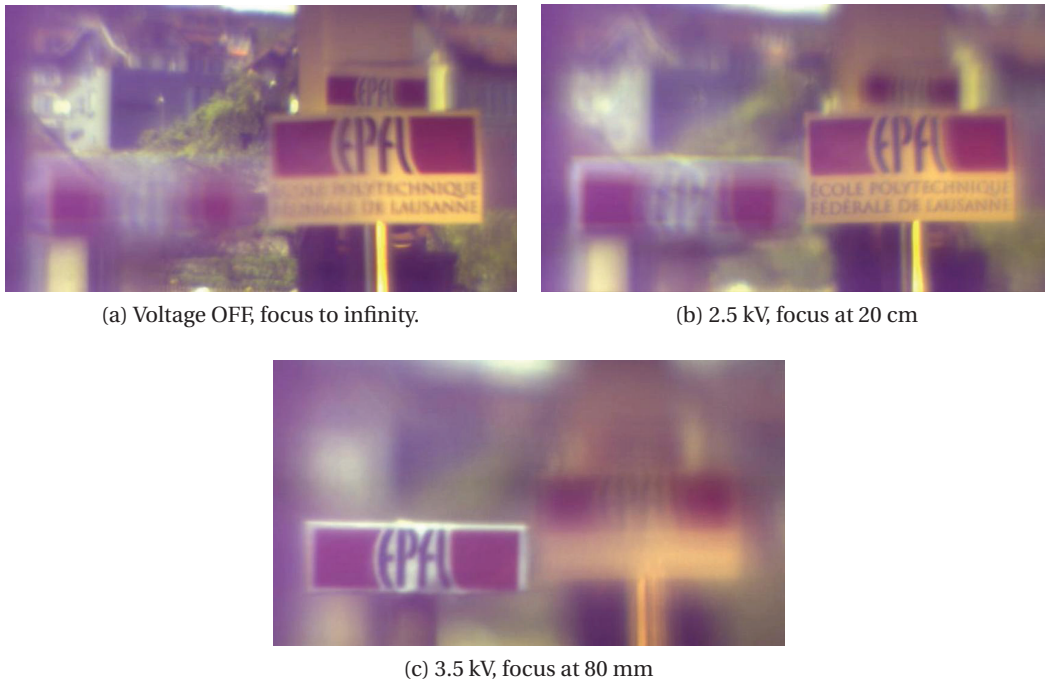
Figure 7.5: Changing the focal plane of a CCD camera with the tunable lens. The lens is the only optical element used for imaging on the CCD.
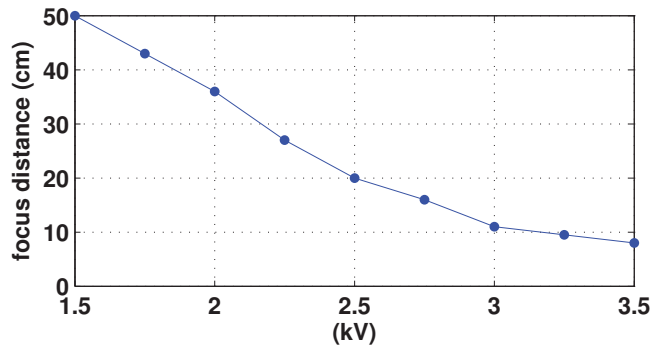
Figure 7.6: Distance of focus versus applied voltage of the setup

was used. It provides a monitoring of the output current. From the capacitance equation, it is known that the voltage on the electrodes V_{cap} is proportional to the integral of the current $i(t)$ (eq. 7.9).

$$V_{cap}(t) \propto \int i(t) dt \qquad (7.9)$$

The driving current signal was acquired from the high voltage amplifier with a triggered

Tektronix oscilloscope, and a numerical integration is performed on the data to obtain the loading voltage of the capacitance of the device.

7.4.2 Mechanical response

Compared to the electrical response, the in-plane motion of the electrodes reflects the ability of the actuator to transduce the electric field into mechanical displacement. The in-plane motion of the electrode border around the lens was imaged with a high-speed camera. The camera model is Phantom V210 from Vision Research. It was mounted on a microscope with a 20x objective and triggered by the function generator. The video resolution was selected at 32x160 pixels, which enables a frame rate of 125 kHz. A black and white threshold was performed and the displacement is converted from pixels to mm using a calibration ruler.

7.4.3 Optical response

The method used for recording the optical response consists in measuring the optical power density after being focused by the lens using a fixed pinhole and a photodiode [155]. As the focus changes, the amount of light that passes through the pinhole varies, which gives a direct representation of the focal length change. The setup is composed of a 633 nm laser followed by a beam expander, a diaphragm and the tunable lens. The pinhole is placed slightly before the focal point at electrical rest, and a band-pass filter cuts off the light noise. The photodiode is a ThorLabs PDA100A with 78 kHz bandwidth, and its signal is recorded with a triggered oscilloscope.

7.4.4 Results and discussion

The figure 7.7 plots the three measured time responses. The electrode voltage reaches 90% of its end value 124 µs after the trigger. The electrode displacement rising edge has a delay in the range of 50 µs to the electrode voltage. The settling time for the optical signal to reach ±10% of its value at 800 µs is 172 µs, the best response of a tunable lens reported so far. Compared to the acrylic-based lens of comparable dimensions reported in [21], this result shows that the use of silicone elastomers and µm-thick printed electrodes allowed for an improvement of 3 orders of magnitude .

The mechanical response time can be affected by two elements: the viscoelastic properties of the electrode-elastomer-electrode stack, and the damping induced by the lens. To determine the contribution of the lens to the damping, an identical device was fabricated, but without filling the lens cavity with any liquid. The result is straightforward: the rising edges of both devices coincide perfectly, with a larger steady-state value for the device without liquid. This indicates that the lens plays a negligible role in the response of the device response, which is not obvious since one could expect the high viscosity contribution of the liquid to the damping to dominate over the viscous component of the membrane. However, the mass of
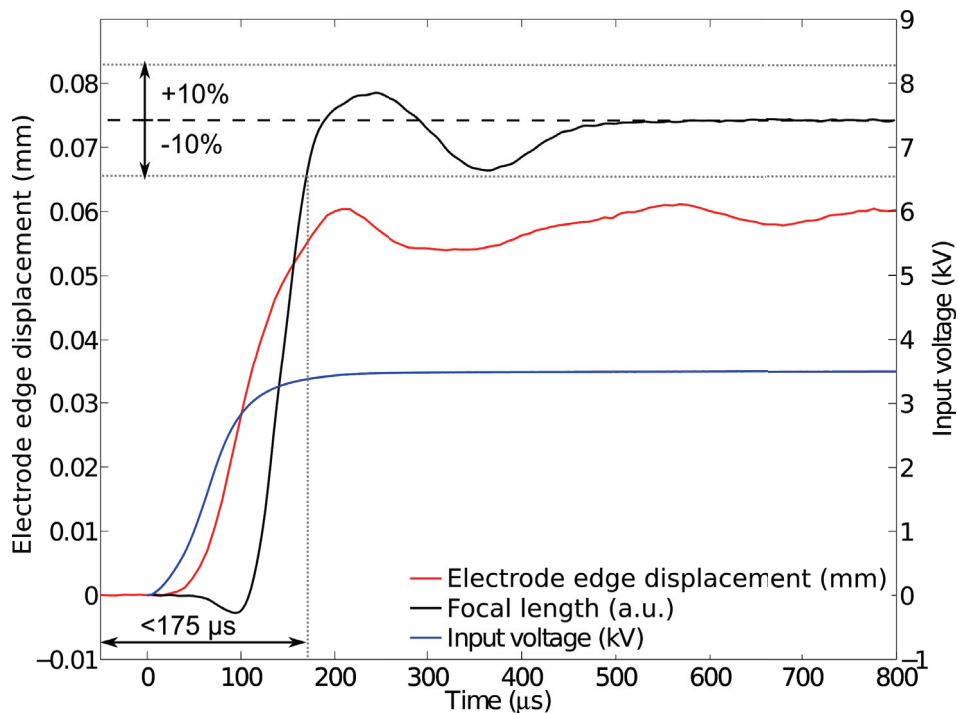
Figure 7.7: Electrical, mechanical and optical time responses of the lens to a step input. Nominal electric field $90\,V\,\mu m^{-1}$. The 0 to 90% optical response time is $172\,\mu s$

the encapsulated liquid is one order of magnitude smaller than the one of the membrane. Moreover, the theoretical amount of liquid to be displaced to change a focal length is also one order of magnitude smaller than the lens volume: the lens design is extremely efficient to provide a fast change of focus.

The optical response is close to a critically damped case, with a positive overshoot of 4.6% and a negative overshoot of -6.5%. The delay between the electrode edge motion and the change in focal length can be interpreted as the time for the wave induced at the periphery of the lens to propagate on the membrane surfaces, as was observed from the side with the high speed camera (fig.7.9). The small negative dip at $100\,\mu s$ as well as the two oscillations around the steady state value are most likely due to the same phenomenon: the lens surface oscillates like a wave before reaching its spherical shape.

7.4.5 Out-of-plane vibration of the membrane

The displacement of the top of the lens was measured with a Laser Doppler Vibrometer. The setup used to record the out-of-plane displacement of the top of the lens is a PSA-400 model from Polytec. The velocity signal is integrated with a displacement decoder to provide the vertical displacement. The observed damped oscillations are visible on figure 7.8, and represent the out-of-plane vibration of the membrane, which oscillates like a drum after the step excitation. This was confirmed by filming devices from the side with a high speed camera

at 63 kfps and comparing the oscillation frequencies (fig.7.9). They range from 325 Hz at 23 V μm^{-1} to 111 Hz at 95 V μm^{-1}, and their amplitude decays within fractions of a second. How will this affect the time response of the focal length change? Even if the amplitude of the vibration compared to the displacement step height looks non-negligible, it remains only a few 10's of μm, 2 orders of magnitude smaller than the focal length change. The focal length tuning is therefore unaffected by this ringing. Unlike VHB-based actuators, the second-range creep is negligible (see 91 V μm^{-1} response).
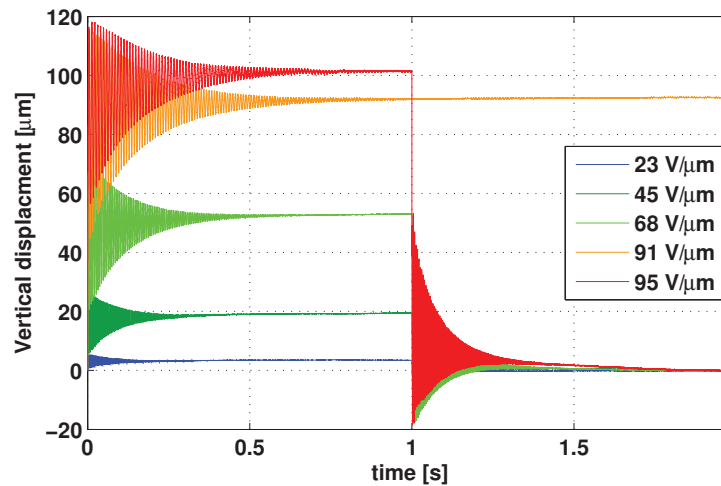
Figure 7.8: Out-of-plane displacement of the top membrane of the lens. A vibration amplitude of 100 μm is 2 orders of magnitude smaller than the focal length, and this oscillation is therefore invisible optically.
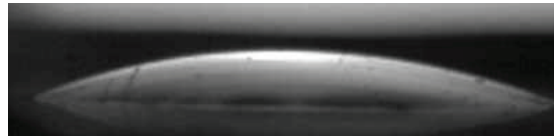
Figure 7.9: Tunable lens filmed from the side with the high-speed camera (available in the supplemental materials).

7.5 Frequency response

The frequency response of the optical signal of the lens was measured with a large-signal excitation, using the same setup as for the time response. The voltage applied is an sinus with offset of the form $V(t) = 750 + 750 \cdot \sin(\omega t)$ V, between 10 and 20 kHz. The setup consists in an Agilent 33220A frequency generator and a Stanford Research SR830 lock-in amplifier, both controlled with Labview. The frequency generator is connected to a Trek 609E-6 high voltage amplifier, which drives the lens with a sinusoidal signal with offset. The gain and phase of the amplifier with a load was measured in the same conditions to assess that the bandwidth of the high voltage amplifier was not affecting the measurement.
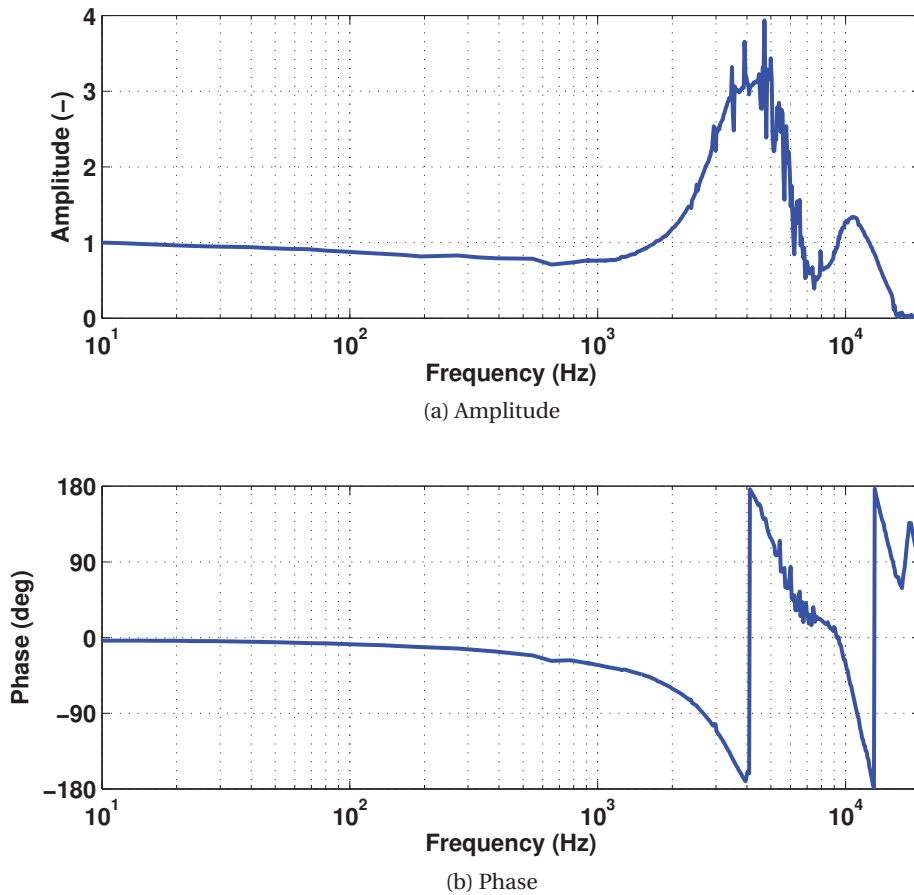
(a) Amplitude

(b) Phase

Figure 7.10: Amplitude and phase of the lens' optical response in frequency.

7.5.1 Results and discussion

The amplitude and phase of the optical signal are displayed on figure 7.10.

The resonance frequency peak lays around 4.7 kHz, close to the estimated value of 4.3 kHz, with a gain higher than 3. The phase angle smaller than −90° on the resonance may reflect the 100 μs delay between the trigger and the focal length change onset. The −3 dB bandwidth is 7.4 kHz, with a nearly flat response up to 2 kHz, which shows that our device can be driven with an arbitrary signal of this bandwidth. Measurements of frequency response of standard devices made with different electrode types shown that that the small decay is due to the losses in the soft PDMS-carbon electrodes.

7.6 Fabrication process

The fabrication process is summarized in figure 7.11.

The silicone membranes are fabricated using a blade casting process, as described previously

(a) Indirect stamping of μm-thick compliant electrodes

(b) O2 plasma treatment to activate the surface of the printed silicone membranes

(c) Placement of a first prestretched silicone membrane with printed compliant electrodes on a vacuum chuck

(d) Application of vacuum to pull down the center of the membrane in a spherical cavity. The hole is filled with a transparent silicone prepolymer.

(e) Application of a second O2-plasma activated identical membrane on top. The bonding is achieved within 30 min.

(f) As the vacuum is released, the bottom part of the lens comes up and the frame is removed from the chuck. The trapped air leaks through the membranes within a few hours.

(g) Gluing of two PCB's on top and on the bottom, which serve as mechanical frame and provides electrical interconnects.

Figure 7.11: Fabrication process

(section 3.2). A water-soluble sacrificial layer is used to release the membrane without stretching it. A Speedy 300 laser cutting system [4] was used to cut the membranes, which were then prestretched equibiaxially using a custom stretcher with 8 movable fingers. The prestretch was computed by measuring the thickness of the membrane before and after prestretch by white light spectrometry. The compliant electrodes are printed using an indirect stamping technique (pad printing) (fig. 7.11a). The ink consisted of carbon particles dispersed in a

---

[4]www.troteclaser.com

soft silicone matrix in a 1:10 mass ratio, whose polymerization produced well-defined electrodes with a homogeneous thickness in the range of 1 μm. Its stiffening impact was measured to be negligible as compared to the 35 μm-thick membrane. Two identical membranes are chemically activated with an oxygen plasma (fig 7.11b). The assembly chuck consisted of a porous material (metapor [5]) and a Sylgard 184 silicone pad (fig. 7.11c). The pad was molded with a 5 mm diameter spherical-shaped hole in its center and a small through-hole at the center of the cavity. The air-permeable material allowed applying vacuum to pull down the membrane in the spherical cavity while offering a flat surface on which the deflected part of the membrane can rest. A first membrane is placed on the chuck and vacuum is applied to create a cavity (fig. 7.11d). Thanks to the compliance of the pad, the process did not damage the membrane on the edge of the lens. The liquid to be encapsulated between the silicone membranes was chosen according to the following desired properties: no penetration within the elastomer membrane, low vapor pressure (since silicones is gas-permeable), excellent optical transparency and same refractive index as the membranes (section 4). The same fluid used in [21], i.e. Sylgard 184 pre-polymer, was found to fulfill all these criteria. The spherical cavity is filled using an automated dispenser (fig. 7.11d). The second membrane was then placed on top of the first one and vacuum is kept on for 45 minutes to allow for bonding to take place (fig. 7.11e). As the vacuum was switched off, the bottom part of the membrane was released, and the lens took its shape (fig. 7.11f). The air bubble trapped inside leaked through the silicone membrane within a few hours. One PCB was then glued on each side. They serve both as mechanical supports and electrical interconnects (fig. 7.11g).

7.7   Conclusions

7.7.1   Results obtained with the high-frequency lens

The settling time of 172 μs of the tunable lens is the second fastest response reported in the literature, despite the relatively large size of the device and the softness of its constitutive materials. Compared to the alternative of TAG lenses, the lens provides a stable focus rather than needing stroboscopic illumination to emulate it, hence allowing much longer and flexible exposure time settings on the selected focal planes. The frequency response under large signal excitation shows a nearly flat response up to 2 kHz, with a −3 dB bandwidth of 7.4 kHz, which is excellent for elastomer actuators. Such silicone-based tunable lenses represent a considerable breakthrough for high-frequency varifocal applications such as 3D and ultra-depth-of-field imaging techniques (light sheet microscopy [173], quasi-simultaneous imaging of multiple focal planes [171], depth from focus [178]) or advanced laser machining techniques [179], with the advantage of step-wise focus stability at high frequencies.

---

[5]www.portec.ch

7.7.2 Fast DEAs

These results demonstrate the possibility of making large bandwidth DEA devices. In order to design them, one should consider wisely the dielectric material (including prestretch), the electrode type, the actuator structure and the size.

First, the choice of the dielectric material is critical: it must have a low viscous component. Its hardness depends on the amount of deformation needed, and a wise tradeoff should be chosen between a stiff material and large displacement. A noticeable advantage of DEAs is that the stiffness can be adjusted not only by changing the material, but by adding pre-stretch to the membrane.

Secondly, as Rosset *et al.* pointed out, the electrode material is crucial [35]. The mechanical properties of DEAs should be considered together with its electrodes. Similarly to the dielectric material, one should first add as low damping component as possible, and second a trade-off exists between the stiffening impact and the amount of displacement needed. Carbon grease must be avoided. Metallic thin films [80, 180] have in general a large stiffening impact but one could expect them to barely add any viscous damping, whereas softer ones such as dispersed conductive particles in a polymer matrix [79] have a low stiffening impact but add a damping contribution. Au ion implantation might be the best compromise between stretchability and low viscous component [35, 36].

The importance of the actuator structure is obvious: one should keep the mass of the moving parts (frames, hinges, etc.) as low as possible. The lens design proposed by Carpi *et al.* with the liquid lens embedded in the same membrane as the actuator is an excellent example of efficient transduction mechanism between actuator work and change in focal length.

Finally, size matters. It can be considered that the in-plane resonance frequency scales like the inverse of the dimensions: smaller DEAs will have higher resonance frequencies.

8 | Conclusions

This chapter lists the main achievements and scientific outcomes of the work and gives an outlook on future developments of zipping DEAs and DEA-driven microfluidic actuators.

8.1   Main achievements

The thesis has focused on the development of new types of miniature Dielectric Elastomer Actuators for two types of applications where large-displacement integrated actuators operating in contact with liquids are needed: tunable optofluidic lenses and microfluidics.

A first experimental section presents **liquid compatibility tests** that are candidates to be encapsulated as mechanical coupling media or optical fluid between silicone membranes. 12 encapsulated liquids were monitored over up to 37 days. The main scientific outputs of this study will be summarized here. Liquids such as polar solvents considered as compatible with silicones based on swelling tests on bulk parts may penetrate into thin silicone membranes. This is problematic for DEAs since it would lead to device failure. Based on the fact that swelling is dependent on the crosslinking density, it was expected that two silicones membranes with very different mechanical properties would also behave differently when exposed to solvent. However, no difference was observed between Silbione LSR4305 from Bluestar (5 Shore A hardness) and CF19-2186 from NuSil (27 Shore A hardness). The most important result of these tests is that silicone un-polymerized bases and the ionic liquid TF_2N from iolitec perfectly match the requirements of physico-chemical compatibility. Both have moreover negligible vapor pressure (so that the volume does not vary when encapsulated) and high optical transparency (can be used as optical medium) but the viscosity of the pre-polymer is higher than the one of the ionic liquid (mechanical losses). The combination of excellent physico-chemical compatibility with silicones and electrical conductivity of the ionic liquid TF_2N enables its use as liquid electrode for DEAs.

The ability to make liquid electrodes opens new design and integration possibilities. In particular, a liquid electrode does not need to be patterned but is defined by a fluidic channel:

DEAs can be fabricated using fabrication processes of microfluidic technologies. Compared to a patterned electrode, it also solves the issue of the electrical interconnects, since the liquid can be contacted at any point. Finally, liquid electrodes do not induce any stiffening of the elastomer membrane, which would reduce the achievable strain. Fluidically-coupled actuator have two main advantages: the sensitive DEA membrane is protected from being damaged by the object it has to move (such as a random liquid to be pumped). Secondly, the actuator motion can be transferred to another direction and it is possible to play with the relative sizes, materials and prestretch state of the active and passive membrane to achieve force-displacement conversion.

Zipping DEAs have been presented as a new class of actuators that have completely novel features compared to standard DEAs, most remarkably:

- Bistable operation was analytically predicted and has been experimentally demonstrated. On standard DEAs, bistable behavior is achieved by special structures which harness the pull-in instability. For zipping DEAs, the bistable threshold can be tuned by both the chamber geometry and the membrane parameters (silicone type, thickness, prestretch). Moreover, specific chamber sidewalls profiles would enable to obtain deflection versus voltage characteristic of virtually any shape, including multi-sable states.

- The compliant membrane deflects be being electrostatically pulled against a rigid electrode which covers the chamber sidewalls. This would enable effective sealing of holes or channels that cover the sidewalls, for application for instance to valving systems.

An analytical model for the steady state of zipping DEAs has been developed. The model uses the contribution of the mechanical and electrostatic energies, as commonly adopted for zipping devices. However, the use of a soft elastomer makes the problem more complex because of the non-slipping conditions with the sidewalls that must be assumed. As a consequences, the stretch state and the thickness greatly vary along the deflected membrane shape. This very specific deflection state was implemented analytically using hyperelastic energy density functions of the elastomers. Three generation of devices have been fabricated and characterized, for application to microfluidic actuators. The main results obtained from the modeling and from the experimental result are the following:

- The model accurately predicts the effect of sidewalls angle (varied as a parameter) but underestimates the bistable zipping voltage threshold by about 1 kV. This can be attributed to the neglected bending energy.

- It was theoretically predicted and experimentally demonstrated that zipping DEAs have the unique feature of highly tunable bistable operation. Full zipping was measured at 1.5 and 2 kV on mm-size devices with 15 and 22.5° sidewalls angle. The diameter to

depth ratio of the chambers is 1:10 or more, which corresponds to the common aspect ratio of microfluidic channels.

- The membrane should provide sufficient restoring force to overcome stiction on the walls. The most efficient approach is to use prestretch. Experimental tests assess that a value as low as 1.13 is sufficient on the devices studied.

- It was experimentally determined that axi-symmetric chambers are less sensitive to breakdown than pyramidal-shaped ones, and that biasing a zipping DEA with an offset pressure introduces a sidewards-directed motion that does not favor the displaced volume.

- 385 µm vertical deflection was achieved in 2 mm side chambers. Among three silicones tested, CF19-2186 offers the best actuation performance.

The third generation of zipping DEAs are composed three in-line 1.5 mm actuators coupled to 800 µm diameter passive membranes. Their coupled structure protects the sensitive DEA membrane from the liquid that has to be pumped, and biases the active membrane with the internal pressure of the fluid. These actuators have been characterized statically (up to $0.07 \, \text{mm}^3$ displaced volume) and dynamically (45 ms 0 to 90% response time). The displaced volume is however not sufficient to achieve pumping, unlike expected from experimental design test which had been conducted before. The lower displaced volume than expected is most likely due to a sidewards-motion of the bulged center part of the membrane. This puts in evidence the complexity of design of zipping actuators operating with a pressure bias. Routes for further developments will be presented in the next section.

Membrane-based tunable lenses are a type of devices for which DEAs are probably the best choice for an integration of the actuator. This is true not only because of the actuation properties of DEAs (large strains, electrical control, fast response) but also because the membrane which composes the lens is very similar to those used for making the actuators, thus enabling high integration. Two generations of fluidically-coupled tunable lenses have been built and analytically modeled. Main outcomes of this part of the work are:

- Development of three analytical models for the determination of the steady state performance of fluidically-coupled DEA-driven tunable lenses, the last one including hyperelastic material parameters.

- Experimental validation of the models on the two generations of devices.

- Following liquid compatibility tests, experimental proof that the ionic liquid TF_2N can be used as reliable liquid electrode by operating the devices up to 10 to 20 thousand cycles before breakdown under various high voltage conditions, without evidence that the breakdown is due to the use of a liquid electrode.

- 60% tuning range of the focal length (28.5 to 45.5 mm) was measured on the second generation of devices.

- Development of two fabrication processes. On the second generation of devices, the fabrication process is specifically optimized for keeping the best optical quality of the lens membrane, and features adjustment of the operating point. When using thin elastomer membranes to make lenses, the main aberrations come from a direction-dependent mechanical stiffness, which results in non-spherical shape under inflation. This is due to the Mullins effect, and reflects anisotropic stretching prior operation. To address this, the fabrication process of the second generation of lenses includes a water-soluble sacrificial layer to release the membrane from the substrate on which it has been fabricated, and a way to progressively increase the internal pressure after the device has been sealed to avoid over-stretching of the membrane while pushing the trapped air bubbles out of the structure.

- Characterization of the optical aberrations of the second generation of lenses in function of voltage and of operating point using a Schack-Hartmann setup. The optical quality is good: aberration coefficients are in the range of 0.05 μm or below except noticeable astigmatism, and it is observed that optical aberrations decrease with decreasing inflation level.

High speed biconvex tunable lenses have been built and characterized. Their high speed is possible thanks to carefully chosen materials and a semi-automated fabrication process. The device benefits from a very efficient transduction mechanism from the DEA to the lens reported previously in the literature. The main achievements obtained are:

- Fastest lens ever reported regardless of actuation technology with 172 μs 0 to 90% optical response time. This was achieved by using the silicone elastomer CF19-2186 which has a low viscous component, and μm thin electrodes whose impact on the damping of the device is almost negligible. The in-plane design of the lens is also optimal to couple the actuator motion to a change of shape, by minimizing displaced masses.

- A characterization of the optical, electrical and mechanical step responses provides an in-depth understanding of transient state.

- The observation of the lens motion from the side with a high-speed camera explains the transient dynamics of the optical response.

- Measured flat response up to 2 kHz, resonance frequency peak of 4.7 kHz with a gain between 3 and 4, -3 dB bandwidth of 7.4 kHz. This large flat bandwidth is excellent since it means that the device can be driven with an arbitrary signal of that bandwidth without inducing distortions of the optical response.

- Measured focal length tunable range of -28% (19.4 to 14 mm). This is roughly half the performance of the second generation of lenses. A future improvement of the device

may include integration of passive zones on the electrode which may increase the amount of displacement.

Conclusions on this high-speed lens are obvious: it is demonstrated that DEAs based on silicone materials with low viscous component are able to be operated in large signal mode at several kilohertz. The drift in position commonly observed on acrylic elastomer-based DEAs is negligible when using such silicones.

8.2 Outlook

Several types of fluidically-coupled DEA-powered devices have been fabricated and characterized in details.

Although zipping DEAs provide great actuation features such as bistable operation, their use with a bias pressure coming from the encapsulated liquid pocket does not provide the required amount of displacement with the current chamber geometry. Indeed, the displaced volume is lower than expected, probably because the membrane is pulled sidewards rather than only downwards. For further steps of the work toward replacement of the microfluidic pneumatic actuators, the same fabrication process basis can be directly adapted to the normal DEA operation mode by patterning a second compliant electrode. This solution would surely enhance the amount of displaced volume, but is however not new [135] and would definitely abandon the target of low actuation voltages.

This latter objective of voltage reduction should be addressed by tests on fluidically coupled zipping chambers with a cross-section specifically adapted to the pressure bias conditions (for instance manufactured by replica molding) and the use of thin high-quality rigid dielectric coatings such as parylene. But given the fact that the study of zipping DEAs is only at its beginning, this might be a demanding development.

Multilayer actuators and thickness reduction of the active layers may still be the best route to pursue to achieve a reduction of operating voltage (see study on scaling of section 2.2). The membrane thickness can be reduced from at least a factor 2 with the current processes ($15\,\mu m$). Thinner layers are possible, but would require further developments. Multilayer actuators also implies to work on the quality of the electrodes (thin and compliant), on the possibility to stack them and on electrical connection of the buried layers.

Further evolution of the fluidically-coupled tunable lenses may include an increase of the active area surface by changing the number or shape of the actuators, similarly as in Wei's work [158]. Optical properties can be further improved by more care on the fabrication process, notably astigmatism which represents orientation-dependent radii of curvature. Commercially available silicone membranes would be a convenient solution. Imaging applications can be targeted for this high quality large tunable range tunable lens.

The high speed tunable lens presented in this thesis could be used on a varifocal imaging system, as for instance light sheet microscopy. Compared to the current state of the art of light sheet microscopy [173], using the high speed lens developed in this thesis with its settling time lower than 200 µs would increase the time resolution by a factor 10, moreover guaranteeing stable foci during image acquisition. The development of fast varifocal lenses could also be pushed by the arrival on the market of low-cost high-speed cameras[1] that potentially push back the limits of optical techniques such as real time depth from focus [181]. Its further characterization should therefore include a quantified measure of the optical quality, which could result in further evolution of the fabrication process. In its current state, much care has been taken not to stretch the lens membrane anisotropically (molded spherical vacuum pad shape), but one side of the lens is still stretched over its working range.

Other new technologies might be developed in the future to push further the features and integration level of DEAs. Thin film transistors might for instance be integrated directly on the DEA or next to it to provide switching. Self sensing might also boost the autonomy and intelligence of DEAs, similarly as reported on some pioneering works [27]. As stressed in chapter 3, a combination of good electrical and mechanical properties of the elastomer is so crucial to DEAs that a breakthrough in this domain would directly boost all possibilities of application. Up to now, research labs did not reach that goal, but an emerging market of mass-produced devices may push industries to tackle this challenge.

---

[1]http://edgertronic.com/

List of publications

Journal articles

1. **L. Maffli**, S. Rosset, and H. R. Shea. Zipping dielectric elastomer actuators: characterization, design and modeling. *Smart Materials and Structures*, 22(10):104013, 2013.

2. L. De Sio, G. Palermo, V. Caligiuri, A. E. Vasdekis, A. Pane, J.-W. Choi, **L. Maffli**, M. Niklaus, H. R. Shea, C. Umeton. Electro and pressure tunable cholesteric liquid crystal devices based on ion-implanted flexible substrates. *Journal Of Materials Chemistry C*, vol. 1, num. 47, p. 7798-7802, 2013

3. P. Romano, S. Rosset, **L. Maffli**, H. Shea, J. Perruisseau-Carrier. Electromagnetic characterisation of flexible conductive membranes at millimetre-waves. *Electronics Letters* vol. 49, num. 5, p. 353-354, 2013

In preparation

4. **L. Maffli**, M. Ghilardi, S. Rosset, F. Carpi, H. Shea. Ultrafast all-polymer electrically tuneable silicone lenses. Will be proposed as a RSC Soft Matter full paper.

5. **L. Maffli**, S. Rosset, H. Shea. Large tuning range tunable lens with highly integrated polymer actuator and high optical quality. Will be proposed as a journal paper.

Conference proceedings

6. **L. Maffli**, B. O'Brien, S. Rosset, H. Shea. Pump it up. in *Proc. SPIE*, volume 8340, pages 8340-2Q, 2012.

7. **L. Maffli**, S. Rosset, H. Shea. Mm-size bistable zipping dielectric elastomer actuators for integrated microfluidics. in *Proc. SPIE*, volume 8687, pages 86872M, 2013.

8. P. Gebbers, C. Grätzel, **L. Maffli**, C. Stamm and H. Shea. Zipping it up: DEAs independent of the elastomer's electric breakdown field. in *Proc. SPIE*, volume 8340, pages 8340-2P, 2012.

9. S. Rosset, **L. Maffli**, S. Houis and H. Shea. An instrument to obtain the correct biaxial hyperelastic parameters of silicones for accurate DEA modelling. in *Proc. SPIE*, volume 9056, pages 90560M, 2014.

10. P. Romano, S. Rosset, **L. Maffli**, H. Shea, J. Perruisseau-Carrier. Surface impedance measurements of thin flexible metallization at millimeter-waves. 7th European Conference on Antennas and Propagation, Gothenburg, Sweden, April 8-12, 2013

Poster presentations

11. **L. Maffli**, P. Moser, H. Shea. Response time of tunable lenses driven by ion-implanted DEAP actuators. EuroEAP 2011 conference, Pisa, Italy, June 8-9, 2011

12. **L. Maffli**, S. Rosset, H. Shea. Zipping Dielectric Elastomer Actuators for microfluidics. EuroEAP 2012 conference, Potsdam, Germany, May 29-30, 2012

Provisional patent

13. US Provisional Patent Application No. 61/697,393 filed on September 6, 2012.
"HIGH THROUGHPUT CELL STRETCHING DEVICE"
Inventors: Samin AKBARI, Herbert SHEA, Luc MAFFLI

List of Figures

List of Tables

Bibliography

[1] Federico Carpi, Roy Kornbluh, Peter Sommer-Larsen, and Gursel Alici. Electroactive polymer actuators as artificial muscles: are they ready for bioinspired applications? *Bioinspiration & Biomimetics*, 6(4):045006, 2011.

[2] Gursel Alici, Brian Mui, and Chris Cook. Bending modeling and its experimental verification for conducting polymer actuators dedicated to manipulation applications. *Sensors and Actuators A: Physical*, 126(2):396 – 404, 2006.

[3] J. G. Rocha, V. Cardoso, V. Correia, S. Lanceros Mendez, and G. Minas. Piezoelectric micropump for lab-on-a-chip applications. In *Microelectronics (ICM), 2009 International Conference on*, pages 410–413, Dec 2009.

[4] W. Lehmann, H. Skupin, C. Tolksdorf, E. Gebhard, R. Zentel, P. Kruger, M. Losche, and F. Kremer. Giant lateral electrostriction in ferroelectric liquid-crystalline elastomers. *Nature*, 410(6827):447–450, March 2001.

[5] R. Pelrine, R. Kornbluh, Q. Pei, and J. Joseph. High-speed electrically actuated elastomers with strain greater than 100%. *Science*, 287:836–839, 2000.

[6] Feng Xia, Srinivas Tadigadapa, and Q.M. Zhang. Electroactive polymer based microfluidic pump. *Sensors and Actuators A: Physical*, 125(2):346 – 352, 2006.

[7] V. Vunder, A. Punning, and A. Aabloo. Variable-focal lens using electroactive polymer actuator. In *Proc. SPIE 7977*, volume 7977, pages 79771E–79771E–6, 2011.

[8] Ji Sun Yun, Kwang Suk Yang, Nak-Jin Choi, Hyung-Kun Lee, Seung Eon Moon, and Do Hyun Kim. Microvalves based on ionic polymer-metal composites for microfluidic application. *Journal of Nanoscience and Nanotechnology*, 11(7):5975–5979, 2011-07-01T00:00:00.

[9] P. Romano, O. Araromi, S. Rosset, H. Shea, and J. Perruisseau-Carrier. Tunable millimeter-wave phase shifter based on dielectric elastomer actuation. *Applied Physics Letters*, 104(2):–, 2014.

[10] Kwangmok Jung, Ja Choon Koo, Jae do Nam, Young Kwan Lee, and Hyouk Ryeol Choi. Artificial annelid robot driven by soft actuators. *Bioinspiration & Biomimetics*, 2(2):S42, 2007.

Bibliography

[11] Roman Karsten and Helmut F. Schlaak. Adaptive absorber based on dielectric elastomer stack actuator with variable stiffness. In *Proc. SPIE 8340*, volume 8340, pages 834020–834020–8, 2012.

[12] Rahimullah Sarban and Richard W. Jones. Active vibration control using deap actuators. In *Proc. of SPIE Vol. 7642*, volume 7642, pages 76422E–76422E–12, 2010.

[13] Roy D. Kornbluh, Ron Pelrine, Harsha Prahlad, and Richard Heydt. Electroactive polymers: an emerging technology for mems. In *Proc. SPIE 5344*, volume 5344, pages 13–27, 2004.

[14] Ron Pelrine, Peter Sommer-Larsen, Roy D. Kornbluh, Richard Heydt, Guggi Kofod, Qibing Pei, and Peter Gravesen. Applications of dielectric elastomer actuators. In *Proc. SPIE Vol. 4329*, volume 4329, pages 335–349, 2001.

[15] F. Carpi, S. Bauer, and D. De Rossi. Stretching dielectric elastomer performance. *Science*, 330(6012):1759–1761, 2010.

[16] R. E. Pelrine, R. D. Kornbluh, and J. P. Joseph. Electrostriction of polymer dielectrics with compliant electrodes as a means of actuation. *Sensors and Actuators A: Physical*, 64(1):77 – 85, 1998. Tenth IEEE International Workshop on Micro Electro Mechanical Systems.

[17] Iain A. Anderson, Todd A Gisby, Thomas G McKay, Benjamin M. O'Brien, and Emilio P. Calius. Multi-functional dielectric elastomer artificial muscles for soft and smart machines. *Journal Of Applied Physics*, 112:04110–041101–20, 2012.

[18] C. Jordi, S. Michel, and E. Fink. Fish-like propulsion of an airship with planar membrane dielectric elastomer actuators. *Bioinspiration and Biomimetics*, 5:1–9, 2010.

[19] Holger Moessinger and D Brokken. Demonstrating the application of dielectric polymer actuators for tactile feedback in a mobile consumer device. Technical report, 2010.

[20] M. Matysek, P. Lotz, T. Winterstein, and H.F. Schlaak. Dielectric elastomer actuators for tactile displays. In *EuroHaptics conference, 2009 and Symposium on Haptic Interfaces for Virtual Environment and Teleoperator Systems. World Haptics 2009. Third Joint*, pages 290–295, March 2009.

[21] F. Carpi, G. Frediani, S. Turco, and D. De Rossi. Bioinspired tunable lens with muscle-like electroactive elastomers. *Advanced Functional Materials*, 21:4152–4158, 2011.

[22] M. Aschwanden, M. Beck, and Andreas Stemmer. Diffractive transmission grating tuned by dielectric elastomer actuator. *Photonics Technology Letters, IEEE*, 19(14):1090–1092, July 2007.

[23] Takehiro Sugimoto, Kazuho Ono, and Akio Ando. Semicylindrical acoustic transducer from a dielectric elastomer film with compliant electrodes. *Journal of the Acoustical Society of America*, 130:744–752, 2011.

[24] Samin Akbari and Herbert R. Shea. An array of 100 µm x 100 µm dielectric elastomer actuators with 80% strain for tissue engineering applications. *Sensors and Actuators, A: Physical*, 186:236–241, 2012.

[25] Soo Jin Adrian Koh, Christoph Keplinger, Tiefeng Li, Siegfried Bauer, and Zhigang Suo. Dielectric elastomer generators: How much energy can be converted? *IEEE/ASME Transactions on Mechatronics*, 16(1):33–41, 2011.

[26] Roy D. Kornbluh, Ron Pelrine, Harsha Prahlad, Annjoe Wong-Foy, Brian McCoy, Susan Kim, Joseph Eckerle, and Tom Low. From boots to buoys: Promises and challenges of dielectric elastomer energy harvesting. In *Proc. SPIE*, volume 7976, pages 1–19, 2011.

[27] Benjamin M. O'Brien, Emilio P. Calius, Tokushu Inamura, Sheng Q. Xie, and Iain A. Anderson. Dielectric elastomer switches for smart artificial muscles. *Applied Physics A: Materials Science & Processing*, 100:385–389, 2010.

[28] Aurelien R. Hubert, Douglas S. Brodie, Ian A. McAllister, and Jeffrey N. Gleason. Artificial muscle camera lens actuator, 2014.

[29] Zhigang Suo. Theory of dielectric elastomers. *Acta Mechanica Solida Sinica*, 23(6):549 – 578, 2010.

[30] Samuel Rosset. *Metal Ion Implated Electrodes for Dielectric Elastomer Actuators*. PhD thesis, EPFL, 2009.

[31] Roy Kornbluh, Ron Pelrine, Qibing Pei, Seajin Oh, and Jose Joseph. Ultrahigh strain response of field-actuated elastomeric polymers. In *Proc. SPIE*, volume 3987, pages 51–64, 2000.

[32] Michael Wissler and Edoardo Mazza. Modeling and simulation of dielectric elastomer actuators. *Smart Materials and Structures*, 14:1396–1402, 2005.

[33] Christoph Keplinger, Tiefeng Li, Richard Baumgartner, Zhigang Suo, and Siegfried Bauer. Harnessing snap-through instability in soft dielectrics to achieve giant voltage-triggered deformation. *Soft Matter*, 8:285–288, 2012.

[34] Matthias Kollosche, Jian Zhu, Zhigang Suo, and Guggi Kofod. Complex interplay of nonlinear processes in dielectric elastomers. *Phys. Rev. E*, 85:051801, May 2012.

[35] Samuel Rosset, Pit Gebbers, Benjamin M. O'Brien, and Herbert R. Shea. The need for speed. In *SPIE proc.*, volume 8340, pages 834004–834004–12, 2012.

[36] S. Rosset, M. Niklaus, P. Dubois, and H.R. Shea. Large-stroke dielectric elastomer actuators with ion-implanted electrodes. *Journal of Microelectromechanical Systems*, 18(6):1300–1308, 2009.

[37] Samin Akbari, Samuel Rosset, and Herbert R. Shea. Improved electromechanical behavior in castable dielectric elastomer actuators. *Applied Physics Letters*, 102(7):–, 2013.

[38] Guggi Kofod, Peter Sommer-Larsen, Roy Kornbluh, and Ron Pelrine. Actuation response of polyacrylate dielectric elastomers. *Journal of Intelligent Material Systems and Structures*, 14:787–793, 2003.

[39] Jiangshui Huang, Samuel Shian, Roger M. Diebold, Zhigang Suo, and David R. Clarke. The thickness and stretch dependence of the electrical breakdown strength of an acrylic dielectric elastomer. *Applied Physics Letters*, 101(12):–, 2012.

[40] S.J.A. Koh, T. Li, J. Zhou, X. Zhao, W. Hong, J. Zhu, and Z. Suo. Mechanisms of large actuation strain in dielectric elastomers. *Journal of Polymer Science, Part B: Polymer Physics*, 49(7):504–515, 2011.

[41] Xuanhe Zhao and Qiming Wang. Harnessing large deformation and instabilities of soft dielectrics: Theory, experiment, and application. *Applied Physics Reviews*, 1(2):–, 2014.

[42] S. Akbari, Samuel Rosset, and Herbert R. Shea. More than 10-fold increase in the actuation strain of silicone dielectric elastomer actuators by applying prestrain. In *Proc. SPIE 8687*, volume 8687, pages 86871P–86871P–13, 2013.

[43] Gabor Kovacs, Patrick Lochmatter, and Michael Wissler. An arm wrestling robot driven by dielectric elastomer actuators. *Smart Materials and Structures*, 16(2):S306, 2007.

[44] A. Wingert, M.D. Lichter, and S. Dubowsky. On the design of large degree-of-freedom digital mechatronic devices based on bistable dielectric elastomer actuators. *IEEE/ASME Transactions on Mechatronics*, 11(4):448–456, 2006.

[45] G. Kofod, W. Wirges, M. Paajanen, and S. Bauer. Energy minimization for self-organized structure formation and actuation. *Applied Physics Letters*, 90(8):081916 – 081916–3, 2007.

[46] C. Jordi, S. Michel, C. Dürager, A. Bormann, C. Gebhardt, and G. Kovacs. Large planar dielectric elastomer actuators for fish-like propulsion of an airship. In *Proc. SPIE 7642*, volume 7642, pages 764223–764223–12, 2010.

[47] Roy Kornbluh. Fundamental configurations for dielectric elastomer actuators. In Elsevier, editor, *Dielectric Elastomers as Electromechanical Transducers*. Federico Carpi, Danilo De Rossi, Roy Kornbluh, Ronald Edward Pelrine, Peter Sommer-Larsen, 2011.

[48] Iain A. Anderson, Todd A. Gisby, Thomas G. McKay, Benjamin M. O'Brien, and Emilio P. Calius. Multi-functional dielectric elastomer artificial muscles for soft and smart machines. *Journal of Applied Physics*, 112(4):–, 2012.

[49] Gabor Kovacs, Lukas Düring, Silvain Michel, and Giovanni Terrasi. Field induced deformation of active structures based on dielectric elastomers. In *19th International Conference on Adaptive Structures and Technologies*, 2008.

[50] Federico Carpi, Claudio Salaris, and Danilo De Rossi. Folded dielectric elastomer actuators. *Smart Materials and Structures*, 16(2):S300, 2007.

[51] G. Kofod, M. Paajanen, and S. Bauer. Self-organized minimum-energy structures for dielectric elastomer actuators. *Applied Physics A*, 85(2):141–143, 2006.

[52] Samuel Rosset, Oluwaseun A Araromi, Jun Shintake, and Herbert R Shea. Model and design of dielectric elastomer minimum energy structures. *Smart Materials and Structures*, 23(8):085021, 2014.

[53] P. Gebbers, C. Graetzel, L. Maffli, C. Stamm, and H. R. Shea. Zipping it up: Deas independent of the elastomer's electric breakdown field. In *Proc. SPIE*, volume 8340, pages 2P–1–2P–14, 2012.

[54] M.T.A. Saif, B.E. Alaca, and H. Sehitoglu. Analytical modeling of electrostatic membrane actuator for micro pumps. *Journal of Microelectromechanical Systems*, 8(3):335–345, 1999.

[55] J. Han and M.A. Shannon. Smooth contact capacitive pressure sensors in touch- and peeling-mode operation. *IEEE Sensors Journal*, 9(3):199–206, 2009.

[56] Robert Horning. Polymems actuator: a polymer-based microelectromechanical (mems) actuator with macroscopic action. Technical report, Honeywell International, Inc., Plymouth MN, 2002.

[57] Ji Su, Qiming Zhang, Pen-Cheng Wang, Alan. G. MacDiarmid, and Kenneth J. Wynne. Preparation and characterization of electrostrictive polyurethane films with conductive polymer electrodes. *Polymers for Advanced Technologies*, 9(6):317–321, 1998.

[58] Sohil Arora, Tushar Ghosh, and John Muth. Dielectric elastomer based prototype fiber actuators. *Sensors and Actuators A: Physical*, 136(1):321 – 328, 2007. 25th Anniversary of Sensors and Actuators A: Physical.

[59] Soo Jin Adrian Koh, Christoph Keplinger, Tiefeng Li, Siegfried Bauer, and Zhigang Suo. Dielectric elastomer generators: How much energy can be converted? *Mechatronics, IEEE/ASME Transactions on*, 16(1):33–41, Feb 2011.

[60] C Jean-Mistral, A Sylvestre, S Basrour, and J-J Chaillout. Dielectric properties of polyacrylate thick films used in sensors and actuators. *Smart Materials and Structures*, 19(7):075019, 2010.

[61] Ron Pelrine, Roy Kornbluh, Jose Joseph, Richard Heydt, Qibing Pei, and Seiki Chiba. High-field deformation of elastomeric dielectrics for actuators. *Materials Science and Engineering: C*, 11(2):89 – 100, 2000.

[62] P. Brochu. *Dielectric Elastomers for Actuation and Energy Harvesting*. PhD thesis, UCLA, 2012.

[63] Samuel Rosset, Luc Maffli, Simon Houis, and Herbert R Shea. An instrument to obtain the correct biaxial hyperelastic parameters of silicones for accurate dea modelling. In *Proc. SPIE 9056*, volume 9056, pages 90560M–90560M–12, 2014.

[64] Lei Liu, Hualing Chen, Junjie Sheng, Junshi Zhang, Yongquan Wang, and Shuhai Jia. Effect of temperature on the electric breakdown strength of dielectric elastomer. In *Proc. SPIE 9056*, volume 9056, pages 905634–905634–9, 2014.

[65] Silvain Michel, Xuequn Q Zhang, Michael Wissler, Christiane Loewe, and Gabor Kovacs. A comparison between silicone and acrylic elastomers as dielectric materials in electroactive polymer actuators. *Polymer International*, 59(3):391–399, 2010.

[66] F. Carpi and D.D. Rossi. Improvement of electromechanical actuating performances of a silicone dielectric elastomer by dispersion of titanium dioxide powder. *Dielectrics and Electrical Insulation, IEEE Transactions on*, 12(4):835–843, Aug 2005.

[67] Dorina M. Opris, Martin Molberg, Christian Walder, Yee Song Ko, Beatrice Fischer, and Frank A. Nüesch. New silicone composites for dielectric elastomer actuator applications in competition with acrylic foil. *Advanced Functional Materials*, 21(18):3531–3539, 2011.

[68] Zhen Zhang, Liwu Liu, Jiumin Fan, Kai Yu, Yanju Liu, Liang Shi, and Jinsong Leng. New silicone dielectric elastomers with a high dielectric constant. In *Proc. SPIE 6926*, volume 6926, pages 692610–692610–8, 2008.

[69] Giuseppe Gallone, Federico Carpi, Danilo De Rossi, Giovanni Levita, and Augusto Marchetti. Dielectric constant enhancement in a silicone elastomer filled with lead magnesium niobate–lead titanate. *Materials Science and Engineering: C*, 27(1):110 – 116, 2007.

[70] Huu Chuc Nguyen, Vu Thuy Doan, JongKil Park, Ja Choon Koo, Youngkwan Lee, Jae do Nam, and Hyouk Ryeol Choi. The effects of additives on the actuating performances of a dielectric elastomer actuator. *Smart Materials and Structures*, 18(1):015006, 2009.

[71] S. M. Ha, W. Yuan, Q. Pei, R. Pelrine, and S. Stanford. Interpenetrating polymer networks for high-performance electroelastomer artificial muscles. *Advanced Materials*, 18(7):887–891, 2006.

[72] Soon Mok Ha, Wei Yuan, Qibing Pei, Ron Pelrine, and Scott Stanford. Interpenetrating networks of elastomers exhibiting 300electrically-induced area strain. *Smart Materials and Structures*, 16(2):S280, 2007.

[73] Soon Mok Ha, Michael Wissler, Ron Pelrine, Scott Stanford, Gabor Kovacs, and Qibing Pei. Characterization of electroelastomers based on interpenetrating polymer networks. In *Proc. SPIE 6524*, volume 6524, pages 652408–652408–10, 2007.

[74] Zhibin Yu, Xiaofan Niu, Paul Brochu, Wei Yuan, Huafeng Li, Bin Chen, and Qibing Pei. Bistable electroactive polymers (bsep): large-strain actuation of rigid polymers. In *Proc. SPIE 7642*, volume 7642, pages 76420C–76420C–9, 2010.

[75] Xiaofan Niu, Paul Brochu, Brandon Salazar, and Qibing Pei. Refreshable tactile displays based on bistable electroactive polymer. In *Proc. SPIE 7976*, volume 7976, pages 797610–797610–6, 2011.

[76] L. Mullins. Softening of rubber by deformation. *Rubber Chemistry and Technology*, 42(1):339–362, 1969.

[77] V. Linder, B.D. Gates, D. Ryan, B.A. Parviz, and G.M. Whitesides. Water-soluble sacrificial layers for surface micromachining. *Small*, 1(7):730–736, 2005.

[78] K. Flittner, M. Schlosser, and H. F. Schlaak. Influence of solvents on the mechanical properties of dielectric elastomer actuators. In *EuroEAP 2012 International conference on EAP transducers and artificial muscles*, 2012.

[79] L Maffli, S Rosset, and H R Shea. Zipping dielectric elastomer actuators: characterization, design and modeling. *Smart Materials and Structures*, 22(10):104013, 2013.

[80] Mohamed Y Benslimane, Hans-Erik Kiil, and Michael J Tryson. Dielectric electro-active polymer push actuators: performance and challenges. *Polymer International*, 59(3):415–421, 2010.

[81] P. Lotz, M. Matysek, and H.F. Schlaak. Fabrication and application of miniaturized dielectric elastomer stack actuators. *Mechatronics, IEEE/ASME Transactions on*, 16(1):58–66, Feb 2011.

[82] S. Rosset and H.R. Shea. Flexible and stretchable electrodes for dielectric elastomer actuators. *Applied Physics A: Materials Science and Processing*, 110(2):1–27, 2012.

[83] AP. Gerratt, B. Balakrisnan, I Penskiy, and S. Bergbreiter. Batch fabricated bidirectional dielectric elastomer actuators. In *Solid-State Sensors, Actuators and Microsystems Conference (TRANSDUCERS), 2011 16th International*, pages 2422–2425, June 2011.

[84] Samuel Rosset, Muhamed Niklaus, Philippe Dubois, and Herbert R. Shea. Metal ion implantation for the fabrication of stretchable electrodes on elastomers. *Advanced Functional Materials*, 19(3):470–478, 2009.

[85] M. Niklaus and H.R. Shea. Electrical conductivity and young's modulus of flexible nanocomposites made by metal-ion implantation of polydimethylsiloxane: The relationship between nanostructure and macroscopic properties. *Acta Materialia*, 59(2):830 – 840, 2011.

[86] O.A Araromi, I Gavrilovich, J. Shintake, S. Rosset, M. Richard, V. Gass, and H.R. Shea. Rollable multisegment dielectric elastomer minimum energy structures for a deployable microsatellite gripper. *Mechatronics, IEEE/ASME Transactions on*, PP(99):1–9, 2014.

[87] Martin Molberg, Yves Leterrier, Christopher J. G. Plummer, Christian Walder, Christiane Löwe, Dorina M. Opris, Frank A. Nüesch, Siegfried Bauer, and Jan-Anders E. Månson.

Frequency dependent dielectric and mechanical behavior of elastomers for actuator applications. *Journal of Applied Physics*, 106(5):054112–1–7, 2009.

[88] Tzikang Chen. Determining a prony series for a viscoelastic material from time varying strain data. Technical Report TM-2000-210123, NAS 1.15:210123, ARL-TR-2206, L-17978, NASA, May 2000. 2000.

[89] Michael Bozlar, Christian Punckt, Sibel Korkut, Jian Zhu, Choon Chiang Foo, Zhigang Suo, and Ilhan A. Aksay. Dielectric elastomer actuators with elastomeric electrodes. *Applied Physics Letters*, 101(9):091907–1–5, 2012.

[90] Sebastian Döring, Matthias Kollosche, Torsten Rabe, Joachim Stumpe, and Guggi Kofod. Electrically tunable polymer dfb laser. *Advanced Materials*, 23(37):4265–4269, 2011.

[91] Thomas McKay, Benjamin O'Brien, Emilio Calius, and Iain Anderson. An integrated, self-priming dielectric elastomer generator. *Applied Physics Letters*, 97(6):062911–1–2, 2010.

[92] Ron Pelrine, Roy D. Kornbluh, Joseph Eckerle, Philip Jeuck, Seajin Oh, Qibing Pei, and Scott Stanford. Dielectric elastomers: generator mode fundamentals and applications, 2001.

[93] Xiaofan Niu, Ruby Leo, Dustin Chen, Wei Hu, and Qibing Pei. Multilayer stack actuator made from new prestrain-free dielectric elastomers. In *Proc. of SPIE Vol. 8687*, volume 8687, pages 86871M–86871M–8, 2013.

[94] Christoph Keplinger, Jeong-Yun Sun, Choon Chiang Foo, Philipp Rothemund, George M. Whitesides, and Zhigang Suo. Stretchable, transparent, ionic conductors. *Science*, 341(6149):984–987, 2013.

[95] Samuel Rosset, Benjamin M. O'Brien, Todd A Gisby, Daniel Xu, Herbert R Shea, and Iain A Anderson. Self-sensing dielectric elastomer actuators in closed-loop operation. *Smart Materials and Structures*, 22(10):104018–1–10, 2013.

[96] Richard Heydt, Ron Pelrine, Jose Joseph, Joseph Eckerle, and Roy D. Kornbluh. Acoustical performance of an electrostrictive polymer film loudspeaker. *J. Acoust. Soc. Am*, 107(2):833–839, 2000.

[97] R. Sarban, B. Lassen, and M. Willatzen. Dynamic electromechanical modeling of dielectric elastomer actuators with metallic electrodes. *Mechatronics, IEEE/ASME Transactions on*, 17(5):960–967, Oct 2012.

[98] Sungryul Yun, Suntak Park, Bongjae Park, Seung Koo Park, H. Prahlad, P. Von Guggenberg, and Ki-Uk Kyung. Polymer-based flexible visuo-haptic display. *Mechatronics, IEEE/ASME Transactions on*, 19(4):1463–1469, Aug 2014.

[99] Roman Karsten, Klaus Flittner, Henry Haus, and Helmut F. Schlaak. Development of an active isolation mat based on dielectric elastomer stack actuators for mechanical vibration cancellation. In *Proc. of SPIE Vol. 8687*, volume 8687, pages 86870Y–86870Y–8, 2013.

[100] Marc Matysek, Peter Lotz, Klaus Flittner, and Helmut F. Schlaak. Vibrotactile display for mobile applications based on dielectric elastomer stack actuators. In *Proc. of SPIE Vol. 7642*, volume 7642, pages 76420D–76420D–9, 2010.

[101] Nakhiah C. Goulbourne, Mary I. Frecker, and Eric Mockensturm. Electro-elastic modeling of a dielectric elastomer diaphragm for a prosthetic blood pump. In *Proc. SPIE 5385*, volume 5385, pages 122–133, 2004.

[102] Peter Lotz, Marc Matysek, and Helmut F. Schlaak. Peristaltic pump made of dielectric elastomer actuators. In *Proc. of SPIE Vol. 7287*, volume 7287, pages 72872D–72872D–8, 2009.

[103] Luc Maffli, Benjamin M. O'Brien, Samuel Rosset, and Herbert R. Shea. Pump it up. In *Proc. SPIE*, volume 8340, pages 2Q1–2Q16, 2012.

[104] Philippe Jean, Ambroise Wattez, and Guillaume Ardoise. Standing wave tube electro active polymer wave energy converter. In *Proc. of SPIE Vol. 8340*, volume 8340, pages 83400C–1–21, 2012.

[105] Karsten Ahnert, Markus Abel, Matthias Kollosche, Per Jorgen Jorgensen, and Guggi Kofod. Soft capacitors for wave energy harvesting. *J. Mater. Chem.*, 21:14492–14497, 2011.

[106] Samuel Shian, Roger M. Diebold, and David R. Clarke. High-speed, compact, adaptive lenses using in-line transparent dielectric elastomer actuator membranes. In *SPIE proc.*, volume 8687, pages 86872D–86872D–7, 2013.

[107] F. Carpi, G. Frediani, and D. De-Rossi. Hydrostatically coupled dielectric elastomer actuators. *Mechatronics, IEEE/ASME Transactions on*, 15(2):308–315, April 2010.

[108] F. Carpi, G. Frediani, S. Tarantino, and D. De Rossi. Millimetre-scale bubble-like dielectric elastomer actuators. *Polymer International*, 59(3):407–414, 2010.

[109] Samuel Shian, Roger M. Diebold, and David R. Clarke. Tunable lenses using transparent dielectric elastomer actuators. *Opt. Express*, 21(7):8669–8676, Apr 2013.

[110] Gih-Keong Lau, Thanh-Giang La, Li-Lynn Shiau, and Adrian W. Y. Tan. Challenges of using dielectric elastomer actuators to tune liquid lens. In *Proc. of SPIE 9056*, volume 9056, pages 90561J–90561J–6, 2014.

[111] Jessamine Ng Lee, Cheolmin Park, and George M. Whitesides. Solvent compatibility of poly(dimethylsiloxane)-based microfluidic devices. *Analytical Chemistry*, 75(23):6544–6554, 2003.

Bibliography

[112] Ivan Javni, Doo Pyo Hong, and Zoran S. PetroviÄ‡. Soy-based polyurethanes by nonisocyanate route. *Journal of Applied Polymer Science*, 108(6):3867–3875, 2008.

[113] U. S. Aithal, T. M. Aminabhavi, R. H. Balundgi, and S. S. Shukla. Interactions of organic solvents with polyurethane. *Journal of Macromolecular Science, Part C: Polymer Reviews*, 30(1):43–105, 1990.

[114] Thanh-Giang La and Gih-Keong Lau. Very high dielectric strength for dielectric elastomer actuators in liquid dielectric immersion. *Applied Physics Letters*, 102(19):–, 2013.

[115] Baohong Chen, Jing Jing Lu, Can Hui Yang, Jian Hai Yang, Jinxiong Zhou, Yong Mei Chen, and Zhigang Suo. Highly stretchable and transparent ionogels as nonvolatile conductors for dielectric elastomer transducers. *ACS Applied Materials & Interfaces*, 6(10):7840–7845, 2014.

[116] Hristiyan Stoyanov, Matthias Kollosche, Sebastian Risse, Rémi Waché, and Guggi Kofod. Soft conductive elastomer materials for stretchable electronics and voltage controlled artificial muscles. *Advanced Materials*, 25(4):578–583, 2013.

[117] Coleman Murray, David McCoul, Elodie Sollier, Taylor Ruggiero, Xiaofan Niu, Qibing Pei, and DinoDi Carlo. Electro-adaptive microfluidics for active tuning of channel geometry using polymer actuators. *Microfluidics and Nanofluidics*, 14(1-2):345–358, 2013.

[118] Rajendrani Mukhopadhyay. When pdms isn't the best. *Analytical Chemistry*, 79(9):3248–3253, 2007.

[119] E. Favre. Swelling of crosslinked polydimethylsiloxane networks by pure solvents: Influence of temperature. *European Polymer Journal*, 32(10):1183 – 1188, 1996.

[120] A. Werber and H. Zappe. Tunable, membrane-based, liquid-filled micro-lenses. In *Solid-State Sensors, Actuators and Microsystems, 2005. Digest of Technical Papers. TRANSDUCERS '05. The 13th International Conference on*, volume 1, pages 1018–1021, June 2005.

[121] Christoph Friese, Armin Werber, Florian Krogmann, Wolfgang MÃ¶nch, and Hans Zappe. Materials, effects and components for tunable micro-optics. *IEEJ Transactions on Electrical and Electronic Engineering*, 2(3):232–248, 2007.

[122] F. Carpi, G. Frediani, M. Nanni, and D. De Rossi. Granularly coupled dielectric elastomer actuators. *Mechatronics, IEEE/ASME Transactions on*, 16(1):16–23, Feb 2011.

[123] Wei Zhang, Hans Zappe, and Andreas Seifert. Wafer-scale fabricated thermo-pneumatically tunable microlenses. *Light: Science & Applications*, 3(e145):1–6, 2014.

[124] P. Abgrall and A.-M. Gué. Lab-on-chip technologies: making a microfluidic network and coupling it into a complete microsystem - a review. *Journal of Micromechanics and Microengineering*, 17(5):R15, 2007.

[125] Todd Thorsen, Sebastian J. Maerkl, and Stephen R. Quake. Microfluidic large-scale integration. *Science*, 298(5593):580–584, 2002.

[126] Luis M. Fidalgo and Sebastian J. Maerkl. A software-programmable microfluidic device for automated biology. *Lab on a Chip*, 11:1612–1619, 2011.

[127] E. C. Jensen, A. M. Stockton, T. N. Chiesl, J. Kim, A. Bera, and R. A. Mathies. Digitally programmable microfluidic automation for multiscale combinatorial mixing and sample processing. *Lab on Chip*, 13:288–296, 2013.

[128] M. A. Unger, H.-P. Chou, T. Thorsen, A. Scherer, and S. R. Quake. Monolithic microfabricated valves and pumps by multilayer soft lithography. *Science*, 288:113–116, 2000.

[129] Amit V. Desai, Joshua D. Tice, Christopher A. Apblett, and Paul J. A. Kenis. Design considerations for electrostatic microvalves with applications in poly(dimethylsiloxane)-based microfluidics. *Lab Chip*, 12:1078–1088, 2012.

[130] M.-P. Chang and M. M. Maharbiz. Electrostatically-driven elastomer components for user-reconfigurable high density microfluidics. *Lab on a Chip*, 9:1274–1281, 2009.

[131] Roy Kornbluh. *Dielectric Elastomers as Electromechanical Transducers*, chapter 8: Fundamental Configurations for Dielectric Elastomer Actuators, pages 79–90. Elsevier, 2008.

[132] F. Carpi, G. Frediani, and D. De Rossi. Hydrostatically coupled dielectric elastomer actuators. *IEEE/ASME Transactions on Mechatronics*, 15(2):308–315, 2010.

[133] F. Carpi, C. Salaris, and D. De Rossi. Folded dielectric elastomer actuators. *Smart Materials and Structures*, 16(2):S300–S305, 2007.

[134] G. Kovacs, L. Duering, S. Michel, and G. Terrasi. Stacked dielectric elastomer actuator for tensile force transmission. *Sensors and Actuators, A: Physical*, 155(2):299–307, 2009.

[135] J. J. Loverich, I. Kanno, and H. Kotera. Concepts for a new class of all-polymer micropumps. *Lab Chip*, 6:1147–1154, 2006.

[136] Jens Branebjerg and Peter Gravesen. A new electrostatic actuator providing improved stroke length and force. In *Proceedings of the IEEE Micro Electro Mechanical Systems Workshop*, pages 6–11, 1992.

[137] C. Divoux, J. Charton, W. Schwartz, E. Stadler, J. Margail, L. Jocou, T. Enot, J. C. Barbe, J. Chiaroni, and P. Berruyer. A novel electrostatic actuator for micro deformable mirrors: fabrication and test. In *TRANSDUCERS, Solid-State Sensors, Actuators and Microsystems, 12th International Conference on, 2003*, volume 1, pages 488–491 vol.1, June 2003.

[138] R. Legtenberg, J. Gilbert, S.D. Senturia, and M. Elwenspoek. Electrostatic curved electrode actuators. *Microelectromechanical Systems, Journal of*, 6(3):257–265, Sep 1997.

Bibliography

[139] Jinsheng Gao, Dongzhi Guo, S. Santhanam, YingJu Yu, A.J.H. McGaughey, Shi-Chune Yao, and G.K. Fedder. Release and transfer of large-area ultra-thin pdms. In *Micro Electro Mechanical Systems (MEMS), 2014 IEEE 27th International Conference on*, pages 544–547, Jan 2014.

[140] Jessica Melin and Stephen R Quake. Microfluidic large-scale integration: the evolution of design rules for biological automation. *Annu. Rev. Biophys. Biomol. Struct*, 36:213–231, 2007.

[141] J.-S. Plante and S. Dubowsky. Large-scale failure modes of dielectric elastomer actuators. *International Journal of Solids and Structures*, 43(25-26):7727–7751, 2006.

[142] Q. Wang, L. Zhang, and X. Zhao. Creasing to cratering instability in polymers under ultrahigh electric fields. *Physical Review Letters*, 106(11):118301, 1–4, 2011.

[143] I. M. Ward and J. Sweeney. *The Mechanical Properties of Solid Polymers*. John Wiley & Sons, Ltd, Chichester, 2004.

[144] Denis Bartolo, Guillaume Degre, Philippe Nghe, and Vincent Studer. Microfluidic stickers. *Lab Chip*, 8:274–279, 2008.

[145] T. Bourlet, A. Signori-Schmuck, L. Roche, V. Icard, H. Saoudin, M.-A. Trabaud, J.-C. Tardy, P. Morand, B. Pozzetto, R. Ecochard, and P. André. Hiv-1 load comparison using four commercial real-time assays. *Journal of Clinical Microbiology*, 49(1):292–297, 2011.

[146] Robert Graham. A variable focus lens and its uses. *Journal of the Optical*, 30:560–563, July 1940.

[147] B. Berge and J. Peseux. Variable focal lens controlled by an external voltage: An application of electrowetting. *Eur. Phys. J. E*, 3:159–163, 2000.

[148] N.-T. Nguyen. Micro-optofluidic lenses: A review. *Biomicrofluidics*, 4(3):031501–1–15, 2010.

[149] N.B. Justis, D.Y. Zhang, and Y. H Lo. Integrated dynamic fluidic lens system for in vivo biological imaging. In *Engineering in Medicine and Biology Society, 2004. IEMBS '04. 26th Annual International Conference of the IEEE*, volume 1, pages 1256–1259, Sept 2004.

[150] H.-C. Lin, M.-S. Chen, and Y.-H. Lin. A review of electrically tunable focus liquid crystal lenses. *Trans. on Electrical and Electronic Materials*, 12(6):234–240, Dec 2011.

[151] Kuo-Sheng Chao, Meng-Shiang Lin, and Ruey-Jen Yang. An in-plane optofluidic microchip for focal point control. *Lab Chip*, 13:3886–3892, 2013.

[152] D. Graham-Rowe. Liquid lenses make a splash. *Nature photonics*, pages 2–4, 2006.

182

[153] Randall Marks, David L. Mathine, Jim Schwiegerling, Gholam Peyman, and Nasser Peyghambarian. Astigmatism and defocus wavefront correction via zernike modes produced with fluidic lenses. *Appl. Opt.*, 48(19):3580–3587, Jul 2009.

[154] Peter Liebetraut, Sebastian Petsch, Wolfgang Mönch, and Hans Zappe. Tunable solid-body elastomer lenses with electromagnetic actuation. *Appl. Opt.*, 50(19):3268–3274, Jul 2011.

[155] Hongbin Yu, Guangya Zhou, Fook Siong Chau, and Sujeet K. Sinha. Tunable electromagnetically actuated liquid-filled lens. *Sensors and Actuators A: Physical*, 167(2):602 – 607, 2011. Solid-State Sensors, Actuators and Microsystems Workshop.

[156] Seok Woo Lee and Seung S. Lee. Focal tunable liquid lens integrated with an electromagnetic actuator. *Applied Physics Letters*, 90(12):–, 2007.

[157] Hiromasa Oku, Koichi Hashimoto, and Masatoshi Ishikawa. Variable-focus lens with 1-khz bandwidth. *Opt. Express*, 12(10):2138–2149, May 2004.

[158] Kang Wei, Nicholas Wade Domicone, and Yi Zhao. Electroactive liquid lens driven by an annular membrane. *Opt. Lett.*, 39(5):1318–1321, Mar 2014.

[159] Muhamed Niklaus, Samuel Rosset, and Herbert Shea. Array of lenses with individually tunable focal-length based on transparent ion-implanted eaps. In *Proc. SPIE 7642*, volume 7642, pages 76422K–76422K–12, 2010.

[160] J. E. Adkins and R. S. Rivlin. Large elastic deformations of isotropic materials. ix. the deformation of thin shells. *Phil. Trans. R. Soc. Lond. A*, 244(888):505–531, 1952.

[161] L.J. Hart-Smith and J.D.C. Crisp. Large elastic deformations of thin rubber membranes. *International Journal of Engineering Science*, 5(1):1 – 24, 1967.

[162] Henrik Bruus. *Theoretical Microfluidics*. Oxford University Press Inc., New York, 2001 edition, 2008.

[163] N.C. Goulbourne, E.M. Mockensturm, and M.I. Frecker. Electro-elastomers: Large deformation analysis of silicone membranes. *International Journal of Solids and Structures*, 44(9):2609 – 2626, 2007.

[164] N. Reuge, F. M. Schmidt, Y. Le Maoult, M. Rachik, and F. Abbé. Elastomer biaxial characterization using bubble inflation technique. i: Experimental investigations. *Polymer Engineering & Science*, 41(3):522–531, 2001.

[165] H. Vaughan. Inflation of a finitely stretched circular membrane. *The Quarterly Journal of Mechanics and Applied Mathematics*, 34(1):111–127, 1981.

[166] Lauren R. Finkenauer and Carmel Majidi. Complaint liquid metal electrodes for dielectric elastomer actuators. In *Proc. SPIE 9056*, volume 9056, pages 90563I–90563I–7, 2014.

[167] Yiin-Kuen Fuh, Ming-Xin Lin, and Shyong Lee. Characterizing aberration of a pressure-actuated tunable biconvex microlens with a simple spherically-corrected design. *Optics and Lasers in Engineering*, 50(12):1677 – 1682, 2012.

[168] Armin Werber and Hans Zappe. Tunable microfluidic microlenses. *Appl. Opt.*, 44(16):3238–3245, Jun 2005.

[169] Yiin Kuen Fuh, Kuo Chan Hsu, Jia Ren Fan, and Ming Xien Lin. Induced aberrations by combinative convex/concave interfaces of refractive-index-mismatch and capability of adaptive optics correction. *Microwave and Optical Technology Letters*, 53(11):2610–2615, 2011.

[170] Florian Schneider, Jan Draheim, Robert Kamberger, Philipp Waibel, and Ulrike Wallrabe. Optical characterization of adaptive fluidic silicone-membrane lenses. *Opt. Express*, 17(14):11813–11821, Jul 2009.

[171] Marti Duocastella, Bo Sun, and Craig B. Arnold. Simultaneous imaging of multiple focal planes for three-dimensional microscopy using ultra-high-speed adaptive optics. *Journal of Biomedical Optics*, 17(5):050505–1–050505–3, 2012.

[172] Ryoichi Kuwano, Tsuyoshi Tokunaga, Yukitoshi Otani, and Norihiro Umeda. Liquid pressure varifocus lens. *Optical Review*, 12(5):405–408, 2005.

[173] F. O. Fahrbach, F. F. Voigt, B. Schmid, F. Helmchen, and J. Huisken. Rapid 3d light-sheet micromicro with a tunable lens. *Optics Epxress*, 21(18):21010–21026, 2013.

[174] Alexandre Mermillod-Blondin, Euan McLeod, and Craig B. Arnold. High-speed varifocal imaging with a tunable acoustic gradient index of refraction lens. *Opt. Lett.*, 33(18):2146–2148, Sep 2008.

[175] Hongwen Ren, Yun-Hsing Fan, Yi-Hsin Lin, and Shin-Tson Wu. Tunable-focus microlens arrays using nanosized polymer-dispersed liquid crystal droplets. *Optics Communications*, 247(1-3):101 – 106, 2005.

[176] S. Kuiper and B. H. W. Hendriks. Variable-focus liquid lens for miniature cameras. *Applied Physics Letters*, 85(7):1128–1130, 2004.

[177] Tongqing Lu, Shengqiang Cai, Huiming Wang, and Zhigang Suo. Computational model of deformable lenses actuated by dielectric elastomers. *Journal of Applied Physics*, 114(10):104104–1–8, 2013.

[178] Roushanak Rahmat, Aamir Saeed Malik, Nidal Kamel, and Humaira Nisar. 3d shape from focus using lulu operators and discrete pulse transform in the presence of noise. *Journal of Visual Communication and Image Representation*, 24(3):303 – 317, 2013.

[179] M. Duocastella and C. B. Arnold. Enhanced depth of field laser processing using an ultra-high-speed axial scanner. *Applied Physics Letters*, 102(6):061113–1–4, 2013.

[180] S. Sasikala, K.T. Madhavan, G. Ramesh, and P. Chowdhury. The electro-mechanical performance of electro-active polymer based actuators fabricated using ultra thin metal electrode. *Sensors and Actuators A: Physical*, 207(0):43 – 48, 2014.

[181] Jawad Humayun and AamirSaeed Malik. Real-time processing for shape-from-focus techniques. *Journal of Real-Time Image Processing,* pages 1–14, 2013.

LUC MAFFLI

luc.maffli@gmail.com
Route du Closel 10 ⋄ CH-2074 Marin-Epagnier

EDUCATION

Ecole Polytechnique Fédérale de Lausanne (EPFL), LMTS   2010-2014
Doctoral program in microsystems and microelectronics

EPFL, MSc in micro-engineering   2010
Orientation micro and nanosystems

EXPERIENCE

EPFL-LMTS   2010 - 2014
Teaching assistant

· Statics and Dynamics class

EPFL-LME   2003 - 2008
Student assistant

· Technical assignments for a cooperation project in the High Atlas, Morocco
· Tasks in the frame of the STS (Science-Technique-Société) program of the EPFL

TECHNICAL SKILLS

Cleanroom processing	standard silicon processes, SU-8
Programming	LabVIEW, C/C++, Matlab, Assembly
Specialized softwares	Solidworks, masks design (Silvaco Expert)

LANGUAGE SKILLS

French	fist language
English	C1
German	B2